UNIVERSITÀ DEGLI STUDI DI MODENA E REGGIO EMILIA

Scuola di Dottorato in
Physics and Nano Sciences
XXVIII Ciclo

Supramolecular assembly of Single-Molecule Magnets with redox-active centres: synthetic, structural and magnetic studies

Candidato: *Andrea Nava*
Supervisor: *Prof. Andrea Cornia*

Anno Accademico 2016 – 2017

Contents

List of acronyms and abbreviations

ac	Alternating Current
anh	anhydrous
CTM	Cantilever Torque Magnetometry
dc	Direct Current
DCM	dichloromethane
DMSO	dimethylsulphoxide
EA	Elemental Analysis
ER	Electron Reservoir
ESI	Electron Spray Ionization
ET	Electron Transfer
Et_2O	diethyl ether
EtOH	ethanol
Fc	Ferrocene
HF-EPR	High-Frequency Electron Paramagnetic Resonance
Hdpm	Dipivaloylmethane
^{1}H NMR	Proton Nuclear Magnetic Resonance
MALDI	Matrix-Assisted Laser Desorption Ionization
MeOH	methanol
MS	Mass Spectroscopy
MW	Molecular Weight
OS	oxidation state
p^{t}BuTPP	Tetra(*p*-*tert*-butylphenyl)porphyrin
QT	Quantum Tunneling
QTM	Quantum Tunneling Mechanism
SMM	Single-Molecule Magnet
SQUID	Superconducting QUantum Interference Device
THF	tetrahydrofuran
ToF	Time-of-Flight
XRD	X-Ray Diffraction
zfs	zero-field splitting

1 Introduction

The interest in nanoscience has certainly increased in the last years due to the promising properties for systems with reduced dimensions. When approaching the nanoscale, unconventional properties arise which make nanosystems interesting for technological developments and also for fundamental research. Molecular electronics is one of the fields that first attracted attention in this sense. In particular, Single-Molecule Magnets (SMMs) have attracted a lot of interest because of their peculiar quantum properties, such as slow magnetic relaxation, quantum tunnelling (QT) of the magnetization and quantum phase interference.[1] All these properties look very promising in view of possible future developments in ultra-high density memories or quantum information processing.

To this aim weak coupling between two or more SMMs can be used to further enhance their functionality. Furthermore, SMMs whose magnetic behaviour can be switched by applying external stimuli[2] – such as temperature, light, pressure, electric fields, magnetic fields, oxidation/reduction, spin injection, etc. – is appealing for applications.

Starting from these ideas, various research groups have focused their attention on the possibility to reversibly tune SMM behaviour on different systems. A very recent example is given by two-dimensional Dy(III) and Ho(III) homometal coordination polymers containing the photochromic ligand 1,2-bis(5-carboxyl-2-methyl-3-thienyl)perfluorocyclopentene (DTE).[3] The Dy(III) compound exhibits slow magnetic relaxation without an external dc field when the DTE ligand is in both open and closed forms, but with significantly different QT relaxation processes. Although reversible photoswitching of magnetic properties was not demonstrated, photo-isomerization changes the structure of the ligand and affects the coordination sphere of Dy(III) ions.

In 2015, Pinkowicz et al. published a work demonstrating that the energy barriers of a particular class of trinuclear complexes (containing Mn, Fe, and Ru or Os) can be reversibly switched several times by desolvation/solvation of the crystalline phases without decomposition.[4]

Furthermore, Ababei and co-workers in 2013 synthesized a coordination network of SMMs linked by spin-crossover units inducing thermally- and photo-reversible magnetic and optical properties.[5]

I was inspired by these results and undertook the design of supramolecular compounds based on SMM building blocks and tunable redox-active groups.

In this Thesis I'm going to present the experimental work I performed on the synthesis of supramolecular assemblies of Fe_4 clusters - the chosen class of SMMs - with different redox active moieties. In particular, the aim of this work is to study the interplay between SMMs and units which can act as electrons reservoirs (ER). The research required a multidisciplinary approach which ranged from organic and inorganic synthesis, through structural characterization, to magnetic studies on polycrystalline and single-crystal samples.

The Thesis is thus organized as follows: **Chapter 2** briefly describes the main features of SMMs and their properties; in particular propeller-like Fe_4 clusters are introduced. **Chapter 3** presents the first system made by an Fe_4 complex and two ferrocene pendants and the attempts made to oxidize one of the two ferrocene units. **Chapter 4** introduces a new Fe_4 SMM with two tripodal ligands bearing a pyridyl ring and then suitable to coordinate metal ions. In **Chapter 5** I show the synthesis and characterization of a new class of chain compounds featuring Fe_4 units and diruthenium paddlewheels, whose magnetic behaviour is further analyzed in **Chapter 6**. Finally, **Chapter 7** reports the main results obtained assembling an Fe_4 cluster with a ruthenium(II) porphyrin, a unit which is photo-excitable. In **Chapter 8** the first three-dimensional Metal-Organic Frameworks (3D-MOF) of Fe_4 clusters and silver(I) ions will be shown, together with its complete magnetic characterization.

2 Single-Molecule Magnets and propeller-like Fe_4 clusters

2.1 Introduction

The last two decades have been characterized by an intense research on a new class of molecular materials known as SMMs.[1,6] Such systems are paramagnetic metal complexes exhibiting slow relaxation of their magnetization, purely of molecular origin. Generally such systems are polynuclear transition-metal complexes,[7] but since 2003 several mononuclear complexes (with lanthanide, actinide or transition-metal ions)[8–10] were synthesized showing SMM behaviour and they have also been called “single-ion magnets” or “mononuclear single-molecule magnets”.

Due to their interesting quantum properties like QT of magnetization and quantum phase interference, SMMs have been proposed as systems to store information,[1,11–13] although the temperatures (around liquid helium) at which the hysteresis is observed nowadays remain prohibitive for technological applications, except for some rare cases.[14]

In any case, these compounds are continuously studied for their quantum phenomena. The possibility to address the magnetism of a single molecule is fundamental to build electronic devices using SMMs; furthermore, this gives the possibility to combine the quantum dynamics of SMMs with transport properties, in the field known as molecular spintronics.[11,13,15,16]

For such applications, weak coupling between two or more SMMs can be used to further enhance their functionality. First, each SMM can act as a bias on its neighbours, generating a better memory effect. Second, entanglement between quantum states is an important resource for quantum information processing.

This first chapter contains a brief introduction about key concepts in molecular nanomagnetism, *i.e.* magnetic exchange, magnetic anisotropy and magnetization dynamics. Furthermore, I show some examples of SMMs and their arrangement in supramolecular assemblies and networks. Finally, I describe the class of SMMs used in this work, *i.e.* propeller-like tetrairon(III) complexes, which I usually refer to as **Fe_4**.[17–19]

2.2 Fundaments of Single-Molecule Magnets

2.2.1 Magnetic superexchange interactions

At the origin of slow magnetic relaxation in most SMMs[1] is a high-spin ground state (S) and a strong easy-axis magnetic anisotropy, which corresponds to a large and negative zfs parameter D (for a clear-cut example of a SMM which does not fulfils these requirements, see Ref [20]). If one excludes the case of mononuclear lanthanide complexes of high symmetry[9,10,21,22] and recent developments in mononuclear transition-metal compounds,[9,23] all other molecules presenting slow relaxation of the magnetization are constituted by polynuclear complexes of interacting paramagnetic metal ions. Although considerable next-nearest neighbour interactions are sometimes encountered, only nearest-neighbour couplings between magnetic sites are usually considered. The dominant interaction is often Heisenberg superexchange (“exchange” in brief) and the corresponding spin Hamiltonian is written as:

$$H_{ex} = \sum_{i<j} J_{ij} \mathbf{S}_i \cdot \mathbf{S}_j \tag{2.1}$$

where *i* and *j* run over all metal sites of the cluster.[24,25] The resulting spin states are derived by following a vector coupling procedure and are characterized by a total spin quantum number *S*.[25] The energy of the different *S* states can be calculated analytically only in some high symmetry cases, in particular when a central spin exhibits the same exchange interaction with the neighbouring ones. This is also known as the Kambe approach[26] and spin systems comprising up to 13 coupled spins have been handled in this way.[27] Tetranuclear units encountered in the family of Fe_4 clusters[28,29] and schematized in Fig. 2.1 can be treated with this approach.

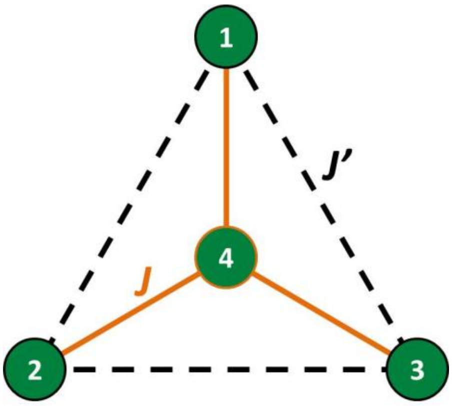

Fig. 2.1. Coupling scheme of the spin centres in a tetranuclear cluster like **Fe**$_4$.

Assuming threefold symmetry, the spin Hamiltonian that describes exchange interactions is

$$H_{ex} = J[\mathbf{S}_1 \cdot \mathbf{S}_4 + \mathbf{S}_2 \cdot \mathbf{S}_4 + \mathbf{S}_3 \cdot \mathbf{S}_4] + J'[\mathbf{S}_1 \cdot \mathbf{S}_2 + \mathbf{S}_2 \cdot \mathbf{S}_3 + \mathbf{S}_1 \cdot \mathbf{S}_3] \tag{2.2}$$

Every spin state arising from the coupling of the four spins is defined by three quantum numbers: $|S_a, S_{\text{ext}}, S>$, where $\mathbf{S}_a = \mathbf{S}_1 + \mathbf{S}_2$, $\mathbf{S}_{\text{ext}} = \mathbf{S}_a + \mathbf{S}_3$, and $\mathbf{S} = \mathbf{S}_4 + \mathbf{S}_{\text{ext}}$. There are many spin states with the same S_T but differing for the other quantum numbers. Owing to the high symmetry, however, the total energy depends only on two of them, S and S_{ext}, according to

$$E(S, S_{\text{ext}}) = \frac{J}{2}[S(S+1) - S_{\text{ext}}(S_{\text{ext}}+1) - S_4(S_4+1)] + \frac{J'}{2}[S_{\text{ext}}(S_{\text{ext}}+1) - S_3(S_3+1) - S_2(S_2+1) - S_1(S_1+1)] \tag{2.3}$$

Considering that all terms involving local spins S_i introduce only an energy offset, Eq. 2.3 can be simplified as

$$E(S, S_{\text{ext}}) = \frac{J}{2}[S(S+1) - S_{\text{ext}}(S_{\text{ext}}+1)] + \frac{J'}{2}[S_{\text{ext}}(S_{\text{ext}}+1)] \tag{2.4}$$

Thus, it is necessary only to properly count all possible states arising from the coupling of four spins, in order to consider their correct degeneracy and to calculate their energy according to Eq. 2.4. Knowledge of the energy of the spin states then gives full access to the thermodynamic properties of the spin system. In general, however, it is necessary to diagonalize big matrices and, as soon as the number of magnetic centres increases, the calculation of the energy of all resulting spin states becomes very demanding, and different approaches have been developed to simplify the task.[30,31]

2.2.2 Magnetic anisotropy

As stated in 2.2.1, in most SMMs a high-spin ground state is accompanied by an easy-axis magnetic anisotropy. Unlike in traditional magnets, where surface, strain and shape anisotropies also play a role, magnetic anisotropy in SMMs is mostly of magnetocrystalline origin and is brought in by a combination of spin-orbit coupling with the low-symmetry environment around the metal centres. Dipolar contributions are in most cases negligible. A quantitative treatment of the magnetic anisotropy is based on the effective spin Hamiltonian approach where only the spin variables appear, while the orbital contributions are introduced through parameters. For a system with no symmetry at all and spin S, the relevant spin Hamiltonian can be written as:

$$H_{anis} = \mathbf{S} \cdot \mathbf{D} \cdot \mathbf{S} = D\left[S_z^2 - \frac{1}{3}S(S+1)\right] + E(S_x^2 - S_y^2) \tag{2.5}$$

where the coordinate frame *xyz* is taken along the principal axes of the zfs tensor **D**. Its diagonal elements are related to the zero-field splitting parameters D and E, which describe the axial and rhombic components of anisotropy, according to the relations $D = D_{zz} - (1/2)D_{xx} - (1/2)D_{yy}$ and $E = ½(D_{xx} - D_{yy})$. By convention, $0 \leq E \leq |D|/3$ because going beyond this limit corresponds merely to a different choice of reference frame. The effect of the magnetic anisotropy on the $(2S+1)$ states of the spin multiplet is that of removing their degeneracy even in the absence of an external field. The term $(1/3)S(S+1)$ introduces an offset of all levels to preserve the centre of gravity of the energy spectrum and can thus be dropped off when dealing with the relative energies within the S multiplet.

A negative D in Eq. 2.5 implies that the system can be more easily magnetized when the field is applied along the principal, *i.e.* z, axis, giving rise to what is called an easy axis magnetic anisotropy, and the ground doublet is characterized by $M_S = \pm S$, which corresponds to two potential wells separated by an energy barrier as reported in Fig. 2.2.

In the case of a spin system constituted by a single paramagnetic centre carrying $2S$ unpaired electrons, the value of D can be experimentally determined through Electron Paramagnetic Resonance (EPR),[32] or alternatively through Inelastic Neutron Scattering (INS).[33] Also magnetometry, especially if performed on a single crystal sample, can provide accurate values. The magnetic anisotropy can also be estimated theoretically.

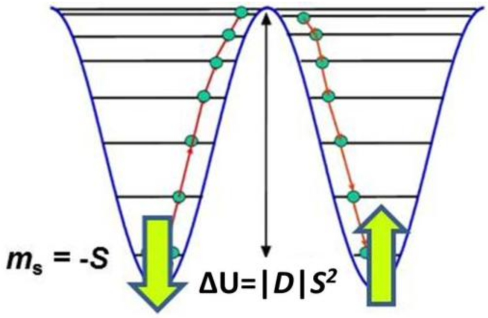

Fig. 2.2 Splitting in zero field of the 2S+1 levels due to an axial anisotropy with $D < 0$, as described in Eq. 2.5. The application of a strong field populates selectively one of the two wells and equilibrium in zero field is re-established by transferring population in the other well through a multiphonon process.

The situation is more complicated in the case of a polynuclear system, such as most SMMs. In general, when working with first row transition metal ions, it is found that the magnetic anisotropy is weaker than intramolecular exchange interactions. Hence, the resulting states are well described by the total spin quantum number, as derived from Eq. 2.1, and the magnetic anisotropy is introduced as a perturbation. The magnetic anisotropy of a given total spin state S_T can be related to the single ion contributions, or to the anisotropic part of the interaction, either dipolar or exchange in nature, by using projection techniques:[34]

$$\mathbf{D}_{S_\mathrm{T}} = \sum_i d_i \mathbf{D}_i + \sum_{i>j} d_{ij} \mathbf{D}_{ij} \tag{2.6}$$

where i and j refer to the magnetic centres inside the SMM. The projection coefficients d_i and d_{ij} depend on how the individual spins project on the total spin state under consideration, and $\mathbf{D}_i$ and $\mathbf{D}_{ij}$ are anisotropy tensors associated with the single ion contributions and with two-spin interactions, respectively. The calculation of d_i and d_{ij} is based on a relatively simple recursive algorithm, and very small values are typically found. This indicates that it is not straightforward to combine a large spin with a large magnetic anisotropy.

Slow relaxation of magnetization is normally exhibited by molecular clusters that combine a high spin ground state (S) (*i.e.* many unpaired electrons) and a large easy-axis type magnetic anisotropy, as measured by the axial zfs parameter, $D < 0$. This leads to a significant energy barrier to magnetization reversal between the two M_S wells, whose upper limit (ΔU) is given by $|D|S^2$ or $|D|(S^2 - ¼)$ for integer and half-integer spins, respectively.[35]

2.2.3 The dynamics of the magnetization

Slow relaxation of the magnetization was first observed in the ancestor cluster called **Mn_{12}ac** (featuring twelve coupled manganese ions in the +3 and +4 oxidation states), thanks to alternating current (ac) susceptibility measurements. Operating at sufficiently low temperature, the relaxation becomes so slow that an opening of the magnetic hysteresis is observable.[36] This dramatic slowing down has its origin in the double well potential reported in Fig. 2.2, characteristic of a large spin with a negative D parameter. The application of a magnetic field has the effect of stabilizing and populating preferentially one of the two wells. When the field is removed, an equal population of the two wells, corresponding to zero magnetization, is only re-established by transferring part of the population to the other well. Transitions from one M_S state to another are promoted by deformations of the metal coordination environment (rotations, vibrations and geometrical strains) which can affect the spin degrees of freedom thanks to spin-orbit coupling. However, at a first level of approximation, these deformations are only able to induce transitions between states differing in M_S by ±1 and ±2. To overcome the full energy barrier a multiphonon mechanism is therefore necessary. In analogy to a chemical reaction involving many elementary processes, the overall rate is determined by the slowest step. In the case of an SMM, the slowest step is the one on top of the barrier, because at low temperature the highest states are less populated and also because of the quadratic energy spacing induced by Eq. 2.5. The combination of these two factors yields an exponential temperature dependence of the relaxation time, which is typical of a thermally-activated mechanism:

$$\tau = \tau_0 \exp(U_{\mathrm{eff}}/k_B T) \qquad (2.7)$$

where $U_{\mathrm{eff}} \leq \Delta U$ is the effective anisotropy energy barrier and τ_0 is a pre-exponential factor representing the characteristic time of the process.

Although apparently coupling more and more spins to increase S should lead to a quadratic effect on the height of the barrier (as described above, the energy barrier is $|D|S^2$ for integer or $|D|(S^2 - ¼)$ for half-integer spins), projection coefficients in Eq. 2.6 make the barrier to scale linearly with S.[37]

In Fe_4 clusters[17,19,28] and other SMMs[35,38] it is possible to observe also quantum effects, such as the tunnelling of the magnetization. Whenever two states lying on opposite sides of the barrier have the same energy and the wavefunction of the left well extends to the right well with a nonzero value, the probability of observing a through-barrier transition is different from zero[39]. This phenomenon was first detected in the ac magnetic susceptibility of **$Mn_{12}ac$** and then, more spectacularly, in its hysteresis curve, which is characterized by steps at the resonant fields (see Fig. 2.3). In fact the vertical segments of the curve reflect accelerations of the relaxation rate and thus can be attributed to the QT mechanism (QTM)[36].

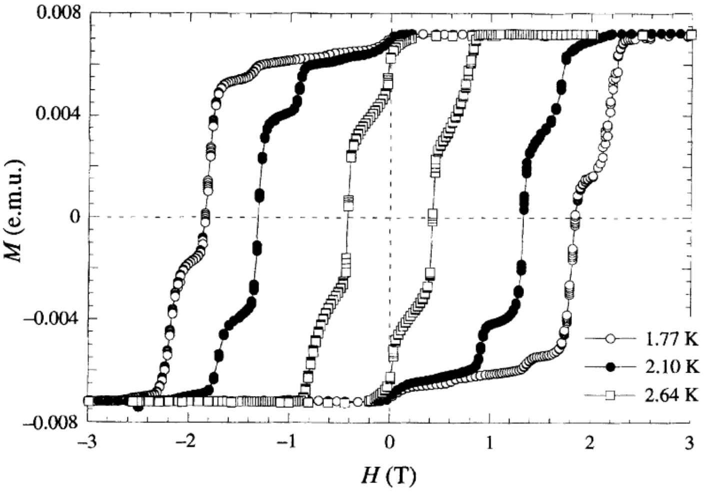

Fig. 2.3. Hysteresis loops of a Mn_{12}ac single crystal at different temperatures with the field applied along the easy axis. (Adapted from ref. [36])

The fascinating interplay between quantum and classical effects in the dynamics of the magnetization of molecular nanomagnets has attracted great interest among physicists and chemists and many other spectacular phenomena have been observed in the last ten years, as topological interferences[40] and quantum coherence[41]. These features can be triggered by weak interactions between SMMs, which will be the focus of 2.3.

2.3 Interaction between SMMs

SMMs can act as building blocks for supramolecular assemblies with discrete or extended structures, which often exhibit enhanced magnetic properties as compared with the constituent SMMs. The required linkages are provided by hydrogen bonds or, more conveniently, by coordination bonds, as proposed by the research groups of Clérac, Christou and Hendrickson.[42–45] This coordination strategy presents a significant challenge since the intrinsic magnetic properties of SMMs can be modified, which consequently also provides the opportunity to investigate new magnetic behaviour. Furthermore, the design of systems with “enhanced” SMM properties is possible by choosing suitable coordinating linkers which could favour an effective ferromagnetic arrangement of the SMMs.

The first 3D network of SMMs,[46] based on SMMs Mn_4 building blocks and paramagnetic Mn^{II} bridges, opened a promising way to obtain high-temperature magnets. Following this work, many systems were designed introducing simple diamagnetic or paramagnetic coordinating linkers between SMMs,[42,45,47,48] displaying interesting features, like for example an enhancement of the SMM energy barrier or a modulation of the quantum behaviour.

In addition, the introduction of functional linkers such as photochromic,[3] spin-crossover, luminescent or conducting complexes will give an unique opportunity to design multi-functional SMMs in which two or more co-existing properties interplay.[2] Fig. 2.4 shows a possible design of photo-induced SMM-network compounds using photo-active bridging ligand.

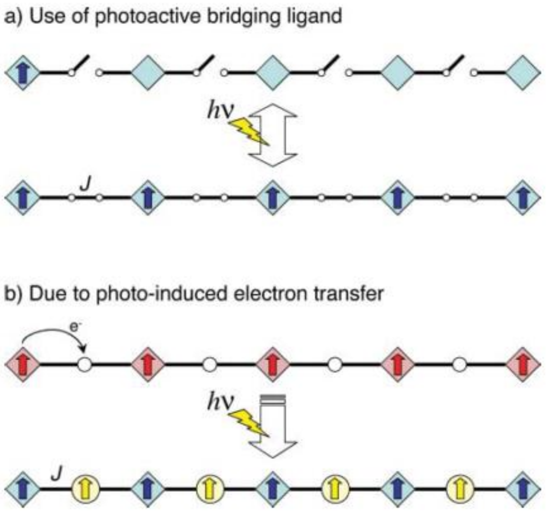

Fig. 2.4. Proposed design of photo-induced SMM-network compounds using photo-active bridging ligand (Adapted from ref. [2]).

For example, Ohkoshi and co-workers described a new type of three dimensional Co-W bimetallic network, which exhibits a photoinduced magnetization with a high Curie temperature of 40 K and a large coercive field.[49] Furthermore, as mentioned in Chapter 1, Ababei and co-workers in 2013 synthesized a coordination network of SMMs linked by spin-crossover units inducing thermally- and photo-reversible magnetic and optical properties.[5]

2.3.1 Exchange-biased QT of magnetization

An SMM can act as a bias on its neighbours through weak exchange-coupling interactions mediated *e.g.* by hydrogen bonds and this may generate a better memory effect. Furthermore, entanglement between quantum states is an important resource for quantum information processing.[15]

The first example in literature was reported by Wernsdorfer et al. in 2002[50]: the supramolecular linkage between two $[Mn_4O_3Cl_4(O_2CEt)_3(py)_3]_2$ (**Mn₄**) units introduces an exchange interaction via both C–H···Cl and Cl···Cl pathways. This coupling is manifested as an exchange bias of tunnelling transitions, and the hysteresis loops consequently display unique features, such as the absence of a QTM step at zero field (Fig. 2.5).

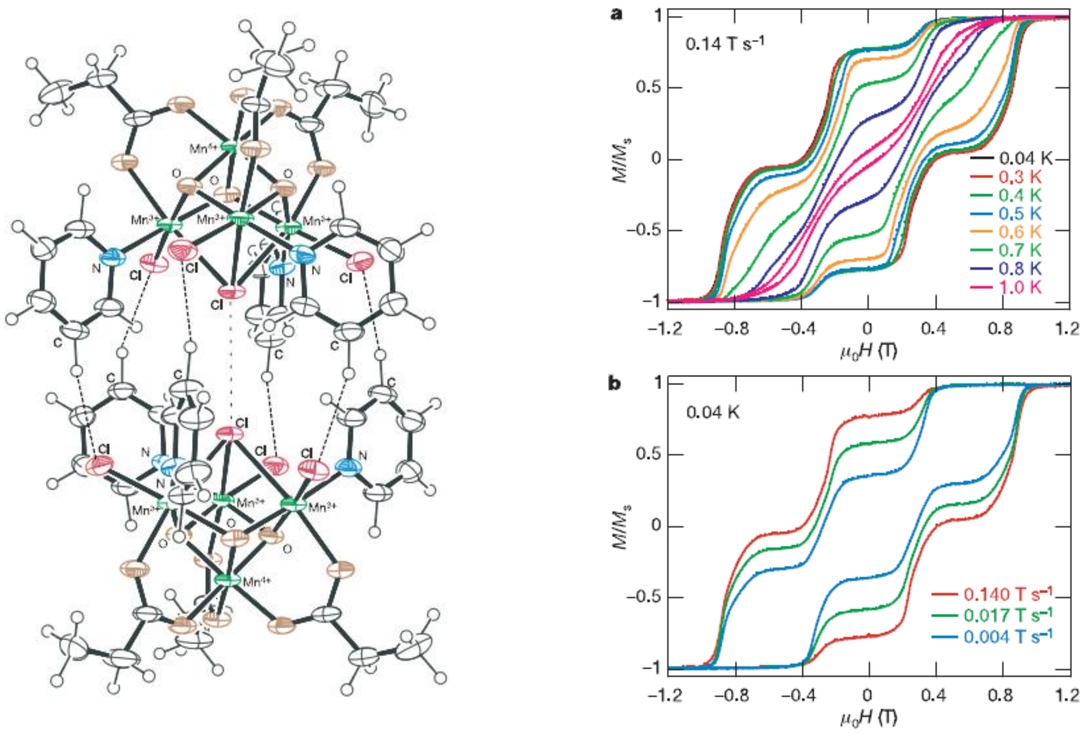

Fig. 2.5. Left: structure of $[\mathbf{Mn_4}]_2$. The dashed lines are C–H···Cl hydrogen bonds and the dotted line marks the closest Cl···Cl contact. Right: Magnetization (M) of $[\mathbf{Mn_4}]_2$ (plotted as fraction of saturation magnetization, M_s) versus applied magnetic field ($\mu_0 H$). The resulting hysteresis loops are shown at different temperatures (**a**) and different field sweep rates (**b**). Adapted from ref. [50].

Since then, more supramolecular dimers,[51] chains,[52] and 3D networks[53–57] have been described in which SMMs interact weakly through hydrogen bonds or other short contacts and show exchange-bias effects. Anyway, such supramolecular organizations are largely serendipitous in nature and are disrupted upon dissolution. Consequently, further efforts are still necessary to improve the state of the art of this interesting field (see Chapters 5).

2.4 Fe_4 clusters

Propeller-like tetrairon(III) clusters with a centred triangular topology (Fe_4) are among the simplest inorganic systems showing SMM behaviour.[28,58] In spite of their subkelvin operating temperatures, these compounds are robust,[59] chemically versatile and easy to be functionalized.[60,61] Such features make them perfect candidates for the design of supramolecular SMM-based structures.

2.4.1 General synthetic procedure

The first member of this class, discovered in 1999, is tetrairon(III) compound $[Fe_4(OMe)_6(dpm)_6]$ (Hdpm = dipivaloylmethane) (Fig. 2.6), which we abbreviate as **Fe_4std**.[28]

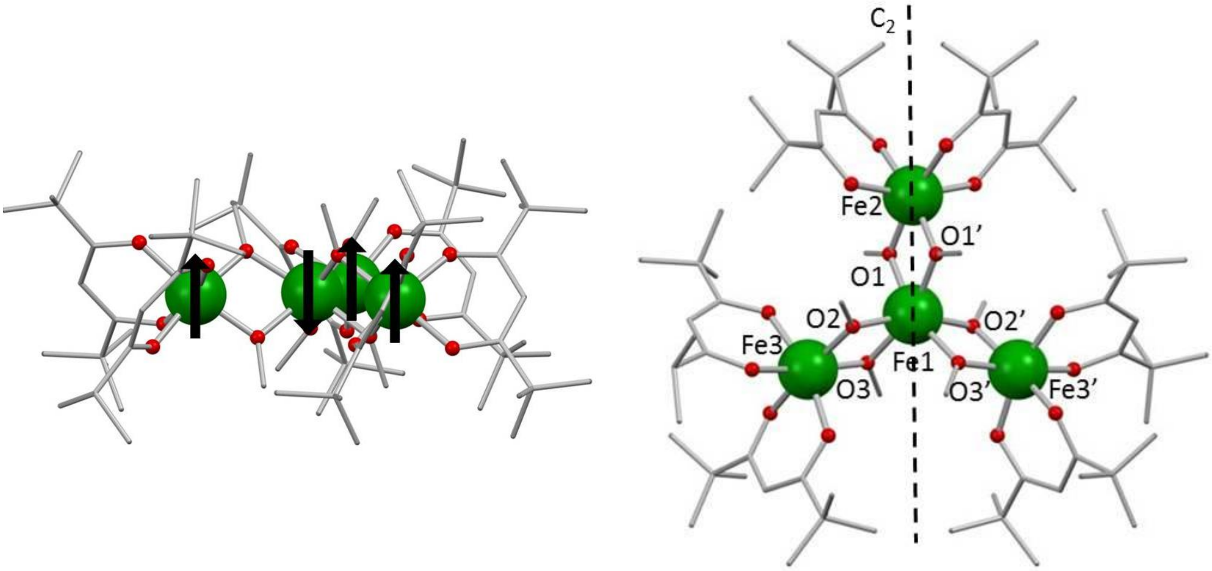

Fig. 2.6. Molecular structure of **Fe_4std** viewed along crystallographic axes *a* (left) and *c* (right). The black arrows in the left panel represent the $s = 5/2$ spins of iron(III) ions, which combine to give the $S = 5$ ground spin state of the molecule. The right panel highlights the crystallographic C_2 axis and shows atoms labels. Colour code: Fe = green, O = red, C = grey (H atoms omitted).

Fe_4std is synthesized in two successive steps. The first one involves reaction of $FeCl_3$, Hdpm and NaOMe in MeOH according to Eq. 2.8:

$$2\ FeCl_3 + 4\ Hdpm + 6\ NaOMe \rightarrow [Fe_2(OMe)_2(dpm)_4] + 4\ MeOH + 6\ NaCl \qquad (2.8)$$

The dimer $[Fe_2(OMe)_2(dpm)_4]$ is then allowed to react with stoichiometric amounts of $FeCl_3$ and NaOMe in a Et_2O:MeOH 4:1 solvent mixture (Eq. 2.9). This second step gives a yellow-orange solution and a white precipitate (NaCl). Vapour diffusion of anhydrous MeOH into the filtered reaction mixture affords **Fe_4std** as orange crystals in good yield (60-70%).

$3\ [Fe_2(OMe)_2(dpm)_4] + 2\ FeCl_3 + 6\ NaOMe \rightarrow 2\ [Fe_4(OMe)_6(dpm)_6] + 6\ NaCl$ (2.9)

Moisture exclusion and pH control (neutrality) are essential for this last step, which otherwise invariably results in recrystallization of the dimer.

The molecule[28] (shown in Fig. 2.6) has crystallographic 2-fold symmetry due to the presence of a C_2 axis passing through Fe1 and Fe2. The four metal ions lie exactly on a plane, while the six methoxido ligands bridge the central ion to the three peripheral ones arranged at the vertices of an isosceles (quasi equilateral) triangle. In fact, the intramolecular Fe···Fe distances are 3.146(2) Å for the Fe1···Fe2 pair and 3.133(1) Å for the Fe1···Fe3 one, while Fe2-Fe1-Fe3 and Fe3-Fe1-Fe3' angles are 117.65(3)° and 124.70(6)°, respectively. The three peripheral iron ions complete their coordination sphere with two bidentate β-diketonato dpm^- anions. The Fe-O-Fe angles at the bridging methoxido ligands are 104.3(2)°.

The central iron(III) atom Fe1 binds six methoxido ligands and its coordination environment approaches 3-fold symmetry. The coordination geometry of Fe2 and Fe3 is somewhat more irregular due to the presence of different ligands, *i.e.* two methoxido and two dpm^- anions. In particular, the peripheral metal ions form shorter bonds with OMe than with dpm^-. The Fe1-O2-Fe3-O3 moiety is nearly planar (maximum deviation 0.03 Å) and forms dihedral angles of 99.5° and 105.9° with the planes through Fe1-O1-Fe2-O1' and Fe1-O2'-Fe3'-O3', respectively. Consequently, the molecule has a propeller shape and is chiral. However, the space group is centrosymmetric, so the two enantiomeric species are both present in the crystal.

The six methoxido groups of **Fe_4std** can be easily and specifically substituted with two tripodal ligands $R–C(CH_2OH)_3$ or H_3L^R (R = substituent group on the quaternary carbon) (Fig. 2.7), as discovered in 2002[29] and shown in some previous works[62,17]:

$[Fe_4(OMe)_6(dpm)_6] + 2\ H_3L^R \rightarrow [Fe_4(L^R)_2(dpm)_6] + 6\ MeOH$ (2.10)

The synthetic procedure depends on the nature of the tripodal ligand. For example, with H_3L^{Ph} the reaction proceeds in Et_2O at room temperature overnight and affords $[Fe_4(L^{Ph})_2(dpm)_6]\cdot Et_2O$ (**Fe_4Ph**$\cdot Et_2O$) in good yield by vapour diffusion of MeOH (60-80%).

Et_2O can be replaced by other organic solvents of low or moderate polarity, in which **Fe_4std** is soluble (*e.g.* toluene). However, when the tripodal ligand is only sparingly soluble in such solvents, alternative procedures have to be used, as described in 4.3. As for all coordination complexes, the equilibrium can be significantly shifted towards the product by an excess of the incoming ligand, and the yield is in fact significantly improved when an excess of H_3L^R (usually 2.5 equivalents per mole of **Fe_4std**) is used. The chelating effect of the tripodal ligands makes the complex more stable in solution than its precursor.[17]

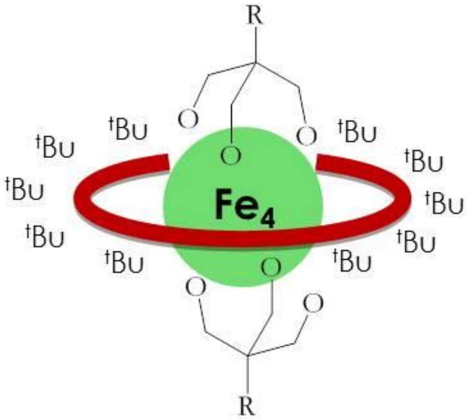

Fig. 2.7. Sketch of a general tetrairon(III) cluster Fe_4R with tripodal ligands $R\text{-}C(CH_2O^-)_3$.

Fe_4 systems also evidence a striking magnetostructural correlation between the height of the anisotropy barrier and the helical pitch of the propeller structure (measured as the dihedral angle between the Fe_4 plane and the $Fe_c(O)_2Fe_p$ planes, where Fe_c is the central iron ion and Fe_p is one of the iron ions on the apexes of triangle),[18] with both $|D|$ and U_{eff} increasing with increasing helical pitch, as shown in Table 2.1.

Table 2.1. Propeller pitch and magnetic parameter *D* for tetrairon(III) propellers.[18]

	Propeller pitch (°)	D (cm^{-1})
Fe_4std	63.2	-0.206
Fe_4Ph	68.8	-0.418
Fe_4Me	70.8	-0.445

2.4.2 Magnetic behaviour

Despite the crystallographic C_2 symmetry, the inter-ion distances in **Fe_4std** are very similar to each other and the metal core approaches D_3 symmetry quite closely. In fact, many of its magnetic properties are satisfactorily described assuming threefold symmetry under the framework of the previously-mentioned Kambe's approach (Eq. 2.2).

Quantitative information on exchange coupling constants in this and related tetrairon(III) propellers is customarily retrieved from $\chi_M T$ vs. T data, which are analyzed using a Heisenberg (Eq. 2.2) *plus* Zeeman Hamiltonian:

$$H_{ext+Zee} = H_{ext} + \mu_B g\mathbf{S}\cdot\mathbf{H} \qquad (2.11)$$

This procedure gave J = 21.1 cm^{-1}, J' = -1.1 cm^{-1} and g = 1.97 for **Fe_4std**. Thus, the iron(III) ions interact antiferromagnetically and the ground state has total spin S = 5, as confirmed by HF-EPR.

A Curie-Weiss correction can be introduced to reproduce the drop of the $\chi_M T$ product at very low temperature due to magnetic anisotropy effects:

$$(\chi_M T)' = (\chi_M T)\cdot T / (T - \theta) \qquad (2.12)$$

Magnetic anisotropy is however best evaluated (and the S value confirmed) from the field dependence of the isothermal molar magnetization, which is customarily analyzed using an S = 5 giant-spin model based on a zfs (Eq. 2.5) *plus* Zeeman Hamiltonian, *i.e.*

$$H_{anis+Zee} = H_{anis} + \mu_B g\mathbf{S}\cdot\mathbf{H} \qquad (2.13)$$

where the rhombic zfs parameter E is normally fixed to zero. This procedure gave D = –0.20 cm^{-1} in **Fe_4std**, a value confirmed by HF-EPR. Further studies evidenced that the easy magnetic axis is perpendicular to the plane containing the four iron(III) ions and then directed along the idealized D_3 axis. SMM behaviour can indeed be observed, although only at very low temperature due to the low anisotropy barrier.[28] Studying the dynamics of the magnetization usually requires ac susceptibility measurements in zero or applied static field H, as a function of both temperature and frequency of the oscillating field (ν). In isothermal conditions, the appearance of maxima in the out-of-phase component of the magnetic susceptibility (χ_M'') plotted as a function of v is a signature of slow magnetic relaxation. The ac responses can be analysed within the Debye model,[63,64] in which the maximum in χ_M'' is observed when the relaxation time τ equals $(2\pi v)^{-1}$. The frequency dependence of χ_M'' at constant temperature is then fitted using the following equation, which accounts for a distribution of relaxation times through the width parameter α:

$$\chi''(\omega) = (\chi_T - \chi_S)\frac{(\omega\tau)^{1-\alpha}\cos(\alpha\pi/2)}{1+2(\omega\tau)^{1-\alpha}\sin(\alpha\pi/2)+(\omega\tau)^{2-2\alpha}} \qquad (2.14)$$

In the above Equation, $\omega = 2\pi v$ and χ_T and χ_S are the isothermal and adiabatic susceptibilities, that is, the susceptibilities observed in the two limiting cases $v \rightarrow 0$ and $v \rightarrow \infty$, respectively. The model is generally satisfactory for Fe_4 clusters and affords α values which decrease toward zero upon heating. The relaxation times τ obtained from this analysis can be plotted as $\ln(\tau)$-vs-$1/T$ and a linear dependence indicates a thermally-activated relaxation mechanism in the explored temperature range, as described by the Arrhenius law:

$$\tau = \tau_0 \exp\left(U_{eff} / k_B T\right) \qquad (2.15)$$

Such a procedure gave $U_{eff}/k_B = 3.5$ K in **Fe_4std**, a value much lower than the total splitting of the $S = 5$ multiplet ($\Delta U/k_B = 7.2$ K) as a likely result of efficient QT relaxation.

The site-specific ligand replacement of methoxides with tripodal ligands preserves the $S = 5$ ground state of Fe_4 clusters but enhances their magnetic anisotropy up to $D = -0.45$ cm^{-1}; larger energy barriers of up to 17 K are correspondingly observed.[17,18] Nevertheless, the energy barriers of Fe_4 systems are still low compared to those typical, for instance, of Mn_{12} clusters.[65] Consequently, it is necessary to reach subkelvin temperatures to observe the blocking of the magnetization. However, in the last years, Fe_4 clusters have been extensively studied because they can be easily functionalized by properly designing the R group of the tripodal ligands[17,66] or by modifying the ancillary β-diketonates.[67] Structurally similar compounds were also prepared in which the central iron(III) ion is replaced by chromium(III),[68] vanadium(III)[69] or lanthanide(III) ions.[61,70] Major achievements were the chemisorption of functionalized derivatives as self-assembled monolayers on surfaces[66,71] and the preparation of variable-thickness deposits using thermal evaporation in high vacuum ($P = 10^{-7}$ mbar).

The following Chapters describe efforts made during my PhD thesis to further exploit this remarkable versatility of Fe_4 SMMs in order to assemble more complex supramolecular architectures.

3 A promising but too fragile supramolecular assembly: the case of Fe_4Fc

3.1 Introduction

In order to prepare supramolecular ER-Fe_4-ER systems (where ER is an electron reservoir), I scrutinized a wide range of possible redox-active groups to be connected to the SMM core. Well studied ER in literature are ferrocene derivatives, which will be described below in 3.2.

In the rest of this Chapter I will show the design and the synthesis of a tripodal ligand which carries a ferrocene pendant. After the synthesis and characterization of the target supramolecular ER-Fe_4-ER assembly, a series of attempts to oxidize the compound to ER-Fe_4-ER^+ were made using different oxidants, *e.g.* iodine, tris(4-bromophenyl)ammoniumyl hexachloroantimonate (TBA($SbCl_6$) or "Magic Blue"), chlorine, and acetyl-ferrocenium.

3.2 Ferrocene

Ferrocene (Fc) is a historically important molecule and the initial recognition of its structure - $Fe(\eta^5\text{-}C_5H_5)_2$ - in 1951 produced a vast research area in transition metal organometallic chemistry. This field is still developing and encompasses now a huge number of compounds in which saturated, unsaturated, and aromatic organic fragments are bonded directly to metals. All carbon atoms in the two cyclopentadienyl rings of Fc are equally bonded to the central ion by π electrons, as shown in Fig. 3.1.

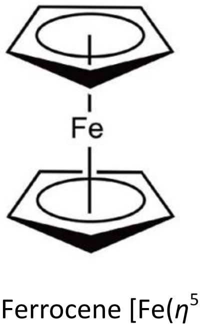

Fig. 3.1 Ferrocene [$Fe(\eta^5\text{-}C_5H_5)_2$]

This sandwich structure proposed by Wilkinson and Fischer[72,73] (Nobel prize in 1973) in early 1952 has been supported by X-ray diffraction (solid state)[74] and electron diffraction data (gas phase).[75] Ferrocene is an orange compound that exhibits the properties of a typical aromatic molecule and is stable to more than 500 °C. It does not react readily with acids or bases; however, it is sensitive toward oxidizing agents. Ferrocene does not give addition reactions typical of cyclopentadiene, but readily undergoes electrophilic aromatic substitution.

Furthermore, in the last decades ferrocene was well studied as an ER: after oxidation, ferrocene maintains its structure, becoming blue ferrocenium (Fc^+) ion. This generates a lot of applications for ferrocene in sensing, catalysis, electrochemistry, organometallic chemistry, etc.

Intramolecular ET between ferrocene/ferrocenium units was observed in compounds as diferrocenylpolyenes,[76] where an intervalence transition is detected in the mixed valence state. Differently, in the works of Yip and collaborators,[77,78] two ferrocene groups are bridged by $C\equiv(M^I)_3\equiv C$ (with M = Cu, Ag or Pt) or $-C\equiv Pt^I-Pt^I\equiv C-$ cores; the latter shows electronic communication mediated by Pt^I-Pt^I σ bond. In another work published on *Angew. Chem. Int. Ed.* in 2005,[79] the authors show the first example of an ET from a metallic cluster (Pt_6 core) towards a ferrocenium acceptor.

These examples stimulated and motivated us to explore a new field: combining in a supramolecular assembly two ferrocene groups and the Fe_4 SMM, in such a way that, after oxidation of one Fc to Fc^+, any possible ET is forced to occur *through* the magnetic core. Such a phenomenon was expected to impact the relaxation dynamics of the Fe_4 SMM, evidencing new interplays between ET and SMM behaviour.

3.3 Synthesis of H_3L^{Fc}

The synthesis of a suitable tripodal ligand with a ferrocene pendant is already available in the recent literature; in 2000, Hu and Lewis Mattern described the preparation of 2-(4-ferrocenylphenyl)-2-(hydroxymethyl)propane-1,3-diol (hereafter called H_3L^{Fc}), shown in Fig. 3.2. Briefly, 2-(4-nitrophenyl)-2-(hydroxymethyl)propane-1,3-diol (**2**) was prepared from 4-nitro-toluene (**1**) and formaldehyde in KOH. Catalytic hydrogenation at 2.8 atm overnight was used to reduce the nitro group to amine. The resulting anilino derivative (**3**) was diazotized and reacted with a ferrocene/ferrocenium mixture in sulfuric acid. H_3L^{Fc} was finally purified by SiO_2 column chromatography with gradient elution DCM:MeOH, giving the tripodal ligand in 35.3% of the yield (more information is given in Experimental Section).

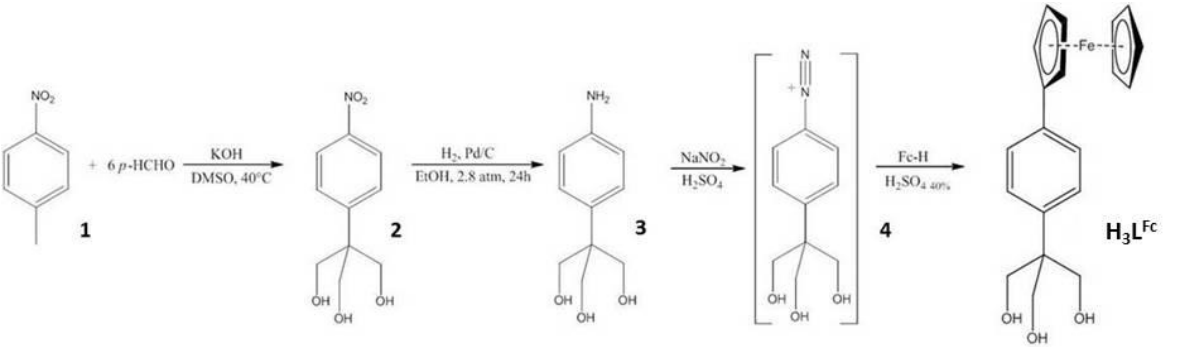

Fig. 3.2. Synthesis of the tripodal ligand H_3L^{Fc}.

3.4 Synthesis of Fe4Fc

The synthesis of **Fe_4Fc** follows the traditional procedure for Fe_4 clusters.[29,62,17] **Fe_4std** (see Eq. 2.9 and Eq. 2.10) was dissolved in Et_2O and, subsequently, the tripodal ligand H_3L^{Fc} was added to the solution and left stirring overnight.

$$[Fe_4(OMe)_6(dpm)_6] + 2H_3L^{Fc} \xrightarrow[\text{MeOH vapour diffusion}]{Et_2O} [Fe_4(L^{Fc})_2(dpm)_6] + 6\ MeOH$$

The solution was filtered and put in vapour diffusion of MeOH. The big red crystals formed after two weeks were washed with MeOH and dried, giving the target product in 76.3% yield (for more synthetic information, see Experimental Section).

Characterization was based, among the other techniques, on proton NMR. ^1H NMR spectra of **Fe_4Fc** were recorded in toluene-d_8/CD_3OD solution and in CD_2Cl_2 (see Fig 3.3 and Fig. 3.15_1). Concerning the first experiment, the spectrum shows at 10.4 ppm the broad band characteristic of dpm^- *t*Bu hydrogens (108 H) in Fe_4 clusters.[17] The shoulder visible at 12.1 ppm is attributed to *m*-Ph hydrogens of tripodal ligands (4 H). The peaks at 4.20 and 3.90 are the hydrogens of ferrocene (18 H), while the other peaks at 7.09, 6.98, 2.09 ppm and 3.26, 3.13, 1.06 ppm are due, respectively, to residual protons of toluene and methanol. For paramagnetic species, in particular for Fe_4 complexes, NMR signals are broad and peak integration is rather difficult. In particular, the intense peak of residual aromatic protons of toluene hampers accurate integration of the band at 10.4 ppm. Setting the signals of Fc hydrogens to 18 H, the band integrates to 85.0 H rather than to the expected value of 112

H. In opposite, in the ^{1}H NMR spectrum of **Fe$_4$Fc** in CD_2Cl_2 (see Fig. 3.15_1), the hydrogen integrals are correct: setting Fc bands to 18 H, the broad band around 10.4 ppm integrates to 112 H.

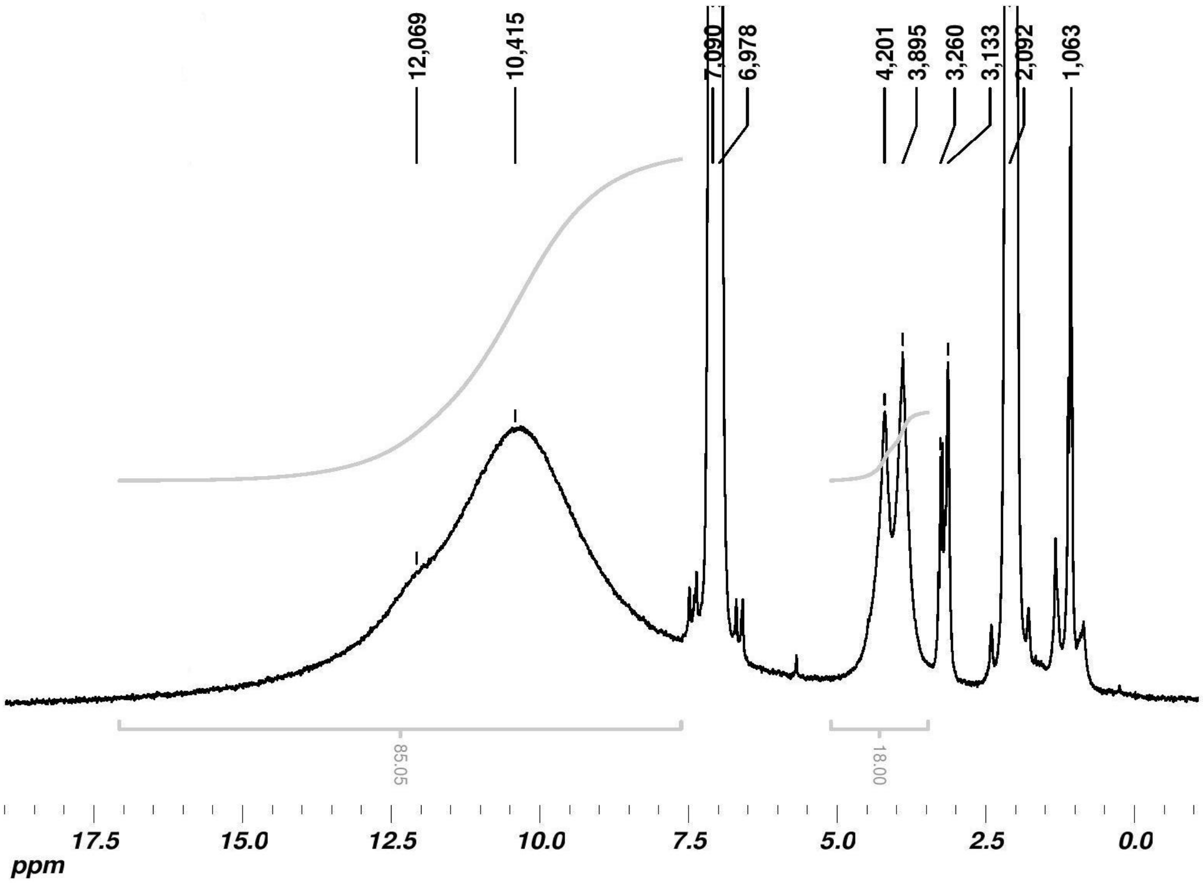

Fig. 3.3 ^{1}H NMR spectrum of **Fe$_4$Fc** in toluene-d_8 and CD_3OD.

3.5 Molecular structure

Crystals grow as big red parallelepipeds; the space group is monoclinic $P2_1/n$ and the asymmetric unit contains one molecule of **Fe$_4$Fc**. Its structure is reported in Fig. 3.4 and shows that the substituents on tripodal ligands are not collinear, but significantly bent. Moreover, the Fc units are not parallel to each other. The carbon atoms of cyclopentadienyl rings show high Anisotropic Displacements Parameters (ADPs) and some unaccounted-for electron density appears around the ^{t}Bu groups and the ferrocene units. These findings suggest that unresolved disorder effects, possibly related to the flexibility ferrocene pendants, may be present. The unit cell contains four tetrairon(III) molecules that develop in two directions, with the Fe$_4$ planes forming an angle of 77.6° with each other, as shown in

Fig 3.5. The crystals are very stable in air, as confirmed by the absence of solvent molecules in the lattice. Solvent accessible voids provided by PLATON software amount to 412 Å^3 over a unit cell volume of 11084 Å^3. However, the largest void has a volume of 38 Å^3 only and is thus too small to host solvent molecules, which typically require accessible voids of 100-300 Å^3 (40 Å^3 for a hydrogen bonded H_2O molecule); consequently, no solvent molecules can be trapped inside the crystal.

Selected geometrical parameters show that the cluster is structurally very similar to other Fe_4 complexes with tripodal ligands;[17,18] for example, the $Fe_c \cdots Fe_p$ distances, where Fe_c is Fe1 and Fe_p can be Fe2, Fe3 or Fe4, are respectively 3.09, 3.06 and 3.08 Å. The pitch of the propeller-like Fe_4O_6 cores, evaluated as the average of dihedral angle between the $Fe_c(O)_2Fe_p$ and Fe_4 planes, is 68.7° (68.0, 69.3 and 68.7° for planes with Fe2, Fe3 and fe4 respectively). The distances Fe1–O1, Fe1–O2 and Fe1–O3 are 1.972, 1.985, 1.989 Å while for the second tripodal ligand the distances Fe1–O4, Fe1–O5 and Fe1–O6 are 1.993, 1.984, 1.985 Å. Crystal data and structure refinement information are shown in Table 3.1.

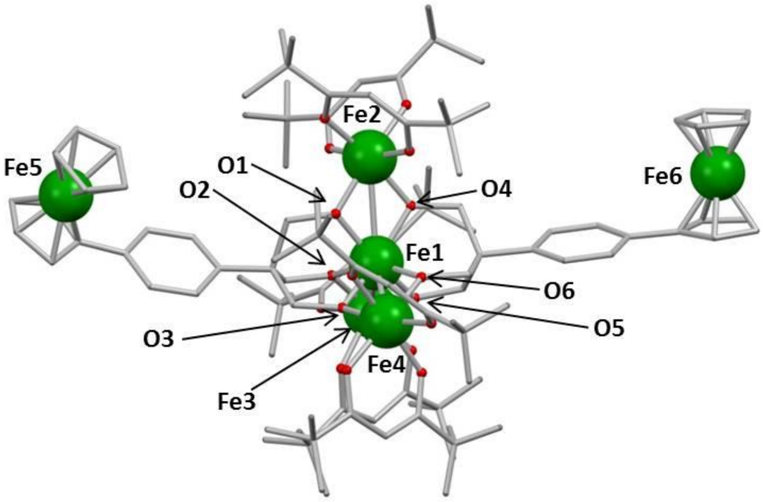

Fig. 3.4 Molecular structure of **Fe_4Fc**. Colour code: Fe = green, O = red, C = grey. Hydrogens omitted for carity.

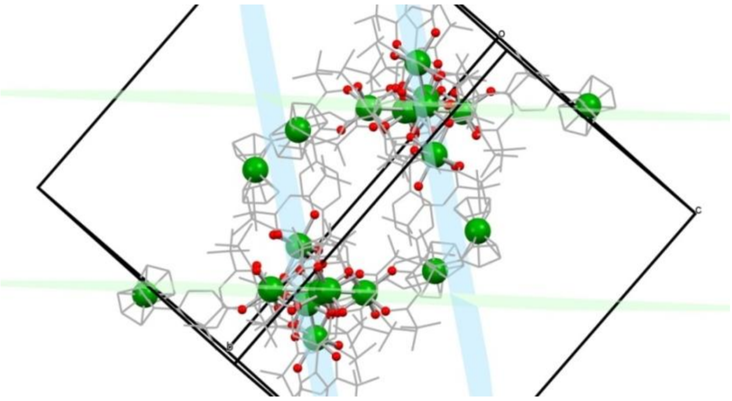

Fig. 3.5 Packing of four Fe_4 complexes in the unit cell of **Fe_4Fc**. Colour code: Fe = green, O = red, C = grey. Hydrogens omitted for clarity.

Table 3.1. Crystal data and structure refinement for **Fe_4Fc**.

Empirical formula	$C_{106}H_{152}Fe_6O_{18}$	
Formula weight	2049.39	
Temperature	200(2) K	
Wavelength	0.71073 Å	
Crystal system	monoclinic	
Space group	$P2_1/n$	
Unit cell dimensions	a = 14.6739(3) Å	α = 90°
	b = 23.4342(5) Å	β = 100.473(1)°
	c = 32.7786(7) Å	γ = 90°
Volume	11083.8(4) $Å^3$	
Z	4	
Density (calculated)	1.228 g cm^{-3}	
Absorption coefficient	0.824 mm^{-1}	
Reflections collected	86936	
Independent reflections	19512 [R(int) = 0.0382]	
Completeness to theta = 25.013°	99.8 %	
Refinement method	Full-matrix-block least-squares on F^2	
Data / restraints / parameters	19512/0/1171	
Final R indices [I>2σ(I)]	R_1 = 0.0768, wR_2 = 0.1802	
R indices (all data)	R_1 = 0.1150, wR_2 = 0.2205	
Largest diff. peak and hole	1.330 and -1.334 e$Å^{-3}$	
Goodness of fit	1.034	

3.6 Oxidizing Fe_4Fc: reagents and results

In order to perform a one-electron oxidation of **Fe_4Fc** to a mixed-valent species, in which one electron can potentially shuttle through the SMM core (see Fig. 3.6), I started scrutinizing possible oxidants compatible with the known chemical properties Fe_4 complexes. For instance Fe_4 species are unstable in acidic solution (*e. g.* they slowly decompose in chloroform). Considering this, after inspection of the redox potentials of ferrocene and of traditional oxidants, I focussed on iodine, tris-(*p*-bromophenyl)ammoniumyl hexachloroantimonate (TBA($SbCl_6$) or “Magic Blue”), chlorine and acetyl ferrocenium. Versus the normal hydrogen electrode (NHE), redox potential of ferrocene is +0.400 V,[80] but our H_3L^{Fc} ligand is more similar to phenyl ferrocene, which shows a redox potential of +0.425 V.[81] Turning now to the oxidant, iodine has a redox potential of +0.543 V, while tris-(*p*-bromophenyl) ammoniumyl radical is a much stronger oxidant (+1.30 V). Finally the redox potential is +0.648 V for acetyl ferrocene.

The many attempts and tests I have carried out indicate that **Fe_4Fc** does not survive oxidation.

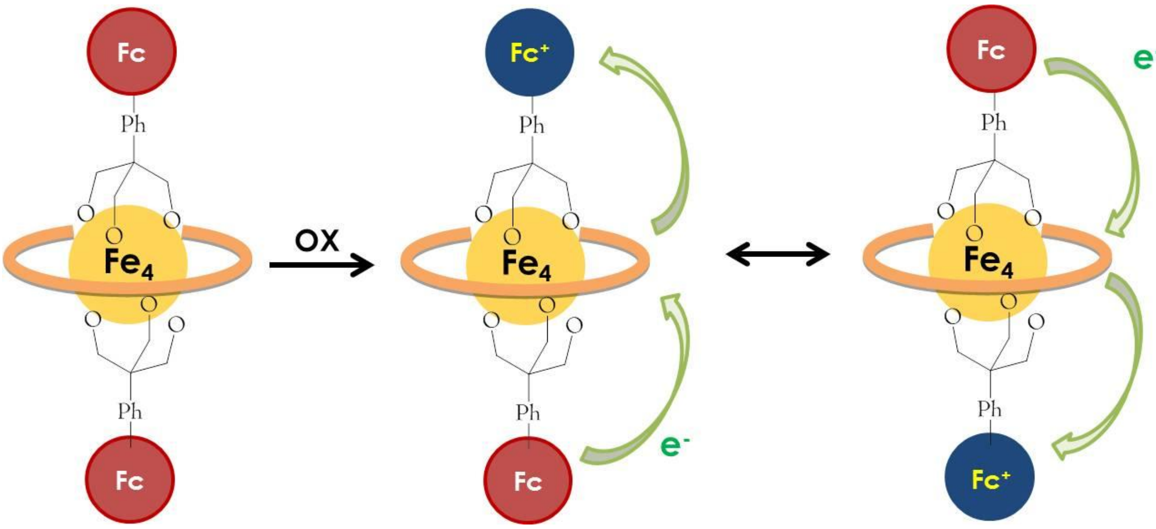

Fig. 3.6 Sketch of a possible ET phenomenon in a mixed-valent derivative obtained by the one-electron oxidation of **Fe_4Fc**.

3.6.1 Iodine

A mild oxidant of widespread use is iodine, I_2. The literature contains many examples of oxidations of ferrocene derivatives using I_2. In a paper by Grimes and co-workers,[82] the equilibrium:

$$\mathrm{Fc} + {}^{3}/_{2}\,\mathrm{I}_2 \rightarrow \mathrm{Fc}^{+}\mathrm{I}_3^{-}$$

was studied in benzene, a solvent with a low dielectric constant in which the product ion couple can be considered completely undissociated. The concentration of the product was followed measuring the absorbances of I_3^- at 380 nm and of Fc^+ at 625 nm. Ferrocene has an equlibrium constant for the reaction (*K*) of 174. The redox potential and the value of *K* are different for substituted ferrocenes. For instance, a *K* value of around 35 is found for phenyl-ferrocene, which is quite similar to our tripodal ligand H_3L^{Fc}. Furthermore, in another work[83] the authors highlight the influence of the polarity of the solvent on the equilibrium.

UV-vis characterization

An UV-vis study of the reaction between I_2 and **Fe_4Fc** (0.0257 mM) in DCM solution was performed up to an I_2:**Fe_4Fc** molar ratio of 1.22. The results (Fig 3.7) show no absorption band typical of ferrocenium derivatives around 600-800 nm. Consistent with literature data[83], the equilibrium constant is too low for oxidation to proceed to a significant extent in these diluted solutions.

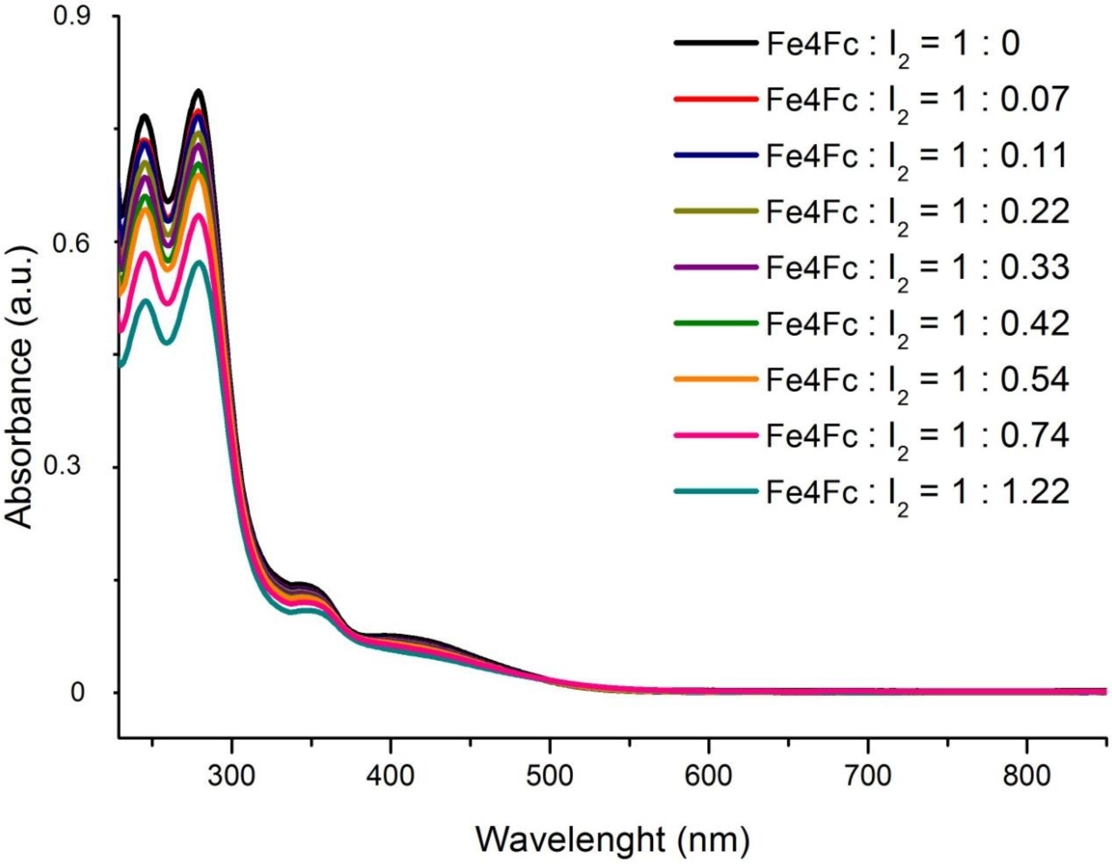

Fig. 3.7. UV-vis spectra of a DCM solution of **Fe_4Fc** (0.0257 mM) upon successive additions of iodine. There is no increase of ferrocenium band around 600-800 nm.

NMR characterization

^1H NMR spectroscopy was used to understand the behaviour of **Fe_4Fc** in the presence of excess I_2. To this aim, 0.0833 mmol (1 eq.) of **Fe_4Fc** and 0.2035 mmol (2.4 eq.) of I_2 were dissolved separately in 0.7 mL of anhydrous Et_2O and then mixed together. The solution became dark and, after evaporation of the solvent, the product was dissolved in CD_2Cl_2. In the recorded ^1H NMR spectrum (Fig. 3.8), ferrocene peaks around 4 ppm indeed disappear,[84] consistent with the formation of paramagnetic ferrocenium group, which causes major shifts and broadenings of NMR signals. However, the spectrum cannot be easily reconciled with that expected for oxidized but structurally intact **Fe_4Fc**. In fact, the 12 CH_2 protons of iron(III)-bound tripodal ligands are expected to be invisible in ^1H NMR spectra, as in all Fe_4 derivatives. Similarly, the 6 methine C-H protons of iron(III)-bound dpm$^-$ ligands should resonate at negative chemical shift values. Of the remaining 152 – 12 – 6 = 134 protons, 108 are *t*Bu hydrogens, which should thus account for > 80% of the signal intensity in the probed chemical shift region. The peak of *t*Bu protons at 10.5 ppm is accompanied by many new bands, whose overall intensity clearly exceeds 1/4 of the *t*Bu signal. Among the sharper bands, those at 16.3, 5.5 and 1.3 ppm are typical of free Hdpm (enolic OH, enolic =CH– and *t*Bu hydrogens, respectively). Among the broader bands, the signal at 13.1 ppm is characteristic of $Fe(dpm)_3$, a common decomposition product of Fe_4 complexes. I thus conclude that **Fe_4Fc** is likely to decompose upon treatment with excess I_2 at the used concentrations. Looking for a stronger oxidant to carry out mono-oxidation at stoichiometric concentrations, I tested tris(4-bromophenyl)ammoniumyl salts.

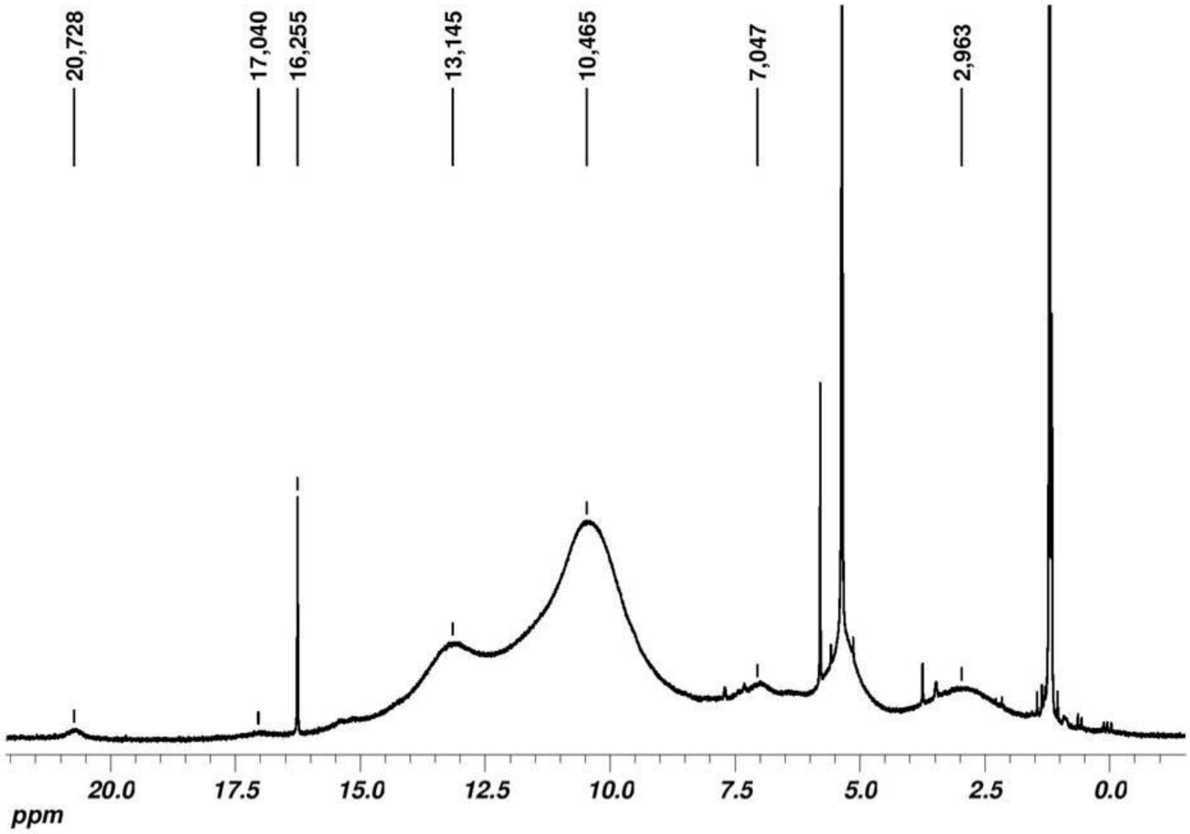

Fig. 3.8 ^1H NMR spectrum of **Fe_4Fc** after oxidation with I_2 in CD_2Cl_2 (to be compared with that of **Fe_4Fc** in Fig. 3.15-1).

3.6.2 TBA(SbCl$_6$)

Tris-(*p*-bromophenyl)ammoniumyl (TBA$^+$) is a radical cation used as a one-electron oxidising agent for organic molecules,[85,86] according to the reaction:

$$\mathrm{Ar_3N^{\cdot+}X^-} + \mathrm{substrate} \rightarrow (\mathrm{substrate^{\cdot+}})\mathrm{X^-} + \mathrm{Ar_3N}$$

Its radical character allows following the course of the reaction by ESR spectroscopy. However, UV-vis spectroscopy is a more convenient choice, since the radical has an intense blue colour whereas Ar$_3$N is normally colourless. In previous work,[87] TBA$^+$ salts were shown to cleanly oxidize ferrocene derivatives. The salt used here is tris(4-bromophenyl)ammoniumyl hexachloroantimonate (TBA(SCl$_6$) or "Magic Blue"), whose structure is shown in Fig. 3.9.

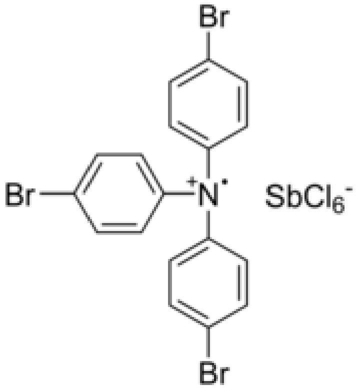

Fig. 3.9. Molecular structure of TBA(SbCl$_6$).

I have explored the oxidation of **Fe4Fc** with Magic Blue, monitoring the reaction by UV-vis and ^{1}H NMR spectroscopies.

UV-vis characterization

The reaction between **Fe$_4$Fc** and TBA$^+$ was studied by UV-vis spectroscopy, as the two species both feature strong absorbances. TBA$^+$ shows peaks at 260, 370, 630 and 730 nm (Fig. 3.10). On the other hand, **Fe$_4$Fc** has four characteristic bands at 245, 279, 349, 410 nm due to the presence of the Fe$_4$ core and ferrocene units. A major expected change upon oxidation is the appearance of ferrocenium band at 600-800 nm.

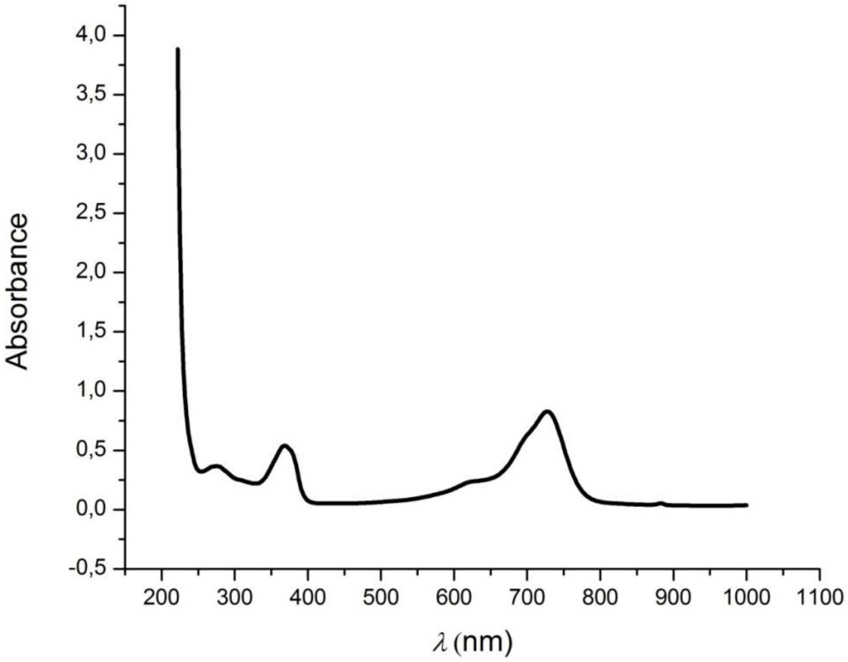

Fig. 3.10. UV-vis spectrum of a 0.725 mM solution of TBA($SbCl_6$) in DCM.

First at all, I performed a preliminary study on $(AcO)_3L^{Fc}$, an acetylated and quite soluble variant of H_3L^{Fc} whose molecular structure is sketched in Fig. 3.11. The recorded UV-vis spectra (see Fig 3.11) indeed show the appearance of ferrocenium band at 787 nm, which increases in intensity upon successive additions of TBA($SbCl_6$). For a TBA($SbCl_6$):$(AcO)_3L^{Fc}$ ratio larger than 1.0, the band is partially masked by the intense absorption of excess oxidant at 730 nm. Thus, our study confirms that $(AcO)_3L^{Fc}$ can be neatly and quantitatively oxidized by stoichiometric Magic Blue.

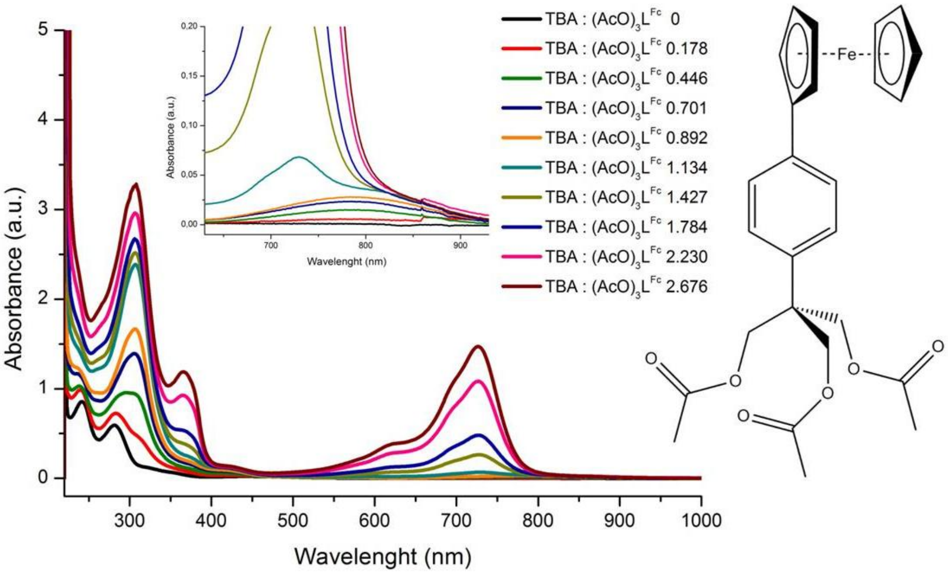

Fig. 3.11. UV-vis spectra of a solution of $(AcO)_3L^{Fc}$ in DCM upon addition of variable amounts of TBA($SbCl_6$). The molecular structure of $(AcO)_3L^{Fc}$ is depicted on the right. A zoom of the spectra between 630 and 930 nm is shown in the inset to highlight the evolution of the ferrocenium band.

In a similar experiment, variable amounts of TBA($SbCl_6$) were added to a solution of **Fe_4Fc** in DCM, up to a TBA($SbCl_6$):**Fe_4Fc** molar ratio of 2.50 (see Fig. 3.12). The UV-vis characterization shows an important increase of the band of ferrocenium groups at 816 nm. Furthermore, the spectra recorded at molar ratios of 2.0 and 2.5 are virtually identical. The shift of the absorption maximum to 796 nm is likely due to the underlying contribution of excess oxidant and a contemporary effect of dilution. Our data thus confirm that oxidation of all ferrocene units is complete upon addition of two equivalents of TBA($SbCl_6$) to **Fe_4Fc** in DCM.

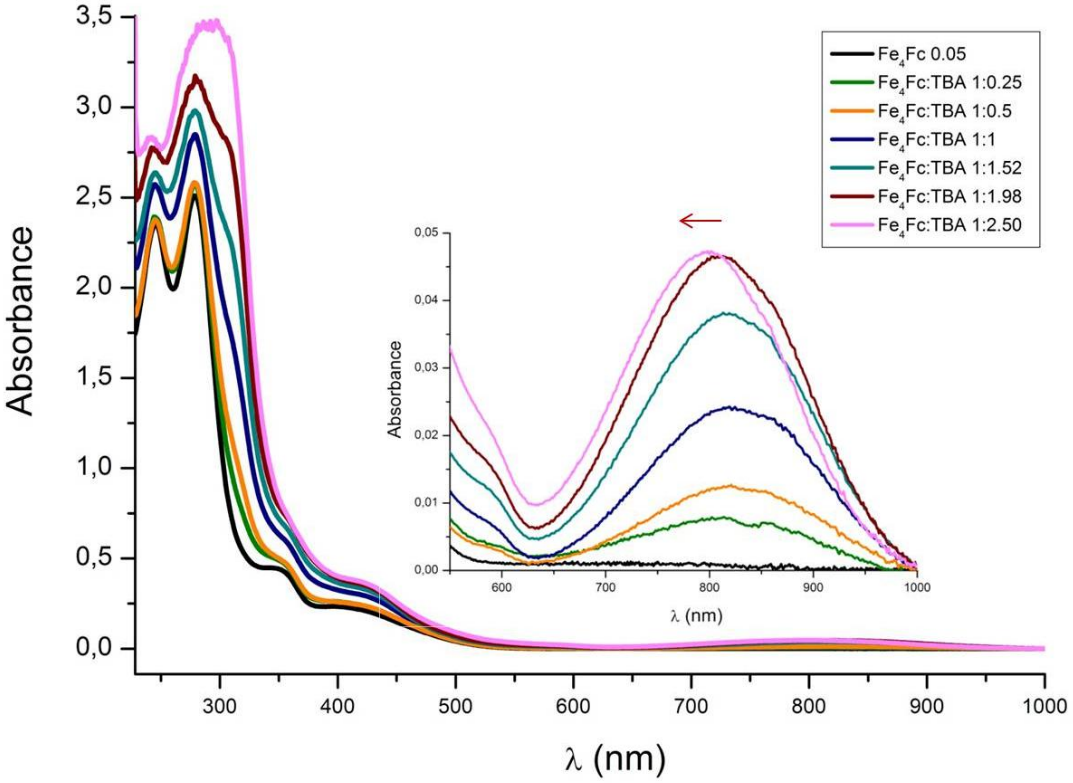

Fig. 3.12. UV-vis spectra of **Fe_4Fc** and TBA($SbCl_6$) in DCM at various molar ratios. The inset shows a zoom of the spectra between 550 and 1000 nm to highlight the evolution of the ferrocenium band.

^{1}H NMR characterization

The oxidation of **Fe_4Fc** by TBA($SbCl_6$) in DCM was also followed by ^{1}H NMR. The spectrum recorded with a 1:1 molar ratio between the two reagents is presented in Fig. 3.13. The peaks of TBA hydrogens around 7 ppm confirm reduction of TBA($SbCl_6$). As in the oxidation with iodine (Fig. 3.8), ferrocene peaks around 4 ppm disappear. This is consistent with fast electron exchange between paramagnetic ferrocenium groups and the remaining ferrocene units. However, the sharp signals from free Hdpm at 16.1 and 5.5 ppm (enolic OH and enolic =CH–, respectively) hint to partial decompostion. The broader bands at 13 and 17 ppm, attributable to $Fe(dpm)_3$ and $Fe(dpm)_3H^+$, respectively, are also indicative of structural instability of **Fe4Fc** in these conditions. Other very broad bands, highlighted by yellow horizontal segments in Fig. 3.13, may also be attributed to ferrocene/ferrocenium fragments in fast electron exchange.

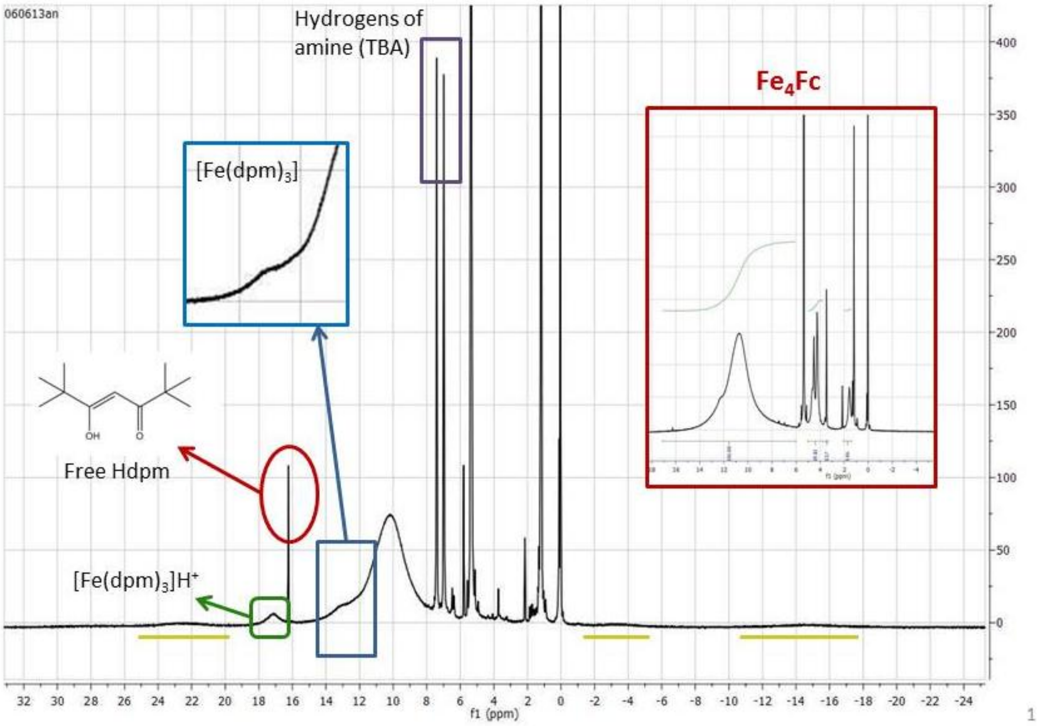

Fig. 3.13. ^{1}H NMR spectrum of **Fe$_4$Fc** and TBA(SbCl$_6$) in CD$_2$Cl$_2$ at a 1:1 molar ratio, compared with the initial spectrum of **Fe$_4$Fc** in CD$_2$Cl$_2$ (red inset).

3.6.3 Chlorine

I also tested oxidation with gaseous Cl$_2$. Chlorine is a very toxic and irritant gas and all operations involving its generation and use must be carried out in an efficient fume cupboard. Small quantities of chlorine were prepared as reported in literature[88], by the action of concentrated hydrochloric acid upon potassium permanganate in the apparatus shown in Fig. 3.14 (1.000 g of KMnO$_4$ requires 6.2 mL of concentrated hydrochloric acid). The gas was dried by passing it through concentrated sulphuric acid in two Drechsel bottles and then introduced in a desiccator containing two Petri dishes, one with some **Fe$_4$Fc** crystals

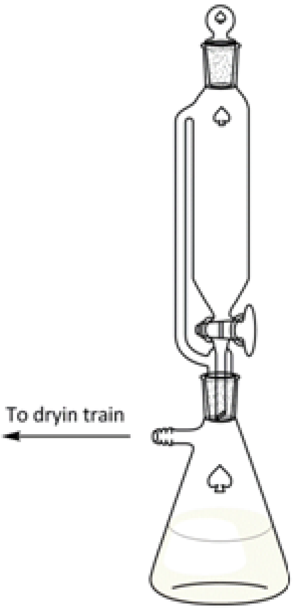

Fig. 3.14. Apparatus for the generation of chlorine.

and one with crystals of a tetrairon(III) complex containing no ferrocene groups, **Fe_4Ph**. Although stoichiometric oxidation could not be performed using this methodology, both crystalline species became dark blue on the surface upon exposure to chlorine, indicating that chlorine is too strong as oxidant and leads to decomposition of Fe_4 complexes.

3.6.4 Acetyl Ferrocenium

As published in many papers in the last decades[89–91], the redox potentials of ferrocene derivatives are greatly influenced by substituents on the cyclopentadienyl rings. For instance, the reduction potentials of phenyl ferrocene is 0.025 V vs. oxidation potential of ferrocene, while for acetyl ferrocene is 0.248 V.[81] The similarity between phenyl ferrocene and the ferrocene pendants in **Fe_4Fc** has suggested using an acetyl ferrocenium salt for the smooth oxidation of **Fe_4Fc**.

Acetyl ferrocene (AcFc) was synthesized starting from ferrocene and acetic anhydride in the presence of phosphoric acid; after neutralization with Na_2CO_3, the product was filtered and chromatographed with silica column. Acetylferrocenium tetrafluoroborate, [Fe(η-C_5H_4COMe)Cp](BF_4) or AcFc(BF_4), was prepared as described in the review of Connely and Geiger[92]: to a stirred solution of AcFc (1.1 eq.) in Et_2O at room temperature, $AgBF_4$ (1 eq.) was added. After 30 minutes the blue-green reaction mixture was evaporated to dryness, and the residue was extracted with DCM. After filtration, the volume was reduced *in vacuo* and the solution layered with Et_2O. The desired product was obtained as a crystalline material after one week (yield 64.68%).

Oxidation of **Fe_4Fc** by AcFc(BF_4) was followed by ^{1}H NMR over a time window of 24 h, hinting to progressive decomposition (Fig. 3.15.1-3). The peaks observed at 4.77, 4.53, 4.24 and 2.39 ppm (Table 3.1) are characteristic of AcFc[93] and confirm reduction of AcFc$^+$. However, the spectra also show peaks of free Hdpm at 16.22 and 5.79 ppm (enolic OH and enolic =CH–, respectively), which increase in intensity with time. Moreover, some intense and very broad bands appear in the spectrum, pointing to the formation of new paramagnetic fragments.

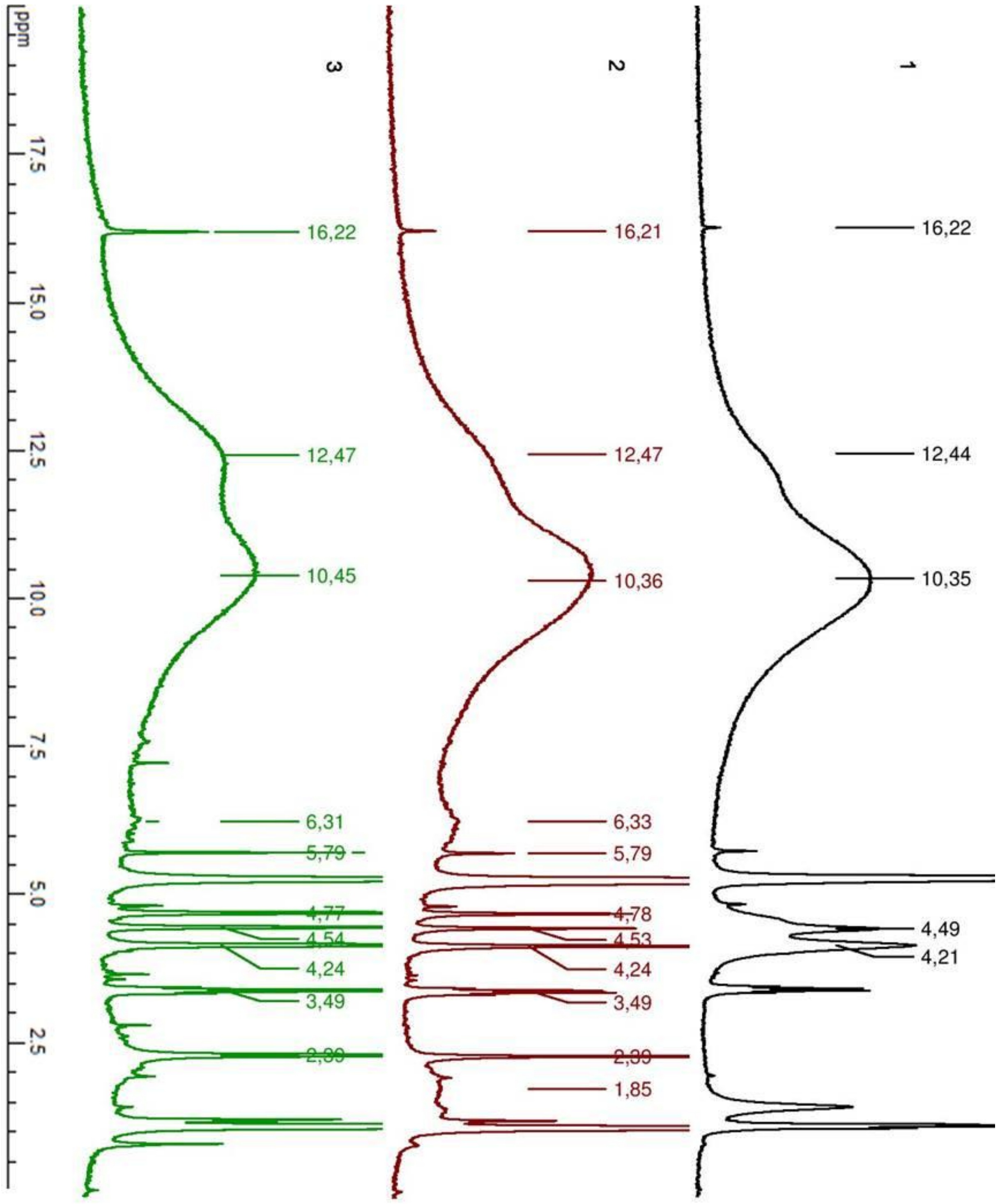

Fig. 3.15. ^{1}H NMR spectra of **Fe$_4$Fc** (1), **Fe$_4$Fc** immediately after the addition of 1 equiv. of AcFc(BF$_4$) (2), and after 24 h from the addition (3) (solvent = CD$_2$Cl$_2$).

Table 3.16. Chemical shift of acetyl ferrocene protons obtained from ^{1}H NMR spectra in $CDCl_3$.

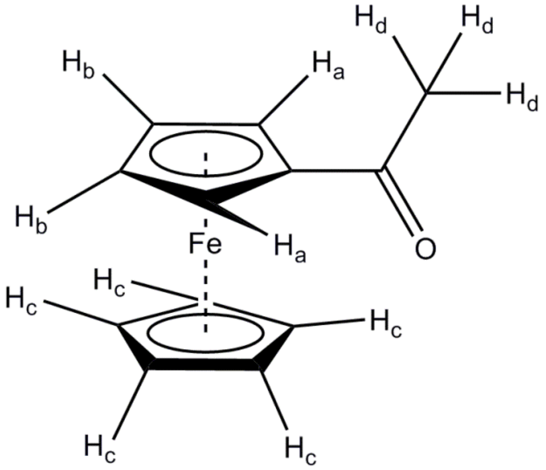

	ppm
$\mathbf{H_a}$	4.77
$\mathbf{H_b}$	4.54
$\mathbf{H_c}$	4.24
$\mathbf{H_d}$	2.39

3.7 Conclusion

In this chapter I described the design of a tripodal ligand carrying a ferrocene pendant and its incorporation in tetrairon(III) SMMs to give a supramolecular ER-SMM-ER assembly with two ferrocene units, **Fe_4Fc**. After optimizing the synthesis and performing product characterization, I attempted the oxidation of **Fe_4Fc** to (**Fe_4Fc^+**)(X^-), where X^- is a counterion like BF_4 or I_3^-. Various oxidants with different redox potentials like iodine, TBA($SbCl_6$), chlorine and AcFc(BF_4) were used. In all cases, the tetrairon(III) complex was found to decompose over time, affording mostly unidentified species.

Although a structurally appealing species, **Fe_4Fc** seemingly does not withstand oxidation of its ferrocene pendants in solution. Solid-state oxidation, with the complex embedded in a solid matrix, could be an option and an interesting target for future studies.

4 A new Fe_4 cluster for supramolecular assemblies: Fe_4pPy

4.1 Introduction

As already mentioned, the structure of Fe_4 clusters can be easily modulated by introducing suitable functionalities on tripodal ligands[62,17] or by modifying the ancillary β-diketonates.[67] The first Fe_4 system featuring a tripodal ligand was obtained by selective substitution of methoxido groups in **Fe_4std** with 2-(hydroxymethyl)propane-1,3-diol (H_3L^{Me}).[29] After that, the chemical versatility of this molecular system has been demonstrated by incorporating more complex tripodal ligands.[18,62,17,94] In very recent years, for example, the introduction of the 1,2-dithiolan-3-yl moiety allowed to graft Fe_4 clusters on gold surface[66] or nanoparticles.[71]

In this chapter, the syntheses of a new tripodal ligand carrying a 4-pyridyl ring, 2-(hydroxymethyl)-2-(pyridin-4-yl)propane-1,3-diol (H_3L^{pPy}), will be described along with the synthesis and structural and magnetic characterization of the corresponding tetrairon(III) complex **Fe_4pPy**.

4.2 The tripodal ligand H_3L^{pPy}

In order to connect Fe_4 clusters to redox-active units, like ruthenium dimers or metal porphyrins, through coordination bonds it is necessary to synthesize a tripodal ligand carrying a metal-coordinating group. Moreover, it is important to design the ligand in such a way that the donor atom is distant enough from the Fe_4 core to avoid steric crowding with the bulky *t*Bu groups.

For these reasons, I focused our attention on the tripodal ligand with a 4-pyridyl group on the quaternary carbon, H_3L^{pPy},[17] whose synthesis was reported by Dalcanale, Cornia et al. in 2010.[95] The product was obtained by refluxing 4-picoline in aqueous formaldehyde for 24 h, subsequent work-up of the crude product with methanol, vacuum pumping and final

SiO_2 column chromatography (CH_2Cl_2:CH_3OH 8:2), with a yield of 57%. Presumably, methyl hydrogen atoms of 4-picoline are acidic enough for the hydroxymethylation reaction to proceed without the addition of an exogenous base.

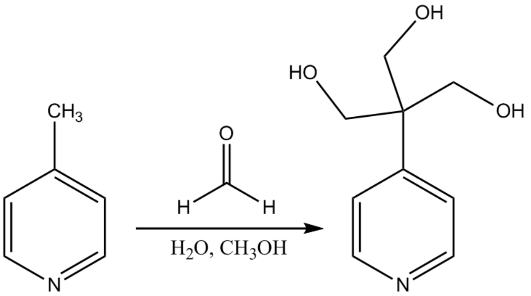

Fig. 4.1. Synthesis of H_3L^{pPy}.

Like other tripodal ligands, H_3L^{pPy} is very insoluble in low-polarity organic solvents due to the three hydroxymethyl arms, but slightly soluble in ethanol and more soluble in hot methanol, water and DMSO. The purity of the ligand was then further increased by recrystallization from hot methanol, yielding big colourless crystals in 47.3% yield. Detailed synthetic procedure is reported in the Experimental Section.

4.3 Assembly of Fe_4pPy

Generally, Fe_4 clusters can be prepared from **Fe_4std** by site-specific substitution of methoxido groups with the chosen tripodal ligand, as described in Chapter 2. For this type of tripodal ligand, which is only sparingly soluble in solvents like Et_2O and toluene, the best synthetic procedure starts from the dimeric species $[Fe_2(OEt)_2(dpm)_4]$, which is reacted with $FeCl_3$ and piperidine in a Et_2O:EtOH 4:1 mixture. Following the addition of the base, piperidinium chloride appears as a crystalline precipitate and then H_3L^{pPy} is introduced in the reaction mixture. After 4 h of stirring, the solution is filtered and put in vapour diffusion of EtOH, affording big rod-like red crystals of $[Fe_4(L^{pPy})_2(dpm)_6]\cdot 2EtOH$ (**Fe_4pPy**·2EtOH) in one week. Detailed synthetic procedure is reported in the Experimental Section.

$$3/2\ [Fe_2(OEt)_2(dpm)_4] + FeCl_3 + \text{piperidine} + 2H_3L^{pPy} \xrightarrow[\text{EtOH vapour diffusion}]{Et_2O\text{:EtOH 4:1}} [Fe_4(L^{pPy})_2(dpm)_6] + 3\text{piperidium}^+Cl^- + 3EtOH$$

The ^1H NMR spectrum of **Fe_4pPy**·2EtOH in toluene-d_8 (see Fig. 4.2) shows the presence of two molecules of EtOH per formula (CH_2 and CH_3 peaks at 3.2 and 0.9 ppm, respectively) and traces of Et_2O. As shown in Fig. 4.2, a broad band of *t*-butyl hydrogens appears at 10.5 ppm with a shoulder at 13.0 ppm corresponding to Py_a hydrogens (*m*-Py); Py_b hydrogens aren't visible because too close to paramagnetic core while the H_m hydrogens shift to negative fields (-14.1 ppm).

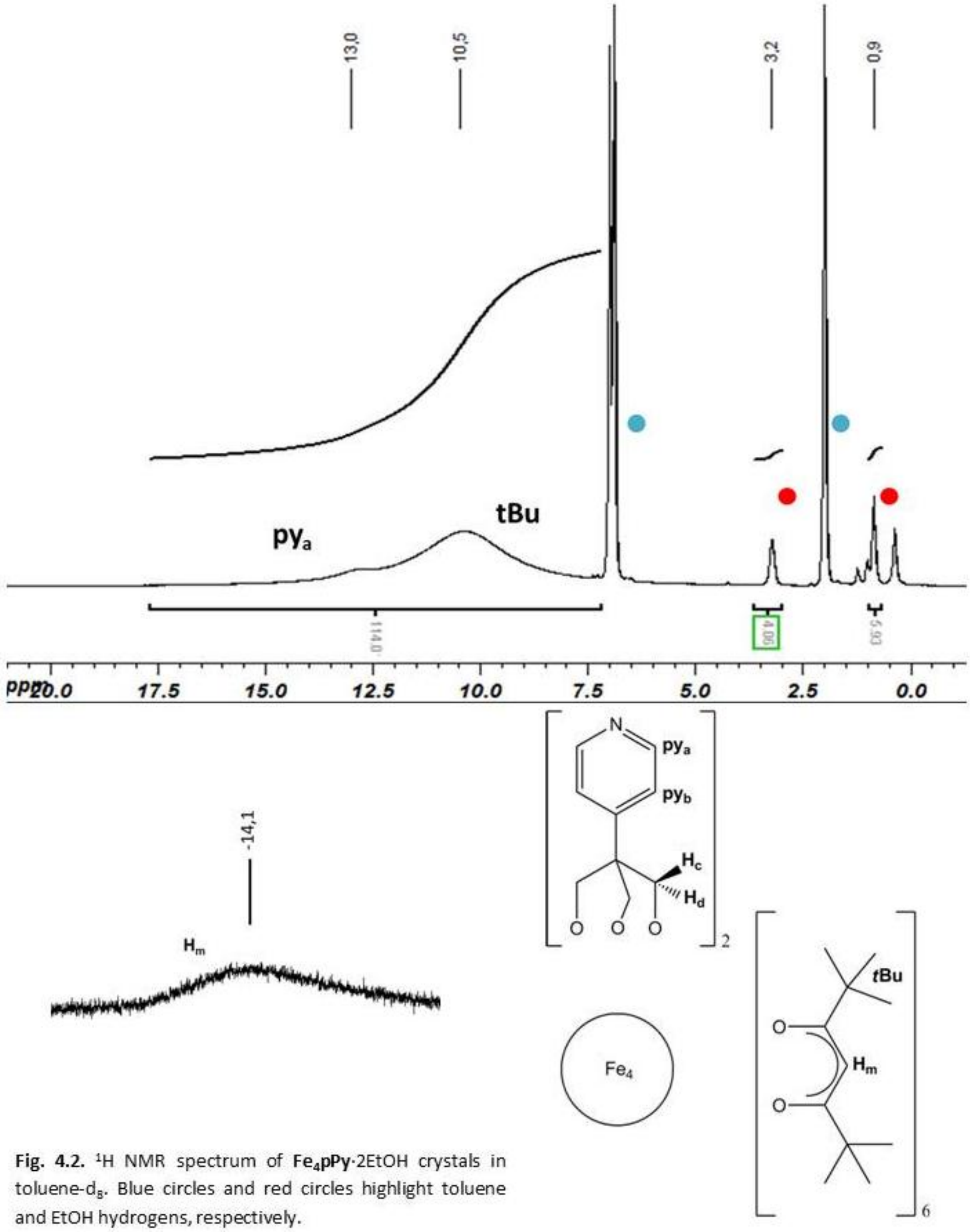

Fig. 4.2. ^1H NMR spectrum of **Fe_4pPy**·2EtOH crystals in toluene-d_8. Blue circles and red circles highlight toluene and EtOH hydrogens, respectively.

4.4 Molecular structure of Fe$_4$pPy·2EtOH

Crystals of **Fe$_4$pPy**·2EtOH grow as big rod-like individuals which lose crystallinity on prolonged standing in air or under vacuum, due to the loss of interstitial ethanol. The space group is monoclinic *C*2/*c* and the asymmetric unit contains half Fe$_4$ cluster and one ethanol molecule. Hence, two ethanol molecules are present per formula, consistent with ^{1}H NMR data. The structure of **Fe$_4$pPy** is reported in Fig. 4.3.

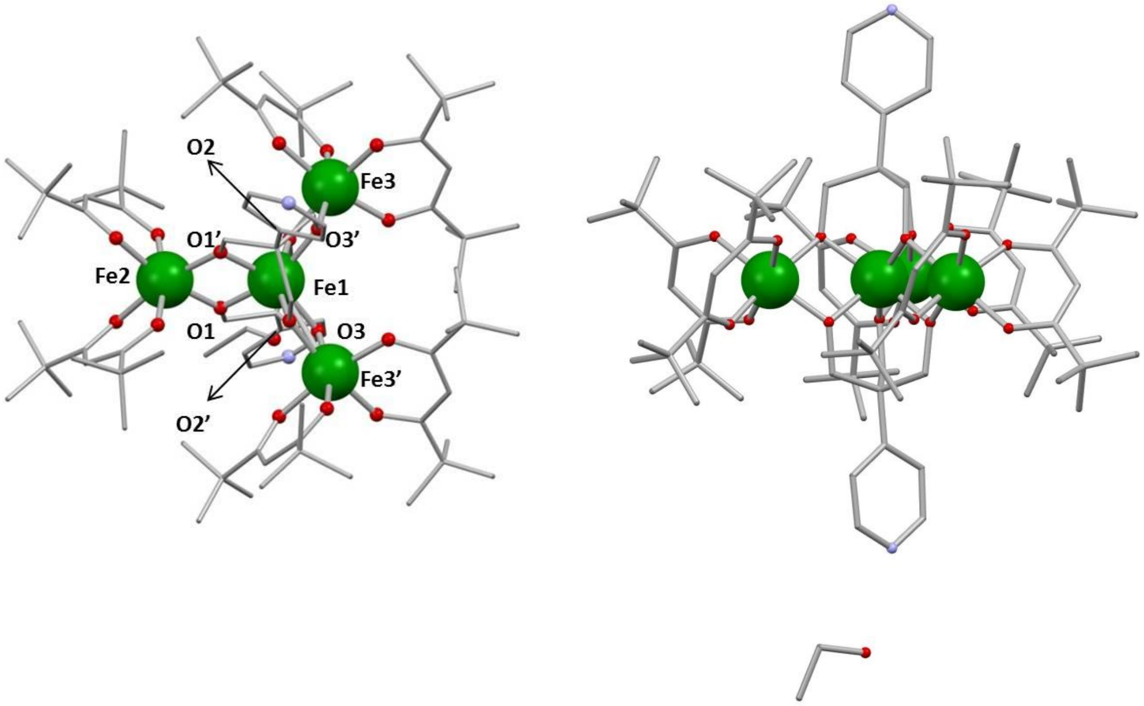

Fig. 4.3 Molecular structure of **Fe$_4$pPy**·2EtOH; colour code: Fe = green, O = red, N = blue, C = grey. Hydrogen atoms are omitted and only one EtOH molecule is shown for clarity.

The unit cell contains four tetrairon(III) molecules that develop around twofold axes and therefore have crystallographically-imposed *C*$_2$ point-group symmetry. The ethanol molecule is found hydrogen-bonded to the 4-pyridyl nitrogen atom, but disordered over three positions.

Selected geometrical parameters, reported in Experimental Section, show that the cluster is structurally very similar to other Fe$_4$ complexes with tripodal ligands.[17,18] For example, the Fe$_c$···Fe$_p$ distances, where Fe$_c$ is Fe1 and Fe$_p$ can be Fe2 or Fe3, are all in the 3.08–3.13 Å range and the pitch of the propeller-like Fe$_4$O$_6$ cores, evaluated as the average dihedral angle between the Fe$_c$(O)$_2$Fe$_p$ and Fe$_4$ planes is 68.7°. The distances Fe1–O1, Fe1–O2 and

Fe1–O3 are 1.9850(17), 1.9635(16), 1.9921(16) Å. Crystal data and structure refinement information are gathered in Table 4.1.

Table 4.1 Crystal data and structure refinement for **Fe_4pPy**·2EtOH.

Empirical formula	$C_{88}H_{146}Fe_4N_2O_{20}$	
Formula weight	1775.47	
Temperature	120(2) K	
Wavelength	0.71073 Å	
Crystal system	Monoclinic	
Space group	*C2/c*	
Unit cell dimensions	a = 19.2336(5) Å	α = 90°
	b = 21.4653(5) Å	β = 108.4249(10)°
	c = 24.6894(6) Å	γ = 90°
Volume	9670.6(4) $Å^3$	
Z	4	
Density (calculated)	1.219 g cm^{-3}	
Absorption coefficient	0.652 mm^{-1}	
Crystal size	0.41 x 0.15 x 0.15 mm^3	
Reflections collected	43560	
Independent reflections	9456 [R(int) = 0.0269]	
Completeness to theta = 26.01°	99.4 %	
Max. and min. transmission	0.9086 and 0.7760	
Refinement method	Full-matrix-block least-squares on F^2	
Data / restraints / parameters	9456/561/73	
Final R indices [I>2σ(I)]	R_1 = 0.0427, wR_2 = 0.1139	
R indices (all data)	R_1 = 0.0598, wR_2 = 0.1252	
Largest diff. peak and hole	0.720 and -0.574 e $Å^{-3}$	
Goodness of fit	1.036	

4.5 Magnetic behaviour

The temperature dependence of the $\chi_M T$ product for **Fe_4pPy**·2EtOH shows the typical trend of antiferromagnetically-coupled systems with uncompensated spin moments. The presence of dominant antiferromagnetic interactions is clearly revealed by the room-temperature $\chi_M T$ value (13.89 emu K mol^{-1}), which is significantly lower than expected for four uncoupled S_i = 5/2 spins (17.5 emu K mol^{-1} with g = 2.00). On decreasing the temperature the curve features a minimum at around 100 K, then rises again up to a maximum around 10 K. At this point $\chi_M T$ is 13.9 emu K mol^{-1}, very close to the expected value of the Curie constant for an S = 5 spin ground state (C = 15.0 emu K mol^{-1} with g = 2.00). The best-fit parameters obtained from Eqs. 2.11 and 2.12 are g = 1.9412(14), J = 15.94(6) cm^{-1}, J' = 0.45(4) cm^{-1} and θ = –0.126(6) K, which are typical for propeller-like Fe_4 systems.[17]

Isothermal M_M data recorded at low temperature show pronounced nesting when plotted as a function of H/T (Fig. 4.4), indicating the presence of magnetic anisotropy acting on the spin ground state. Fit of magnetization curves with Eq. 2.13 gave g = 1.921(8) and an axial zfs parameter D = –0.439(12) cm^{-1}, a value in the range typically found in Fe_4 complexes bearing two tripodal ligands.[17]

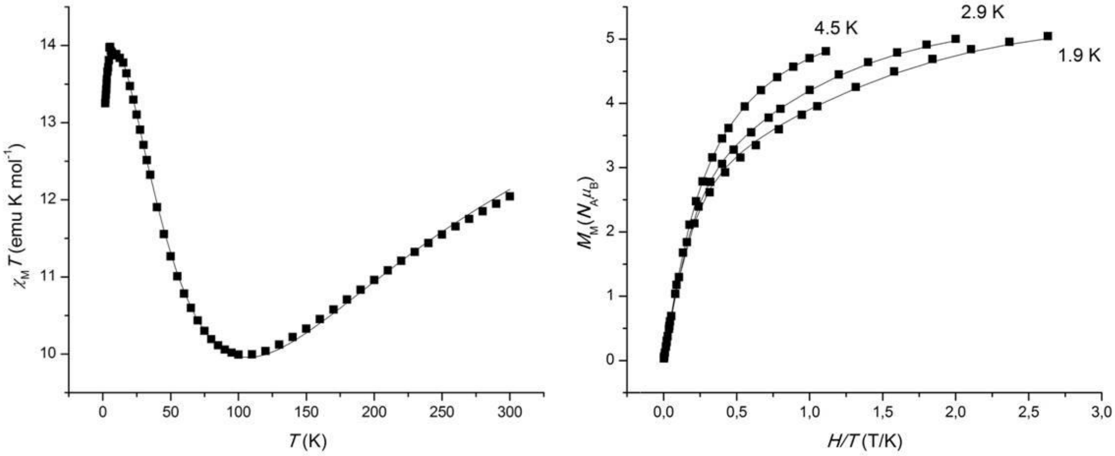

Fig. 4.4 Temperature dependence of the molar susceptibility (χ_M) multiplied by temperature (left) and field dependence of the isothermal molar magnetization (M_M) at 4.5, 2.5 and 1.9 K for **Fe$_4$pPy**·2EtOH (right). Solid lines are given by the best-fit parameters.

The dynamics of the magnetization was investigated by means of ac susceptibility measurements in zero and 1 kOe applied static field as a function of both temperature and frequency of the oscillating field (see Fig. 4.5 and Fig. 4.6). The appearance of maxima in χ_M'' is a clear signature of slow magnetic relaxation, meaning that SMM behaviour is preserved upon insertion of the pyridyl ring.[6] I thus fitted the curves to the extended Debye model[1] to extract the temperature dependence of relaxation time τ. The linear ln(τ)-vs-1/T plots (see Fig. 4.7) indicate a thermally activated relaxation mechanism with U_{eff}/k_B =

14.9(3) K and $\tau_0 = 6.3(7) \times 10^{-8}$ s at $H = 0$ and $U_{\mathrm{eff}}/k_{\mathrm{B}} = 17.2(1)$ K and $\tau_0 = 3.53(8) \times 10^{-7}$ s at H = 1 KOe in the Arrhenius law of Eq. 2.15.

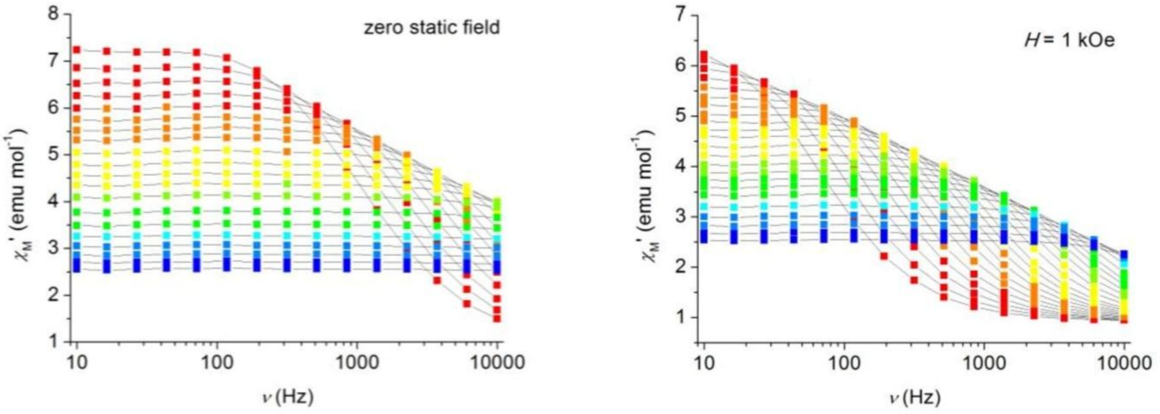

Fig. 4.5. Real component of the molar ac susceptibility (χ_M') of **Fe$_4$pPy**·2EtOH measured at zero and 1-kOe applied static fields in the 10−10000 Hz frequency range from 1.8 (red) to 5.5 K (blue).

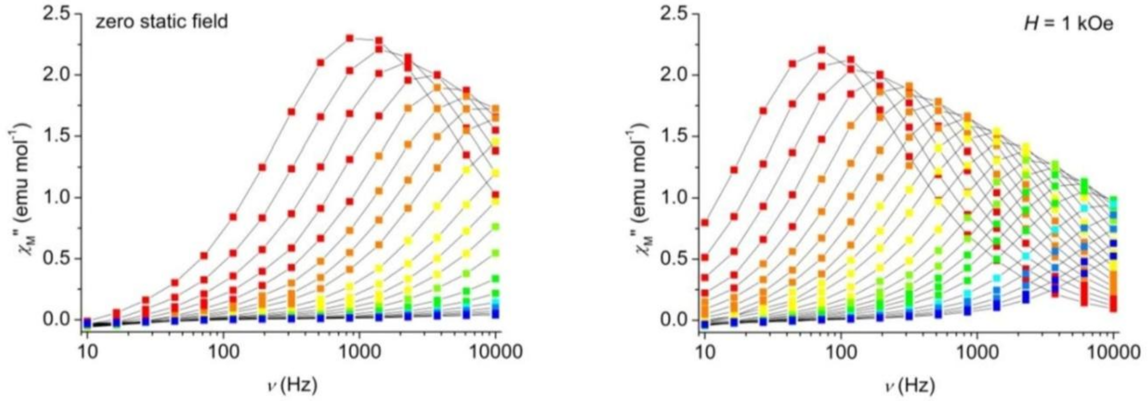

Fig. 4.6. Imaginary component of the molar ac susceptibility (χ_M'') of **Fe$_4$pPy**·2EtOH measured at zero and 1-kOe applied static fields in the 10−10000 Hz frequency range from 1.8 (red) to 5.5 K (blue).

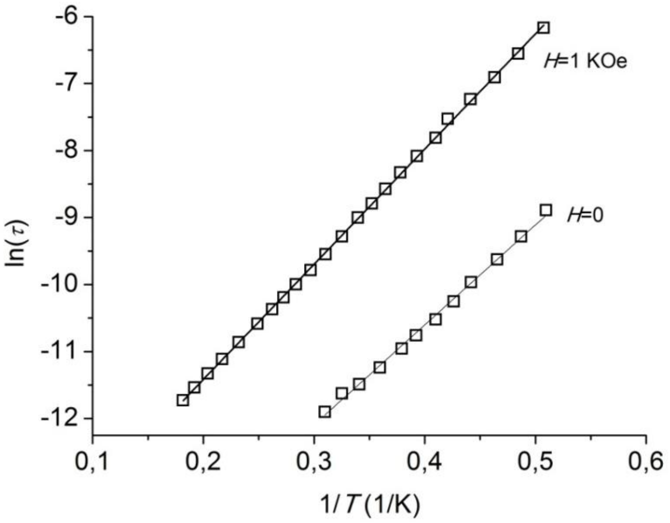

Fig. 4.7. Arrhenius plots for **Fe_4pPy**·2EtOH obtained from ac susceptibility measurements in zero and 1 kOe applied static fields.

4.5.1 MicroSQUID measurements

Magnetic hysteresis loops were recorded on a single crystal of **Fe_4pPy**·2EtOH using a microSQUID apparatus (see Experimental Section) and applying the magnetic field along the molecular easy axis, in collaboration with Dr. Wolfgang Wernsdorfer (Institut Néel – CNRS, Grenoble, France). Coercivity was found to increase with decreasing temperature and increasing scan rate, as expected for SMM behaviour (Fig. 4.8 and 4.9).[17] Measurements showed that temperature-independent, QT-driven relaxation is reached below 0.3 K (Fig. 4.8). In this temperature regime, resonant QT of individual Fe_4 centres leads to faster relaxation and steps in the hysteresis loops at regular field intervals of $|D|/(g\mu_B) \approx 0.5$ T. As the field is scanned from -1.1 to 1.1 T (lower branch of the hysteresis loops) magnetization steps are detected at 0.01, 0.50, and 0.95 T and correspond to reversal of the magnetic moment through transitions from $M_S = +5$ to –5, –4 and –3, respectively, in agreement with the behaviour of isolated Fe_4 units. Dipolar interactions through the lattice are responsible for the shift of the “zero-field” QT resonance to a slightly positive field value (about 10 mT), in accordance with previous findings;[96] Fig. 4.9 shows that such relaxation process around zero field remains visible even at the lowest temperature (0.03 K) and with the fastest scan rate (0.280 T s^{-1}). Intermolecular dipole-dipole interactions also promote spin-spin cross relaxation,[96] which is at the origin of the pre-step features observable in Fig. 4.9.

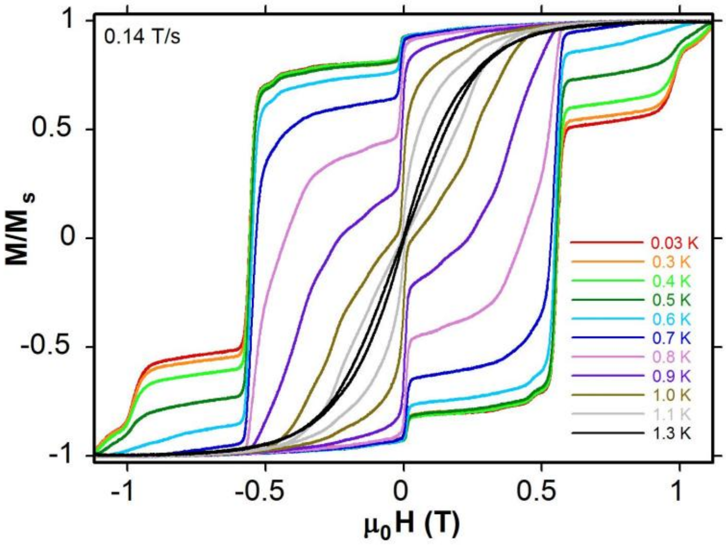

Fig. 4.8. Magnetization versus dc field hysteresis loops for a single crystal of **Fe_4pPy**·2EtOH at 0.14 T s^{-1} and variable temperature from 0.03 K (red) to 1.3 (black) K. M_s is the saturation magnetization.

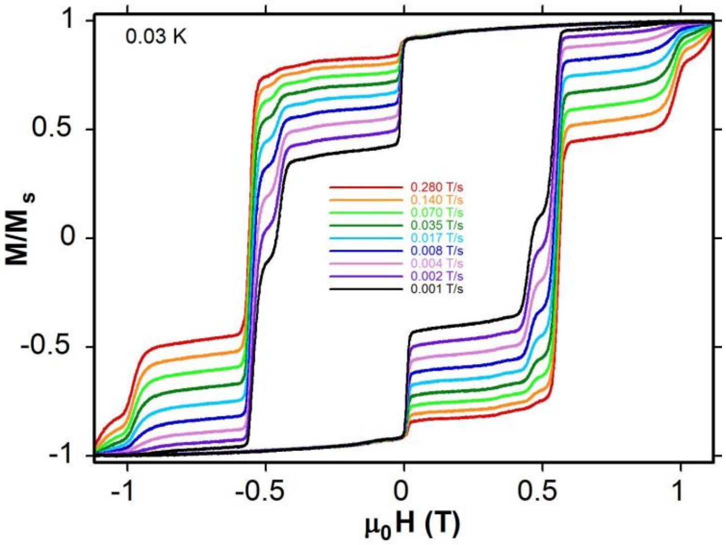

Fig. 4.9. Magnetization versus dc field hysteresis loops for a single crystal of **Fe_4pPy**·2EtOH at 0.03 K and variable sweep rate from 0.001 (black) to 0.280 (red) Ts^{-1}. M_s is saturation magnetization.

5 Supramolecular chains of Fe₄pPy and diruthenium paddlewheels

5.1 Introduction

In order to obtain supramolecular assemblies of **Fe_4pPy** and ER, ruthenium "paddlewheel"-like dimers attracted our attention for their chemical robustness and unique magnetic properties, as described in 5.2. In particular, ruthenium dimers with carboxylate bridging ligands exist in two main oxidation states: (II,II) and (II,III). Both types of diruthenium units are paramagnetic with s = 1 and s = 3/2, respectively. However, because of their large easy-plane anisotropy normal to the direction of the metal-metal bond, at low temperature they act as effective spins with s_{eff} = 0 and 1/2, respectively. For these reasons, ruthenium dimers appear as suitable redox-active groups for tuning SMM behaviour. From the supramolecular assembly of diruthenium paddlewheels and **Fe_4pPy**, I was unable to isolate discrete diads or triads. Rather, I obtained chain-like structures, whose synthesis, structural features and magnetic behaviour are described in this chapter.[19]

5.2 Ruthenium dimers

Diruthenium tetracarboxylates are part of the familiy of dimetal tetracarboxylates, $[M_2(O_2CR)_4]^n$ (with M = Cr, Mo, W, Tc, Re, Ru, Os, Co, Rh, Ir, Ni, Cu and $-2 \leq n \leq +4$), which receive much prominence in literature.[97,98] Their structure is shown in Fig. 5.1 and consists of two metals linked by a metal-metal bond and bridged by four carboxylates, to give a "paddlewheel"-like shape. Most diruthenium compounds of this type contain either homovalent $[Ru_2^{II,II}(\mu\text{-}O_2CR)_4]$ or mixed-valent $[Ru_2^{II,III}(\mu\text{-}O_2CR)_4]^+$ species. In the latter, the extra electron is delocalised between the two metals, so that the ruthenium centres have an effective oxidation state of +2.5. Additional monodentate ligands (L) can coordinate the metal centres in apical position.

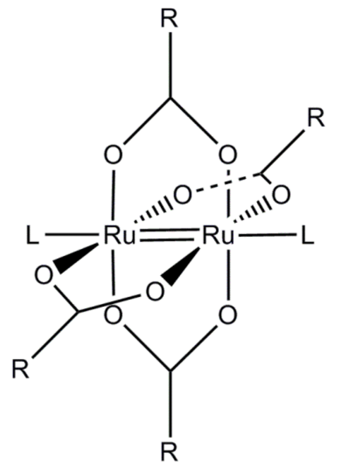

Fig. 5.1 Typical “paddlewheel” structure of $[Ru_2(O_2CR)_4L_2]$ complexes.

The first synthesis of a diruthenium tetracarboxylate was reported in 1966 by Stephenson and Wilkinson,[99] who obtained the mixed-valent species $[Ru_2(\mu\text{-}O_2CR)_4Cl]$ with R = Me, Et or ^{n}Pr. These compounds are very stable and present a one dimensional polymeric structure supported by bridging chlorides, which occupy apical positions. Subsequently, from these first ancestors it was possible to synthesize a series of isolated dimers by replacing chlorides with two axially coordinated ligands.[100,101]

Differently from the mixed-valent species, the $Ru^{II}Ru^{II}$ complexes are very air-sensitive. They can be prepared by reduction of $Ru^{II}Ru^{III}$ using hydroquinone and triethylamine in anhydrous MeOH, following a facile procedure proposed by Barral and co-authors in 2005.[102]

Turning now to magnetic properties, $Ru^{II}Ru^{II}$ and $Ru^{II}Ru^{III}$ complexes are both paramagnetic with $s = 1$ and $s = 3/2$, respectively. Furthermore, diruthenium paddlewheels show a large and positive axial zfs parameter D, which implies that the low energy states have the minimum spin component along z ($M_S = 0$ for integer s and $\pm½$ for half-integer s). Consequently, these complexes have a large easy-plane anisotropy normal to the metal-metal bond and at low temperature they act as effective spins with $s_{eff} = 0$ and ½, respectively.

For $Ru^{II}Ru^{II}$ ($s = 1$), the zero-field energies $E(M_S)$ of the M_S substates are: $E(0) = -2D/3$ and $E(\pm 1) = D/3$. For $Ru^{II}Ru^{III}$ ($s = 3/2$) the energies are: $E(\pm 1/2) = -D$ and $E(\pm 3/2) = D$. The two compounds used in this work, $[Ru_2^{II,II}(AcO)_4(MeOH)_2]$[97,103,104] and $[Ru_2^{II,III}(AcO)_4(THF)_2](BF_4)$,[97,103,105,106] have $D \approx 270$ cm^{-1} and 63 cm^{-1}, respectively (Fig. 5.2).

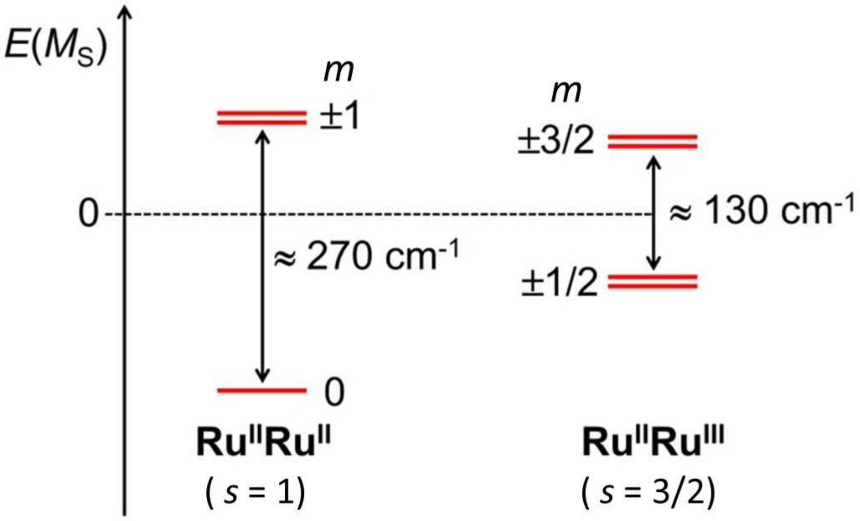

Fig. 5.2. Energy of spin states for $s = 1$ (left) and 3/2 (right) in the presence of easy-plane anisotropy ($D > 0$). The two cases correspond to the species Ru^{II}Ru^{II} and Ru^{II}Ru^{III}, respectively. The dashed line represents the centre of gravity of the energies.

5.3 Synthesis

5.3.1 Fe_4Ru_2(II,II)

The starting reagent for the synthesis of diruthenium paddlewheels is $RuCl_3$. By heating a mixture of $RuCl_3$, acetic acid, acetic anhydride and LiCl overnight under an oxygen atmosphere, an insoluble red-brown powder of $[Ru_2^{II,III}(AcO)_4Cl]$ is obtained.[99]

The second step is the substitution of chlorides with THF ligands: a suspension of $[Ru_2^{II,III}(AcO)_4Cl]$ in THF is treated with stoichiometric $AgBF_4$ overnight under inert atmosphere to afford a red solution of $[Ru_2^{II,III}(AcO)_4(THF)_2](BF_4)$.[100] After solvent evaporation, the solid residue is reacted with hydroquinone and NEt_3 in anhydrous MeOH, again under inert atmosphere, to afford $[Ru_2^{II,II}(AcO)_4(MeOH)_2]$. The compound can be isolated in crystalline form by cooling the solution to –18 °C and subsequent filtering.[102]

Slow diffusion of a THF solution of the diruthenium(II,II) complex $[Ru_2^{II,II}(AcO)_4(MeOH)_2]$ into a solution of **Fe_4pPy**·2EtOH in CH_2Cl_2 under inert atmosphere affords $[Fe_4(pPy)_2(dpm)_6][Ru_2(OAc)_4]$ (**Fe_4Ru_2(II,II)**) as tiny red crystals in one week.

$$[Fe_4(pPy)_2(dpm)_6]*2EtOH + [Ru_2(AcO)_4(MeOH)_2] \xrightarrow[\text{liquid diffusion}]{\text{THF/DCM}} [Fe_4(pPy)_2(dpm)_6][Ru_2(AcO)_4] + 2MeOH + 2EtOH$$

The dry crystals undergo fast loss of interstitial solvent (DCM and THF molecules). For more information see Experimental Section. The compound was characterized by EA, IR and MALDI-ToF. The MALDI-ToF spectrum obtained from a solution of the compound in THF gives a peak at *m/z* = 2122.52 with the correct isotopic pattern for $[Fe_4(pPy)_2(dpm)_6][Ru_2(OAc)_4]^+$ ($[M]^+$, 5%), as shown in Fig. 5.3.

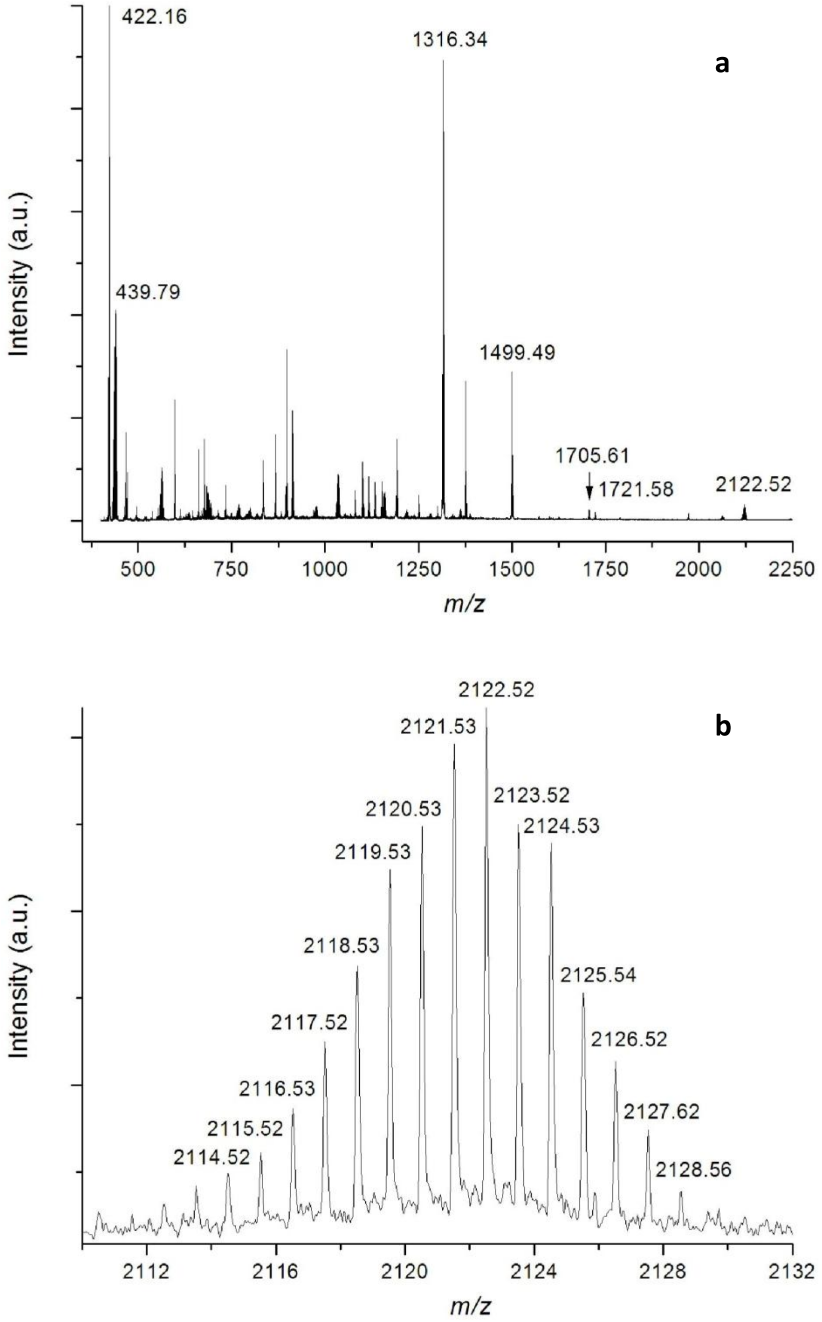

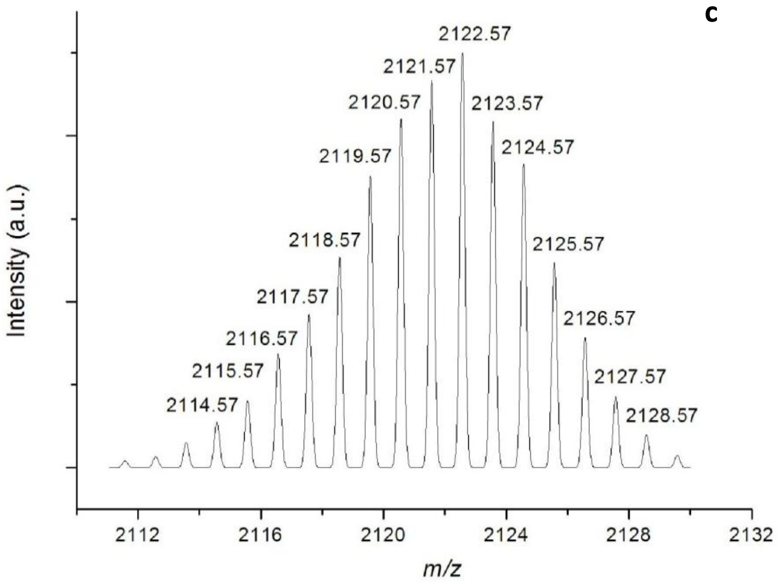

Fig. 5.3. MALDI-ToF full-scan mass spectrum (a) and mass scale-expanded segment for compound **Fe_4Ru_2(II,II)** (b), along with calculated isotopic pattern for $[Fe_4(pPy)_2(dpm)_6][Ru_2(OAc)_4]^+$ or $C_{92}H_{146}Fe_4N_2O_{26}Ru_2$ (*m/z* = 2122.57) (c).

5.3.2 Fe_4Ru_2(II,III)

Compounds containing **Fe_4pPy** and mixed-valent $[Ru_2^{II,III}(OAc)_4(THF)_2](BF_4)$ were prepared using two different methods. In the first one (*Method a*), toluene vapours were allowed to diffuse into a THF solution of the two reagents. The second method (*Method b*) is similar to that used for assembling the **Fe_4Ru_2(II,II)** adduct and implies the slow diffusion of a THF solution of the diruthenium(II,III) complex $[Ru_2(OAc)_4(THF)_2](BF_4)$ into a solution of **Fe_4pPy**·2EtOH in CH_2Cl_2. The red crystals obtained with *Method a* are stable to the air and apparently don’t lose interstitial solvent. More synthetic information is provided in Experimental Section.

Method a:

$$[Fe_4(pPy)_2(dpm)_6]*2EtOH + [Ru_2(AcO)_4(THF)_2](BF_4) \xrightarrow[\text{vapour diffusion}]{\text{THF/toluene}} [Fe_4(pPy)_2(dpm)_6][Ru_2(AcO)_4](BF_4) + 2THF + 2EtOH$$

Method b:

$$[Fe_4(pPy)_2(dpm)_6]*2EtOH + [Ru_2(AcO)_4(THF)_2](BF_4) \xrightarrow[\text{liquid diffusion}]{\text{THF/DCM}} [Fe_4(pPy)_2(dpm)_6][Ru_2(AcO)_4](BF_4) + 2THF + 2EtOH$$

Also for compound **Fe_4Ru_2(II,III)** MALDI-ToF spectra show a peak at *m/z* = 2122.41 with the correct isotopic pattern for $[Fe_4(pPy)_2(dpm)_6][Ru_2(OAc)_4]^+$ (see Fig. 5.4), confirming the successful assembly of Fe_4 and Ru_2 components.

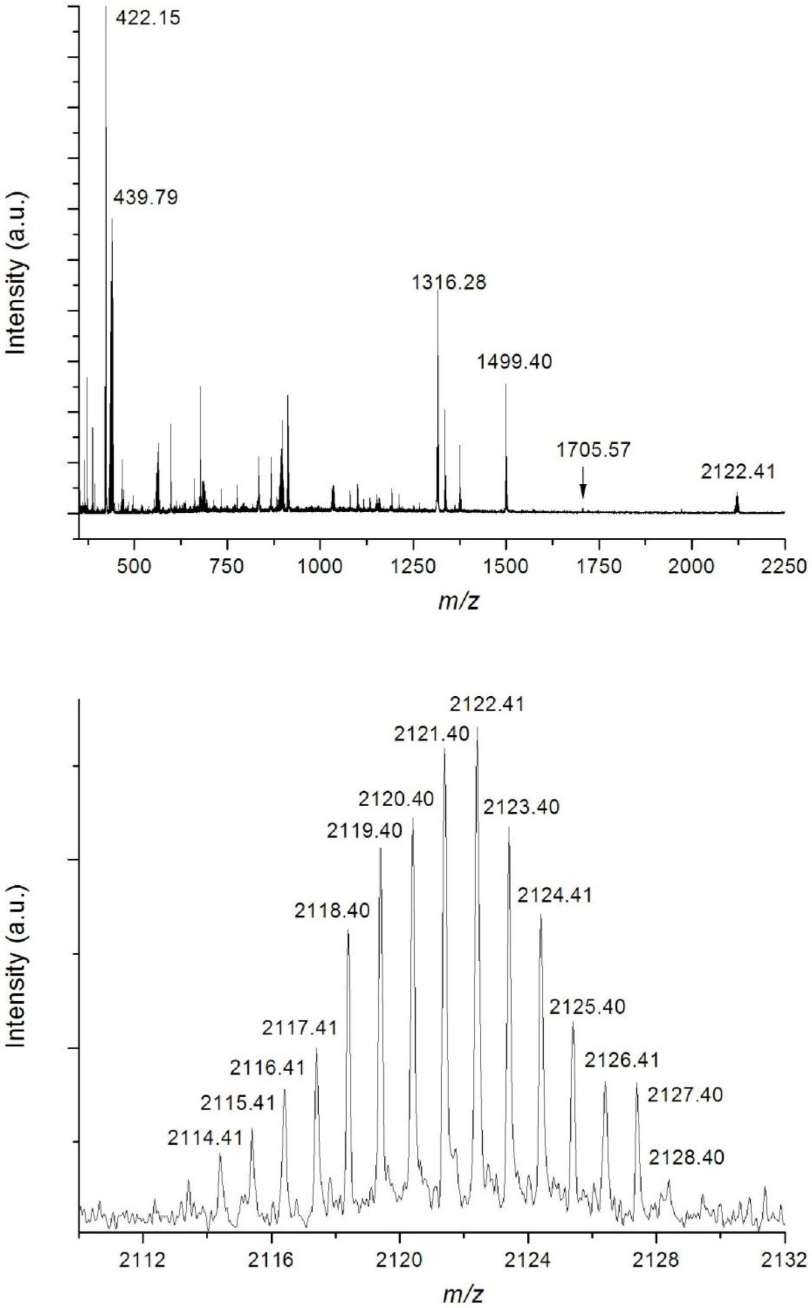

Fig. 5.4. MALDI-ToF full-scan mass spectrum (top) and mass scale-expanded segment (bottom) for compound **Fe_4Ru_2(II,III)**; see Fig. 5.3c for calculated isotopic pattern of $[Fe_4(pPy)_2(dpm)_6][Ru_2(OAc)_4]^+$ or $C_{92}H_{146}Fe_4N_2O_{26}Ru_2$ (*m/z* = 2122.57).

5.4 Structural characterization

5.4.1 Fe_4Ru_2(II,II)

The tiny red crystals of the compound undergo very quick loss of interstitial solvent, are air-sensitive and diffract too weakly to be analysed with a traditional X-ray diffractometer. A proposal for beamtime was thus submitted to Elettra synchrotron and approved. The compound crystallizes in monoclinic space group $P2_1$/n with one tetrairon(III) SMM, one diruthenium complex, and interstitial solvent molecules (DCM and THF) in the asymmetric unit. The pyridyl nitrogen atoms of Fe_4 complexes coordinate the ruthenium atoms in the apical positions replacing MeOH molecules and affording a chain-like structure (Fig. 5.5).

Selected geometrical parameters show that **Fe_4Ru_2(II,II)** and **Fe_4pPy**·2EtOH have Fe_4 units with similar structure.

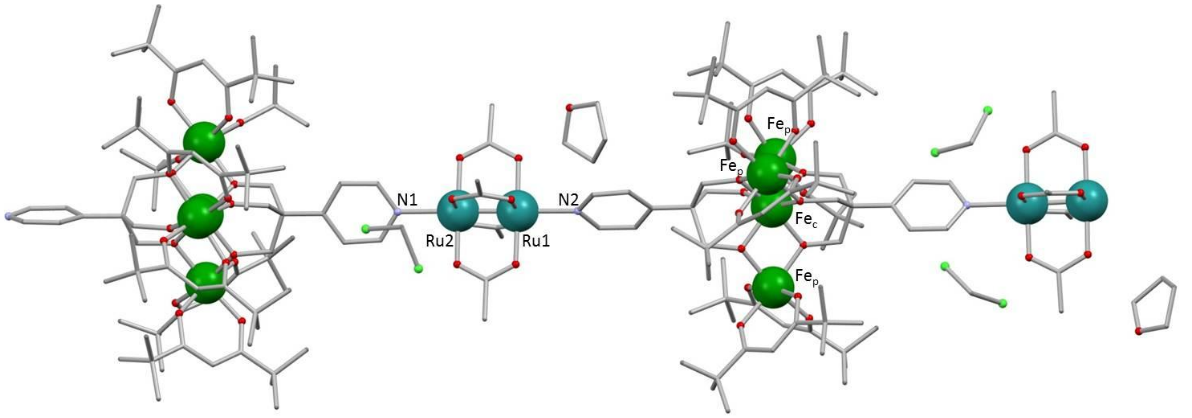

Fig. 5.5. Chains of **Fe_4Ru_2(II,II)** viewed along *b* direction. Interstitial solvent molecules are also included.

The Fe_c···Fe_p distances are all in the 3.07–3.08 Å range. The dihedral angles between the $Fe_c(O)_2Fe_p$ and Fe_4 planes, which define the pitch of the propeller-like Fe_4O_6 core, take the values 68.15°, 68.77° and 68.90° and are typical of Fe_4 complexes with tripodal ligands.[18,17]

The Fe_c···Ru separation is 9.68 Å, hence similar to the value (9.6 Å) found in the structure of **Fe_4Ru_2(II,III)** described below. The N1···Ru2 and N2···Ru1 distances are 2.297 Å and 2.300 Å, respectively, as expected for a Ru–N coordination bond.

The dihedral angles between Fe_4 and RuO_4 planes have an average value of 4.18° for Ru1 and 4.05° for Ru2. These values indicate that the structure entails approximately linear chains, as opposed to **Fe_4Ru_2(II,III)** obtained with *Method a* (see below). Neighbouring Fe_4 units in the chain are rotated by 26.45° away from each other, as shown in Fig. 5.6.

The large voids between chains are occupied by interstitial solvent molecules (DCM and THF), as confirmed by elemental analysis and by the fast loss of crystallinity upon drying. Approximately one DCM and one THF molecule per formula unit were located and refined, while the remaining electron density residuals were treated with the SQUEEZE routine.

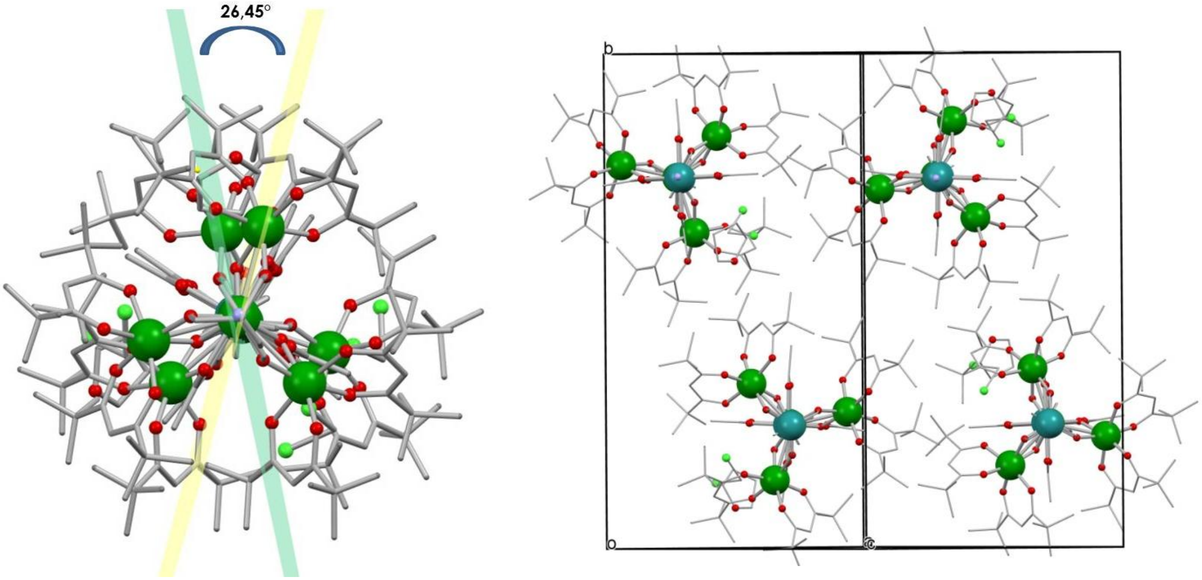

Fig. 5.6. Rotation of neighbouring Fe_4 units along the chain by 26.45° (left). Crystal packing inside the unit cell, which comprises four asymmetric units, *Z* = 4 (right).

Table 5.1 Crystal data and structure refinement for **Fe_4Ru_2(II,II)**

Empirical formula	$C_{98}H_{158}Cl_4Fe_4N_2O_{27}Ru_2$	
Formula weight of chain	2122.56	
Temperature	100(2) K	
Wavelength	0.7107 Å	
Crystal system	Monoclinic	
Space group	*P*2(1)/n	
Unit cell dimensions	*a* = 16.258(3) Å	$\underline{\alpha}$ = 90°
	b = 26.482(5) Å	β = 100.44(3)°
	c = 37.209(7) Å	γ = 90°
Volume	15755(6) $Å^3$	
Z	4	
Density (calculated)	0.940 gcm^{-3}	
Absorption coefficient	0.610 mm^{-1}	
Crystal size	-	
Reflections collected	83317	
Independent reflections	24322 [*R*(int) = 0.0292]	
Completeness to theta = 24.686°	90.8 %	
Max. and min. transmission	0.9086 and 0.7760	
Refinement method	Full-matrix-block least-squares on F^2	
Data / restraints / parameters	83317 / 646 / 1549	
Final *R* indices [$I>2\sigma(I)$]	R_1 = 0.0734, wR_2 = 0.2309	

R indices (all data)	R_1 = 0.0961, wR_2 = 0.2524
Largest diff. peak and hole	1.20 and -0.78 eÅ^{-3}
Goodness of fit	1.082

5.4.2 Fe_4Ru_2(II,III) – *Method a*

The tiny red crystals of the compound obtained with *Method a* are air stable but only suitable for single-crystal XRD with synchrotron light. The compound crystallizes in monoclinic space group *Pn* with two tetrairon(III) SMMs, two diruthenium complexes, and two BF_4^- anions in the asymmetric unit, as shown in Fig. 5.7. The pyridyl nitrogen atoms of Fe_4 complexes coordinate the ruthenium atoms in the apical positions replacing THF molecules, and generating two crystallographically-independent 1D chains that run along the *c* axis (Fig. 5.7). Selected geometrical parameters, gathered in Table E.1 in Experimental Section, show that the Fe_4 units in **Fe_4Ru_2(II,III)** are similar to those in **Fe_4pPy**·2EtOH. For example, the Fe_c···Fe_p distances are all in the 3.08–3.13 Å range. The average dihedral angle between the $Fe_c(O)_2Fe_p$ and Fe_4 planes is 70.18°, hence typical of Fe_4 complexes with tripodal ligands.[18,17] The Fe_c···Ru separation is 9.6 Å and the intrachain Fe_c···Fe_c distance is 21.3 Å. Neighbouring chains are closely packed, with BF_4^- anions occupying the cavities in between them, as shown in Fig. 5.7; the shortest interchain Fe_c···Fe_c distance is 13.4 Å, while the minimum interchain Fe···Fe separation is 9.9 Å. The two crystallographically-independent Fe_4 molecules are almost coplanar (5.48°) while the dihedral angle between Fe_4 and RuO_4 planes ranges from 23.8 to 25.38° (average = 24.58°). This is indicative of a zig-zag arrangement of Fe_4 and Ru_2 components, as opposed to the quasi-linear chain structure found in **Fe_4Ru_2(II,II)**.

In both chains, dpm$^-$ ligands adopt only the propeller-like arrangement, *p*, in which the two oxygen donors lie on opposite sides of the molecular plane, as already observed in other Fe_4 clusters.[70]

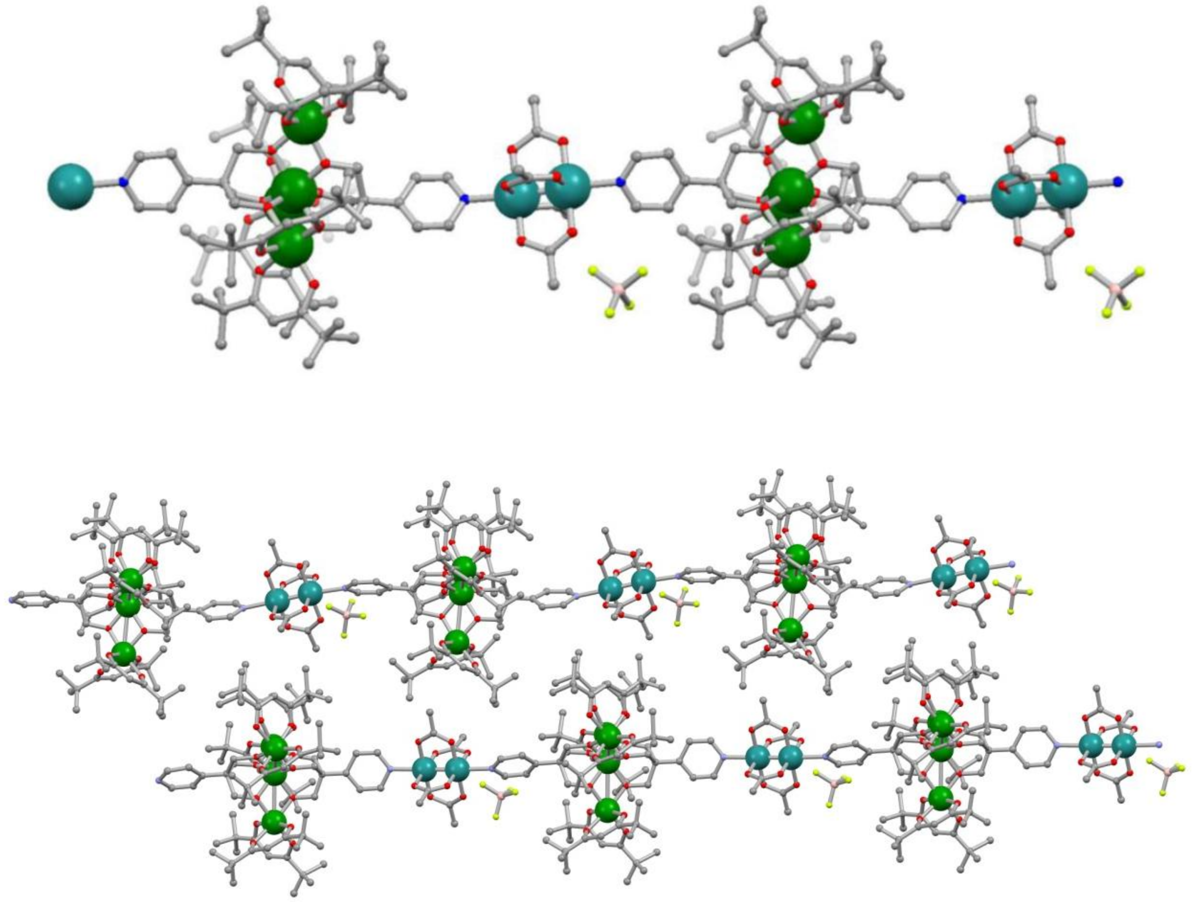

Fig. 5.7. Molecular structure (upper panel) and crystal packing (lower panel) in **Fe_4Ru_2(II,III)**, with the polymeric chains A and B running along **c**. Colour code: Fe = green, Ru= light blue, O = red, N = blue, C = grey, B = pink, F = yellow. Hydrogen atoms are omitted for clarity, and only one position is represented for disordered BF_4^-.

Table 5.2. Crystal data and structure refinement for **Fe_4Ru_2(II,III)**

Empirical formula	$C_{92}H_{146}BF_4Fe_4N_2O_{26}Ru_2$	
Formula weight	2208.96	
Temperature	100(2) K	
Wavelength	0.7000 Å	
Crystal system	Monoclinic	
Space group	*Pn*	
Unit cell dimensions	a = 16.969(9) Å	α = 90°
	b = 33.403(3) Å	β = 109.16(2)°
	c =21.324(4) Å	γ = 90°
Volume	11417(7) Å^3	
Z	4	
Density (calculated)	1.285 g cm^{-3}	

Absorption coefficient	0.823 mm^{-1}
Reflections collected	42546
Independent reflections	42507 [R(int) = 0.0269]
Completeness to theta = 26.34°	88.5 %
Refinement method	Full-matrix-block least-squares on F^2
Data / restraints / parameters	42507 / 2332 / 1547
Final R indices [$I>2\sigma(I)$]	R_1 = 0.0893, wR_2 = 0.2401
R indices (all data)	R_1 = 0.1036, wR_2 = 0.2553
Largest diff. peak and hole	2.142 and -1.958 eÅ^{-3}
Goodness of fit	1.042

5.4.3 Fe_4Ru_2(II,III)BF_4 – *Method b*

Method b afforded big hexagonal red crystals of **Fe_4Ru_2(II,III)** suitable for single crystal XRD with synchrotron light. The crystals are not air-stable, probably due to the loss of interstitial solvent. The compound crystallizes with a metrically-hexagonal unit cell: $a = b$ = 15.865(2) Å, c = 21.519(4), $\alpha = \beta$ = 90°, γ = 120°, V = 4960 (16) Å^3 and Z = 1. Diffraction symmetry is indicative of hexagonal Laue group 6/mmm, which would involve major disorder effects or crystal twinning. Preliminary structure solution and refinement in trigonal space group $P321$ allowed to clearly locate the Fe_4O_6 core and Ru atoms, confirming a chain-like structure. The former develops on a D_3-symmetry site, consistent with its maximum symmetry. The Fe_4 complex and the diruthenium unit exhibit rotational disorder around the c axis, but the geometrical parameters are not far from those found in the structure of **Fe_4Ru_2(II,III)** obtained with *Method a* (Fe1···Ru1 = 9.678 Å, Ru-N = 2.077 Å and Fe1···Fe2 = 3.076 Å). However, in this case crystal symmetry requires the chains to be perfectly linear, as opposed to the zig-zag arrangement found in **Fe_4Ru_2(II,III)** prepared by *Method a*.

5.5 Magnetic behaviour

The $\chi_M T$-vs-T and M_M-vs-H/T curves, reported in Fig. 5.8, are typical of Fe_4 systems,[18,17] with **Fe_4Ru_2(II,III)** significantly more magnetic than the other two compounds because of the presence of the s = 3/2 Ru_2 unit.[97,103] Since Fe_4-Ru_2 magnetic interactions are expected to cover a much smaller energy scale than intramolecular Fe-Fe couplings and magnetic anisotropies, I assumed independent Fe_4 and Ru_2 units and subtracted the expected Ru_2 contribution from the data using typical g-values and zfs parameters (D') for $Ru^{II}Ru^{II}$ (s = 1,

g_{Ru} = 2.15, D' = 270 cm^{-1})[97,103,104] and Ru$^{\mathrm{II}}$Ru$^{\mathrm{III}}$ (s = 3/2, g_{Ru} = 2.08, D' = 63 cm^{-1}).[97,106] The resulting data were satisfactorily reproduced by Eqs. 2.11-2.13 with parameters typical for Fe$_4$ SMMs (see the Experimental Section).[18,17]

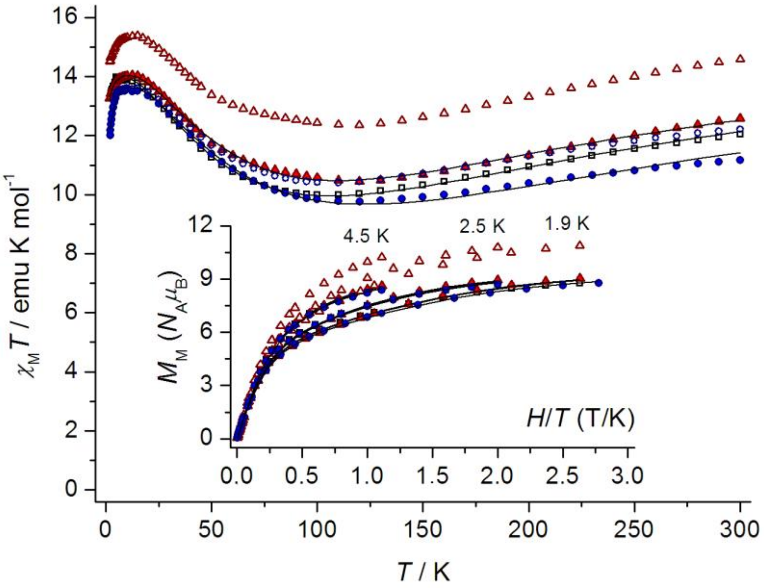

Fig. 5.8. Temperature dependence of the molar magnetic susceptibility (χ_M) multiplied by temperature and field dependence of the isothermal molar magnetization (M_M) at 4.5, 2.5 and 1.9 K (inset) for compounds **Fe$_4$pPy**·2EtOH (□), **Fe$_4$Ru$_2$(II,II)** (○) and **Fe$_4$Ru$_2$(II,III)** (△). Filled triangles and circles represent data obtained subtracting the s = 1 or 3/2 contribution, given by the [Ru$_2$(OAc)$_4$]$^{0/+}$ fragments, from the data of **Fe$_4$Ru$_2$(II,II)** or **Fe$_4$Ru$_2$(II,III)**, respectively. In the inset, original magnetization data for **Fe$_4$Ru$_2$(II,II)** are not reported for clarity, since they practically coincide with the corrected ones. Solid lines are given by the best-fit parameters.

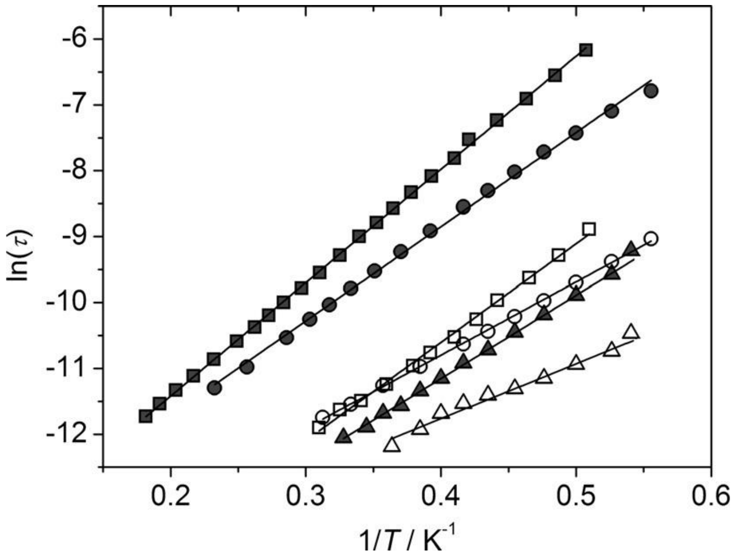

Fig. 5.9. Arrhenius plots for compounds **Fe$_4$pPy**·2EtOH (□), **Fe$_4$Ru$_2$(II,II)** (○), and **Fe$_4$Ru$_2$(II,III)** (△) obtained from ac susceptibility measurements in zero (empty symbols) and 1 kOe (full symbols) applied static fields.

The magnetization dynamics of **Fe_4Ru_2(II,II)** and **Fe_4Ru_2(II,III)** was then investigated by alternating current (ac) susceptibility measurements at temperatures above 1.8 K and in both zero and 1 kOe applied static field. This H value was found effective in minimizing relaxation by QT (see Figs. 5.11-5.16). In all cases a temperature dependence of the maxima in the χ_M''-vs-ν plots was observed, demonstrating that the two compounds behave as SMMs. Data were then fitted within the Debye model[63,64] and a linear ln(τ)-vs-1/T dependence found in the Arrhenius plots of Fig. 5.9, pointing to thermally activated relaxation in the explored temperature range (see Table 5.3 for best-fit parameters). Significantly, while Fe_4 units display similar zfs D values in the three compounds, the anisotropy barriers U_{eff}/k_B follow the trend **Fe_4Ru_2(II,III)** (12.63(7) K) < **Fe_4Ru_2(II,II)** (14.30(17) K) < **Fe_4pPy**·2EtOH (17.20(7) K) at 1 kOe, indicating that both $Ru^{II}Ru^{II}$ and $Ru^{II}Ru^{III}$ bridges enhance under barrier relaxation over isolated Fe_4 units. The greater effect of $Ru^{II}Ru^{III}$ is explained by the m = 1/2 doublet stabilized by the large positive zfs, as opposed to the m = 0 singlet of $Ru^{II}Ru^{II}$ (in the following, the Fe_4 and Ru_2 spin substates will be labelled by M and m quantum numbers, respectively). The two complexes then behave as effective s_{eff} = 1/2 and 0, respectively, and fast fluctuations of the former may provide a source of QT (see Fig. 5.10). Zero field ac measurements show shorter τ values and lower barriers but a similar trend in the three compounds. All measurements indicate a narrow distribution of relaxation times, with in-field α values[63,64] ranging from 0.13 to 0.17 at 1.9 K.

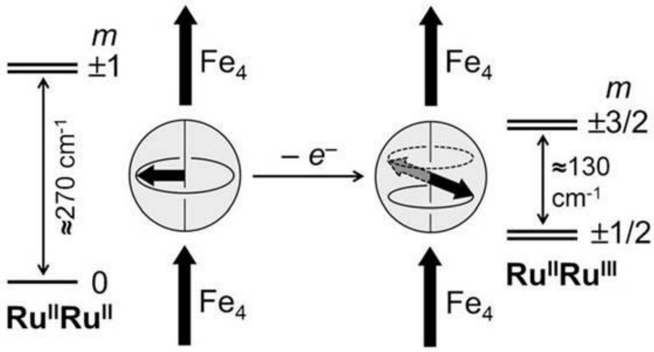

Fig. 5.10. Effect of electron count on the magnetic properties of Ru_2 bridges in **Fe_4Ru_2(II,II)** and **Fe_4Ru_2(II,III)**. Bold arrows depict spin vectors at Fe_4 and Ru_2 sites. The leftmost and rightmost diagrams show the large zfs that give rise to a nonmagnetic m = 0 ground singlet and an m = ±1/2 ground doublet in $Ru^{II}Ru^{II}$ (s = 1) and $Ru^{II}Ru^{III}$ (s = 3/2), respectively.

Table 5.3. Best-fit parameters obtained from the analysis of dc and ac magnetic data on **Fe$_4$pPy**·2EtOH, **Fe$_4$Ru$_2$(II,II)** and **Fe$_4$Ru$_2$(II,III).**

	Fe$_4$pPy·2EtOH	**Fe$_4$Ru$_2$(II,II)**	**Fe$_4$Ru$_2$(II,III)**
dc measurements			
$\chi_M T$ vs T curves			
G	1.9412(14)	1.9501(15)	1.937(3)
J (cm^{-1})	15.94(6)	15.47(7)	19.05(17)
J' (cm^{-1})	0.45(4)	−0.37(4)	1.04(10)
θ (K)	−0.126(6)	−0.154(6)	−0.325(17)
M_M vs H/T curves			
G	1.921(8)	1.935(5)	1.903(5)
D (cm^{-1})	−0.439(12)	−0.449(8)	−0.430(8)
ac measurements			
$H = 0$			
U_{eff}/k_B (K)	14.9(3)	8.3(3)	11.11(8)
τ_0 (s)	6.3(7) 10^{-8}	2.8(4) 10^{-7}	2.40(9) 10^{-7}
$H = 1$ kOe			
U_{eff}/k_B (K)	17.20(7)	12.63(7)	14.30(17)
τ_0 (s)	3.53(8) 10^{-7}	9.2(3) 10^{-8}	4.7(3) 10^{-7}

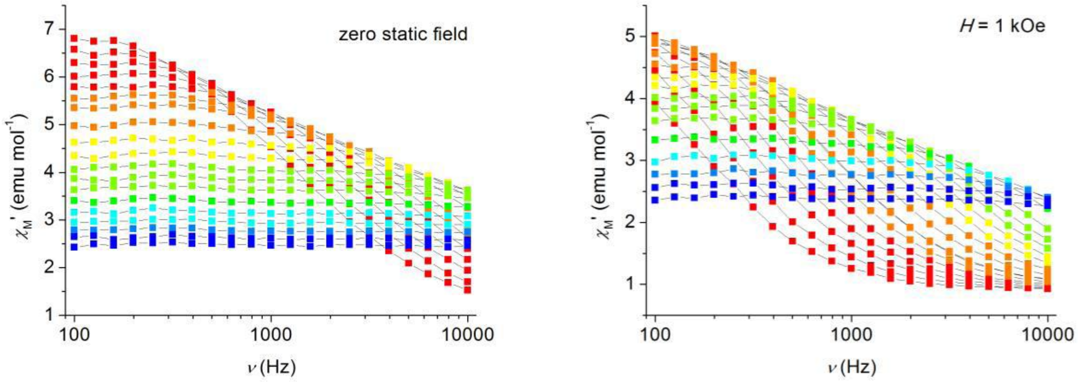

Fig. 5.11. Real component of the molar ac susceptibility (χ_M') of **Fe$_4$Ru$_2$(II,II)** measured at zero and 1-kOe applied static fields in the 10−10000 Hz frequency range from 1.8 (red) to 5.5 K (blue).

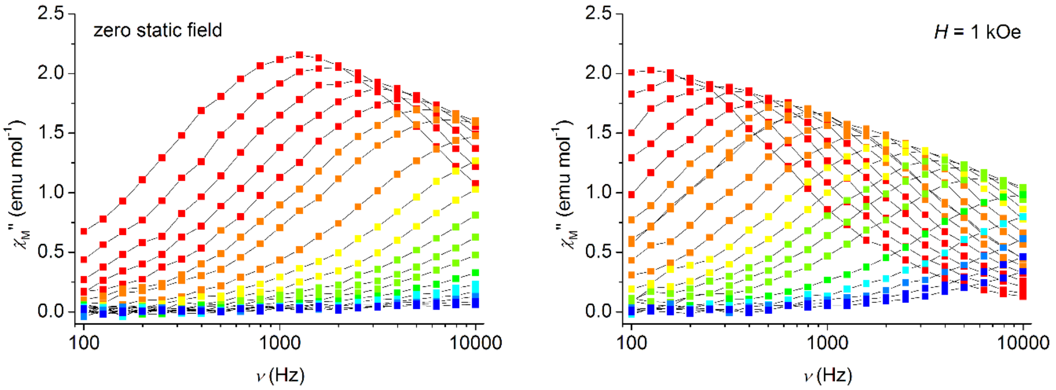

Fig. 5.12. Imaginary component of the molar ac susceptibility (χ_M'') of **Fe_4Ru_2(II,II)** measured at zero and 1-kOe applied static fields in the 10−10000 Hz frequency range from 1.8 (red) to 5.5 K (blue).

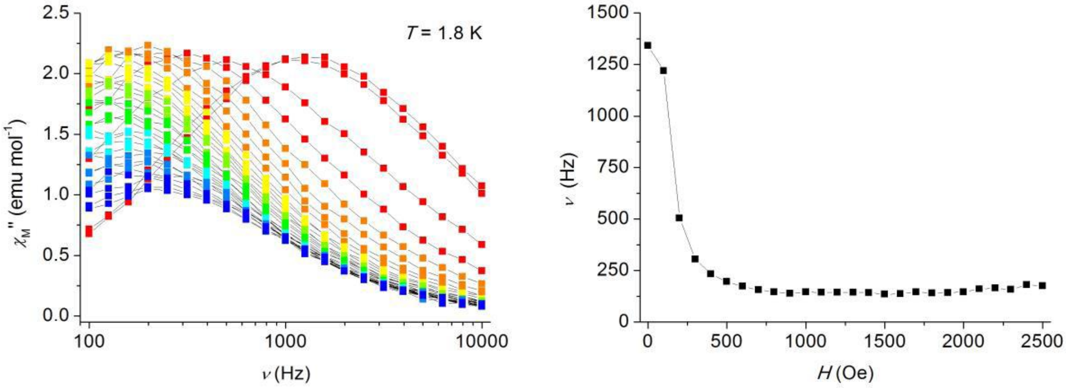

Fig. 5.13. Dependence of the relaxation frequencies on applied static field H from zero (red) to 2.5 kOe (blue) for **Fe_4Ru_2(II,II)** at 1.8 K.

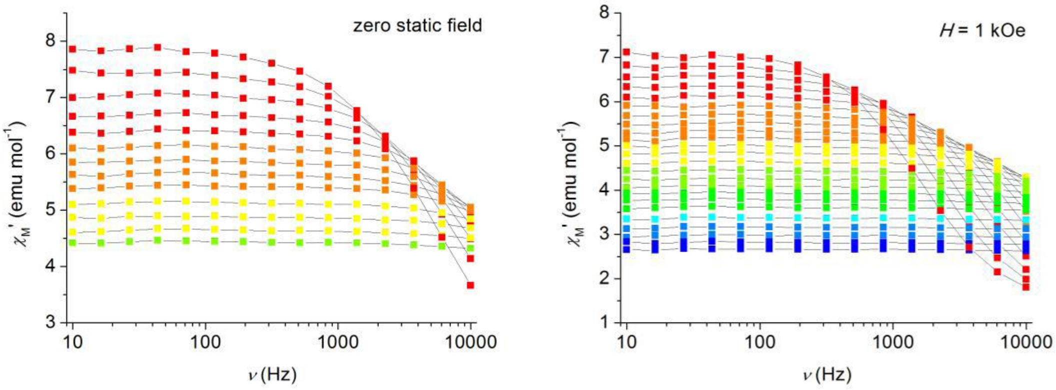

Fig. 5.14. Real component of the molar ac susceptibility (χ_M') of **Fe_4Ru_2(II,III)** measured at zero and 1-kOe applied static fields in the 10−10000 Hz frequency range from 1.8 (red) to 5.5 K (blue).

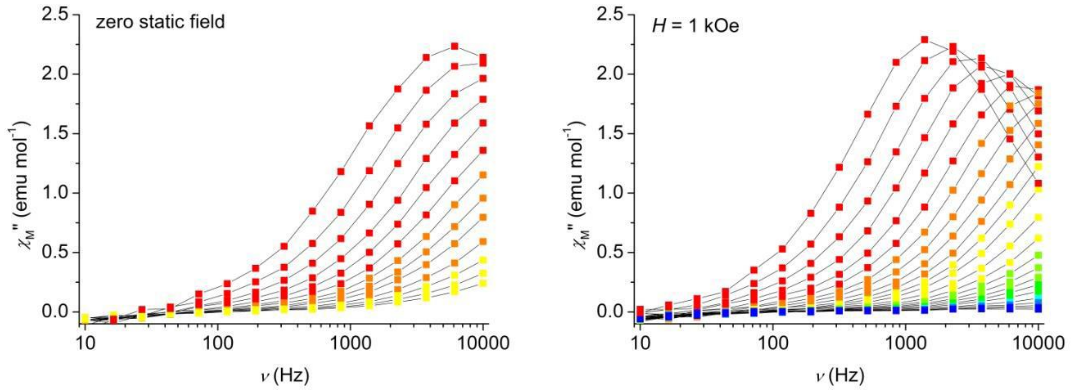

Fig. 5.15. Imaginary component of the molar ac susceptibility (χ_M'') of **Fe_4Ru_2(II,III)** measured at zero and 1-kOe applied static fields in the 10−10000 Hz frequency range from 1.8 (red) to 5.5 K (blue).

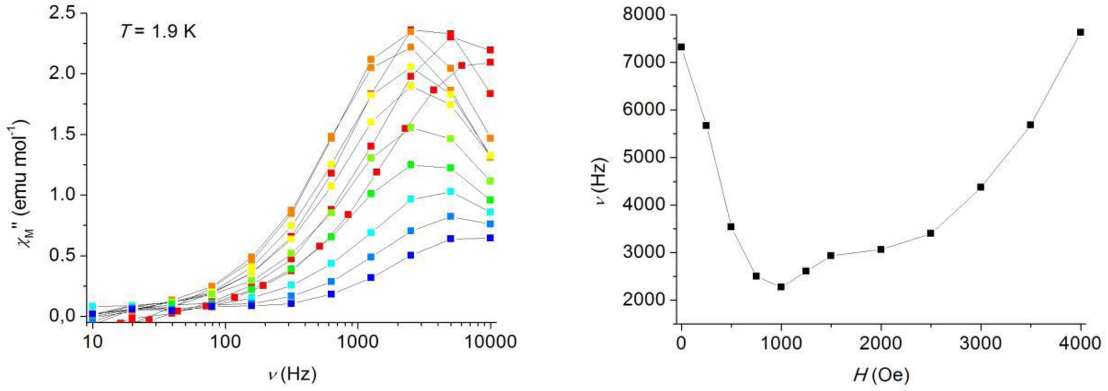

Fig. 5.16. Dependence of the relaxation frequency on applied static field *H* from zero (red) to 5 (blue) for **Fe_4Ru_2(II,III)** at 1.9 K.

5.6 MicroSQUID measurements

To probe the electronic structure over a much smaller energy scale, magnetic hysteresis loops were recorded on single crystals of **Fe_4Ru_2(II,III)** and **Fe_4Ru_2(II,II)** using a microSQUID apparatus and applying the magnetic field along the easy axis. In all cases, coercivity was found to increase with decreasing temperature and increasing scan rate, as expected for SMM behaviour. The hysteresis loops of **Fe_4Ru_2(II,II)** (Fig. 5.17) closely resemble those of **Fe_4pPy**·2EtOH (Fig. 4.8 and 4.9). Magnetization steps are detected at 0.00, 0.46, and 0.90 T, as best appreciated by plotting d*M*/d*H* vs. applied field (Fig. 5.18). The observed behaviour is thus indicative of isolated Fe_4 units, with no intrachain communication. The result can be again explained by considering the integer spin and large positive zfs of the $Ru^{II}Ru^{II}$ complex, which result in a nonmagnetic $m = 0$ ground state (Fig. 5.2 and 5.10).

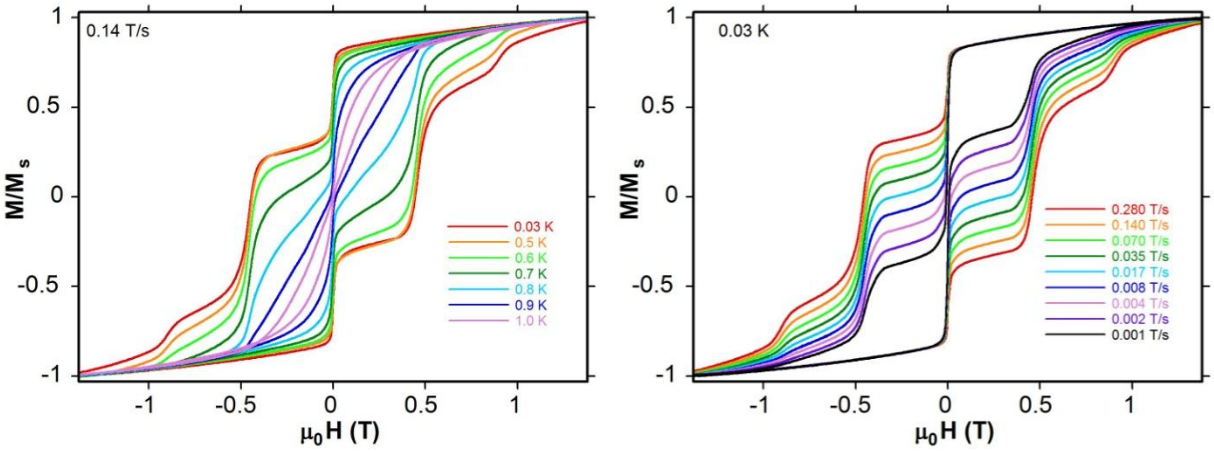

Fig 5.17. Magnetization versus dc field hysteresis loops for a single crystal of **Fe_4Ru_2(II,II)** at variable temperature and field-sweep rate. M_s is saturation magnetization.

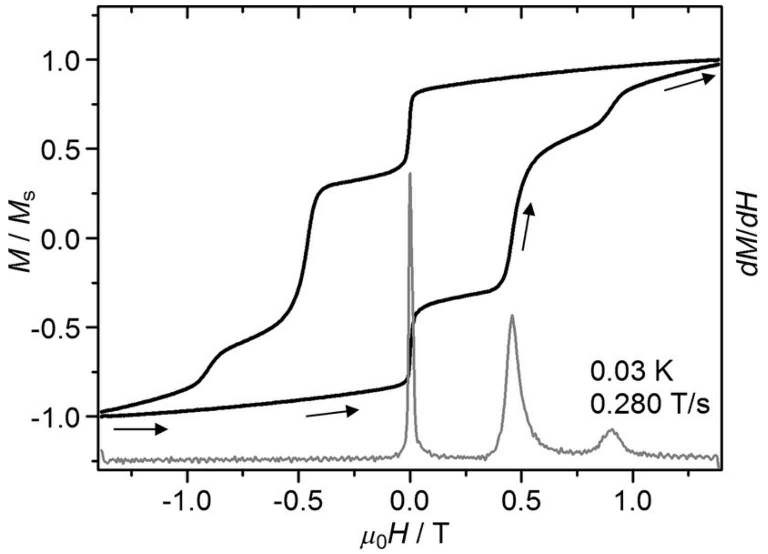

Fig. 5.18. Magnetization versus dc field hysteresis loops recorded at 0.03 K and 0.280 T s^{-1} on a single crystal of **Fe_4Ru_2(II,II),** along with *dM*/*dH* curve (grey). M_s is saturation magnetization.

The behaviour of **Fe_4Ru_2(II,III)** is remarkably different (Fig. 5.19 and 5.20). At 0.03 K saturation is reached in applied fields larger than about 1 T in modulus, following broad, quasi-reversible steps at ±0.84(1) T. Coercivity is reduced as compared with **Fe_4pPy**·2EtOH but a large remnant magnetization, amounting to about 79% of saturation magnetization (M_S), is found in zero field at all sweep rates explored. Following the path marked by red arrows in Fig. 5.20, such enhanced memory effect originates from a shift of the “zero-field” resonance to 0.124 T. A second, pronounced magnetization step is then detected between 0.37 and 0.54 T, that is, close to the field value ($|D|/(g\mu_B)$) where the M = +5 to -4 transition typically occurs in isolated Fe_4 complexes. Since dipolar fields within a chain and between chains would not exceed a few millitesla in both **Fe_4Ru_2(II,II)** and **Fe_4Ru_2(II,III)**, the observed differences in magnetic behaviour must arise from superexchange interactions with the Ru_2 units rather than from crystal packing effects.

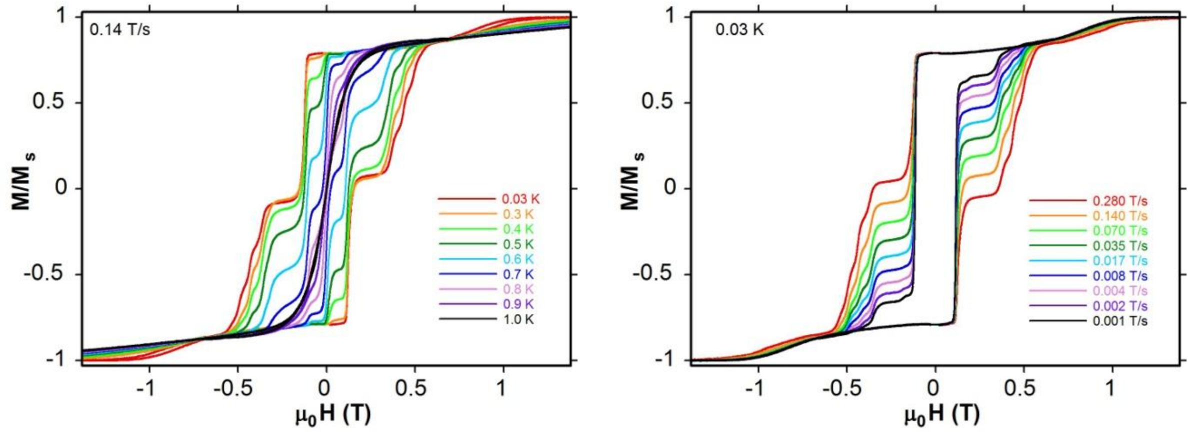

Fig 5.19. Magnetization versus dc field hysteresis loops for a single crystal of **Fe_4Ru_2(II,III)** at variable temperature and field-sweep rate. M_s is saturation magnetization.

Neglecting interchain interactions, the behaviour of **Fe_4Ru_2(II,III)** can be described by a chain model of alternating anisotropic S = 5 and s = 3/2 spins weakly coupled via Heisenberg exchange. However, the low lying spin levels are accurately reproduced by an Ising-like model where only spin components along the Fe_4 easy axis are relevant [Eq. (5.1)].

$$Energy = D\sum_i {M_{2i}}^2 + \sum_i J_{|M|} M_{2i}(m_{2i-1} + m_{2i+1}) + \mu_B B \sum_i (g M_{2i} + g_{\text{eff}} M_{2i-1}) \qquad (5.1)$$

The first term accounts for magnetic anisotropy at Fe_4 centres that are located on even sites. The Ru_2 complexes occupy odd sites and, owing to their large easy-plane anisotropy, are described by m = 1/2 and an anisotropic g-factor $g_{\text{eff}} = (g_\parallel{}^2\cos^2\vartheta + g_\perp{}^2\sin^2\vartheta)^{1/2}$, with $g_\parallel = g_{\text{Ru}}$ and $g_\perp = 2g_{\text{Ru}}$.[24] Here, ϑ is the angle between the Fe_4 and Ru_2 anisotropy axes ($\vartheta \approx 25°$ from crystal structure, whence $g_{\text{eff}} \approx 2.60$). $J_{|M|}$ is the effective Fe_4-Ru_2 exchange-coupling constant, which can be different when the Fe_4 complex occupies the M = ±5 or the M = ±4 doublet. Differences with the electronic structure of **Fe_4Ru_2(II,II)** are pictured in Fig. 5.10.

Based on Eq. 5.1 I now analyse the field dependence of the magnetization as the field is ramped from -1.4 T to +1.4 T, i.e. following the pathway marked by red arrows in Fig. 5.20. To this aim, I focus on the most probable tunnelling events, that is, individual or pairwise spin reversals. The application of a large negative ("down") field aligns all magnetic moments in the downward direction, that is, M = +5 and m = +1/2 at all sites.

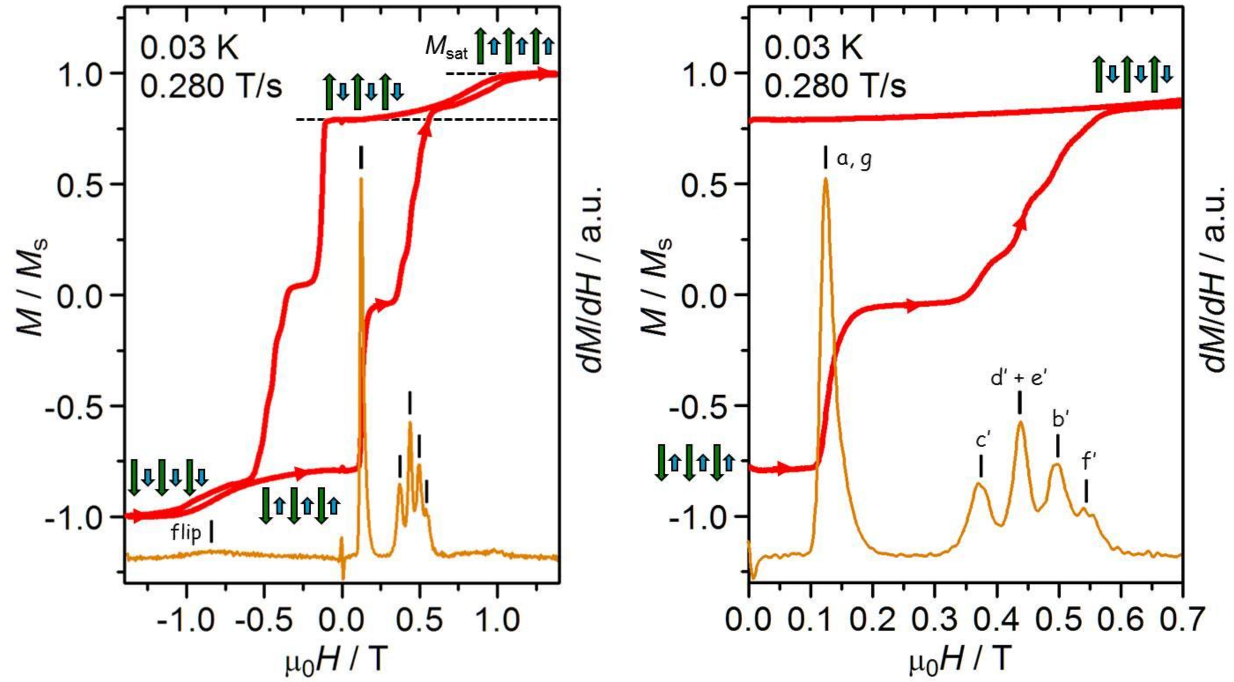

a

b

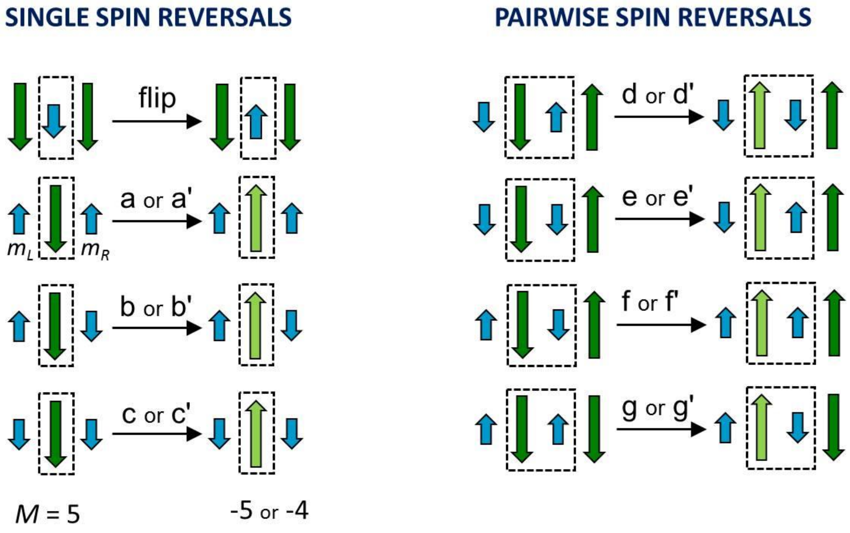

Fig. 5.20. (a) Magnetization versus dc field hysteresis loops recorded on a single crystal of **Fe_4Ru_2(II,III)** (red curve) along with *dM*/*dH* (orange curve). M_s is saturation magnetization. Blue and green arrows depict the magnetic moments of Fe_4 and Ru_2 units, respectively, and are drawn perpendicular to the chain axis rather than parallel to it for an easier representation. Vertical ticks mark the spin-flip transition and QT resonances as the field is ramped from -1.4 T to +1.4 T. The derivative signal at *H* = 0 is an instrumental artifact. (b) Proposed assignment of the steps in the hysteresis loop. Spins undergoing reversal are highlighted by a dashed rectangle, while the other spins remain fixed.

As the field magnitude declines, the broad step detected at -0.84(1) T is suggestive of antiferromagnetic Fe_4-Ru_2 coupling and of a spin-flip transition, whereby all Ru_2 spins reverse to m = -1/2. At the transition field, the decrease in exchange energy exactly equals the increase in Zeeman energy, that is, $|B_{\mathrm{flip}}| = 10\ J_5/(g_{\mathrm{eff}}\mu_B)$, whence $J_5 \approx 0.10$ cm^{-1} for $g_{\mathrm{eff}} \approx 2.60$. By consequence, an effective ferromagnetic coupling is established between Fe_4 units, a rare situation in supramolecular SMM assemblies.[57,107] This coupling strength confirms that in the temperature range explored by ac susceptibility measurements the condition $k_BT > 10\ J_5$ holds and substantial fluctuations of $Ru^{II}Ru^{III}$ spins are to be expected. After the spin-flip transition, the magnetization remains virtually constant up to about 0.10 T and no zero-field QT resonance is detected. In fact, for a resonant tunnelling event to occur the initial and final states must have the same energy, that is, the decrease in Zeeman energy upon QT must exactly compensate the increase in exchange and anisotropy energies. Using Eq. (5.1), it is straightforward to show that, for a given Fe_4 centre in the chain, the QT transitions from M= +5 to -5 and from M = +5 to -4 are split into three depending on the $m_{L(R)}$ value of its lefthand L (righthand R) Ru_2 neighbours. The two groups of resonances (a,b,c and a',b',c' in second panel of Fig. 5.20), should occur at fields [Eqs. (5.2) and (5.3)]

$$B = -J_5(m_L + m_R)/(g\mu_B) \tag{5.2}$$

$$B' = |D|/(g\mu_B) - [(5/9)J_5 + (4/9)J_4](m_L + m_R)/(g\mu_B) \tag{5.3}$$

Then, the term proportional to $m_L + m_R$ may be conveniently viewed as "bias field" that adds to the external field and shifts the resonances. Because after the spin-flip transition all Fe_4 spins are "up" (M = +5) and all Ru_2 spins are "down" (m = -1/2), relaxation around zero field may only start through a QT resonance involving this initial state (resonance a in the scheme). Setting J_5 = 0.10 cm^{-1} and $m_L = m_R = -1/2$ in Eq. (5.2) one finds B = 0.11 T, in reasonable agreement with the sharp increase of the magnetization at 0.124 T. The further increase of the magnetization between 0.37 and 0.54 T occurs in four substeps at 0.374, 0.439, 0.494, and 0.545 T, as most clearly shown by the first-derivative curve in Fig. 5.20. The spacing between the first and third substeps (0.120 T) is virtually identical to the bias field that affects the "zero-field" resonance, suggesting that exchange energy may be at the origin of the observed fine structure. When the first and third substeps are assigned to resonances c' and b' [i.e. m_L+m_R = 1 and 0 in Eq. (5.3)], it follows that D = -0.46 cm^{-1}, a realistic value for Fe_4 complexes. With this assignment, resonance a' would occur at 0.61 T, that is, in a field region where "up" Fe_4 spins are no longer available. Notice that approximately half of the Fe_4 spins have already reversed at around 0.2 – 0.3 T, so that $m_L = m_R = -1/2$ is by no means the only accessible initial state. The two remaining substeps are not accounted for by the exchange-biased flipping of individual Fe_4 spins, but can be explained by the simultaneous reversal of a Fe_4 spin and a neighbouring Ru_2 unit. Considering the spin arrangement within the pair and the orientation of the two adjacent spins, eight different QT events of this type can be envisaged, the resonant fields of which are easily worked out from Eq. (5.1). Among them, three resonances are indeed predicted at 0.452 (d'), 0.431 (e'), and 0.525 T (f'), hence close to the second and fourth substeps (see sketch in Fig. 5.20). In addition, resonance g is expected at 0.123 T and can also contribute to the relaxation step around zero field, for it has the same initial state as resonance a. With this assignment, all step positions are reproduced within 4 mT using the following set of spin Hamiltonian parameters: $g = 2.00$ (fixed), $D = -0.465(2)\ \mathrm{cm^{-1}}$, $J_5 = 0.101(1)\ \mathrm{cm^{-1}}$, $J_4 = 0.133(7)\ \mathrm{cm^{-1}}$ and $g_{\mathrm{eff}} = 2.57(4)$. The best-fit g_{eff} value is fully consistent with the typical Landè factor of diruthenium(II,III) paddlewheels[97,103,106,108] and with the ϑ value estimated from the crystal structure. Moreover, the relative magnetization change at the spin-flip transition $(5g - g_{\mathrm{eff}}/2)/(5g + g_{\mathrm{eff}}/2) = 0.77$ is in good agreement with the measured value (0.79).

5.7 Mixed chain compounds

5.7.1 Introduction

Redox-controllable SMMs have been a topic of great interest in the last years.[3,5,109] The results described in 5.5 and 5.6 demonstrate that the electron count on diruthenium units has a profound influence on the low temperature magnetic response of their chain-like assemblies with Fe_4 complexes. Since the structures show only minor variations as the oxidation state (OS) of the bridges is changed, it is likely possible to prepare chains containing bridges in different OS (Fig. 5.22). Such new target compounds could display enhanced electrical conductivity as compared with **Fe_4Ru_2(II,II)** and **Fe_4Ru_2(II,III)** because of a possible electron hopping mechanism. In this section I will describe the synthesis of these new chain compounds and their characterization by IR and Raman spectroscopies.

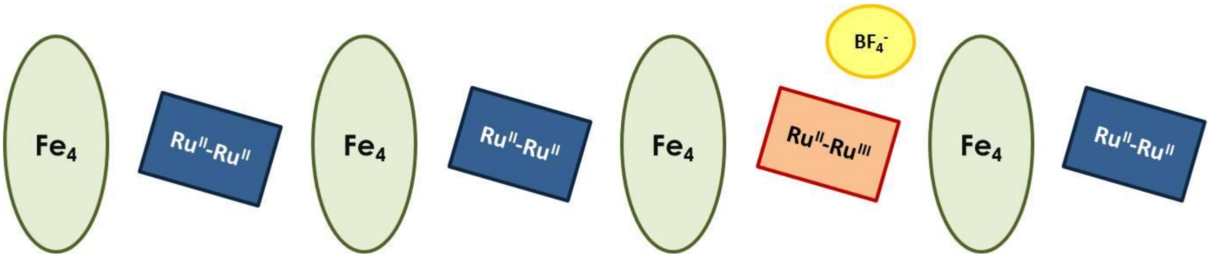

Fig. 5.22. Sketch of an array of Fe_4 units bridged by diruthenium paddlewheels in different OS.

5.7.2 Synthesis

The synthesis of mixed chain compounds was successfully carried out following the procedure used for **Fe_4Ru_2(II,II),** with a Fe4pPy:$Ru^{II}Ru^{III}$:$Ru^{II}Ru^{II}$ ratio of 2:1:1. The tiny red crystals of $[Fe_4(pPy)_2(dpm)_6]_2[Ru_2(AcO)_4]_2(BF_4)_x$ (**Fe_4Ru_2MIX**, $0 < x < 1$) so obtained, when examined under an optical microscope, appear homogeneous in both colour and habit. They can be washed with *n*-hexane to remove mother liquor, but undergo rapid loss of crystallization solvent when dry. For more synthetic information see Experimental Section.

$$2[Fe_4(pPy)_2(dpm)_6]{*}2EtOH + [Ru_2^{II,II}(AcO)_4(MeOH)_2] + [Ru_2^{II,III}(AcO)_4(THF)_2](BF_4)$$

$$\xrightarrow[\text{liquid diffusion}]{\text{THF/DCM}} [Fe_4(pPy)_2(dpm)_6]_2[Ru_2(AcO)_4]_2(BF_4) + 2THF + 2EtOH + 2MeOH$$

5.7.3 Characterization of mixed chain systems

In order to properly characterize **Fe_4Ru_2MIX**, I focused my attention on two easily available but powerful techniques: IR and Raman spectroscopy.

Infrared spectroscopy

The infrared spectra of diruthenium paddlewheels are significantly influenced by the OS of the metals. As shown in the literature,[97] the most diagnostic features in the IR spectra of these tetracarboxylates are the symmetric (ν_{sym}) and asymmetric (ν_{asym}) stretching modes of bridging carboxylates. The ν_{sym}(COO) band usually occurs in the range 1330-1460 cm^{-1} while ν_{asym}(COO) is detected between 1440 and 1650 cm^{-1}. In general, both stretching modes shift to higher frequencies when going from the mixed valent Ru_2^{5+} species to the reduced Ru_2^{4+} variant, reflecting the decreased interaction of the carboxylates with ruthenium centres. Furthermore, $Ru^{II}Ru^{III}$ paddlewheels require a counterion. In our case the counterion is BF_4^- and affords a B-F stretching band around 1084 cm^{-1}. The IR spectra (recorded as KBr pellets) of Ru^{II}Ru^{III} and Ru^{II}Ru^{II} dimers in the carboxylate stretching region are presented in Fig. 5.22, while band frequencies are summarized in Table 5.4.

Table 5.4. Asymmetric and symmetric stretching frequencies of carboxylate groups in Ru^{II}Ru^{III} and Ru^{II}Ru^{II} dimers. Values in parenthesis are the stretching frequencies reported in the literature for the same compounds[97,100,110,111]

	[Ru$_2^{(II,III)}$(AcO)$_4$(THF)$_2$](BF$_4$)	**[Ru$_2^{(II,II)}$(AcO)$_4$(MeOH)$_2$]**
ν_{asym}(COO)	1449 (1460) cm^{-1}	1564 (1575) cm^{-1}
ν_{sym}(COO)	1397 (1400) cm^{-1}	1435 (1440) cm^{-1}
ν_{asym}-ν_{sym}	52 (60) cm^{-1}	129 (135) cm^{-1}

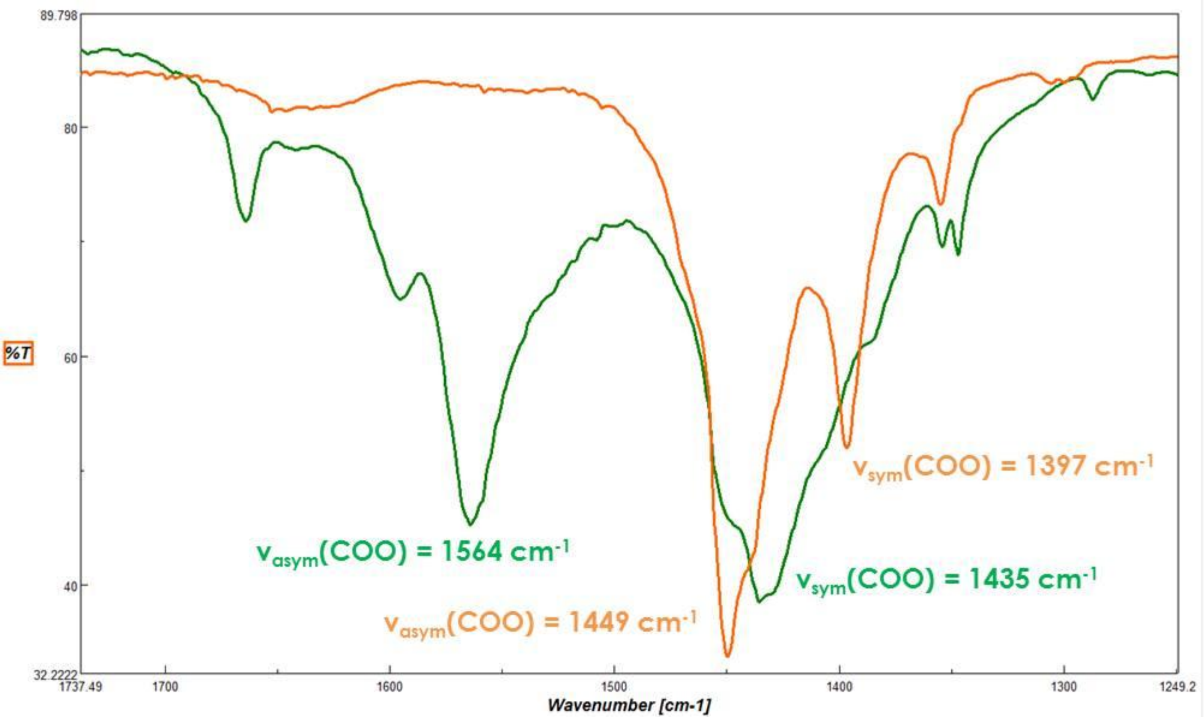

Fig. 5.22. IR spectra between 1738 and 1250 cm^{-1} of Ru^{II}Ru^{III} (orange) and Ru^{II}Ru^{II} (green) dimers.

Although the contribution of Fe$_4$ adds complexity to the IR spectra, the chains **Fe$_4$Ru$_2$(II,II)** and **Fe$_4$Ru$_2$(II,III)** exhibit clear carboxylate stretching bands: ν_{asym} at 1443 cm^{-1} for Ru^{II}Ru^{III} bridges and ν_{sym} at 1433 cm^{-1} for Ru^{II}Ru^{II} ones. The IR spectrum of the mixed chain **Fe$_4$Ru$_2$MIX** is very similar to that of **Fe$_4$Ru$_2$(II,II)** and **Fe$_4$Ru$_2$(II,III)**, due to the dominant Fe$_4$ contribution. However, looking carefully at the carboxylate stretching region (Fig. 5.23), it appears that the spectrum has two contributions centred at the frequency values found in **Fe$_4$Ru$_2$(II,II)** (1433 cm^{-1}) and **Fe$_4$Ru$_2$(II,III)** (1443 cm^{-1}). Thus, IR spectra indicate that **Fe$_4$Ru$_2$MIX** indeed comprises both Ru^{II}Ru^{II} and Ru^{II}Ru^{III} bridges along the chain. Consistent with such a conclusion, a tetrafluoborate stretching signal is observed at 1084 cm^{-1}; as expected, its relative intensity is lower than in **Fe_4Ru_2(II,III)** (Fig. 5.23).

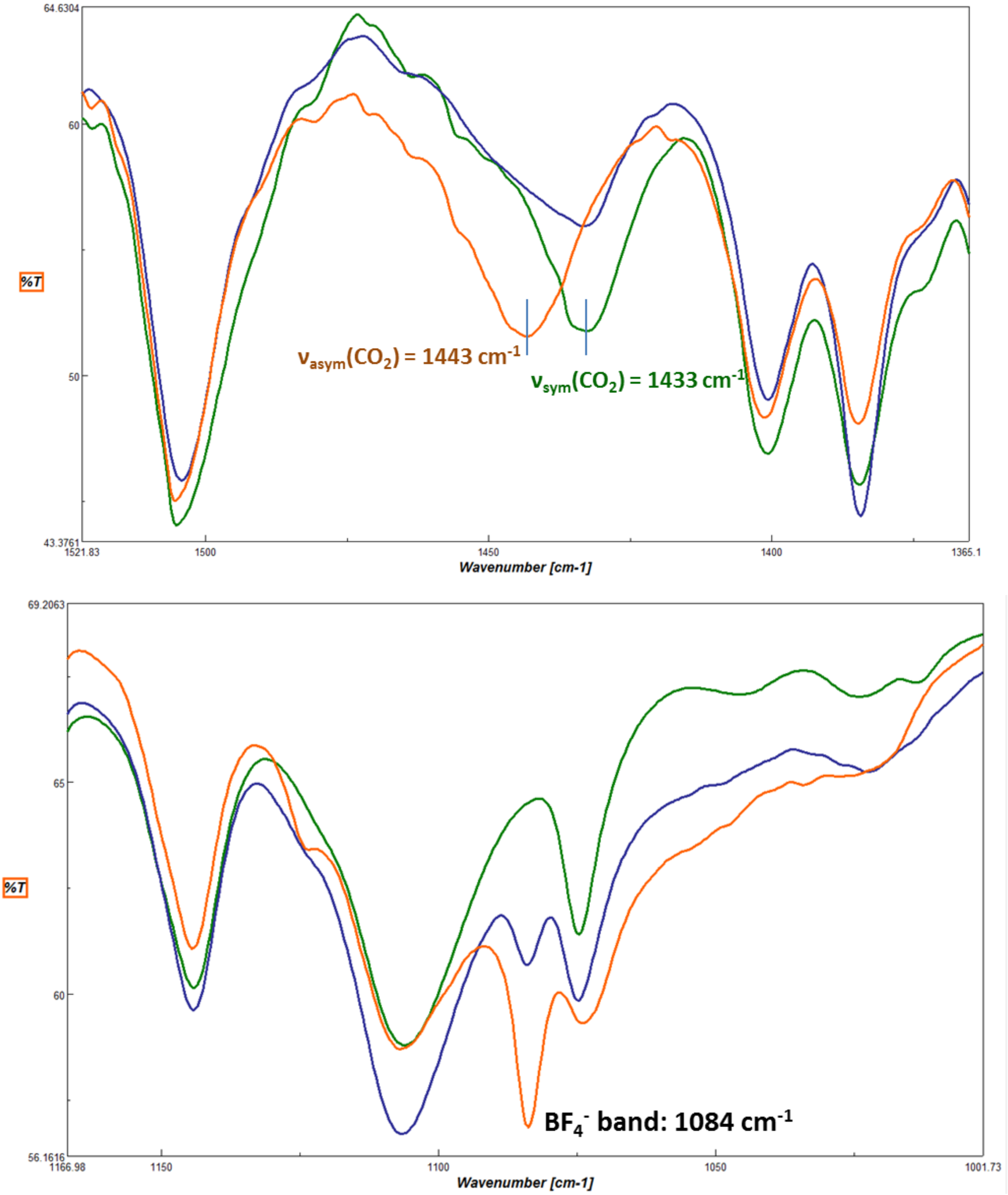

Fig. 5.23. Zoom of IR spectra of **Fe_4Ru_2(II,II)** (green), **Fe_4Ru_2(II,III)** (orange) and **Fe_4Ru_2MIX** (blue) in the 1522-1365 (upper panel) and 1167-1002 cm^{-1} (lower panel) ranges.

Raman spectroscopy

Raman spectroscopy turned out to be a very useful technique and provided the final proof that mixed diruthenium bridges are indeed present in the structure of **Fe_4Ru_2MIX**. As described in old published work,[97,112,113] Ru-Ru and Ru-O bond stretching bands are diagnostic of ruthenium OS, with ν(Ru-Ru) around 330 cm^{-1} (strong) and ν(Ru-O) in the 340-380 cm^{-1} region (medium). Raman spectra were collected in collaboration with Dr. Cecilia Baraldi (Dipartimento di Scienze della Vita, Università degli Studi di Modena e Reggio Emilia). As a major advantage, measurements were made directly on single crystals and were found reproducible over different crystals, thereby ruling out the occurrence of separate **Fe_4Ru_2(II,II)** and **Fe_4Ru_2(II,III)** phases in the sample. The spectrum of **Fe_4Ru_2(II,II)** shows ν_1(Ru-Ru) at 318 cm^{-1} and ν_2(Ru-O) at 349 cm^{-1}. By contrast, the two peaks shift to 331 cm^{-1} and 370 cm^{-1} in **Fe_4Ru_2(II,III)**, as shown in Fig. 5.24. The spectrum of the mixed species **Fe_4Ru_2MIX** indeed features both peak sets, proving that it contains both $Ru^{II}Ru^{II}$ and $Ru^{II}Ru^{III}$ paddlewheels. The higher intensity of the peaks at 331 cm^{-1} and 370 cm^{-1} suggests a $Ru^{II}Ru^{III}$-to-$Ru^{II}Ru^{II}$ ratio greater than one.

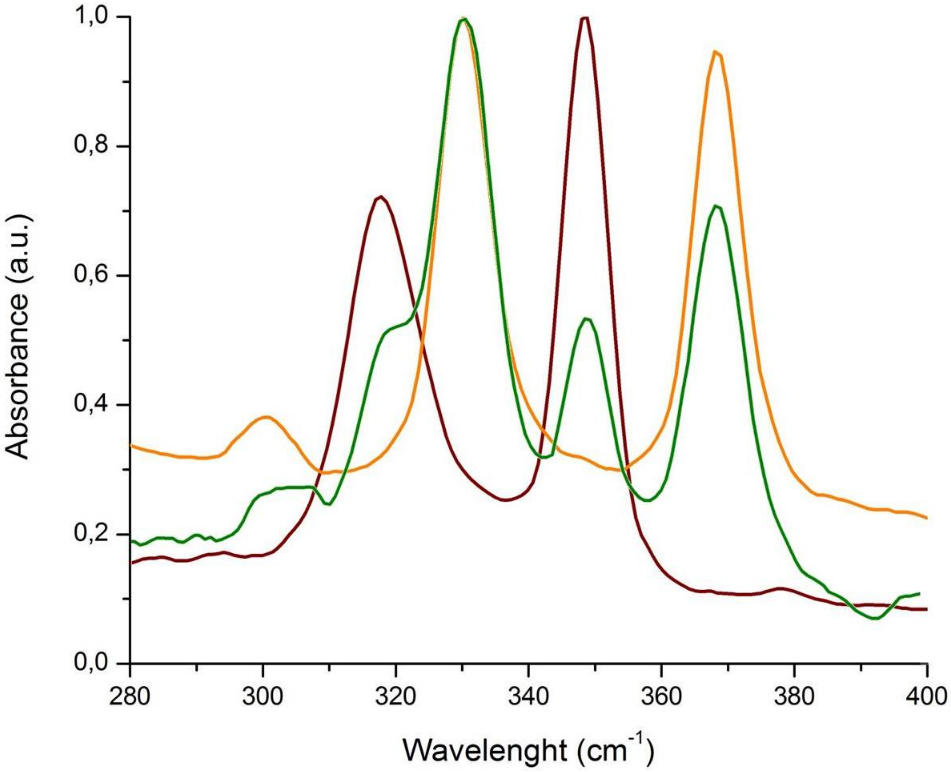

Fig. 5.24. Raman spectra of **Fe_4Ru_2(II,II)** (brown), **Fe_4Ru_2(II,III)** (orange) and **Fe_4Ru_2MIX** (green) in the 280-400 cm^{-1} range.

5.8 Conclusion

In conclusion, I have harnessed the chemical versatility of Fe_4 complexes to prepare chain-like assemblies of SMM units bridged by diruthenium paddlewheels in two different OS, as well as mixed systems comprising paddlewheels in both OS.

Because of the different electron count on the diruthenium bridges, the two chains **Fe_4Ru_2(II,II)** and **Fe_4Ru_2(II,III)** show different magnetic behaviour. The diruthenium(II,II) paddlewheel has an integer spin (s = 1) and a large easy-plane anisotropy, which result in a nonmagnetic m = 0 ground singlet and in negligible intrachain communication. By contrast, the diruthenium(II,III) bridge has half-integer spin (s = 3/2) but maintains a large easy plane anisotropy. By virtue of its m = ±1/2 ground doublet, the mixed-valent bridge then couples neighbouring Fe_4 complexes together and compound **Fe_4Ru_2(II,III)** behaves as a better magnet in zero field as compared with an array of non-interacting Fe_4 centres.[19]

Redox-controllable SMM cores are a topic of great current research interest.[109,114,115] Thus, a required next step is switching the electron count on the bridges *in situ* and reversibly controlling intrachain coupling and remnant magnetization by electron transfer (ET). Concerning the mixed-paddlewheel compound **Fe_4Ru_2MIX**, it will be crucial to measure its electrical conductivity and compare it with that of **Fe_4Ru_2(II,II)** and **Fe_4Ru_2(II,III)**, so as to evidence any conductivity enhancement due to electron hopping processes.

6 Understanding the contribution of diruthenium paddlewheels in Fe_4Ru_2 chains

6.1 Introduction

In the previous chapter, I have described the magnetic behaviour of **Fe_4Ru_2(II,II)** and **Fe_4Ru_2(II,III)** chains but the magnetic parameters of diruthenium paddlewheels were taken from the literature[97,106,108,116]. One useful step now is to study the real magnetic contribution of $Ru^{II}Ru^{II}$ and $Ru^{II}Ru^{III}$ pairs in **Fe_4Ru_2(II,II)** and **Fe_4Ru_2(II,III)**, respectively, through the synthesis of isomorphous compounds in which iron(III) centres are replaced by diamagnetic ions. To this aim, gallium(III) ($3d^{10}$) is a good candidate because it has a similar ionic radius to high-spin iron(III) (0.62 vs 0.65 Å). Furthermore, its coordination chemistry is also quite similar and self-assembly reactions are easier than with the inert cobalt(III) ion, whose size is also comparable (0.61 Å).

In this chapter I will show the synthesis of $[Ga_4(L^{pPy})_2(dpm)_6]\cdot$EtOH (**$Ga_4$pPy**·EtOH), which is isomorphous to **Fe_4pPy**·2EtOH.[17] Next, I will describe its reaction with **$Ru^{II}Ru^{II}$** and **$Ru^{II}Ru^{III}$** paddlewheels to afford $[Ga_4(L^{pPy})_2(dpm)_6][Ru_2(AcO)_4]$ (**Ga_4Ru_2(II,II)**) and $[Ga_4(L^{pPy})_2(dpm)_6][Ru_2(AcO)_4](BF_4)]$ (**Ga_4Ru_2(II,III)**). Finally, I will discuss the magnetic behaviour of these two chain compounds and infer the contribution of diruthenium paddlewheels in **Fe_4Ru_2(II,II)** and **Fe_4Ru_2(II,III)**.

6.2 Ga_4pPy·EtOH

6.2.1 Synthesis

Ga_4pPy·EtOH was synthesised following the same procedure used for **Fe_4pPy**·2EtOH,[19] but replacing iron(III) with gallium(III).[19] Briefly, the dimer $[Ga_2(OMe)_2(dpm)_4]$ was prepared as described in the literature[68] (see Experimental Section) and reacted with $GaCl_3$, piperidine and H_3L^{pPy} tripodal ligand in a Et_2O:EtOH 4:1 solvent mixture. The reaction mixture was left under stirring overnight, filtered and put in vapour diffusion with EtOH, giving colourless crystals of **Ga_4pPy**·EtOH after one week in good yield (79.67%). The IR spectrum of the compound (as a KBr pellet) shows stretching bands $\nu_{O\text{–}H,EtOH}$ at 3388 cm^{-1} and $\nu_{C\text{–}H}$ at 2964, 2926 and 2868 cm^{-1}. Further stretching bands $\nu_{C=O,C=N}$ (1598, 1571, 1554, 1540, 1508 cm^{-1}), $\nu_{C\text{–}O}$ (1103, 1075 cm^{-1}) and pyridyl bending (597 cm^{-1}) are visible. The detailed synthetic procedure is reported in the Experimental Section.

$$3/2\ [Ga_2(OMe)_2(dpm)_4] + GaCl_3 + \text{piperidine} + 2H_3L^{pPy} \xrightarrow[\text{EtOH vapour diffusion}]{Et_2O:EtOH\ 4:1} [Ga_4(L^{pPy})_2(dpm)_6] + 3\text{piperidinium}^+Cl^- + 3MeOH$$

6.2.2 Molecular structure

Crystals of **Ga_4pPy**·EtOH grow as colourless parallelepipeds which easily lose crystallinity on prolonged standing in air or under vacuum, due to loss of ethanol from the lattice. The space group is monoclinic *C*2/*c* and the asymmetric unit contains half Ga_4 cluster, as in **Fe_4pPy**·2EtOH. At variance with the iron(III) compound, however, the solvent molecule in the asymmetric unit has 50% occupancy only. Thus, the compound contains one EtOH per formula unit, as confirmed by ^1H NMR spectra (see below).

The oxygen atoms of two triply-deprotonated tripodal ligands H_3L^{pPy} connect the central ion (Ga1) with the peripheral ones (Ga2, Ga3, Ga3’). The latter complete their distorted octahedral coordination spheres with two dpm^- ligands each. The molecule develops around a crystallographic binary axis that runs through Ga1 and Ga2. Thus, the four gallium(III) ions are exactly coplanar and Ga3 is symmetry equivalent to Ga3’. Disregarding the tripodal ligands, the molecule has idealized D_3 symmetry but the actual crystallographic symmetry is only C_2. While the coordination spheres of Ga1 and Ga2 are ordered within experimental resolution, the *β*-diketonates bound to Ga3 and Ga3’ are disordered and display two coordination modes: propeller (p) and sandwich (s), refined with complementary occupancy factors [0.833(2) and 0.167(2)]. Consequently, the crystal lattice in principle comprises three different isomers called ppp, pps (or psp) and pss. If *β*-diketonato ligands adopt independent coordination modes on Ga3 and Ga3’, the three isomers are expected to occur in the following proportions: 69.39 (ppp), 27.82 (pps or psp) and 2.79 (pss)%. The structure of ppp and pps isomers is shown in Figs. 6.1 and 6.2.

Table 6.1 Crystal data and structure refinement for **Ga_4pPy**·EtOH

Empirical formula	$C_{86}H_{140}Ga_4N_2O_{19}$	
Formula weight	1784.88 g mol^{-1}	
Temperature	140(2) K	
Wavelength	0.71073 Å	
Crystal system	Monoclinic	
Space group	*C*2/*c*	
Unit cell dimensions	*a* = 19.3203(9) Å	*α* = 90°
	b = 21.9357(11) Å	*β* = 106.612(2)°
	c = 23.7468(12) Å	*γ* = 90°
Volume	9543(8) Å^3	
Z	4	
Density (calculated)	1.229 g cm^{-3}	
Absorption coefficient	1.169 mm^{-1}	
Crystal size	0.54 x 0.18 x 0.12 mm^3	
Reflections collected	49881	
Independent reflections	11639 [*R*(int) = 0.0353]	
Completeness to theta = 28.03°	99.4 %	
Max. and min. transmission	0.9086 and 0.7760	
Refinement method	Full-matrix-block least-squares on F^2	
Data / restraints / parameters	11639 / 352 / 636	
Final R indices [$I>2\sigma(I)$]	R_1 = 0.0420, wR_2 = 0.1093	
R indices (all data)	R_1 = 0.0735, wR_2 = 0.1267	
Largest diff. peak and hole	1.384 and -0.986 eÅ^{-3}	
Goodness of fit	1.030	

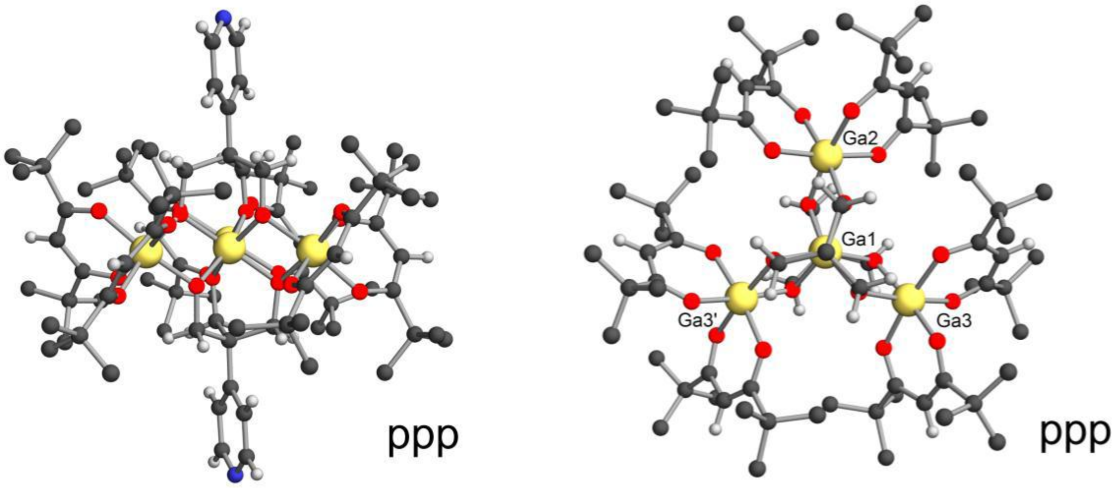

Fig. 6.1. Molecular structure of the tetragallium(III) complex in **Ga$_4$pPy**·EtOH (ppp isomer) viewed along crystallographic binary axis (left) and normal to the metal plane (right, with the 4-pyridyl groups omitted). Colour code: Ga = yellow, O = red, N = blue, C = grey, H = light grey. Hydrogen atoms of *t*Bu groups are omitted for clarity.

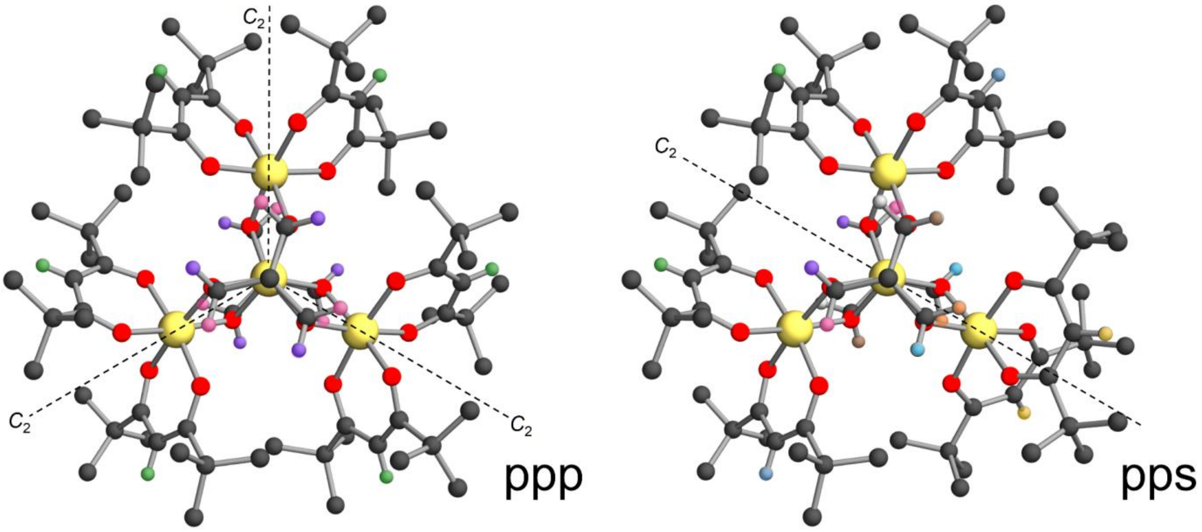

Fig. 6.2. Molecular structure of ppp and pps isomers in **Ga$_4$pPy**·EtOH. For ppp isomer, the dashed lines indicate the three binary axis expected for D_3 symmetry, which is adopted by this isomer in solution. Equivalent hydrogen atoms are highlighted with the same colour: violet and pink for the two diastereotopic groups of methylene hydrogens, green for methine hydrogens of dpm$^-$. The pps isomer has C_2 symmetry and only one binary axis is present along the Ga1-Ga3 direction. Symmetry-equivalent hydrogens in C_2 are highlighted with the same colour. The 4-pyridyl groups and *t*Bu hydrogen atoms are not shown for clarity.

6.2.3 ^{1}H NMR spectra

The ^{1}H NMR spectrum of a freshly-prepared solution of **Ga$_4$pPy**·EtOH in C_6D_6 (8 mg in 0.6 mL) at 298 K shows in the aromatic region various multiplets attributable to 4-pyridyl group of tripodal ligand.[95] Two multiplets (double-doublets) are present at 8.54 and 7.44 ppm with identical intensity. Other peaks of similar shape, but with lower intensity (around 1/3 of the main peaks) are observed at 8.49 and 7.33 ppm. Similar but barely visible double-doublets are also detected at 8.43 and 7.21 ppm. These data indicate the presence of two inequivalent 4-pyridyl groups in a 3:1 ratio, accompanied by trace amounts of a third species.

The chemical shift region around 5.8-5.7 ppm shows an intense singlet at 5.73 ppm and two weaker signals at 5.80 and 5.75 ppm, corresponding respectively to 5H, 0.5H and 0.5H. Furthermore, the main peak has a shoulder on its high-field side. These resonances, which sum to 6H, are assigned to methine hydrogens of dpm$^-$ ligands, in agreement with the ^{1}H NMR spectrum of Ga(dpm)$_3$.[117] In the spectral region between 5.6 and 4.4 ppm, several double-doublets appear with a total intensity corresponding to 12H. These signals are due to methylene groups of tripodal ligand.[68] In the spectrum of the free ligand, these hydrogens resonate at around 4 ppm and the signals shift to lower fields upon complexation. The two dominant signals at 5.44 (4.5H) and 4.90 (4.5H) are accompanied by six weaker signals at 5.48, 5.36, 4.92, 4.86, 4.60 and 4.47 ppm (all 0.5H). In the *t*Bu region from 1.50 ppm to 1.10 ppm[117] two intense singlets are observed at 1.34 and 1.13 ppm, with weaker resonances at 1.48, 1.32, 1.14, 1.14 and 1.12 ppm. Furthermore, an additional signal is observed as a shoulder on the low-field side of the peak at 1.34 ppm. The four higher-field and the four lower-field peaks both amount to 54H and these eight signals can thus be attributed to eight different *t*Bu groups. Considering the relative intensity of the peaks, I deduce that two *t*Bu groups account for 39H each, while the remaining six *t*Bu groups comprise 5H each.

The 4-pyridyl ring can rotate freely in solution and the presence of two main sets of aromatic signals points to the existence of two species in a 3:1 ratio. The dominant peaks can be explained assuming D_3 symmetry (i.e. the maximum symmetry for this type of complexes). In D_3 symmetry, the six dpm$^-$ ligands are equivalent and their methine hydrogens yield a singlet, while the 2 inequivalent *t*Bu groups of each ligand generate two singlets of equal intensity (equivalent hydrogens are highlighted with same colour in Fig. 6.2). The tripodal ligands contain six equivalent –CH$_2$– groups; however, as previously found in an isostructural compound,[68] the two protons of each –CH$_2$– group are diastereotopic and resonate at 5.44 and 4.90 ppm with a geminal coupling constant of -9.6 Hz. The signals show a further hyperfine splitting of 2.8 Hz which probably reflects the coupling between –

CH_2O– groups bound to the same peripheral gallium(III) ion (AA’BB’ system). Disregarding aromatic protons, each peak of this majority species has three corresponding minority peaks. Consequently, about one-fourth of the molecules in solution do not have D_3 symmetry; if the C_3 axis is missing in this minority species, but C_2 symmetry in retained, one expects three different methine hydrogens, six different methylene hydrogens and six different *t*Bu hydrogens, exactly as observed in the spectra. Based on XRD experiment (see 6.3) the high symmetry (D_3) and low symmetry (C_2) species are assigned as ppp and pps isomers, respectively; the species in trace amounts is presumably the pss isomer. The ppp/pps molar ratio determined from NMR spectra (3:1) is in reasonably good agreement with that resulting from XRD data (2.5:1).

Finally, the spectrum shows peaks at 3.31 and 0.94 ppm, attributable to methylene and methyl groups of interstitial EtOH, respectively; an additional signal from the $–CH_2–$ groups of Et_2O is observable at 3.26 ppm (the corresponding $–CH_3$ signal is partially hidden by *t*Bu peaks). The hydroxyl group of water and ethanol gives a broad band around 0.52 ppm. From the intensity of the aforementioned peaks, each cluster unit is accompanied by 0.96 molecules of EtOH and 0.13 molecules of Et_2O. Both NMR and XRD data thus point to the presence of about one EtOH molecule per tetragallium(III) complex. Small amounts of interstitial Et_2O may well escape XRD analysis; alternatively, Et_2O may be adsorbed on the surface or trapped in macroscopic cavities of the crystalline material.

6.3 Ga_4Ru_2(II,II) and Ga_4Ru_2(II,III) chains

6.3.1 Synthesis

The **Ga_4Ru_2(II,II)** and **Ga_4Ru_2(II,III)** chains were isolated as pale-yellow and light-violet crystals, respectively, using the same procedure as for the corresponding iron(III)-based chains (see Chapter 5 and Experimental Section). As for the iron(III) derivatives, **Ga_4Ru_2(II,II)** and **Ga_4Ru_2(II,III)** (*Method b*) are unstable in the air and were prepared in inert atmosphere using a dry-box. **Ga_4Ru_2(II,III)** prepared with *Method a* is an air-stable material only in the solid state; for this reason it was prepared, like the other compounds, in a dry-box. **Ga_4Ru_2(II,III)** prepared with *Method a* was used for magnetic measurements.

6.3.2 Molecular Structures

XRD data were successfully collected at 100 K at ELETTRA synchrotron on **Ga_4Ru_2(II,II)** and **Ga_4Ru_2(II,III)** obtained with *Method b*. In spite of numerous attempts, *Method a* failed to afford X-ray quality crystals of **Ga_4Ru_2(II,III)**, although the product gave satisfactory chemical characterization data. Preliminary structure solution and refinement revealed extensive disorder effects, but confirmed that the two compounds adopt the expected chain-like structure.

Ga4Ru2(II,II)

Crystals of **Ga_4Ru_2(II,II)** proved to be unstable in the air, presumably due to the loss of interstitial solvent, as found for **Fe_4Ru_2(II,II)**. The compound is isomorphous with **Fe_4Ru_2(II,II)** and crystallizes in monoclinic space group $P2_1/n$ with a = 16.143(3) Å, b = 26.4340(5) Å, c = 37.144(7), β = 100.054(3)°, V = 15607(6) $Å^3$ and Z = 4. The asymmetric unit comprises one Ga_4 cluster and one ruthenium dimer, both subject to pronounced disorder. This preliminary structure however confirms the coordination of Ga_4 complexes to Ru_2 units via 4-pyridyl groups: Ga1···Ru1 = 9.684 Å, Ru1-N1 = 2.526 Å, Ru2-N2 = 2.293 Å and Ga1···Ga2 = 2.996 Å, Ga1···Ga3 = 2.970 Å, Ga1···Ga4 = 2.992 Å. These values are comparable to those found in the structure of **Fe_4Ru_2(II,II)**.

Ga4Ru2(II,III) (*Method* b)

Crystals of **Ga_4Ru_2(II,III)** prepared using *Method b* are not air-stable, probably due to the loss of interstitial solvent. Data collection shows similar lattice parameters to **Fe_4Ru_2(II,III)** (*Method b*): a metrically hexagonal unit cell with $a = b$ = 15.861(2) Å, c = 21.434(4), α, β = 90°, γ = 120°, V = 4669.8(16) $Å^3$ and Z = 1 (plausible space group: *P321*). This preliminary structure reveals the same major disorder effects already described for its iron(III) analogue (see Chapter 5), but confirms the expected chain-like structure: Ga1···Ru1 = 9.626 Å, Ru-N = 1.920 Å and Ga_c···Ga_p = 3.033 Å. These values are comparable (except for Ru-N distance) to those found in the structure of **Fe_4Ru_2(II,III)** (*Method b*).

6.3.3 EPR characterization

In order to measure the effective *g*-factor associated with the ground doublet of diruthenium(II,III) paddlewheels in **Fe_4Ru_2(II,III)**, an X-band EPR study was performed in collaboration with Dr. Lorenzo Sorace (Dipartimento di Chimica 'Ugo Schiff', Università degli Studi di Firenze) on **Ga_4Ru_2(II,III)**. The characterization (Fig. 6.3) gives $g_\parallel$ = 1.948 and $g_\perp$ = 4.42. These values are close to those assumed in the analysis of magnetic data for **Fe_4Ru_2(II,III)** (g_{Ru} = 2.08, $g_\parallel$ = g_{Ru} = 2.08 and $g_\perp$ = $2g_{Ru}$ = 4.16. Rewardingly, when introduced into the equation:

$$g_{\mathrm{eff}} = (g_{\mathrm{II}}^2 cos^2\theta + g_\perp^2 sin^2\theta)^{\frac{1}{2}}$$

the new values give g_{eff} = 2.57 for θ = 25°, in perfect agreement with the treatment provided in 5.5.

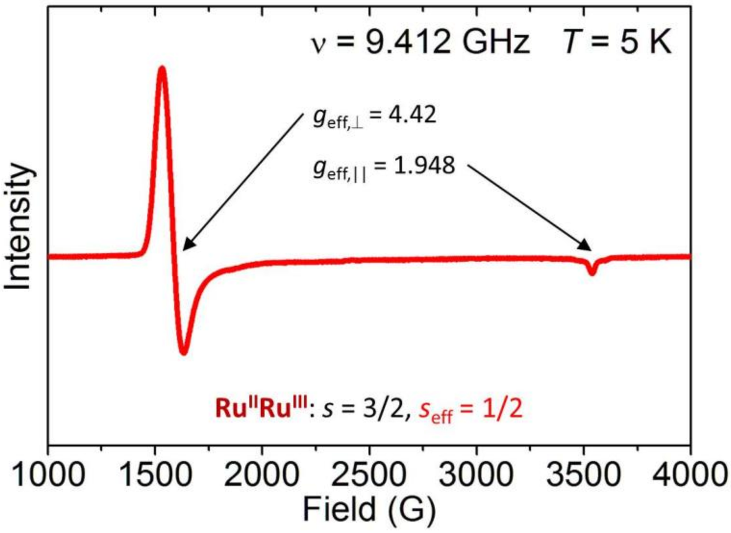

Fig 6.3. X-band EPR spectrum of **Ga_4Ru_2(II,III)** at 9.412 GHz and 5 K.

6.3.4 Magnetic behaviours

The molar magnetization M_M of **Ga_4Ru_2(II,III)** was measured from 2.0 to 300 K with applied fields of H = 1 kOe for T < 25 K and H = 10 kOe for $T \geq$ 25 K. The results are presented in Fig. 6.4 as a $\chi_M T$ vs T plot ($\chi_M = M_M/H$). In the high temperature region, the $\chi_M T$ value (2.29 cm^3 K mol^{-1}) is slightly higher than the Curie constant for a paramagnet with s = 3/2 and g = 2 (1.88 cm^3 K mol^{-1}). $\chi_M T$ decreases gradually with decreasing temperature and reaches 1.38 cm^3 K mol^{-1} at 2.0 K. This behaviour is consistent with the presence of a large magnetic anisotropy, as typically found in this type of paddlewheel complexes.[97] Notice that the compound is magnetic down to 2 K, as expected from its half-integer spin, which implies either a m = ±1/2 (for D > 0) or a m = ±3/2 (for D < 0) ground doublet. The sign and magnitude of D were determined using Eq. 2.13, with E = 0 and treating D and g as adjustable parameters in a least-squares routine. The best-fit values so obtained are D = 63.5(1.1) cm^{-1} and g = 2.196(3) with $R = [\Sigma(\chi_{M,obs}T - \chi_{M,calc}T)^2/\Sigma(\chi_{M,obs}T)^2]^{1/2} = 7.8\cdot10^{-3}$. Therefore, our analysis is in satisfactory agreement with the suggested set of magnetic parameters for diruthenium(II,III) paddlewheels in **Fe_4Ru_2(II,III)** (D = 63 cm^{-1} and g = 2.08, see 5.5).

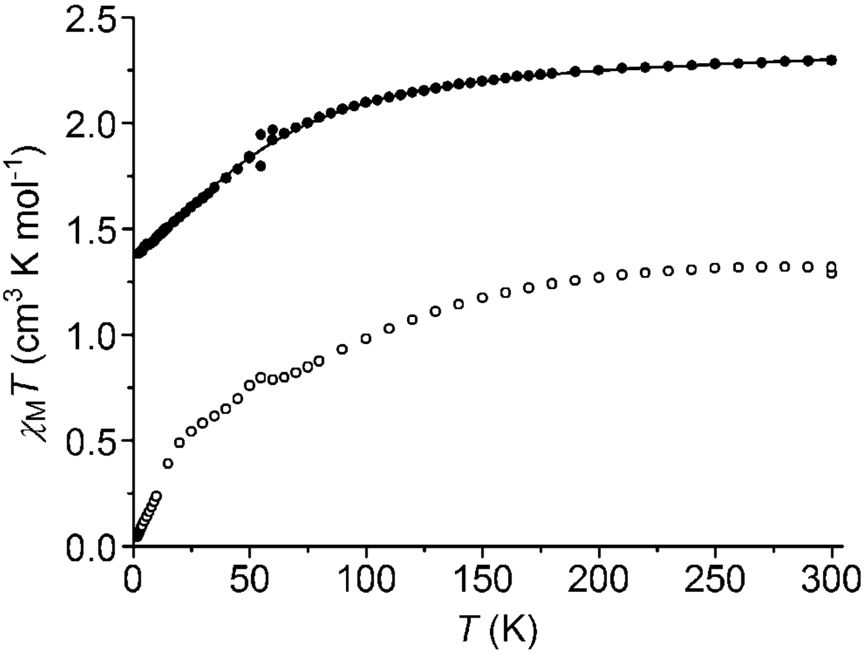

Figura 6.4. $\chi_M T$ vs T plots for **Ga_4Ru_2(II,III)** (•) and **Ga_4Ru_2(II,II)** (o). The continuous line represents calculated data with best-fit parameters, as described in the text.

The magnetic susceptibility of **Ga_4Ru_2(II,II)** was also determined from the molar magnetization measured as a function of temperature from 1.8 to 300 K at H = 30 kOe. The results, presented in Fig. 6.4 as a $\chi_M T$ vs T plot, demonstrate that the compound is much less magnetic than **Ga_4Ru_2(II,III)** at all temperatures. In particular, the $\chi_M T$ product at 2.0 K is 0.05 cm^3 K mol^{-1}, a value approximately 30 times lower than in **Ga_4Ru_2(II,III)**. This very weak magnetic response of **Ga_4Ru_2(II,II)** at low temperature is a consequence of the integer spin state (s = 1) and large hard-axis anisotropy of diruthenium(II,II) paddlewheels, which have an m = 0 ground state (see Fig. 5.2). The quantitative analysis of magnetic behaviour of these $Ru^{II}Ru^{II}$ compounds is complicated by the presence of additional contributions to paramagnetism called Temperature Independent Paramagnetism (TIP).

6.4 Conclusion

In this chapter I have described the synthesis of compound **Ga_4pPy**·EtOH, its characterization by IR, NMR and XRD, and its use for assembling tetragallium(III) analogues of **Fe_4Ru_2(II,II)** and **Fe_4Ru_2(II,III)**. Since the Ga_4 unit is diamagnetic, magnetic measurements have been used to directly probe the behaviour of the two Ru_2 paddlewheels in this type of chain compounds. At 2.0 K, the diruthenium units were found 30 times less magnetic in **Ga_4Ru_2(II,II)** than in **Ga_4Ru_2(II,III)**. The source of the different behaviour lies in the integer (s = 1) and half-integer (s = 3/2) spin of the two paddlewheels, respectively. Since both diruthenium complexes have a hard-axis anisotropy, the ground state has m = 0 in **Ga_4Ru_2(II,II)** but m = ±1/2 in **Ga_4Ru_2(II,III)**. It is now realistic to assume that **Ru_2(II,II)** and **Ru_2(II,III)** units behave similarly in the gallium(III)- and iron(III)-based chains. Our findings then confirm that paramagnetic **Ru_2(II,III)** bridges are present in **Fe_4Ru_2(II,III)**, which features significant intrachain magnetic communication, whereas **Fe_4Ru_2(II,II)** contains nonmagnetic **Ru_2(II,II)** paddlewheels that act as magnetically-insulating units at low temperature.

7 Supramolecular architectures of Ru^{II} porphyrins and Fe$_4$ SMMs

7.1 Introduction

One of the hot topics in molecular magnetism is the readout and modulation of spin states in an SMM by an electric current flowing through the magnetic core. To this aim, photo-active metal porphyrins can be suitable groups for their redox properties and the ability to promote ET once photo-excited (see 7.2).[19]

Aim of this project is the assembly of a supramolecular structure comprising the tetrairon(III) SMM **Fe4pPy** and the ruthenium(II) porphyrin [Ru(p^tBuTPP)(CO)][118] (**1**) (see Fig. 7.1). In fact, compound **1** can be photo-excited from a Ru(II) ground state to a Ru(II)* excited state, which can relax via radiative (emission) and/or non-radiative mechanisms, such as an ET to the close counterpart thus forming a Ru(III) fragment, or an energy transfer. The ET path can then push an extra electron into the Fe$_4$ magnetic core, mimicking the current flow which would occur during the 'readout' process via STM.

In this Chapter I will show that the two components react in a 1:2 ratio yielding the triad **1·Fe$_4$pPy·1**; upon visible-light excitation on the Ru(II) centres of the triad, a strong quenching of the typical emission of the excited ruthenium(II) porphyrin is observed due to an energy transfer process to the Fe$_4$ core and not due to an ETphenomenon as expected.

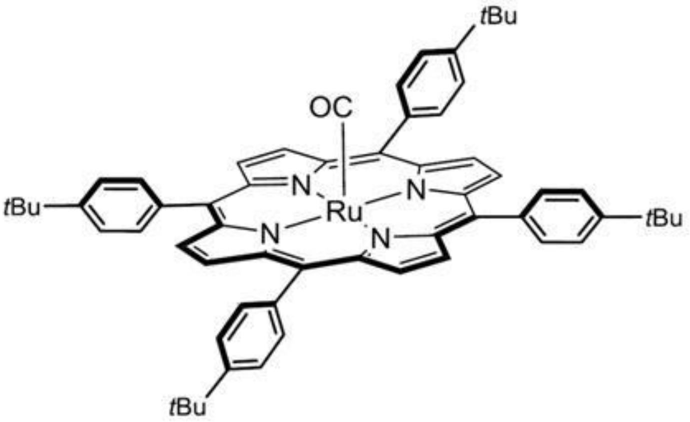

Fig. 7.1. Structure of [Ru(p^tBuTPP)(CO)] (**1**).

7.2 Porphyrins

Porphyrins are planar aromatic macrocycles and are ubiquitous in nature. Their monometallic complexes are involved in many key processes of life, such as respiration and photosynthesis. For example, chlorophyll is involved in the process of photosynthesis and its molecular structure includes a porphyrin unit.

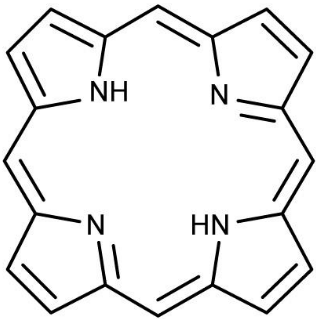

Fig. 7.2 Porphyrin structure without metal atom inside the cycle.

Porphyrin structure (Fig. 7.2) is composed of four modified pyrrole subunits interconnected at their alfa carbon atoms via carbon bridges =CH-. The porphyrin ring is aromatic, with a total of 26 electrons in the conjugated system. One important consequence of the large conjugated system is that porphyrin molecules typically have very intense absorption bands in the visible region and are usually deeply coloured. Porphyrins are the conjugated acids of the ligands that form complexes with metal ions usually in a 2+ or 3+ OS. Porphyrin-based compounds are of interest in molecular electronics and photovoltaics and synthetic porphyrins can act as dyes, incorporated in prototype dye-sensitized solar cells.[119–121] After irradiation, porphyrins can also behave as one-electron donor groups[48]. Furthermore, numerous supramolecular structures comprising porphyrins can be found in the literature.[48,122,123]

Starting from these premises, attention was focused on linking a ruthenium(II) porphyrin to **Fe$_4$pPy** SMM to afford a discrete supramolecular system containing both photoactive units and a magnetically-bistable component.

7.3 Synthesis

The supramolecular assembly of **Fe_4pPy** and **1** required considerable effort and was performed in collaboration with Prof. Elisabetta Iengo (Dipartimento di Scienze Chimiche e Farmaceutiche, Università degli Studi di Trieste). The triad was obtained with two different methods. In the first one (called *Method I*), a mixture of **Fe_4pPy**·2EtOH and **1** in toluene in ratio 1:2 was stirred for 2 h and then allowed to slowly evaporate, giving tiny purple crystals suitable for XRD studies by synchrotron radiation. In *Method IIa*, **2** was added into a **Fe_4pPy** solution in THF:EtOH 3:1 (always the **Fe_4pPy**:**1** ratio is 1:2) and then the solution was stirred for 12h, giving a purple powder. The product was filtered and washed with EtOH and then dried in vacuum. *Method IIb* is similar to *IIa*, except that **Fe_4pPy**·2EtOH and **1** (in ratio 1:2) were both dissolved in THF and the solution layered with EtOH. After 3 weeks, the product appeared as a purple microcrystalline powder at the interface, was collected by filtration, washed with EtOH and dried in vacuum.

All the products obtained with the different methods were characterized by EA and IR spectroscopy, which confirmed the assembly of the triad. IR spectroscopy, in particular, showed the characteristic bands of the Fe_4 unit together with the porphyrin C≡O stretching at 1954 cm^{-1}.

7.4 ^{1}H NMR characterization

The assembly reaction between **Fe$_4$pPy** and **1** in 1:2 ratio can be followed by ^{1}H NMR in toluene-*d*$_8$. The ^{1}H NMR spectrum of **1**, reported in Fig. 7.3, shows the characteristic peaks in the aromatic region of pyrrolyl (8.77 ppm) and phenyl rings (7.55 and 8.25 ppm), while the ^{t}Bu hydrogens appear as a singlet at 1.24 ppm. Due to the paramagnetic effect, the ^{t}Bu hydrogens of Fe$_4$ cluster appear as a broad signal at about 10.5 ppm with Py$_a$ shoulder, while Py$_b$ hydrogens of pyridine are too close to paramagnetic core to be observed in the spectra, as described in Chapter 4 (see Fig. 4.2). In toluene solutions of **Fe$_4$pPy** and **1** (1:2 ratio), the signals of **1** undergo significant broadening, as expected from the influence of the paramagnetic Fe$_4$ core on the porphyrin upon coordination while the ^{t}Bu hydrogens of Fe$_4$ cluster shift from 10.5 ppm to 11 ppm, confirming the happened coordination.

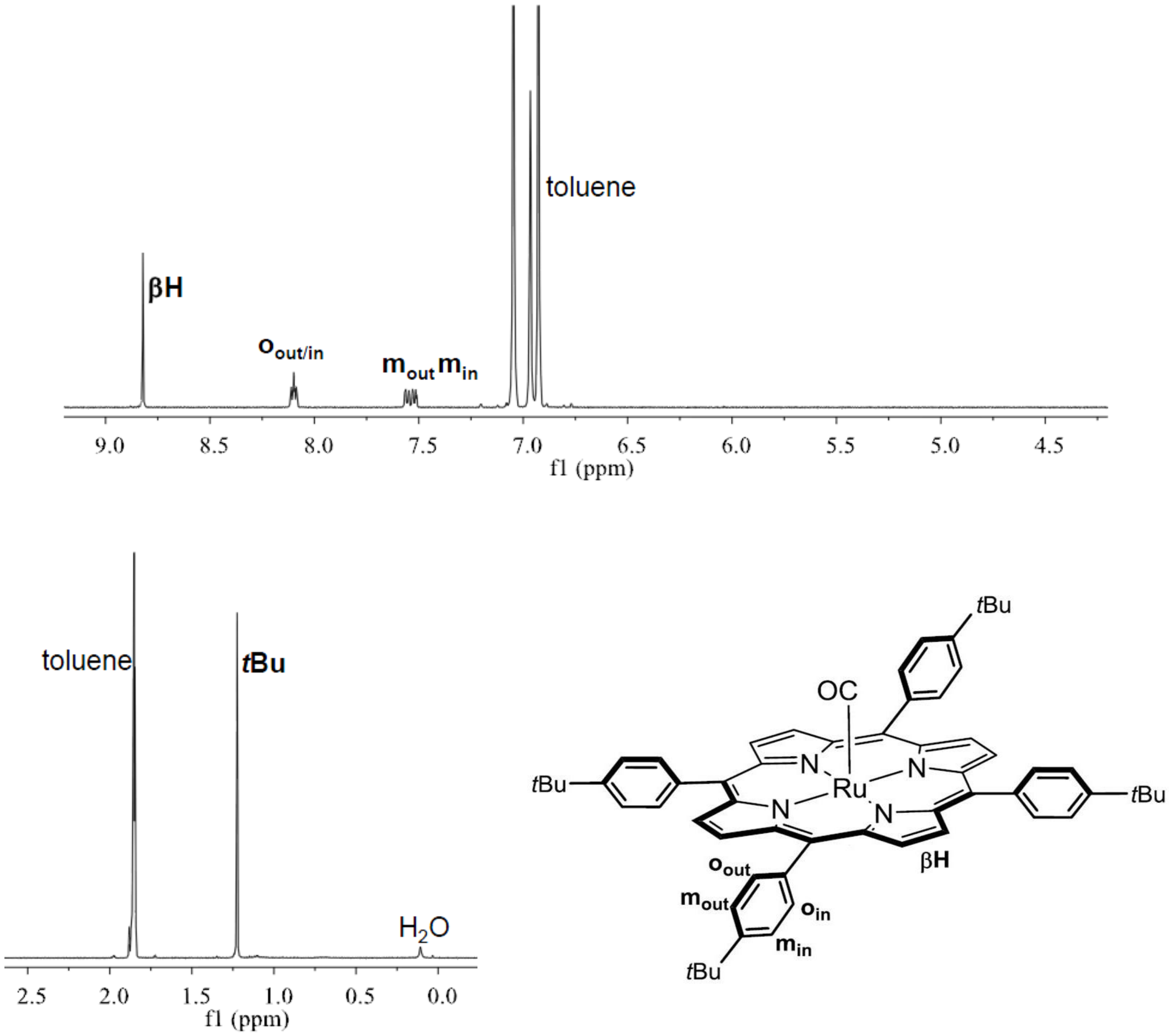

Fig. 7.3. ^{1}H NMR spectrum in toluene-*d*$_8$ and structure of **1** with hydrogen labelling scheme.

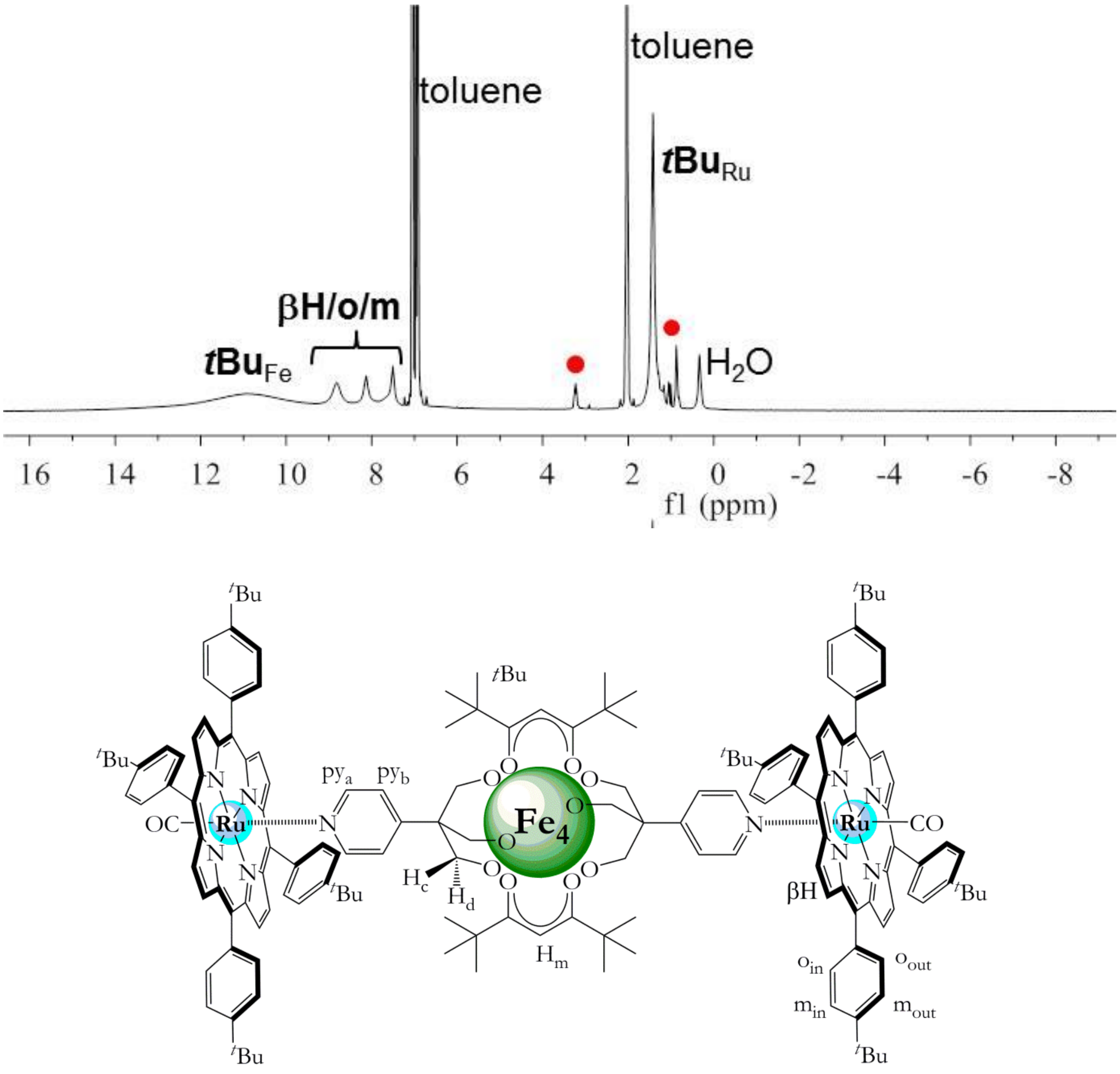

Fig. 7.4. ^{1}H NMR spectrum of a solution of **Fe$_4$pPy**·2EtOH and **1** in toluene-d_8 (up) and structure of **1·Fe$_4$pPy·1** with the hydrogen labelling scheme (bottom). The red circles mark peaks of interstitial EtOH.

7.5 Structural characterization

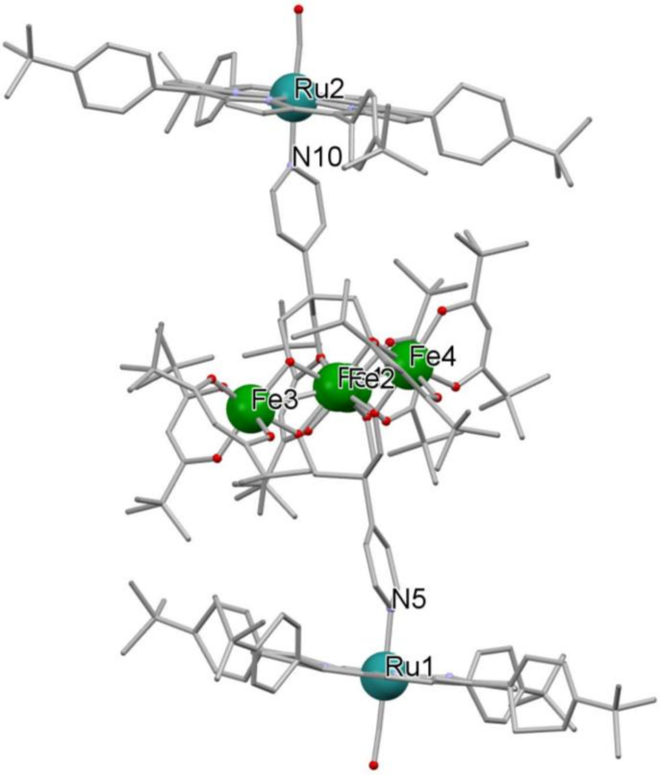

Fig. 7.5. Molecular structure of **1**·**Fe$_4$pPy**·**1**. Colour scale: green = Fe, light blue = Ru, blue = N; red = O; carbon skeleton is shown as grey sticks for clarity. Only carbon atoms of CO are visible as grey sphere.

A preliminary X-ray diffraction data collection using synchrotron radiation at ELETTRA (Trieste) revealed the position of all non-hydrogen atoms and confirmed the structure of **1·Fe$_4$pPy·1**. The asymmetric unit contains one tetrairon(III) and two Ru-porphyrin moieties (Fig. 7.5). The Fe$_c$···Ru1 and Fe$_c$···Ru2 distances are 9.54 and 9.52 Å, respectively, while N5-Ru1 and N10-Ru2 separations are 2.22 and 2.23 Å, respectively. These values are close to those found in chains of **Fe$_4$pPy** and diruthenium paddlewheels (see Chapter 5). The two Ru-porphyrin planes are almost parallel (4.36°) and form dihedral angles of 19.93° (Ru1) and 22.50° (Ru2) with the Fe$_4$ plane.

The geometrical parameters of the Fe$_4$ unit agree with those found in **Fe$_4$pPy**·2EtOH (see Chapter 4). The average pitch angle between the Fe$_c$(O)$_2$Fe$_p$ and Fe$_4$ planes is 68.2°, very close to the value found in **Fe4pPy**·2EtOH (68.7°),[19] while the Fe$_c$···Fe$_p$ distances are 3.11 Å, 3.10 Å and 3.08 Å. One interstitial molecule of toluene, which is the crystallization solvent, is refined near one porphyrin ring and has a parallel displaced π stacking interaction[124] with a porphyrin phenyl ring (3.8 Å).

7.6 Magnetic behaviour

The temperature dependence of the molar magnetic susceptibility, χ_M, in low fields (1–10 kOe) for **1·Fe$_4$pPy·1** was measured between 1.9 and 300 K, and the data are reported in Fig. 7.6. The shape of $\chi_M T$ vs. T curve is characteristic for Fe$_4$ clusters, where antiferromagnetic interactions between the central and the peripheral iron(III) centres lead to spin uncompensation in the ground state. The $\chi_M T$ value at room-temperature is ca. 12.0 emu K mol^{-1}, hence lower than the cumulative Curie constant for four s = 5/2 centres (17.51 emu K mol^{-1} with g = 2.00); upon cooling, it first decreases towards a minimum at around 120 K (ca. 10.5 emu K mol^{-1}) and then increases again reaching 13.6 emu K mol^{-1} at 15 K, before a further drop at the lowest temperatures. The maximum $\chi_M T$ value is getting closer to the Curie constant for the expected S = 5 ground state (15.00 emu K mol^{-1} with g = 2.00).

Magnetic exchange interactions among the four iron(III) centres have been determined by fitting $\chi_M T$ vs. T curves to a Heisenberg *plus* Zeeman spin Hamiltonian that assumes threefold molecular symmetry, as discussed in Chapter 2 (Eq. 2.11). The results (Table 7.1) confirm the presence of dominant nearest-neighbour antiferromagnetic couplings ($J > 0$), with $|J'|$ at least one order of magnitude smaller than J.

The low temperature behaviour was further investigated by recording isothermal molar magnetization data at 4.5 and 1.9 K in fields up to 50 kOe (Fig. 7.6). With increasing field the curves increases but doesn’t approach well the saturation value expected for an S = 5 ground state ($M_M/N_A\mu_B = 5g \cong 10$). The second-order axial anisotropy D was determined by applying the axial zero-field splitting *plus* Zeeman Hamiltonian ($D\hat{S}_z^2$ convention, Eq. 2.13) and resulted in the best fit parameters gathered in Table 7.1. The magnitude and sign of D are typical for the family of Fe$_4$ clusters, although $|D|$ is somewhat smaller than found for the pristine cluster **Fe$_4$pPy**.[19]

The magnetization dynamics of **1·Fe$_4$pPy·1** was then investigated in zero and 1 kOe static field (H) as a function of both temperature (down to 1.9 K) and frequency of the oscillating field (ν = 10–10000 Hz). The results are reported in Fig. 7.7 as χ_M'' vs. ν curves at different T values. In both zero and 1 kOe static fields, frequency (and temperature) dependent maxima appear in the χ_M'' plots, signifying that the triad still behaves as a SMM. Treatment of the data based on generalized Debye model proved fully satisfactory. The relaxation times τ obtained from the analysis of both zero and 1 kOe static field data are shown in Fig. 7.8, where the ln(τ) vs. 1/T plots are essentially linear. This indicates that magnetization reversal is a thermally-activated processes in the temperature range analysed and the Arrhenius law $\tau = \tau_0 \exp(U_{\mathrm{eff}}/k_{\mathrm{B}}T)$ is obeyed. The $U_{\mathrm{eff}}/k_{\mathrm{B}}$ and τ_0 values obtained by fitting ln(τ) vs. 1/T data are reported in Table 7.1, together with those of **$\mathbf{Fe_4}$pPy**.[19] As expected from the lower $|D|$ value, the energy barrier is smaller in the triad than in the pristine cluster; however, $U_{\mathrm{eff}}/k_{\mathrm{B}}$ still increases upon application of an external magnetic field, which suggests the efficient suppression of zero-field resonant tunnelling processes.

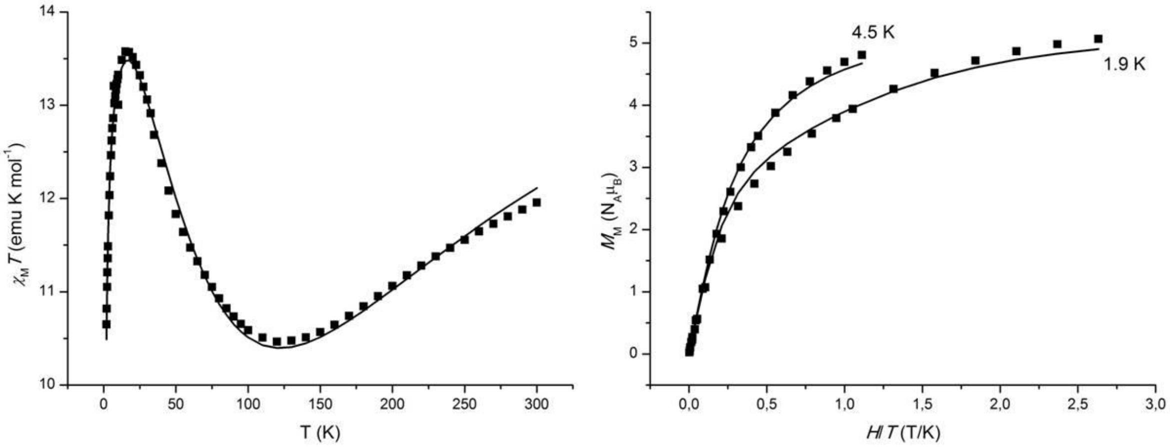

Fig. 7.6. Temperature dependence of the molar susceptibility (χ_M) multiplied by temperature (left) and field dependence of the isothermal molar magnetization (M_M) at 4.5 and 1.9 K for **1·$\mathbf{Fe_4}$pPy·1** (right). Solid lines are given by the best-fit parameters.

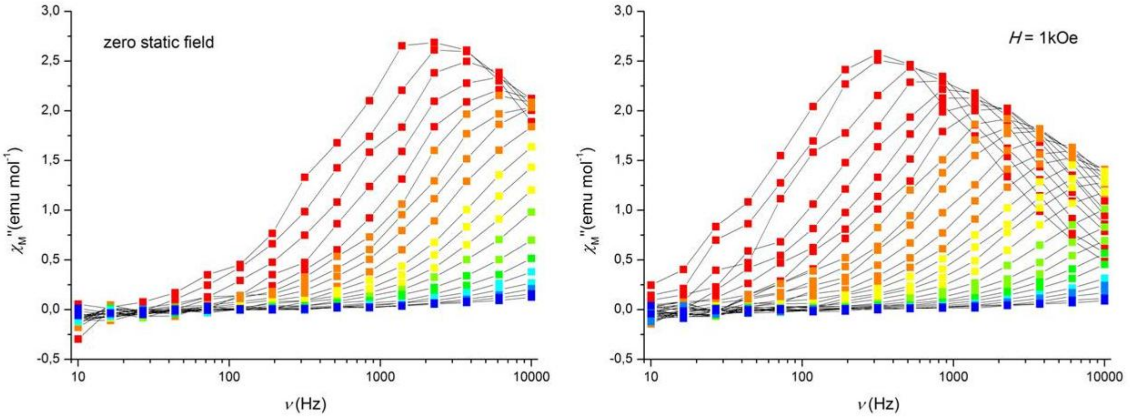

Fig. 7.7. Imaginary component of the molar ac susceptibility (χ_M'') of **1·$\mathbf{Fe_4}$pPy·1** measured at zero and 1-kOe applied static fields in the 10−10000 Hz frequency range from 1.9 (red) to 5.5 K (blue).

Table 7.1. Best-fit parameters obtained from the analysis of dc and ac magnetic data on **Fe_4pPy**·2EtOH[19] and **1·Fe_4pPy·1**.

	Fe4pPy·2EtOH[19]	**1·Fe4pPy·1**
dc measurements		
$\chi_M T$ vs. T		
g	1.9412(14)	1.942(3)
J, cm^{-1}	15.94(6)	17.28(13)
J', cm^{-1}	0.45(4)	–0.51(8)
θ, K[a]	–0.126(6)	–0.664(15)
R[b]	1.50×10^{-1}	1.53×10^{-1}
M_M vs. H/T		
g	1.921(8)	1.863(19)
D, cm^{-1}	–0.439(12)	–0.38(3)
R[b]	8.929×10^{-2}	2.89×10^{-1}
ac measurements		
$H = 0$		
U_{eff}/k_B, K	14.9(3)	8.71(17)
τ_0, s	$6.3(7) \times 10^{-8}$	$6.4(5) \times 10^{-7}$
$H = 1$ kOe		
U_{eff}/k_B, K	17.20(7)	12.33(9)
τ_0, s	$3.53(8) \times 10^{-7}$	$7.1(2) \times 10^{-7}$

[a] Curie-Weiss correction to the susceptibility to account for the low-temperature drop of the $\chi_M T$ product; [b] $R = [\Sigma(\text{obs} - \text{calc})^2 / \Sigma(\text{obs})^2]^{½}$.

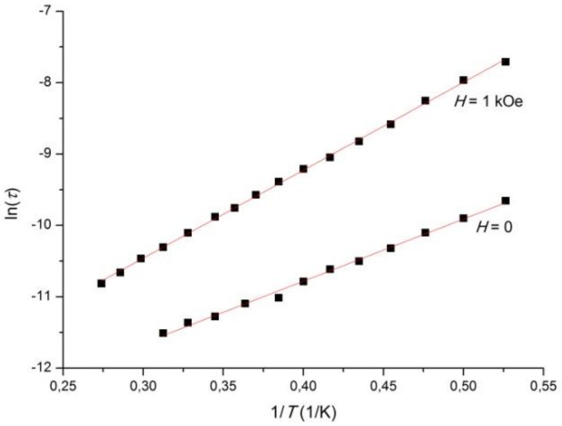

Fig. 7.8. Arrhenius plots for compounds **1·Fe_4pPy·1** obtained from alternating current susceptibility measurements in zero and 1 kOe applied static fields.

7.7 Photophysical measurements

Photophysical measurements on **1·Fe$_4$pPy·1** aimed at understanding the occurrence of an electron- or energy-transfer mechanism inside the assembly upon photoexcitation of the Ru-porphyrin unit. The experiments were made in collaboration with Prof. Maria Teresa Indelli (Dipartimento di Scienze Chimiche e Farmaceutiche, Università degli Studi di Ferrara).

First, UV-vis absorption spectra in dichloromethane were recorded for **1**, **Fe$_4$pPy**·2EtOH and **1**·**Fe$_4$pPy**·**1** (Fig. 7.9). Around 530-540 nm only the ruthenium fragment displays a significant absorbance. In order to selectively excite the ruthenium porphyrin, λ = 534 nm was chosen as the excitation wavelength for the emission experiments.

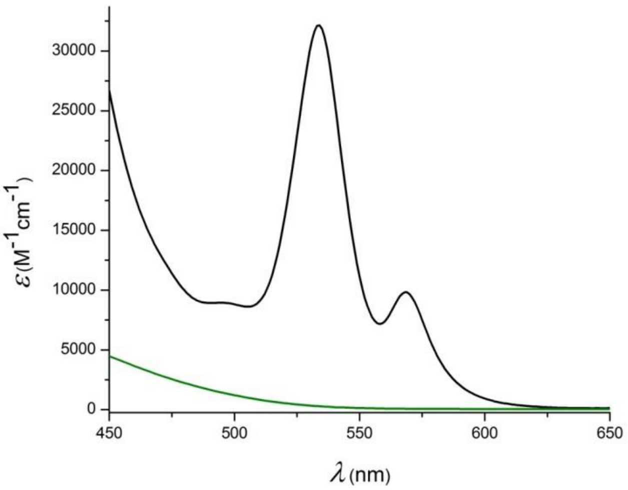

Fig. 7.9. Absorption spectra of **Fe$_4$pPy**·2EtOH (green) and **1·Fe$_4$pPy·1** (black) in the 450–650 nm range in dichloromethane. The spectrum of **1** basically coincides with the black spectrum.

In the emission spectra, the band due to the radiative relaxation pathway of the Ru(II)* porphyrin at 740 nm is maintained also in the triad, but the spectrum shows a strong quenching of around 80% as compared with **1** (Fig. 7.10). Consequently, another non-radiative deactivation process must be present, probably an energy transfer from the excited ruthenium porphyrin to the SMM core.

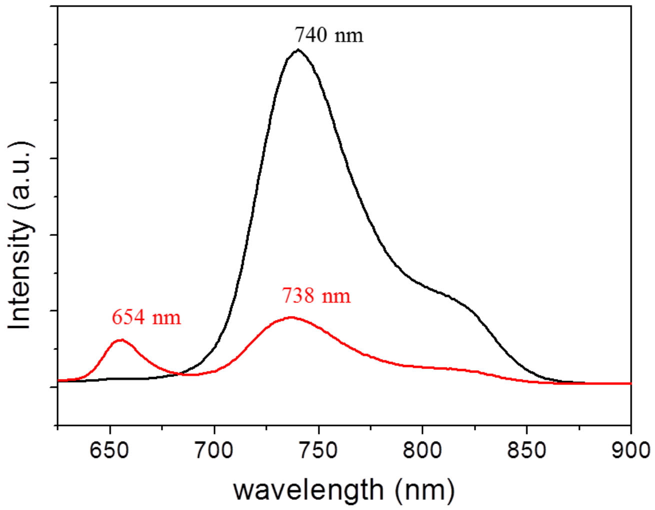

Fig. 7.10. Emission spectra of **1·Fe$_4$pPy·1** (red line) and **1** (black line) in CH_2Cl_2 measured in the same experimental conditions (λ_{exc}= 534 nm).

In order to observe the excited ruthenium porphyrin triplet, laser photolysis was used to excite the triad (λ_{exc} = 532 nm, t_{laser} = 20 ns). The absorption spectrum of excited **1·Fe$_4$pPy·1** is similar to the triplet state spectrum of the ruthenium porphyrin **1**, and this similarity confirms that I are really probing the triplet state of the supramolecular adduct (see Fig. 7.11).

Fig. 7.11. Transient absorption spectra of **1·Fe$_4$pPy·1** (red line) and **1** (black line) obtained by nanosecond laser photolysis (λ_{ecc}= 532 nm) in CH_2Cl_2.

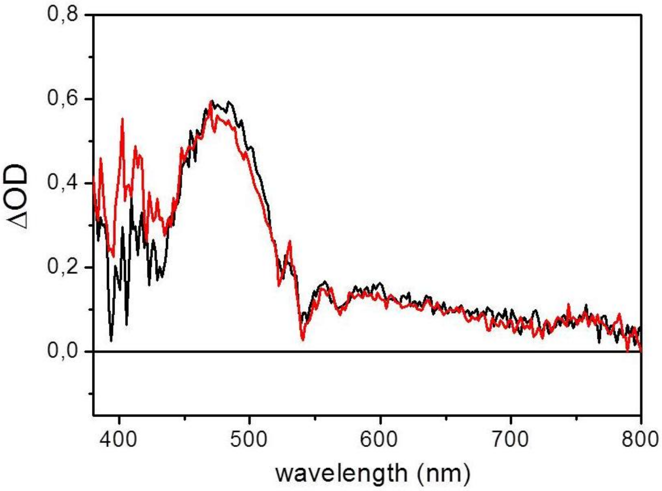

Furthermore, laser photolysis allows to follow the time decay of transient absorption spectra. In this way, the lifetime for the triplet state of the Ru chromophore was found 11 and 2.5 ms, in **1** and **1·Fe$_4$pPy·1**, respectively (Fig. 7.12). This result is consistent with the stationary emission data and clearly indicates that in **1·Fe$_4$pPy·1** the triplet state of Ru chromophore is quenched; however, due to the similarity of the transient absorption spectra of the two excited species, the quenching mechanism is most likely an energy transfer.

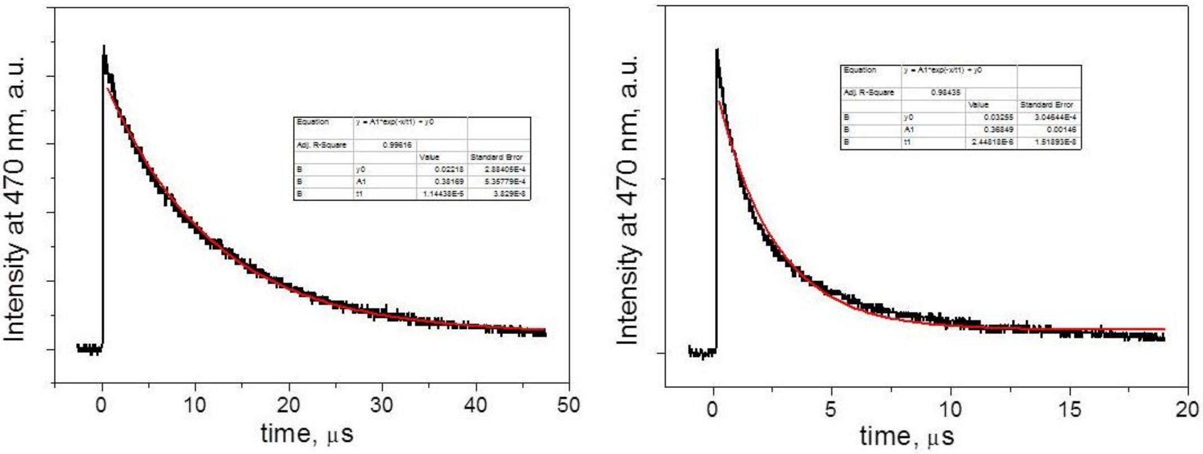

Equation	y = A1*exp(-x/t1) + y0		
Adj. R-Square	0.99616		
		Value	Standard Error
B	y0	0.02218	2.88405E-4
B	A1	0.38169	5.35779E-4
B	t1	1.14438E-5	3.829E-8

Equation	y = A1*exp(-x/t1) + y0		
Adj. R-Square	0.98435		
		Value	Standard Error
B	y0	0.03255	3.04644E-4
B	A1	0.36849	0.00146
B	t1	2.44818E-6	1.51893E-8

Fig. 7.12. Kinetic analysis at 470 nm of the transient observed in the laser photolysis of (a) **2** and (b) **1·Fe$_4$pPy·1**.

7.8 Conclusion

In conclusion, I have optimized the procedure for the preparation of a supramolecular **1·Fe$_4$pPy·1** adduct comprising a Fe$_4$ SMM and two Ru-porphyrins. Dc and ac magnetic measurements confirm that the triad retains SMM properties and its behaviour is similar to other Fe$_4$ SMMs published before.[17,18,28] The photophysical study shows that the emission intensity of the ruthenium porphyrin in **1·Fe$_4$pPy·1** is strongly quenched (80%) with respect the Ru porphyrin itself. Unfortunately, an ET process from the triplet Ru centre to the Fe$_4$ core is probably energetically unfavoured and only an energy transfer process occurs. As a future perspective, a **Fe$_4$pPy** complex with electron-withdrawing ligands, such as pivaloyltrifluoroacetone,[60] could help making the Fe$_4$ core more easily reducible and favour an ET process.

8 A 3D Metal-Organic Framework of Fe_4 SMMs

8.1 Introduction

In addition to the redox-active groups seen in the previous chapters (ferrocene, diruthenium paddlewheel complexes and metalloporphyrins), silver ions also potentially display redox activity. Silver exists in oxidation states 0, +1, +2 and +3, but the most common ones are 0 and +1; furthermore silver is photosensitive. Silver(I) shows linear (sometimes distorted) or tetrahedral coordination geometry and, for this reason, it is an interesting connector to link **Fe_4pPy** into chains or more complex structures.

In this chapter, I will show the outcome of the reaction between the synthon **Fe_4pPy** and $AgClO_4$ salt. The crystalline product so obtained is not a chain-like structure but a 3D MOF, $\{[Fe_4(pPy)_2(dpm)_6]_2Ag\}(ClO_4)$ (**Fe_4Ag**), with interesting magnetic behaviour. Despite its cubic crystal symmetry and, consequently, the absence of second order anisotropy, the material behaves as an SMM, as shown by microSQUID and ac measurements.[125] 8.4.2 and 8.4.4 are largely based on work by Dr. Lorenzo Sorace and Dr. Mauro Perfetti (Dipartimento di Chimica “Ugo Schiff”, Università degli Studi di Firenze) and are included here for completeness.

8.2 Synthesis

The reaction of **Fe_4pPy**·2EtOH with $AgClO_4$ was carried out in different conditions exploiting THF as a good solvent for both reactants. No precipitate is formed when the two reagents are mixed in THF in a 2:1 molar ratio, *i.e.* first dissolving **Fe_4pPy**·2EtOH in the minimum amount of solvent (ca. 7.2 mM) and then adding a $AgClO_4$ solution to give a final Fe_4 concentration of ca. 5.0 mM. Crystal growth can be promoted by liquid diffusion of DCM, toluene vapour diffusion or toluene liquid diffusion. The best product yield was achieved by layering the reaction mixture in THF over an equal volume of DCM (*Method I*). Big red crystals of **Fe_4Ag** suitable for XRD were obtained in five days in acceptable yield (51.6%).

Also vapour diffusion of toluene into the THF reaction mixture (*Method II*) gave crystals of **Fe_4Ag** when slightly understoichiometric $AgClO_4$ was used, i.e. a **Fe_4pPy**·2EtOH:$AgClO_4$ molar ratio slightly larger than 2. An exact 2:1 molar ratio gave large cubes of **Fe_4Ag** mixed with tiny elongated parallelepipeds of a second crystalline species. ESI characterization and elemental analysis suggest a 1:1 ratio between **Fe_4pPy** and silver(I) ions in this second species, as expected for a chain-like structure. About this last species, only crystals of bad quality and in poor yield of **Fe4Ag** were obtained by toluene liquid diffusion.

Another procedure consists in separately dissolving **Fe_4pPy**·2EtOH in DCM (ca. 4.4 mM) and $AgClO_4$ in THF (ca. 2.2 mM) and then allowing the former solution to slowly diffuse into an equal volume of the latter (*Method III*). This method gave good quality crystals of **Fe_4Ag**, although in lower yield than *Method I*. When the reaction was conducted directly in a THF:DCM 1:1 mixture at the same concentration of the reactants, immediate precipitation of an orange powder was observed, whose composition however closely matches that of **Fe_4Ag**.

The large cavities in the structure of this 3D-MOF (see 8.3) can trap solvent molecules and perchlorate counterions. In order to check the ability of encapsulating THF or DCM, few crystals of **Fe_4Ag** prepared using *Method I* were then taken from the mother liquor, quickly dried to remove solvent traces on the surface and then sonicated in deuterated benzene. Using ferrocene as internal standard, ^{1}H NMR spectra gave 2.6 molecules of DCM and 2.1 molecules of THF per formula unit, a result compatible with the dimensions of the cavities. When the crystals were thoroughly dried under vacuum, instead, all solvent was removed, but crystallinity remained unaffected as judged by visual inspection under an optical microscope.

Comparison of the IR spectra of **Fe_4pPy**·2EtOH (see Experimental Section) and **Fe_4Ag** shows important similarities, with common bands arising from the stretching of aromatic and aliphatic C–H bonds as well as of Fe–O, C=O, C=C and C=N bonds. The broad band of ethanol O–H group, found at 3398 cm^{-1} in the spectrum of **Fe_4pPy**·2EtOH, disappears in **Fe_4Ag**, which contains no ethanol molecules. The presence of perchlorate ions into the lattice cavities, dictated by charge balance requirements, can be detected also by infrared spectroscopy. In fact, the narrow band of C–O stretching, observed at 1105 cm^{-1} in compound **Fe_4pPy**·2EtOH, moves to 1108 cm^{-1} in **Fe_4Ag** and becomes stronger and broader due to the overlap with the perchlorate Cl–O stretching. X-ray diffraction studies and magnetic measurements were carried out on thoroughly dried samples, in order to reduce uncertainties in molar mass as well as possible additional sources of disorder

In the MALDI-ToF mass spectra of **Fe_4Ag**, the two most intense peaks at *m/z* = 1791.72 and 1184.27 can be unambiguously attributed to the fragments $[Fe_4(pPy)_2(dpm)_6+Ag]^+$ and $[Fe_4(pPy)_2(dpm)_6–Fe(dpm)_3+Ag]^+$ by comparison of the experimental and theoretical isotopic patterns (see Fig. 8.1), thus confirming the coordination of Ag^+ by the nitrogen atoms of **Fe_4pPy**. The mass spectrum of **Fe_4Ag** recorded in the same ionization conditions but in the absence of matrix shows the same peaks, together with further signals given by the adducts of $[Fe_4(pPy)_2(dpm)_6]$ with sodium and potassium ions.

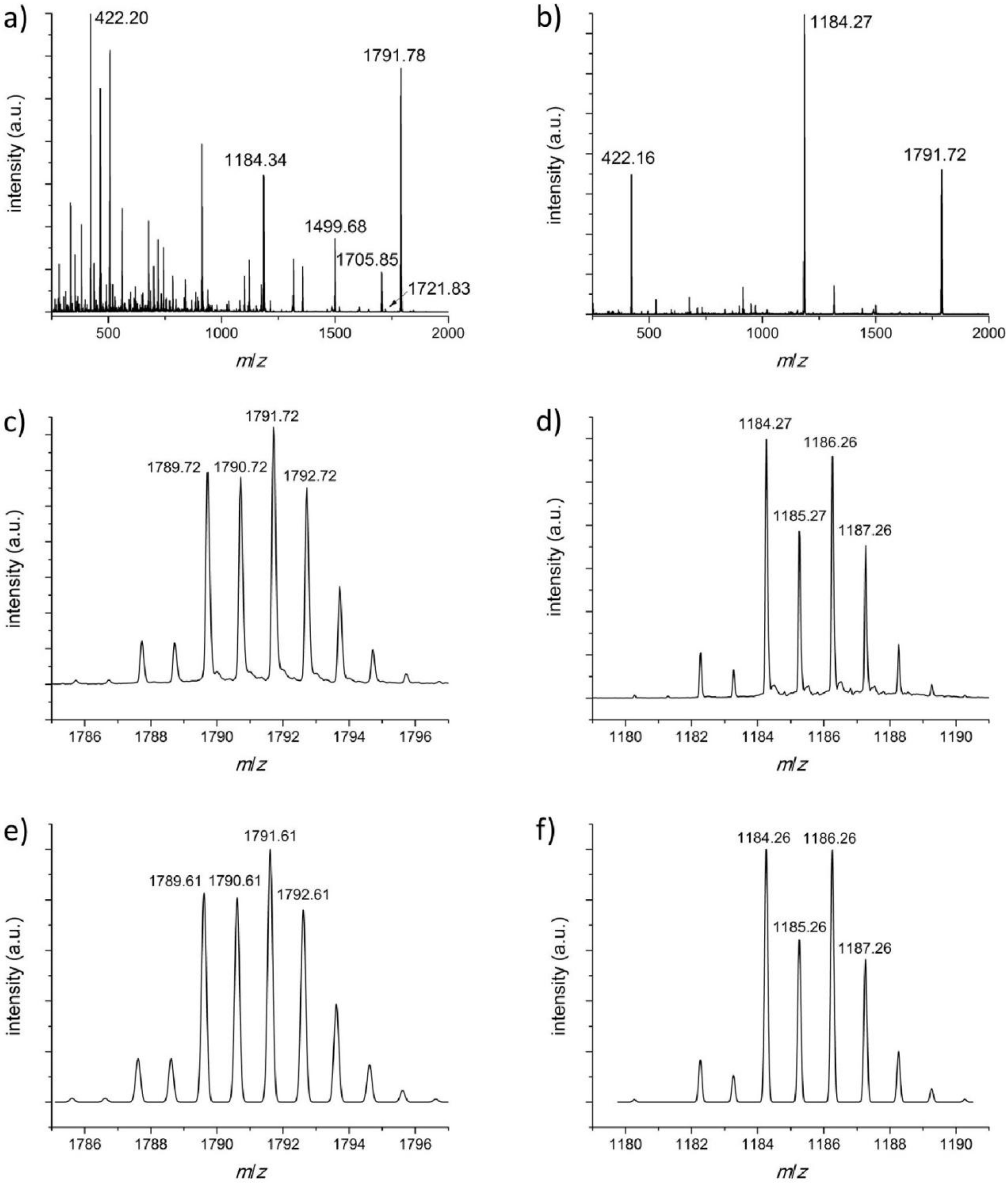

Fig. 8.1. MALDI-TOF full-scan mass spectra of **Fe_4Ag** without (a) or with matrix (b), and mass scale expanded segments of the peaks with *m/z* = 1791.72 (c) and 1184.27 (d), along with calculated isotopic patterns for the formulae $C_{84}H_{134}AgFe_4N_2O_{18}$ for $[Fe_4(pPy)_2(dpm)_6 + Ag]^+$ centred at *m/z* = 1791.61 (e) and $C_{51}H_{77}AgFe_3N_2O_{12}$ for $[Fe_4(pPy)_2(dpm)_6 – Fe(dpm)_3 + Ag]^+$ centred at *m/z* = 1184.26 (f).

8.3 Molecular structure

The structure of **Fe_4Ag** was investigated by single-crystal XRD at 110(2) K. The compound crystallizes in cubic space group *Fd–3c* as good-quality red crystals with a very large unit cell (V = 87037(4) Å^3). The unit cell contains 32 symmetry-equivalent Fe_4 units similar in structure to the tetrairon(III) cluster in **Fe_4pPy**·2EtOH.[19] For instance the dihedral angle between the Fe_4 and Fe1$(O1)_2$Fe2 least-squares planes, a parameter of paramount importance for magnetic anisotropy,[18] has the same value in **Fe_4pPy**·2EtOH and **Fe_4Ag** (68.7°). However, while in **Fe_4pPy** crystallographic molecular symmetry is C_2, Fe_4 complexes in **Fe_4Ag** develop on D_3-symmetry sites and have crystallographically-imposed threefold symmetry along the main diagonals of the cubic unit cell. The Fe_4 units thus adopt four different orientations in the structure, with threefold axes oriented at 109.47° from each other. Each Fe_4 unit coordinates two Ag^+ ions in opposite directions through the nitrogen atoms of 4-pyridyl groups. The Ag^+ ions (16 per unit cell) lie on T symmetry sites and are coordinated by four 4-pyridyl groups each in a perfect tetrahedral geometry (Ag1–N1 = 2.258(7) Å, N1–Ag1–N1 = 109.47°) (Fig. 8.2). This arrangement brings Fe1 at 9.60 Å from Ag1 and at 15.67 Å from equivalent atoms of neighbouring Fe_4 units, whereas the shortest intermolecular Fe···Fe distance in the structure is 12.94 Å. The resulting 4-connected non-centrosymmetric diamondoid lattice (**dia**-net topology according to IUPAC recommendations[126–128]) is interlocked with a second lattice of the same type obtained by inversion (Fig. 8.3 and Fig. 8.4). A survey in CSD showed that very few coordination compounds crystallize in cubic space group *Fd–3c*,[129–132] and none of them contains two interlocked **dia** networks as in **Fe_4Ag**.

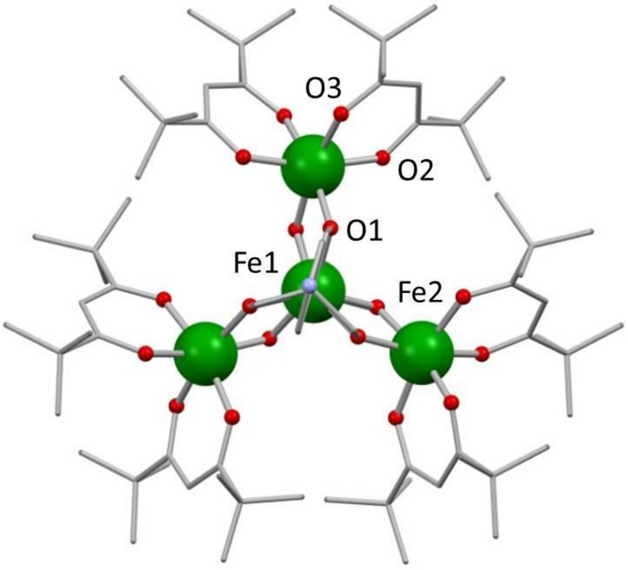

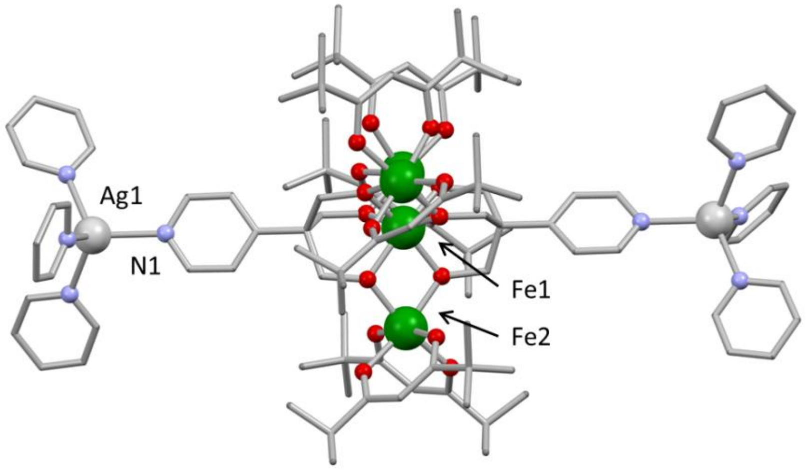

Fig. 8.2 Top (left) and side (below) view of the Fe_4 unit in **Fe_4Ag** highlighting the 180°-ditopic Fe_4 supramolecular linker with two Ag^+ ions coordinated by nitrogen atoms of the 4-pyridyl rings. Colour code: Ag = light grey, Fe = green, O = red, N = light blue, C = grey, H atoms and ClO_4^- anions omitted for clarity, pyridyl rings appear in only one space orientation. Selected interatomic distances and interbond angles: Fe1···Fe2 = 3.1056(15) Å, Fe2···Fe2' = 5.3791(25) Å, Fe1–O1 = 1.977(4) Å, Fe2–O1 = 1.983(4) Å, Fe2–O2 = 1.972(4) and Fe2–O3 = 1.991(4) Å, Fe1–O1–Fe2 = 104.5(8)°.

The structure exhibits three different types of disorder:

1) the 4-pyridyl ring develops along a crystallographic threefold axis and consequently is found disordered over three different positions;

2) a minority fraction [0.133(2)] of Fe_4 linkers is rotated by 60° around the Ag···Fe_4···Ag direction, with coinciding central ions (Fe1) but distinct peripheral metals (Fe2 and Fe2a), a feature that is not unprecedented in the literature;[133]

3) as found in few other isostructural Fe_4 derivatives,[17] the two dpm^- ligands bonded to the same iron(III) ion adopt two different coordination modes, propeller-like (*p*) and sandwich-like (*s*); the ratio *p*:*s* is close to 60:40 and a complex distribution of Fe_4 isomers is therefore expected; the arrangement of dpm^{-} ligands in each unit will contribute to determine its local symmetry, beside influencing the symmetry of neighbouring units.

It follows that the local symmetry of Fe_4 complexes is not necessarily threefold, in agreement with magnetic data (see below). Perchlorate anions were only partially located in the cavities of the structure, which contains 12415 Å^3 (14.3%) of accessible voids per unit cell. This empty space is sufficient to host the solvent content found by NMR experiments, considering the molecular volumes of DCM (110 Å^3) and THF (132 Å^3).

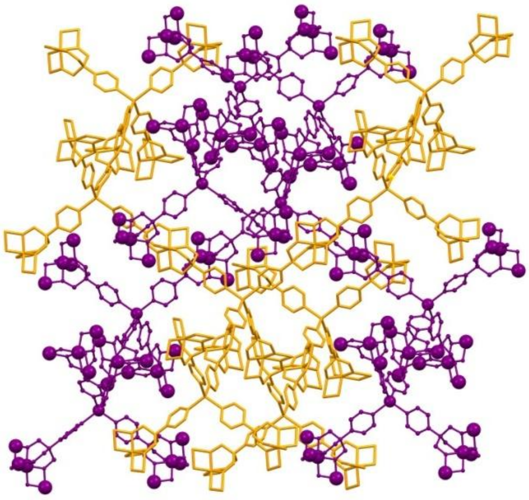

Fig. 8.3. Perspective view of the unit cell of **Fe_4Ag** highlighting the two interlocked diamondoid lattices, depicted in purple and orange; dpm^{-} ligands, H atoms and ClO_4^- anions are omitted for clarity, and pyridyl rings appear in only one space orientation.

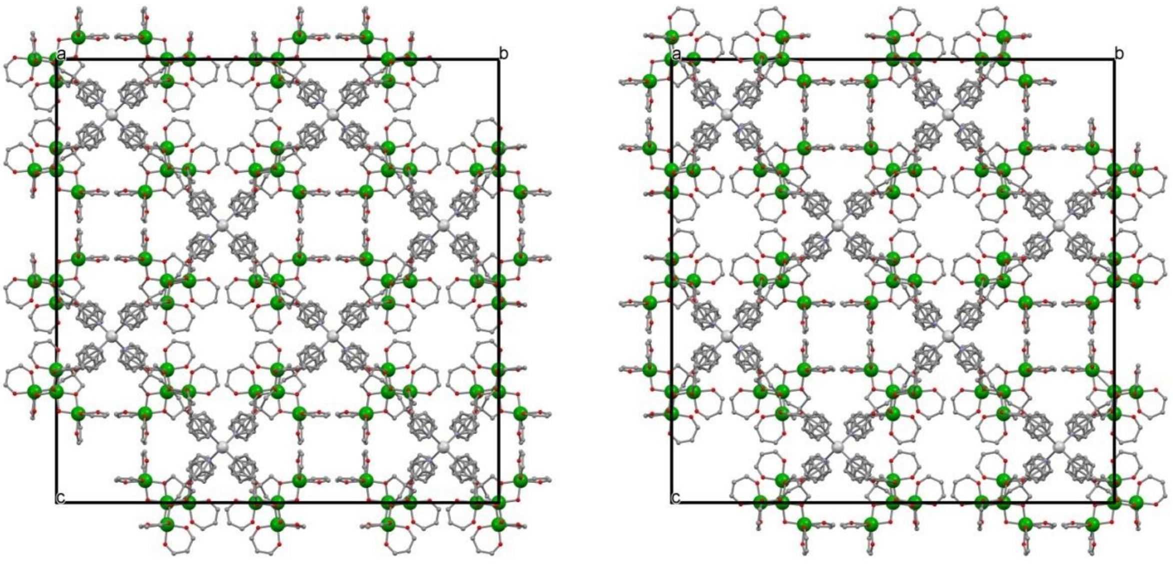

Fig. 8.4. Drawing of the unit cell of **Fe_4Ag** highlighting the two interlocked diamondoid lattices (colour code: Ag = grey, Fe = green, O = red, N = blue, C = grey, *t*Bu carbons, H atoms and ClO_4^- anions omitted for clarity).

Table 8.1 Crystal data and structure refinement parameters for **Fe$_4$Ag**.

Empirical formula	$C_{168}H_{268}AgClFe_8N_4O_{40}$	
Formula weight	3573.97	
Temperature	110(2) K	
Wavelength	1.54184 Å	
Crystal system	Cubic	
Space group	*Fd-3c*	
Unit cell dimensions	$a = b = c$ = 44.317(7) Å	$\alpha = \beta = \gamma$ = 90°
Volume	87037(4) Å^3	
Z	16	
Density (calculated)	1.091 g cm^{-3}	
Absorption coefficient	5.452 mm^{-1}	
Crystal size	0.34×0.32×0.28 mm^3	
Reflections collected	71804	
Independent reflections	2979 [R(int) = 0.0596]	
Completeness to theta = 63.44°	99.4 %	
Max. and min. transmission	0.9086 and 0.7760	
Refinement method	Full-matrix-block least-squares on F^2	
Data / restraints / parameters	71804 / 426 / 353	
Final R indices [$I>2\sigma(I)$]	R_1 = 0.0636, wR_2 = 0.1995	
R indices (all data)	R_1 = 0.0915, wR_2 = 0.2299	
Largest diff. peak and hole	0.318 and -0.189	
Goodness of fit	1.042	

8.4 Magnetic behaviour

8.4.1 dc measurements

The temperature dependence of the low field (1-10 kOe) molar magnetic susceptibility (χ_M) for a polycrystalline sample of **Fe$_4$Ag** was measured between 1.9 and 300 K (data are here given per Fe$_4$ cluster). The $\chi_M T$-vs-T curve, presented in Fig. 8.5, is typical for Fe$_4$ systems.[18,17] Antiferromagnetic nearest-neighbour interactions lead to a room-temperature $\chi_M T$ value lower than expected for four uncoupled high spin iron(III) ions ($\chi_M T$ = 12.29 emu K mol^{-1} vs. 17.51 emu K mol^{-1} for g = 2.00). Upon cooling, the $\chi_M T$ product first decreases, reaching a minimum (10.31 emu K mol^{-1}) at 120 K, and then increases again up to 13.93 emu K mol^{-1} at 12.5 K, in reasonable agreement with the selective population of an $S = 5$ ground state (expected value 15.00 emu K mol^{-1} with $g = 2.00$). Several factors may contribute to the final drop of $\chi_M T$ at the lowest T, including magnetic saturation, anisotropy effects or intermolecular interactions. Assuming three-fold molecular symmetry in a Heisenberg *plus* Zeeman spin Hamiltonian (Eq. 2.11), the best-fit values of J and J' so obtained are 16.41(6) and 0.035(36) cm^{-1}, respectively. The low temperature magnetic properties were better evaluated by measuring the field-dependent isothermal molar magnetization (M_M) at 1.9, 2.5 and 4.5 K. Data are plotted in the inset of Fig. 8.6 as M_M-vs-H/T to highlight the nesting of isothermal curves typically associated with magnetic anisotropy. These data were fitted using an axial zfs *plus* Zeeman Hamiltonian (Eq. 2.13) giving $D = -0.411(2)$ cm^{-1}. The exchange coupling constants and the D parameter are close to those found in **Fe$_4$pPy**·2EtOH (15.94(6) and –0.439(12) cm^{-1}).[19] The static magnetic behaviour of the Fe$_4$ units thus remains largely unaffected by their supramolecular organization.

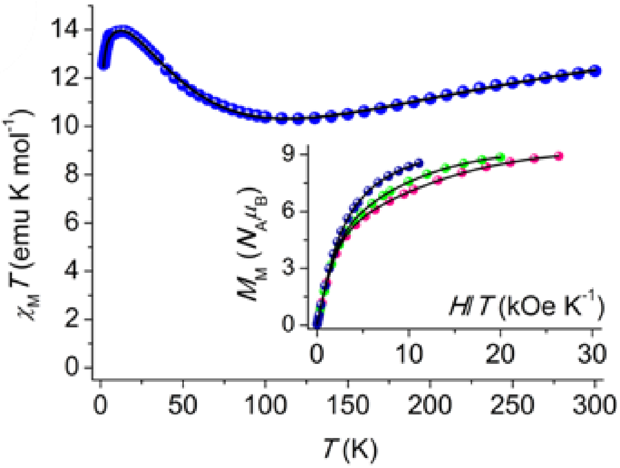

Fig. 8.5. a) Temperature dependence of the molar susceptibility (χ_M) multiplied by temperature (T) for **Fe$_4$Ag**; the inset shows the field dependence of the isothermal molar magnetization (M_M) at 1.9 (pink), 2.5 (green) and 4.5 (blue) K; black lines are calculated data using the best fit parameters (see text).

8.4.2 EPR spectra

In order to obtain independent information on magnetic anisotropy, a W-band ($\nu \approx 94$ GHz) EPR spectrum was recorded on microcrystalline powders of **Fe$_4$Ag** at 40 K by Dr. Lorenzo Sorace (Dipartimento di Chimica "Ugo Schiff", Università degli Studi di Firenze). The spectrum (Fig. 8.6) shows the typical features observed in several Fe$_4$ derivatives measured at this frequency.[59,62,71] Of particular relevance for the determination of the axial zfs parameter D is the low-field transition, assigned to the $M_S = -4 \rightarrow M_S = -3$ resonance.[62]

For a quantitative estimation of the anisotropy parameters we undertook spectral simulations[134] based on the following fourth-order spin Hamiltonian, which contains terms permitted by the crystallographic point-group symmetry of the Fe_4 units (D_3) but also allows for local deviation from axial symmetry:

$$\hat{H}_{EPR} = \mu_B \mathbf{B} \cdot \mathbf{g} \cdot \hat{\boldsymbol{S}} + D\hat{S}_z^2 + E\left(\hat{S}_x^2 - \hat{S}_y^2\right) + B_4^0 \hat{\boldsymbol{O}}_\mathbf{4}^\mathbf{0} + B_4^3 \hat{\boldsymbol{O}}_\mathbf{4}^\mathbf{3} \qquad (2)$$

Here, $\mathbf{g}$ is the Landé matrix, D and B_4^0 are the second- and fourth-order axial anisotropy parameters, respectively, E describes second-order transverse anisotropy, while B_4^3 accounts for transverse trigonal anisotropy.[135] A reasonable reproduction of the spectrum could be obtained with the following parameter set: $S = 5$, $D = -0.409(3)$ cm^{-1}, $E = 0$, $B_4^0 = +3(1) \times 10^{-5}$ cm^{-1}, $B_4^3 = +1.0(2) \times 10^{-3}$ cm^{-1}, $g_{x,y} = 1.992(2)$, $g_z = 2.005(2)$.

It is to be noted that the position of the highest field perpendicular transitions could only be reproduced assuming $E = 0$ and including a nonzero transverse trigonal term. At the same time, the large variation of linewidth across the spectrum hints to broad distributions (i.e. strains) of the parameters around the given average values. Correct spectral simulation required including strains $\sigma(D) = 0.03$ cm^{-1}, $\sigma(B_4^3) = 2.0 \times 10^{-3}$ cm^{-1} and $\sigma(E) = 0.05$ cm^{-1}. The latter should be exactly zero for an axial system, but local deviations from axial symmetry may be triggered by 4-pyridyl substituents and/or by *p*/*s* disorder (see above).

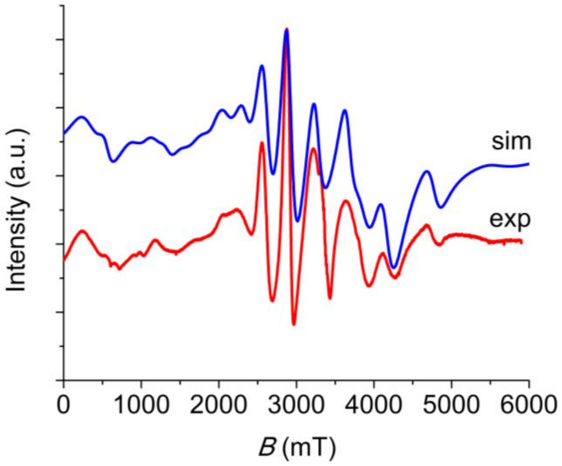

Fig. 8.6. W-band (ν = 94.3247 GHz) EPR spectrum of **Fe_4Ag** measured at 40 K, and simulation obtained using the best-fit parameters reported in the text.

8.4.3 ac magnetic measurements

To investigate the magnetization dynamics, the sample of **Fe_4Ag** used for dc measurements was subject to ac susceptibility studies in zero static field. The analysis was performed as a function of both temperature (down to 1.8 K) and frequency of the oscillating field (ν = 10 –

10000 Hz). χ_M''-vs-T plots indicate that **Fe$_4$Ag** behaves as a SMM like the parent compound **Fe$_4$pPy**·2EtOH (Fig 8.7, Fig 8.8, Fig 8.9).

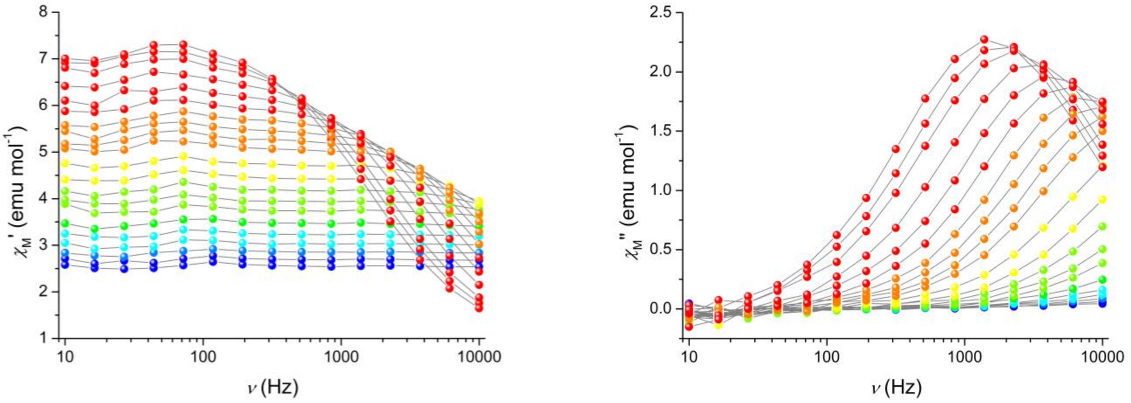

Fig. 8.7. Real (χ_M') and imaginary (χ_M'') components of the molar ac susceptibility of **Fe$_4$Ag** measured at zero applied static field in the 10-10000 Hz frequency range from 1.8 (red) to 5.5 (blue) K.

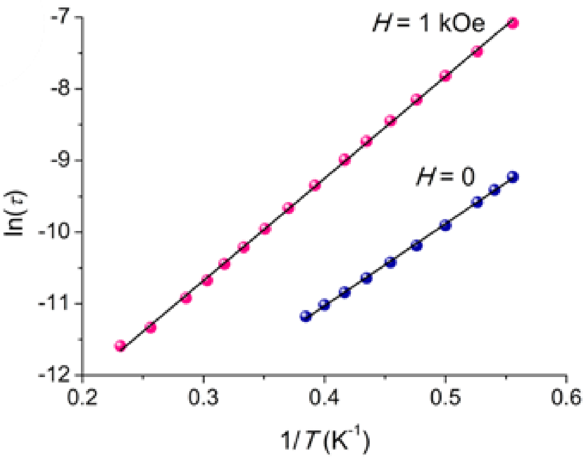

Fig. 8.8. Arrhenius plots of ln(τ) vs 1/T for compound **Fe$_4$Ag** obtained from ac susceptibility measurements at zero and 1 kOe applied static fields.

The values of ln(τ) obtained at both H = 0 and 1 kOe are plotted against 1/T in Fig. 8.8: in both cases, the linear trend indicates that a thermally activated relaxation process is operative in the explored temperature range. A fit of the data with Arrhenius law $\tau = \tau_0 \exp(U_{\mathrm{eff}}/k_B T)$ gave $\tau_0 = 1.65(8) \times 10^{-7}$ s and $U_{\mathrm{eff}}/k_B = 11.46(10)$ K in zero static field, and $\tau_0 = 3.21(11) \times 10^{-7}$ s, $U_{\mathrm{eff}}/k_B = 14.25(8)$ K at 1 kOe. With only a slightly less negative D value, **Fe$_4$Ag** has significantly lower effective relaxation barriers than **Fe$_4$pPy**·2EtOH at both H = 0 and 1 kOe, hinting to more effective QT processes. These may result from the greater rhombic distortion or from weak inter-SMM interactions.

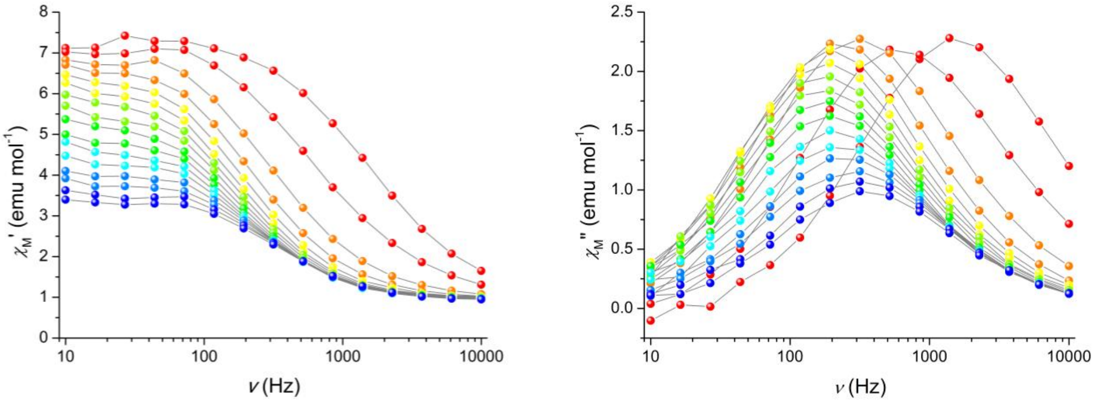

Fig. 8.9. Real (χ_M') and imaginary (χ_M'') components of the molar ac susceptibility of **Fe_4Ag** measured at 1.8 K in the 10-10000 Hz frequency range from 0 (red) to 3 (blue) kOe applied static field. Grey lines are a guide for the eye.

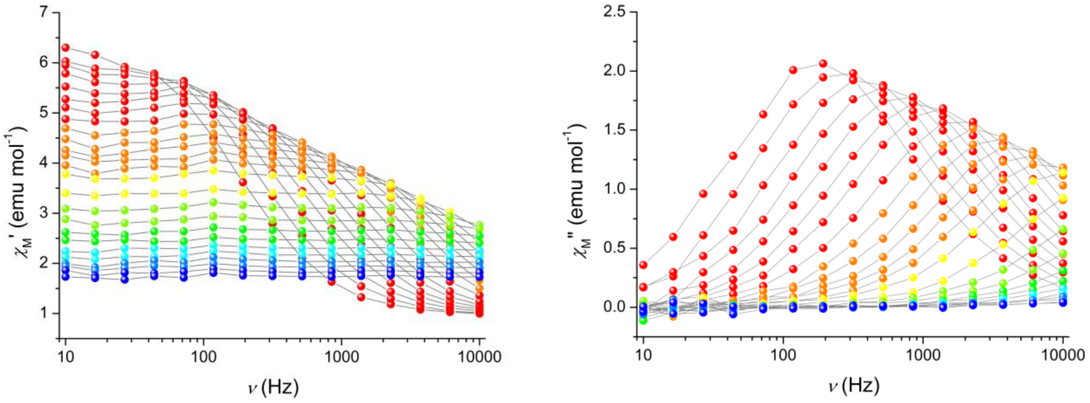

Fig. 8.10. Real (χ_M') and imaginary (χ_M'') components of the molar ac susceptibility of **Fe_4Ag** measured at 1 kOe applied static field in the 10-10000 Hz frequency range from 1.8 (red) to 8.0 (blue) K. Grey lines are a guide for the eye.

8.4.4 Torque magnetometry

To gain further insight into the magnitude, sign and orientation of molecular anisotropies in **Fe_4Ag**, a single-crystal investigation by CTM was performed by Dr. Mauro Perfetti (Dipartimento di Chimica “Ugo Schiff”, Università degli Studi di Firenze). A face-indexed single crystal of **Fe_4Ag** was mounted on a cantilever magnetometer and two rotations were carried out (hereafter referred to as **rot1** and **rot2**).[70] In all cases the torque response was measured along the rotation axis, whereas the magnetic field was applied normal to it. To understand how the two rotations were performed, it is convenient to focus on the four noncollinear Fe_4 units linked to the same Ag^+ ion (Fig. 8.11), as all the other molecules in the unit cell are magnetically equivalent to them. The rotation axis for **rot1** was one of the main diagonals of the cubic unit cell, i.e. the [111] direction, which corresponds to a C_3 axis in the structure (Fig. 8.11a). In **rot2** the rotation axis was one of the edges of unit cell, i.e. the [001] direction, which is parallel to an S_4 axis (Fig. 8.11b). The torque signal recorded at $T = 2$ K and variable field in **rot1** is presented in Fig. 8.11c. The observation of *three* oscillations in the angular range from 0° to 180° provides direct evidence of threefold magnetic symmetry around the rotation axis. In **rot1**, one Fe_4 unit (hereafter denoted as Fe_4-p) lies in the rotation plane and can be safely assumed to provide no contribution to the torque signal in this rotation. The three Fe_4 units related by the C_3 axis (Fe_4-t) provide noncollinear anisotropic contributions which may indeed afford threefold modulation, as long as two requirements are fulfilled. First, the magnetic centres must be only weakly-coupled or magnetically independent. Second, their magnetic response must show deviations from the relationship $\mathbf{M}_i = \boldsymbol{\chi}_i \cdot \mathbf{H}$, where $\boldsymbol{\chi}_i$ is the individual T-dependent magnetic susceptibility tensor. Otherwise, the overall magnetic response would also be tensorial in nature and isotropic in a plane orthogonal to a threefold or fourfold axis. This requires working at sufficiently low temperatures or in large applied fields, as firmly established by previous reports.[70,136,137]

Torque data recorded at $T = 2$ K and variable field in **rot2** (Fig. 8.11b) feature only two oscillations from 0° to 180°. In fact, pairs of Fe_4 units related by twofold rotation along the S_4 axis have coincident projections of their easy axes in the rotation plane and the torque response arises from just two noncollinear contributions.

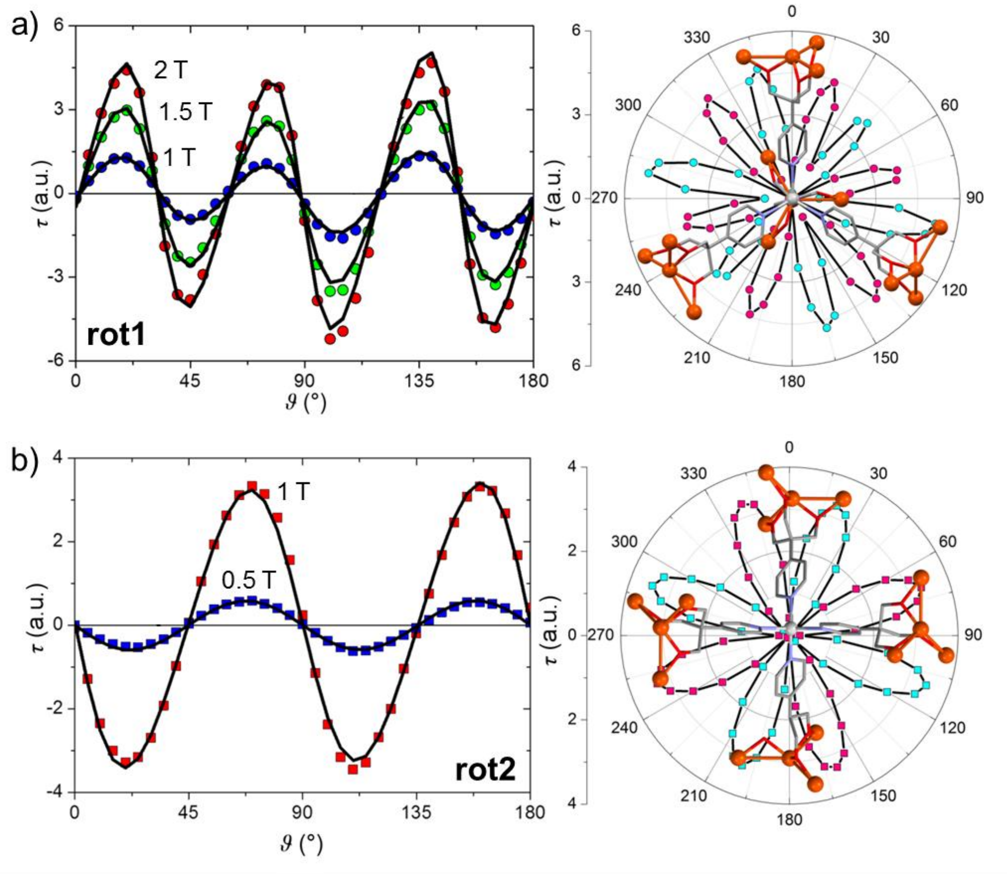

Fig. 8.11. Left panels: Torque signal of **Fe_4Ag** measured at T = 2 K and for different values of the applied field in a) **rot1** and b) **rot2**. The solid black curves provide the best fit to experimental data. Right panels: Polar plot of the absolute value of the torque at T = 2 K and B = 2 T (**rot1**) or B = 1 T (**rot2**) plotted on the molecular structure (pink: positive values, cyan: negative values).

For a quantitative treatment of the data, each Fe_4 unit was described using Eq. 2.13, taking S = 5, g = 2.00, and adjustable D. The four local easy axes z where oriented at 109.47° from each other, in compliance with the T symmetry arrangement found in the structure. The best fit was achieved with $D = -0.426(6)$ cm^{-1} (black lines in Fig. 8.12), in remarkably good agreement with dc magnetic measurements and EPR spectra.

In Fig. 8.12 I present the free magnetic energy (F) surfaces computed for the ensemble of four noncollinear Fe_4 units linked to the same Ag^+ ion. At 2 K and 20 kOe (Fig. 8.12a) F is minimum when the external field is applied along the unit cell axes ([001] and symmetry equivs.), which correspond to easy magnetic directions. Hard directions are found along [110] and symmetry equivs., whereas the main diagonals of the unit cell ([111] and symmetry equivs.) are intermediate magnetic axes for the crystal. As expected, when temperature is increased to 5 K and the applied field is lowered to 10 kOe (Fig. 8.12b) F shows a vastly reduced angular dependence. Fig. 8.12 illustrates in the clearest fashion the most salient magnetic feature of compound **Fe_4Ag**, which entails strongly anisotropic, high-spin units assembled into a highly symmetric cubic lattice with no second-order magnetic anisotropy.

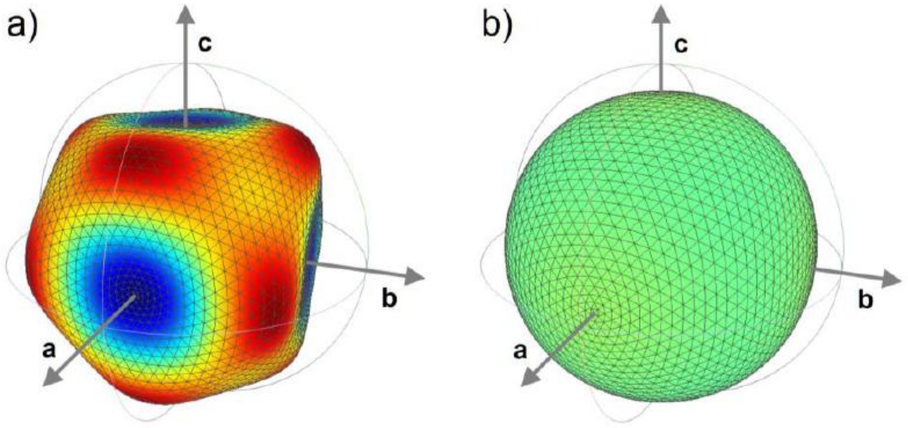

Fig. 8.12. Free magnetic energy F for the ensemble of four noncollinear Fe_4 units in **Fe_4Ag** as a function of applied field orientation, computed with $D = -0.42$ cm^{-1}, $g = 2.000$ and a) $T = 2$ K, $H = 20$ kOe or b) $T = 5$ K, $H = 10$ kOe. The distance of each point from the centre of each diagram is proportional to $F + F_0$, where F_0 is an offset used for a clearer representation. The angular dependence of F is also displayed using a colour scale (from blue to red). The F values in a) and b) span ca. 3.20 and 0.135 cm^{-1}, respectively.

8.4.5 MicroSQUID measurements

The magnetization of a single crystal of **Fe_4Ag** was recorded with the external magnetic field applied along the [111] direction of the cubic cell. With this orientation, **B** is directed parallel to the easy axis of one fourth of the Fe_4 units (Fe_4-p) but lies at 109.47° from the easy axes of the remaining molecules in the crystal (Fe_4-t). Raw magnetization data are strongly affected by such pronounced noncollinearity and display a constant slope with no tendency to saturate up to the highest explored fields (1.2 T). To allow a direct comparison with other Fe_4 systems, a linear contribution was subtracted. Raw and corrected data recorded at 0.03 K and variable field sweep rates are shown in Fig. 8.13.

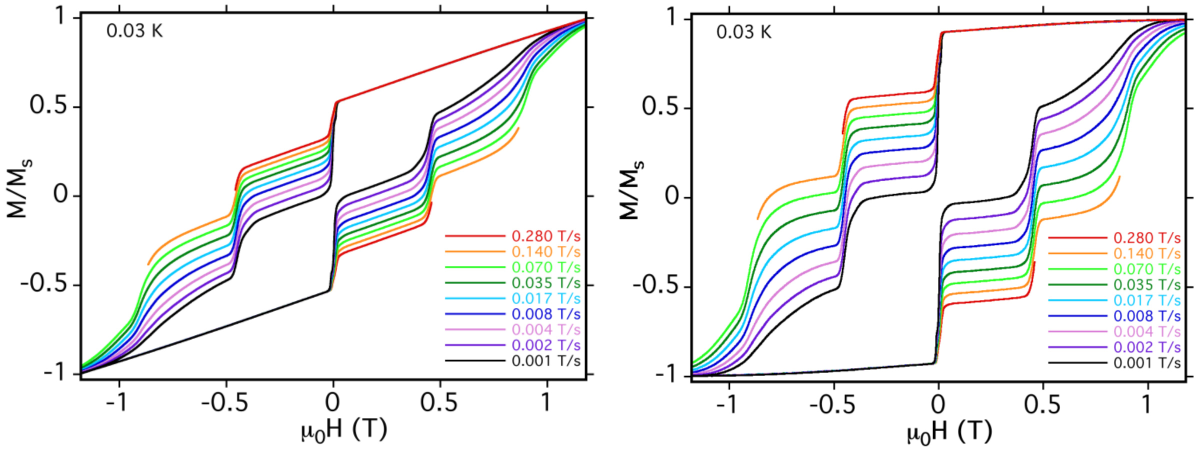

Fig. 8.13. Field-dependence of the magnetization at 0.03 K recorded on a single crystal of $\mathbf{Fe_4Ag}$ at variable field-sweep rate. M_s is the highest measured value of the magnetization. Both raw (left panel) and corrected (right panel) data are presented. The correction consists of subtracting a linear contribution to achieve a field-independent magnetization value in high fields. At the fastest field sweep rates curves are incomplete due to the occurrence of thermal avalanches, which reversed the entire magnetization in the timescale of milli-seconds.

Corrected data at 0.035 T s^{-1} and different temperatures are presented in Fig. 8.14a. Simple paramagnetic behaviour is detected above 1.0 K, while at lower temperatures a hysteresis loop opens, displaying increasing coercivity with decreasing temperature and increasing scan rate. The loop becomes temperature independent below 0.4 K, signalling that a purely QT regime is attained. As clearly outlined by the ln(τ)-vs-1/T plot in Fig 8.14b, the Arrhenius law typical of thermally-activated relaxation is obeyed in the 0.75–1.1 K range, with $U_{\mathrm{eff}}/k_{\mathrm{B}}$ = 11.8(3) K and τ_0 = 4.9(1.7) × 10^{-8} s, in good agreement with ac measurements. At lower temperature, however, the relaxation time approaches a temperature-independent value of ca. 20 s, a distinctive feature of spin relaxation via QT effects.

The steps in the recorded field dependence of the magnetization indicate sudden accelerations of spin reversal; the step positions are best evaluated from the first derivative of the curve recorded at 0.03 K for representative (positive) values of the scan rate (Fig. 8.14c). The peaks in dM/dB at B = 0, ±0.45, ±0.90 T can be readily explained starting from the Zeeman diagram for a $\mathrm{Fe_4}$ system probed by a magnetic field directed along its easy axis. Magnetic moment reversal through transition from $M_S = \pm 5$ to ∓ 5, ∓ 4, ∓ 3 etc. is expected to occur at integer multiples of $\pm|D|/(g\mu_{\mathrm{B}}) = \pm 0.45$ T for g = 2.000 and $D = -0.42$ cm^{-1}.

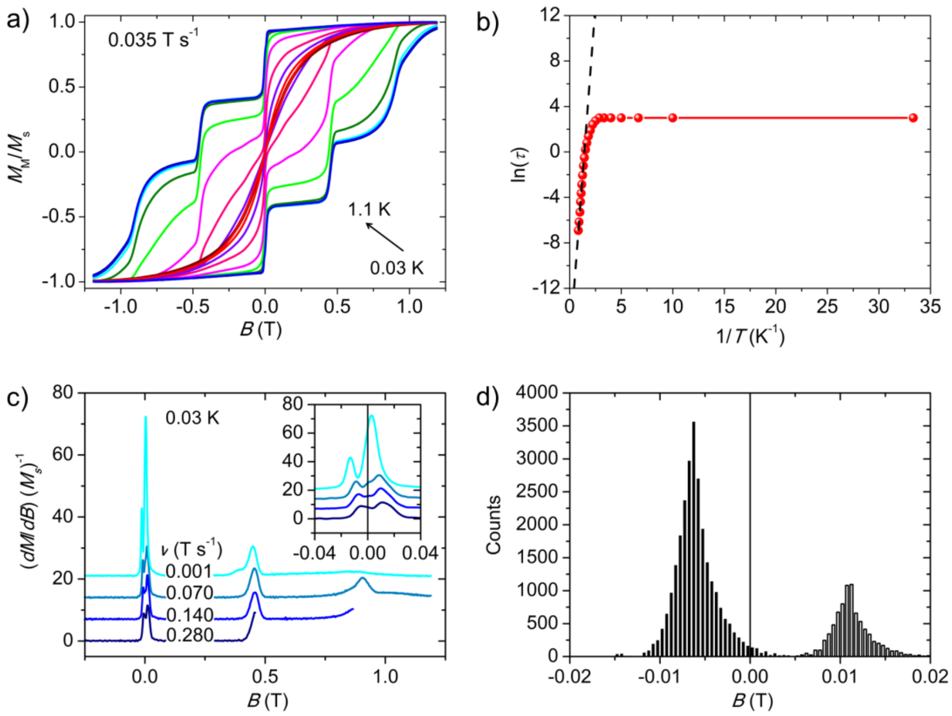

Fig. 8.14. a) Field-dependence of the magnetization M_M/M_s at variable temperature with 0.035 T s^{-1} sweep rate for **Fe$_4$Ag** after subtracting the contribution of the molecules transverse to the applied field (M_s is the saturation magnetization); b) ln(τ)-vs-1/T plot of the experimental data (red circles and line), together with the best linear fit curve using data in the 0.75–1.1 K range. c) first derivative of the lower-branch of hysteresis loops taken at 0.03 K and variable field sweep rates (at the fastest field sweep rates curves are incomplete due to the occurrence of thermal avalanches, which reversed the entire magnetization in the timescale of milli-seconds); d) calculated distribution of internal fields in a model cubic crystal of **Fe$_4$Ag** after magnetic saturation along [111]; a positive value indicates that the internal field is parallel to the crystal magnetization.

Looking in greater detail at the zero-field step, I found that it exhibits a fine structure consisting in two sub-steps whose positions are scan-rate dependent (inset of Fig. 8.14c). This behaviour suggests that Fe$_4$-p and Fe$_4$-t molecules may experience different magnetic bias due to internal fields originating from superexchange or dipolar interactions. The former imply overly long pathways through the 4-pyridyl substituents and the diamagnetic silver(I) ions, whereas dipolar fields can be significant even at long distances. As shown in Fig. 8.14d, the dipolar field distributions for Fe$_4$-p and Fe$_4$-t molecules are peaked at 10.9 and –6.4 mT, respectively. The two types of molecules experience dipolar fields of comparable magnitude but opposite in sign, being parallel and antiparallel to the crystal magnetization, respectively. The scenario is complicated by the fact that, as molecules start to reverse their magnetic moment, the distribution of internal fields changes, a phenomenon known as “dipolar shuffling”.[138]

8.5 Conclusion

In this chapter, I have described an attempt to link **Fe_4pPy** units into supramolecular structures using silver(I) ions. Instead of the expected chain-like arrangement, I isolated a 3D-MOF, **Fe_4Ag**, in which **Fe_4pPy** expectedly behaves as a 180°-ditopic supramolecular synthon, while silver(I) ions act as tetrahedral nodes rather than as linear linkers. A reproducible method for the synthesis and isolation of **Fe_4Ag** as big red single crystals was refined.

The nature of the crystals allowed their magnetic characterization with a whole spectrum of techniques, such as dc and ac magnetic measurements, EPR spectroscopy, CTM and microSQUID methods. The results coherently indicate that the Fe_4 units in **Fe_4Ag** maintain the same behaviour as in **Fe_4pPy**·2EtOH. However, the cubic crystal symmetry produces a unique scenario, with highly noncollinear magnetic anisotropy contributions directed along the axes of AgN_4 tetrahedra. By symmetry, the crystalline compound can then be persistently magnetized parallel or antiparallel to the four main diagonals of the unit cell, although crystals have no overall second-order anisotropy.[125]

As reasons for further interest, the 3D-MOF structure of **Fe_4Ag** and in particular the size of the cavities might be amenable of modification using suitable tripodal ligands. For instance, replacing the 4-pyridyl substituent with a 4-(pyridin-4-yl)phenyl group is expected to afford larger cavities. Host molecules in these cavities might be used to tune the magnetic properties of the framework or, more subtly, to add new functionalities to the compound, an appealing target for future studies.

Experimental Section

Reagents

All compounds were of reagent grade and were used without further purification, unless otherwise stated. Et_2O, from a freshly-opened can and pre-dried by stirring overnight with granular $CaCl_2$, was purified by refluxing over Na/benzophenone and distilled under N_2. MeOH was refluxed over $Mg(OMe)_2/I_2$ and distilled with protection against moisture, whilst EtOH was refluxed over $Mg(OEt)_2/I_2$, distilled with protection against moisture and stored over 3 Å molecular sieves[139]. Ferrocene (Fluka, 98%), *p*-nitrotoluene (Sigma Aldrich, 99%), formaldehyde (Sigma Aldrich, 37% water solution), KOH (Carlo Erba, ≥ 85%), H_2SO_4 (Carlo Erba, 96%), palladium on carbon (Sigma Aldrich, 10% wt. loading), $NaNO_2$ (Sigma Aldrich, ≥ 99%), NaOH (Carlo Erba, ≥ 99%), ethyl acetate (VWR, 98%), acetyl ferrocene (Aldrich, 95%), 4-picoline (Schuchardt, ≥ 98%), gallium(III) chloride (Aldrich, ≥ 99.9%), silver perchlorate (RdH, anhydrous), *n*-hexane (VWR, 95%), toluene (Fluka, 99.8%), $RuCl_3 \times H_2O$ (Sigma Aldrich, degree of hydration ≤1%), $AgBF_4$ (VWR, 98%), anhydrous DCM (VWR, max 10 ppm H_2O), anhydrous toluene (VWR, max 20 ppm H_2O), anhydrous THF (VWR, max 30 ppm H_2O), sublimed iron(III) chloride (Carlo Erba, 99%) and piperidine (Carlo Erba, 99%) were used as received.

$[Fe_2(OEt)_2(dpm)_4]$[16], **Fe_4std**,[28] $[Ru_2(OAc)_4(THF)_2](BF_4)$[100], $[Ru_2(OAc)_4(MeOH)_2]$[102] and [Ru(*p*-*t*BuTPP)(CO)][140] (**2**) were prepared as reported in the literature.

All operations for the synthesis of compounds **Fe_4Ru_2(II,II)**, **Fe_4Ru_2(II,III)**, **Ga_4Ru_2(II,II)** and **Ga_4Ru_2(II,III)** were carried out with strict exclusion of oxygen and moisture under nitrogen using an MBraun Unilab dry-box.

^1H NMR Spectra

^1H NMR spectra were recorded on a Bruker FT-DPX200 NMR spectrometer (200 MHz) or on a Bruker Biospin FT-NMR Avance 400 spectometer (400 MHz) at 303 K. Chemical shifts (δ) are expressed in ppm relative to $SiMe_4$ and coupling constant values (J) are in Hertz. Solvent residual signals: DCM-d_2 5.32 ppm, chloroform-d_3 7.26 ppm, benzene-d_6 7.16 ppm, toluene-d_8 2.08, 6.97, 7.01 and 7.09 ppm, MeOH-d_4 3.31 ppm.

Elemental analysis

Elemental analysis was performed using a Carlo Erba EA1110 CHNS-O automatic analyzer.

IR Analysis

Infrared spectra were recorded as KBr disks using a Jasco FTIR-4700 spectrophotometer with a 2 cm^{-1} resolution.

UV-vis spectroscopy

UV-vis characterization and oxidation studies of $(AcO)_3L^{Fc}$ and **Fe_4Fc** were performed with an UV-vis Lambda 650 (Perkin Elmer) spectrophotometer, operating in the spectral range between 200 and 1000 nm with quartz cuvettes.

MS MALDI ToF

MS MALDI ToF spectra were recorded using an Applied Biosystems/MDS SCIEX 4800 Plus MALDI ToF/ToF analyser equipped with a diode-pumped, solid-state Nd:YAG (355 nm) 200 Hz laser; samples **Fe_4pPy**·2EtOH**, Fe_4Ru_2(II,II)**, **Fe_4Ru_2(II,III)**, **Ga_4Ru_2(II,II)**, **Ga_4Ru_2(II,III)** and **Fe_4Ag** were prepared dissolving the compounds in THF.

Raman spectroscopy

The Raman spectra were recorded with a Labram Instrument (Jobin Yvon-Horiba) with laser radiation at 632.8 nm; the Rayleigh radiation was eliminated with an edge filter, and the Raman radiation was collected by a Charge-Coupled Devicen (CCD) detector (1024 × 256 × 16 pixels) cooled at −70 °C. The analysed spot was focused with the objective Olympus ×50, ×100, and then laser, properly attenuated in order to avoid possible alteration of the material, was applied. The spectra were recorded in backscattering on different crystals of the samples. The maximum power employed was 5 mW: with D0.6 filter the power became 1.3 mW while with D1 filter the power lowered to 0.6 mW. The recording time for good signal-to-noise ratio varied between 10 and 100 s, according to the intrinsic intensity of the radiation. Subsequently, Spekwin32 software was used for the elaboration of spectra.[141]

Single crystal X-ray diffraction

Single-crystal X-ray diffraction studies on **Fe_4Fc**, **Fe_4pPy**·2EtOH, and **Ga_4pPy**·EtOH were carried out using a four-circle Bruker X8-APEX diffractometer equipped with a Mo-Kα

generator (λ = 0.71073 Å), an area detector, and a Kryo-Flex cryostat for data collection at 120(2)K, and controlled by the Bruker-Nonius X8APEX software, used also for following data reduction and cell refinement. The structures were solved by direct methods using the SIR92 program[142]. Full matrix least-squares refinement on F_o^2 was performed with the SHELXL-97 program[143] and implemented in the WINGX v1.80.05 suite.[144] The program Mercury 3.8[145] was used for graphics.

Single-crystal X-ray diffraction studies on **Fe_4Ru_2(II,II)**, **Fe_4Ru_2(II,III)**, **Ga_4Ru_2(II,II)**, **Ga_4Ru_2(II,III)** and **2·Fe_4pPy·2** were carried out at the X-ray diffraction beamline of ELETTRA synchrotron, Trieste (Italy), on a Pilatus CCDC detector with a monochromatic wavelength of 0.70000 Å, and at 100(2) K by using a nitrogen stream cryo-cooler. Data reduction and cell refinement were carried out using the program XDS,[146] while MOSFLM[147] was used for **Fe_4Ru_2(II,III)**.

For **Fe_4Ag,** the X-ray structure determination was carried out with an Oxford Gemini S diffractometer equipped with Cu-Kα generator, area detector and liquid nitrogen cryostat. Crystals of the compound were embedded in an inert oil (Krytox®, GPL107) and a suitable one was selected under an optical microscope and mounted on a CryoLoop (Hampton Research, type: 20 micron and 0.2-0.3 mm diameter), with the CryoLoop fixed on a tiny glass needle.

Magnetic measurements

The magnetic properties of the synthesized compounds were studied in dc mode by Quantum Design MPMS SQUID magnetometer recording low-field $\chi_M T$-vs-T and isothermal M_M-vs-H data, (χ_M is defined as M_M/H). ac susceptibility data were recorded on a Quantum Design PPMS susceptometer. All data were recorded on grinded polycrystalline samples. Spin-Hamiltonian calculations were carried out using an in-house developed software based on ZHEEV routine[148] for matrix diagonalization and either MINUIT[149] or NAG Fortran Library E04FCF[150] routines for least-square fitting.

W-band EPR spectroscopy

W-band EPR spectra were recorded using a Bruker E600 continuous-wave spectrometer operating around 94 GHz, equipped with a split-coil superconducting magnet (Oxford

Instruments) and a continuous flow cryostat (Oxford CF 935), to achieve temperature variation. The samples **Ga_4Ru_2(II,III)** and **Fe_4Ag** were prepared by grinding microcrystalline powder and blocking it in wax to avoid preferential orientation.

MicroSQUID measurements

Magnetization measurements on single crystals of **Fe_4pPy**·2EtOH, **Fe_4Ru_2(II,II)** and **Fe_4Ru_2(II,III)** and **Fe_4Ag** were performed with an array of microSQUIDs.[151] This magnetometer works in the 0.04 – 7 K temperature range, in fields up to 14 kOe and with a time resolution of approximately 1 ms. The field can be applied in any direction of the microSQUID plane with a precision higher than 0.1° by separately driving three orthogonal coils. The field was aligned with the easy axis of magnetization using the transverse field method.[12] To ensure good thermalization, single crystals were fixed with Apiezon grease.

Torque magnetometry measurements

The torque measurements were performed using a two-leg CuBe cantilever and a capacitive detection (Andeen Hegerling Ultra Precision Capacitance Bridge). A crystal of **Fe_4Ag** (ca $0.5\times0.3\times0.2$ mm^3) with cubic habit was fixed on an acetate foil with vacuum grease and its faces were indexed by using an SCD Oxford Xcalibur3 diffractometer. The crystal was mounted with its (–1,1,0) face lying on the surface. For constructive reasons the rotation angle could only range from 0 to 200°, which however already provides redundant angular data due to the 180° periodicity expected for any paramagnetic system. At each temperature the rotation was performed also in zero field in order to correct data for the deflection due to the mass of the sample and of the cantilever. The torquemeter was always operated in the linear response regime but we made no attempt to extract absolute torque values from the measured capacitance variation, since samples in the microgram range would anyway be impossible to weigh with due accuracy. By consequence all torque data are given in arbitrary units (a.u.). Information on spin-Hamiltonian parameters was then extracted from the angle- and field-dependence of the torque signal using a home-made program written in FORTRAN 90. The diagonalization of the matrices was done using the ZHEEV subroutine[148] while least-squares fitting and error analysis were based on MINUIT subroutine.[149]

2-(4-nitrophenyl)-2-(hydroxymethyl)propane-1,3-diol

p-nitrotoluene (7.203 g, 52.23 mmol) and 37% aqueous formaldehyde (9.467 g, 315.3 mmol) were suspended in DMSO (40 mL) at 40 °C. KOH (0.304 g, 5.42 mmol) was added to the mixture and left at 40 °C for 20 h. The reaction was controlled by TLC on SiO_2 with DCM:MeOH 1:1 as eluent. After the mixture returned at room temperature, it was washed with saturated solution of NaCl (40 mL). The product was extracted with DCM (3 × 150 mL). The organic phases were washed with water and dried with $MgSO_4$. The solvent was removed under vacuum, and the obtained orange fluid was purified by SiO_2 column chromatography (from DCM:MeOH 10:1 up to 6:1) and crystalized from DMSO, obtaining the desired product as white crystals (6.5057 g, 54.5%).

^{1}H NMR (200 MHz, DMSO-*d*$_6$; 293 K) δ 3.74 (d, 6H, *J* = 4.99 Hz, –C*H*$_2$OH), 4.55 (t, 3H, *J* = 4.99 Hz, –O*H*), 7.68–7.75 (m, 2H, C*H*Ph), 8.10–8.17 (m, 2H, C*H*Ph) ppm.

2-(4-aminophenyl)-2-(hydroxymethyl)propane-1,3-diol

2-(4-nitrophenyl)-2-(hydroxymethyl)propane-1,3-diol (1.505 g, 6.624 mmol) and Pd/C catalyst (0.025 g) were added in EtOH (100 mL). The mixture was left overnight under stirring at room temperature at 2.8 atm of H_2. The mixture was then filtered and the solvent was removed under vacuum, giving a white powder (1.223 g, 93.1%).

^{1}H NMR (200 MHz, acetone-*d*$_6$; 293 K) δ 3.60 (t, 3H, *J* = 4.57 Hz, –O*H*), 3.93 (d, 6H, *J* = 4.57 Hz, –C*H*$_2$OH), 4.42 (br s, 2H, –N*H*$_2$), 6.52–6.65 (m, 2H, C*H*Ph), 7.12–7.23 (m, 2H, C*H*Ph) ppm.

2(hydroxymethyl)-2-(4-(ferrocene)phenyl)propane-1,3-diol (H_3L^{Fc})[152]

A mixture of ferrocene (1.182 g, 6.35 mmol) in and H_2SO_4 96% (1.4 mL) in water (5.6 mL) at 0 °C was left standing overnight. The solution changed colour from orange to dark blue. $NaNO_2$ (0.226 g, 3.27 mmol) was then added into the mixture. After, 2-(4-aminophenyl)-2-(hydroxymethyl)propane-1,3-diol (54.0 mg, 2.74 mmol) was dissolved into H_2SO_4 (1.8 mL) and water (5.2 mL); this solution was added very slowly to the first one kept at 0 °C. After one hour, NaOH was added until the complete neutralization of the solution acidity. The product is then extracted with ethyl acetate (5 × 130 mL), the solvent removed under vacuum, washed with *n*-hexane, filtered on Gooch G3 and dried under vacuum. The ligand is purified by SiO_2 column chromatography starting with eluent DCM:MeOH 10:1 up to 5:1 (0.377 g, 366.24 g/mol, 35.3%).

^1H NMR (200 MHz, DMSO-d_6; 293 K) δ 3.74 (d, 6H, J = 3.77 Hz, –CH_2OH), 4.02 (s, 5H, unsubstituted Cp ring), 4.30 (t, 2H, *3*-C*H* substituted Cp ring), 4.38 (t, 3H, -O*H*), 4.69 (t, 2H, 2-C*H* substituted Cp ring), 7.38 (dd, 4H, m, p-C*H*Ph) ppm.

$[Fe_4(L^{Fc})_2(dpm)_6]$ (Fe_4Fc)

Fe_4std (0.180 g, 0.120 mmol) was dissolved in diethyl ether (60 mL) and then H_3L^{Fc} (0.120 g, 0.327 mmol) was added as solid and the mixture was left stirred for 5 h 30'. The solution was filtered on Gooch G4 and left in vapour diffusion with MeOH (120 mL) affording big red crystals suitable for X-ray diffraction in two weeks, which were filtered and washed with MeOH (0.090 mg, 37%).

Elemental analysis (%) calcd for $C_{106}H_{152}Fe_6N_2O_{18}$ (2049.19): C, 61.25, H, 7.38, N, 1.35; found: C, 61.58; H, 7.55; N, 1.25.

^1H NMR (200 MHz, CD_2Cl_2, 293 K) δ 4.21 (s, 10H, unsubstituted Cp ring), 4.49 (br s, 8H, substituted Cp ring), 10.35 (br s, 108H, ^{t}Bu-*H*), 12.11 (br s, 4H, m-C*H*Ph) ppm.

Molecular structure

The cluster **Fe_4Fc** crystallizes in the monoclinic *P*21/*n* space group. The structure refinement was solved by direct methods using the SIR92 program,[142] Full matrix least-squares refinement on F_o^2 was performed with the SHELXL-97 program[143] and implemented in the WINGX v1.80.05 suite.[144] The asymmetric unit is formed by one molecule: no disordered ^{t}Bu group was found. All non-hydrogen atoms were refined anisotropically. The hydrogen atoms were added in idealized positions and assigned isotropic displacement parameters constrained to those of the attached carbon atoms.

Acetylferrocenium tetrafluoroborate ($[Fe(\eta\text{-}C_5H_4COMe)Cp][BF_4]$)

The product was prepared as described in the review by Connely and Geiger[92]: solid $AgBF_4$ (0.142 g, 0.717 mmol) was added to a stirred solution of acetylferrocene (0.173 g, 0.761 mmol) in Et_2O (60 mL) at room temperature. After 30' the blue-green reaction mixture was evaporated to dryness under vacuum, and the residue was extracted with DCM (40 mL).

After filtration through celite, the volume of the dark blue extract was reduced to *ca*. 3 mL and Et_2O (40 mL) was added. The dark blue/green precipitate was then further purified from DCM/Et_2O to give dark blue microcrystals (0.146 g, 64.7%).

^1H NMR (200 MHz, CD_2Cl_2, 293 K). δ 4.80 (t, 2H, *o*-H substituted Cp ring), 4.50 (t, 2H, *m*-H substituted Cp ring), 4.19 (s, 5H, unsubstituted Cp ring), 2.4 ppm (s, 3H, CH_3 acetyl group) ppm.

2-(Hydroxymethyl)-2-(pyridin-4-yl)-1,3-propanediol (H_3L^{pPy})

The product was synthesised as reported by Menozzi et al.[95] 4-picoline (2.00 mL, 20.0 mmol) was refluxed in 37% aqueous formaldehyde (27.0 mL, 354 mmol) for 18 h and the reaction was followed by TLC on silica, with DCM:MeOH 8:1 (r.f. 4-picoline = 0.77, r.f. product = 0.12), until disappearing of the 4-picoline spot. The solvent and excess of formaldehyde were removed under reduced pressure and heating at 50 °C. MeOH (50 mL) was added to the residue and removed under vacuum at 50 °C, and the procedure was repeated twice. The liquid crude product was subjected to prolonged vacuum pumping (1 mmHg, 9 h, 50 °C), and purified by SiO_2 column chromatography (DCM:MeOH 3.7:1) to afford the desired compound as a white powder (2.292 g, 62.55%). The product can be further recrystallized from hot MeOH, obtaining colourless crystals (1.861 g, 50.79%).

Elemental analysis (%) calcd for $C_9H_{13}NO_3$ (183.22): C, 59.00; H, 7.15; N, 7.65; found: C, 58.64, H, 7.03, N, 7.58.

^1H NMR (400 MHz, CD_3OD, 293 K) δ 8.45 (d, *J* = 4.8 Hz, 2H, *o*-H), 7.54 (dd, *J* = 4.8 Hz *o*-H, *J'* = 1.6 Hz (2H, *m*-H), 3.93 (s, 6H, CH_2) ppm.

$[Fe_4(L^{pPy})_2(dpm)_6]\cdot 2EtOH$ ($Fe_4pPy\cdot 2EtOH$).

$[Fe_2(OEt)_2(dpm)_4]$ (300.8 mg, 0.3217 mmol) was dissolved in Et_2O:EtOH 4:1 (40 mL) yielding an orange solution. Sublimed $FeCl_3$ (34.8 mg, 0.215 mmol) was added giving a red solution, followed by piperidine (77.0 µL, 0.779 mmol), yielding a white precipitate and a colour change back to orange. Finally solid H_3L^{pPy} (157.8 mg, 0.8614 mmol) was added and the mixture was stirred for 90'. The precipitate was removed by Gooch filtration (G3), and slow vapour diffusion of EtOH (75 mL) into the filtrate gave red cm-sized rod-like crystals in one week (279.5 mg, 73.22%).

Elemental analysis (%) calcd for $C_{88}H_{146}Fe_4N_2O_{20}$ (1775.48): C 59.53, H 8.29, N 1.58, Fe 12.58; found: C 59.48, H 8.08, N 1.77, Fe 12.66.[153]

IR (KBr): 2963 ν(C–H*t*Bu) (s), 1593 (vs), 1577 (vs), 1565 (vs), 1550 (vs), 1538 (vs), 1506 ν(C=Odpm, C=NpPy) (vs), 1401 (vs), 1384 (vs), 1357 $\delta(CH_3)$ (vs), 1105 ν(C–OpPy) (m), 560 δ(py) (s) cm^{-1}.

^1H NMR (200 MHz, CD_2Cl_2, 293 K): δ 10.9 (br, 108H; ^{t}Bu), 13.1 (br, 4H; ar), 3.67 (q, 4H; CH_2 EtOH), 1.26 (s, 2H; OH EtOH), 1.20 (t, 6H; CH_3 EtOH) ppm; ^1H NMR (200 MHz, toluene-d_8, 293 K): δ 13.0 (br, 4H; Ar), 10.5 (br, 108H; ^{t}Bu), 3.31 (q, 4H; CH_2 EtOH), 0.94 (t, 6H; CH_3 EtOH) ppm. MALDI ToF (THF): *m/z* (%) 1705.73 (8) $[Fe_4(pPy)_2(dpm)_6 + Na^+]$, 1499.59 (7) $[Fe_4(pPy)_2(dpm)_5{}^+]$, 1316.44 (30) $[Fe_4(pPy)_2(dpm)_4)^+]$, 422.17 (100) $[Fe(dpm)_2{}^+]$.

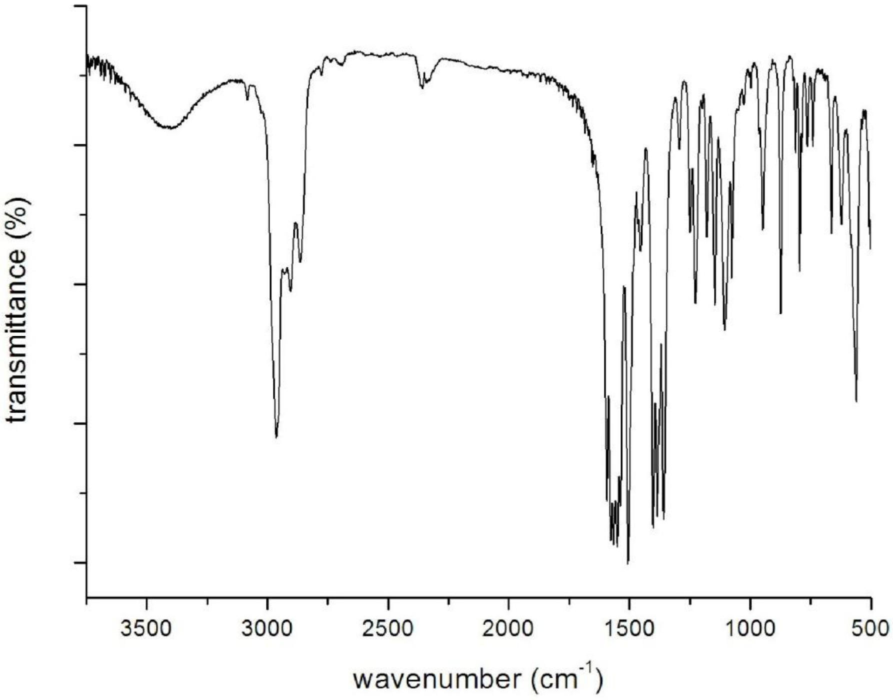

Fig. E1. Infrared spectrum as KBr disk of **Fe₄pPy**·2EtOH

Molecular structure

The cluster **Fe₄pPy**·2EtOH crystallizes in the monoclinic *C*2/*c* space group. The structure refinement was solved by direct methods using the SIR92 program,[142] Full matrix least-squares refinement on $F_o{}^2$ was performed with the SHELXL-97 program[143] and implemented in the WINGX v1.80.05 suite.[144] The asymmetric unit is formed by half molecule: a disordered ^{t}Bu group (C18–C21) could be resolved into two positions that were refined with complementary occupancy factors of 0.489(7) and 0.511(7); the two parts were further restrained to have the same geometry (within 0.02 Å both for 1,2- and 1,3-distances) and quaternary carbons with identical Anisotropic Displacements Parameters (ADPs). The 4-pyridyl ring of the tripodal ligand was also found disordered over two positions (A and B) that were refined with complementary occupancy factors [0.682(3) and 0.318(3)]. The majority part was restrained to be flat within 0.1 $Å^3$ and to approximate isotropic behaviour within 0.02 $Å^2$, with similar ADPs for the *ortho* and *meta* carbons (within 0.01 Å). The minority part was forced to have the same geometry as part A within 0.05 and 0.1 Å for 1,2- and 1,3-distances, respectively, and was treated with a common isotropic thermal parameter. The atoms of the ethanol molecule were refined with a common isotropic thermal parameter and with C–O and C–C distances restrained to realistic values. In the final model, the $N^{py}\cdots O^{EtOH}$ distances range from 2.87(2) to 3.27(1) Å. All non-hydrogen atoms were refined anisotropically, unless otherwise previously noted. The hydrogen atoms were added in idealized positions and assigned isotropic displacement parameters constrained to those of the attached carbon atoms, while hydroxyl H atoms were treated using AFIX 143 instruction. Selected bond distances (Å), angles (°) and other relevant geometrical parameters for **Fe_4pPy**·2EtOH are shown in Table E1.

Magnetic measurements

Magnetic susceptibilities were measured on 23.76 mg crystalline samples of **Fe_4pPy**·2EtOH, packed in a Teflon pellet. Magnetic susceptibility was measured from 1.9 to 300 K with applied fields of 1 kOe below 40 K and of 10 kOe above that temperature. Isothermal magnetization curves were registered up to 50 kOe at 1.9, 2.5 and 4.5 K. Data reductions were carried out subtracting the sample holder and addenda contributions, using 1775.48 as molecular weights and -1025.02×10^{-6} as diamagnetic corrections, estimated from Pascal's constants.[154] Alternating current (ac) susceptibility data were recorded on the same sample. In-field measurements were carried out at 1 kOe, after inspection of the field-dependent ac susceptibility at 1.9 K.

$[Fe_4(pPy)_2(dpm)_6][Ru_2(OAc)_4]$ (Fe_4Ru_2(II,II))

A light brown solution of $[Ru_2(OAc)_4(MeOH)_2]$ (50 mg, 0.099 mmol) in anhydrous THF (20 mL) was layered over a red solution of **Fe_4pPy**·2EtOH (168 mg, 0.0946 mmol) in anhydrous

DCM (20 mL) with a 2-mL layer of clean DCM in between, and left to liquid diffusion for ten days. Tiny red crystals of the title compound formed, that can be isolated, washed with *n*-hexane and dried. In order to preserve the crystallinity, the compound has to be kept in its mother liquor or into grease.

Elemental analysis (%) calcd for $C_{92}H_{146}Fe_4N_2O_{26}Ru_2$ (2121.66): C, 52.08; H, 6.94; N, 1.32. Found for dried sample: C, 51.79; H, 7.05; N, 1.40.

IR (KBr): 2960 $\nu(C{-}H_{tBu})$, 1592, 1576, 1564, 1549, 1505 $\nu(C{=}O_{dpm}, C{=}N_{py})$, 1433 $\nu(C{=}O_{AcO})$, 1401, 1385, 1357 $\nu(CH_3)$, 1106 $\nu(C{-}O_{pPy})$, 689 δ(AcO), 565 δ(py) cm^{-1}.

MALDI ToF (THF): *m/z* 2122.52 ($[M]^+$, 5%), 1721.58 ($[Fe_4(pPy)_2(dpm)_6 + K]^+$, 2), 1705.61 ($[Fe_4(pPy)_2(dpm)_6 + Na]^+$, 2), 1499.49 ($[Fe_4(pPy)_2(dpm)_5)]^+$, 30), 1316.34 ($[Fe_4(pPy)_2(dpm)_4)]^+$, 90), 439.79 ($[Ru_2(OAc)_4]^+$, 40), 422.16 ($[Fe(dpm)_2]^+$, 100).

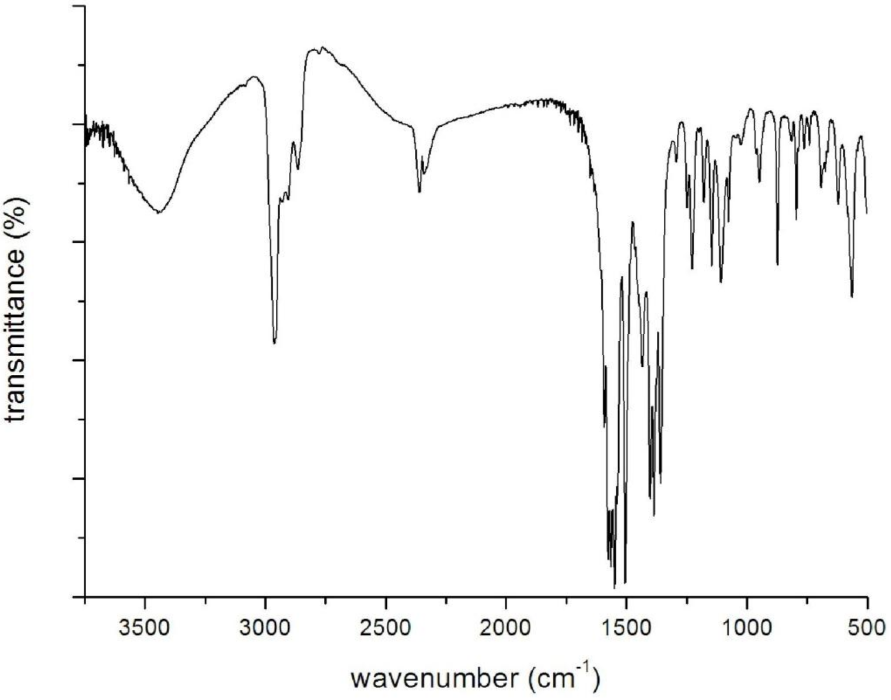

Fig. E2. IR spectrum as KBr disk of **Fe_4Ru_2(II,II)**

Structural Characterization

Crystal XRD on **Fe_4Ru_2(II,II)** was carried out at 100(2) K at ELETTRA synchrotron; the data collection was reduced with XDS and the structure was solved using SIR92[142] and SHELXL2014[155] programs implemented in the WINGX v2013.3 suite.[144] The first type of disorder present in the molecular structure is related to the 4-pyridyl ring, which rotate along chain axis. Two positions were found, with occupancy factor of 0.743 for the first ring and 0.257 for the second. The second type of disorder concerns the two entire DCM molecules, which was refined with a free variable with 0.510 occupancy factor for the first molecule and 0.374 for the second.

Because the different components have extensively overlapping *t*Bu's, dpm$^-$ ligands were refined as rigid groups: DFIX and SADI restraints were introduced on 1,2 and 1,3 distances for the first ^{t}Bu group. In the second step, SAME restraints were used to refined the other ^{t}Bu group. The THF molecule was located near pyridyl group (the short distance N_{py}-C_{THF} is 3.723 Å). All non-hydrogen atoms were refined anisotropically, unless otherwise noted, while hydrogen atoms were added in idealized positions, allowed to ride on the parent carbon atoms and treated isotropically with $U(H) = 1.2U_{eq}(C)$ for methylene, methine and aromatic hydrogens and $U(H) = 1.5U_{eq}(C)$ for methyl hydrogens.

The data set was treated with the command SQUEEZE of the PLATON program.[156] The unit cell contains 7394 Å^3 (46.59%) of solvent-accessible voids and an electron count per unit cell of 1916.

$[Fe_4(pPy)_2(dpm)_6][Ru_2(OAc)_4](BF_4)$ (Fe_4Ru_2(II,III)) *Method a*

Fe_4pPy·2EtOH (101 mg, 0.0569 mmol) and $[Ru_2(OAc)_4(THF)_2](BF_4)$ (40 mg, 0.060 mmol) were dissolved in anhydrous THF (20 and 12 mL, respectively) and mixed together. Slow vapor diffusion of anhydrous toluene (42 mL) gave the title compound as tiny red/brown crystals, which were extensively washed with anhydrous DCM till colorless washing (97.5 mg, 77.6%). Elemental analysis (%) calcd for $C_{92}H_{146}BF_4Fe_4N_2O_{26}Ru_2$ (2208.47): C, 50.03; H, 6.66; N, 1.27. Found: C, 49.69; H, 6.92; N, 1.41.

IR (KBr): 2964 $\nu(C{-}H_{tBu})$, 1592, 1576, 1564, 1549, 1538, 1505 $\nu(C{=}O_{dpm}, C{=}N_{py})$, 1444 $\nu(C{=}O_{AcO})$, 1401, 1385, 1357 $\nu(CH_3)$, 1107 $\nu(C{-}O_{pPy})$, 1084 $\nu(BF_4)$, 691 δ(AcO), 564 δ(py) cm^{-1}.

MALDI ToF (THF): *m/z* 2122.41 ($[M - BF_4]^+$, 5%), 1499.41 ($[Fe_4(pPy)_2(dpm)_5)]^+$, 20), 1316.28 ($[Fe_4(pPy)_2(dpm)_4)]^+$, 30), 438.81 ($[Ru_2(OAc)_4]^+$, 40), 422.15 ($[Fe(dpm)_2]^+$, 100).

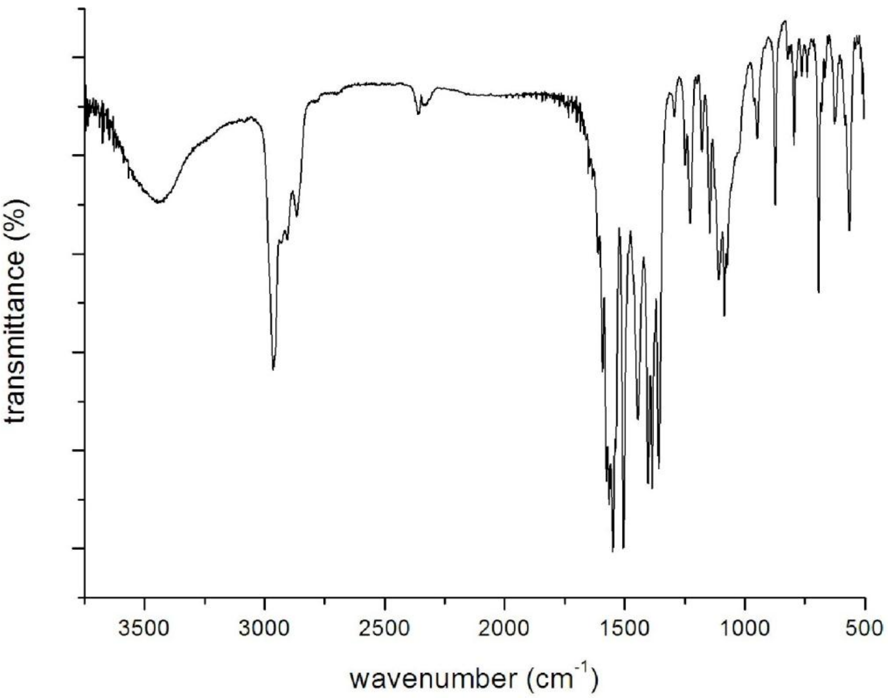

Fig. E2. IR spectrum as KBr disk of **Fe_4Ru_2(II,III)**

Structural characterization

Crystal XRD on **Fe_4Ru_2(II,III)** was carried out at 100(2) K at ELETTRA synchrotron. Due to the low crystallinity and the large thermal parameters, the oxygen atoms of all dpm$^-$ and AcO$^-$ ligands had to be restrained to approximate isotropic behaviour within 0.02 Å^2. Similar restraints, with standard deviations of 0.002–0.03 Å^2, had to be applied to most carbon and nitrogen atoms. One ^{t}Bu group (C61–C64) was found disordered over two positions [occupancy 0.516(15) and 0.484(15)] that were refined with common isotropic thermal parameters for the quaternary and methyl C atoms. Geometrical restraints were applied to few ^{t}Bu groups (including the disordered one) based on *tert*butyl C153–C156 as a reference (standard deviations: 0.02 and 0.04 Å for 1,2- and 1,3-distances, respectively). All non-hydrogen atoms were refined anisotropically, unless otherwise previously noted. Hydrogen atoms were added in idealized positions and assigned isotropic displacement parameters constrained to those of the attached carbon atoms. Of the two BF_4^- anions, one displays full occupancy and was refined by imposing similar B–F and F–F separations (within 0.02 and 0.03 Å, respectively). Its fluorine atoms were restrained to approximate isotropic behaviour (within 0.02 Å^2) and to have similar ADPs to the B atom (within 0.01 Å^2). The second BF_4^- anion was found disordered over two equally populated positions. They were refined with common isotropic displacement parameters for F atoms and with geometry restrained to that of the full-occupancy anion within 0.01 Å and 0.02 Å for 1,2- and 1,3-distances, respectively. Finally, the same isotropic displacement parameter was used for all B atoms. Flack parameter indicated a virtually perfect racemic twinning, and the twin fraction was then treated as least squares parameter through TWIN and BASF instructions.

Table E1. Selected distances (Å) and angles (°) for compounds **Fe$_4$pPy**·2EtOH and **Fe$_4$Ru$_2$(II,III)**, together with other relevant geometrical parameters.

Fe4pPy·2EtOH		**Fe4Ru2(II,III)**			
		chain A		chain B	
Fe1–O1	1.9850(17)	Fe1–O1	1.949(7)	Fe5–O27	1.938(6)
Fe1–O2	1.9635(16)	Fe1–O2	1.963(7)	Fe5–O28	1.976(6)
Fe1–O3	1.9921(16)	Fe1–O3	1.973(7)	Fe5–O29	1.988(8)
		Fe1–O4	2.014(7)	Fe5–O30	2.002(6)
		Fe1–O5	1.988(7)	Fe5–O31	2.000(7)
		Fe1–O6	1.950(6)	Fe5–O32	1.945(7)
Fe2–O1	1.9823(18)	Fe2–O1	2.004(6)	Fe6–O27	1.986(6)
		Fe2–O4	1.979(6)	Fe6–O30	1.990(6)
Fe2–O4	1.9942(18)	Fe2–O7	1.981(8)	Fe6–O33	1.996(8)
Fe2–O5	2.0281(17)	Fe2–O8	2.014(7)	Fe6–O34	1.986(7)
		Fe2–O9	1.970(7)	Fe6–O35	2.016(8)
		Fe2–O10	1.981(7)	Fe6–O36	1.991(7)
Fe3–O2	1.9908(16)	Fe3–O2	1.939(7)	Fe7–O28	1.974(7)
Fe3–O3	1.9806(17)	Fe3–O5	2.007(7)	Fe7–O31	1.985(6)
Fe3–O6	1.9965(18)	Fe3–O11	1.995(8)	Fe7–O37	1.977(7)
Fe3–O7	1.9879(17)	Fe3–O12	1.997(8)	Fe7–O38	2.006(8)
Fe3–O8	2.0011(17)	Fe3–O13	1.978(8)	Fe7–O39	2.011(7)
Fe3–O9	1.9931(18)	Fe3–O14	1.991(9)	Fe7–O40	2.006(8)
		Fe4–O3	1.982(7)	Fe8–O29	1.966(7)
		Fe4–O6	1.998(7)	Fe8–O32	2.013(7)
		Fe4–O15	2.033(8)	Fe8–O41	2.015(7)
		Fe4–O16	1.966(7)	Fe8–O42	2.016(7)
		Fe4–O17	1.954(8)	Fe8–O43	2.020(7)
		Fe4–O18	2.005(8)	Fe8–O44	1.996(8)
Fe1···Fe2	3.0927(7)	Fe1···Fe2	3.107(2)	Fe5···Fe6	3.105(2)
Fe1···Fe3	3.0854(4)	Fe1···Fe3	3.125(2)	Fe5···Fe7	3.100(2)
		Fe1···Fe4	3.079(3)	Fe5···Fe8	3.110(3)
Fe2···Fe3	5.3292(6)	Fe2···Fe3	5.361(2)	Fe6···Fe7	5.384(2)
Fe3···Fe3’ [a]	5.3854(5)	Fe3···Fe4	5.332(4)	Fe7···Fe8	5.460(4)
		Fe4···Fe2	5.430(3)	Fe8···Fe6	5.286(2)
		Fe1···Ru1	9.551(4)	Fe5···Ru3	9.578(4)
		Fe1···Ru2	9.608(4)	Fe5···Ru4	9.580(4)
		Ru1–O19	1.991(9)	Ru3–O45	2.020(8)
		Ru1–O21	2.040(6)	Ru3–O47	2.036(7)

		Ru1–O23	2.026(9)	Ru3–O49	2.036(7)
		Ru1–O25	1.998(7)	Ru3–O51	2.035(6)
		Ru1–N1	2.300(9)	Ru3–N3	2.260(10)
		Ru2–O20	2.023(8)	Ru4–O46	2.019(8)
		Ru2–O22	2.020(6)	Ru4–O48	2.015(7)
		Ru2–O24	2.036(8)	Ru4–O50	2.008(8)
		Ru2–O26	2.007(7)	Ru4–O52	2.013(6)
		Ru2–N2	2.279(10)	Ru4–N4	2.284(8)
		Ru1–Ru2	2.2751(10)	Ru3–Ru4	2.2735(11)
Fe1–O1–Fe2	102.44(8)	Fe1–O1–Fe2	103.6(3)	Fe5–O27–Fe6	104.6(3)
Fe1–O2–Fe3	102.57(8)	Fe1–O4–Fe2	102.2(3)	Fe5–O30–Fe6	102.1(3)
Fe1–O3–Fe3	101.91(7)	Fe1–O2–Fe3	106.4(3)	Fe5–O28–Fe7	103.4(3)
		Fe1–O5–Fe3	102.9(3)	Fe5–O31–Fe7	102.2(3)
		Fe1–O3–Fe4	102.3(3)	Fe5–O29–Fe8	103.7(3)
		Fe1–O6–Fe4	102.5(3)	Fe5–O32–Fe8	103.6(3)
Helical pitches [b]					
‘Fe2’	68.29(6)	‘Fe2’	68.16(20)	‘Fe6’	73.35(25)
‘Fe3’	68.90(5)	‘Fe3’	69.86(24)	‘Fe7’	70.01(19)
		‘Fe4’	68.24(23)	‘Fe8’	71.12(21)

[a] Fe3’ is related to Fe3 by the twofold axis directed along *b*; [b] only the peripheral iron ion Fe^p is reported as abbreviation of the Fe^{c}O$_2$Fe^p plane, where Fe^c is Fe1 for **Fe$_4$pPy**·2EtOH and chain A of **Fe$_4$Ru$_2$(II,III)**, and Fe5 for chain B of **Fe$_4$Ru$_2$(II,III)**.

Magnetic measurements

Dc and ac susceptibility data were recorded on 6.27 and 12.50 mg crystalline samples of **Fe$_4$Ru$_2$(II,II)** and **Fe$_4$Ru$_2$(II,III)** obtained with *Method a*, respectively; in-field measurements were carried out at 1 kOe, after inspection of the field-dependent ac susceptibility at 1.9 K. The first sample undergoes fast oxidation in air, then the sample was subject to special treatment: it was prepared into a dry-box and the crystals coated with vacuum grease inside a polycarbonate capsule, which was finally sealed and wrapped with Teflon. Magnetic susceptibilities were measured from 1.9 to 300 K with applied fields of 1 kOe below 45 or 25 K, respectively, and 10 kOe in the remaining temperature range. Isothermal magnetization curves were registered up to 50 kOe at 1.9, 2.5 and 4.5 K. Data reductions were carried out subtracting the sample holder and addenda contributions, using 2121.66 and 2208.47 as molecular weights and -1150.00×10^{-6} and -1183.60×10^{-6} emu mol^{-1} as diamagnetic corrections, estimated from Pascal’s constants.[154]

Powder-averaged molar susceptibility and magnetization data for the diruthenium units in **Fe_4Ru_2(II,II)** and **Fe_4Ru_2(II,III)** were simulated using typical *g*-values and zero-field splitting (zfs) parameters (*D*) for $Ru_2^{II,II}$ ($S = 1$, $g = 2.15$ and $D = 270$ cm^{-1})[97,103,104] and Ru2^{II,III} ($S = 3/2$, $g = 2.08$ and $D = 63$ cm^{-1}).[97,106,108] After subtraction of the Ru_2 contribution, $\chi_M T$-vs-T data were fitted to the Heisenberg *plus* Zeeman spin Hamiltonian shown in Eq. 2.11. Furthermore, after subtraction of the Ru_2 contribution, M_M-vs-H data were fitted to the axial zfs *plus* Zeeman Hamiltonian shown in Eq. E.2.13.

$[Fe_4(pPy)_2(dpm)_6][Ru_2(OAc)_4](BF_4)$ (Fe_4Ru_2(II,III)) *Method b*

A light red solution of $[Ru_2(OAc)_4(THF)_2](BF_4)$ (57 mg, 0.085 mmol) in anhydrous THF (20 mL) was layered over a red solution of **Fe₄pPy**·2EtOH (150 mg, 0.0845 mmol) in anhydrous DCM (20 mL) with a 2-mL layer of clean DCM in between, and left to liquid diffusion for ten days. Tiny red crystals of the title compound formed, that can be isolated, washed with *n*-hexane and dried. In order to preserve the crystallinity, the compound has to be kept in its mother liquor or into grease.

Elemental analysis (%) calcd for $C_{92}H_{146}BF_4Fe_4N_2O_{26}Ru_2$ (2208.47): C, 50.03; H, 6.66; N, 1.27. Found on dried sample: C, 49.59; H, 6.96; N, 1.40.

IR (KBr): 2963 ν(C–H$_{tBu}$), 1591, 1574, 1563, 1547, 1539, 1505 ν(C=O$_{dpm}$, C=N$_{py}$), 1442 ν(C=O$_{AcO}$), 1399, 1383, 1356 $\nu(CH_3)$, 1105 ν(C–O$_{pPy}$), 1084 $\nu(BF_4)$, 689 δ(AcO), 563 δ(py) cm^{-1}.

$[Fe_4(pPy)_2(dpm)_6]_2[Ru_2(OAc)_4]_2(BF_4)_x$ $(0 < x < 1)$ (Fe_4Ru_2MIX)

$[Ru_2(OAc)_4(MeOH)_2]$ (1.4 mg, 0.0042 mmol) and $[Ru_2(OAc)_4]_2(BF_4)$ (2.1 mg, 0.0042) in anhydrous THF (1.5 mL) was layered over a red solution of **Fe₄pPy**·2EtOH (15.0 mg, 0.00845 mmol) in anhydrous DCM (2.5 mL) and left to liquid diffusion for five days. Tiny red crystals formed, that could be isolated, washed with *n*-hexane and dried. In order to preserve the crystallinity, the compound has to be kept in its mother liquor or into grease.

IR (KBr): 2962.1 ν(C–H$_{tBu}$), 1592.9, 1576.5, 1563.5, 1548.6, 1535.5, 1504.2 ν(C=O$_{dpm}$, C=N$_{py}$), 1443 and 1433.3 ν(C=O$_{AcO}$), 1399.1, 1356.7 $\nu(CH_3)$, 1106 ν(C–O$_{pPy}$), 1084.1 (BF_4^-), 690.4 δ(AcO), 562.3 δ(py) cm^{-1}.

[$Ga_2(OMe)_2(dpm)_4$][68]

A solution of Hdpm (2.537 g, 13.77 mmol) and NaOMe (8.0 mL of a 3.081 M solution in MeOH, 25 mmol) in MeOH (33 mL) was added dropwise to a solution of $GaCl_3$ (1.212 g, 6.884 mmol) in MeOH (67 mL) under stirring. After 12 h, the precipitate was removed by Gooch filtration (G3). The white solid was washed with MeOH (15 mL) and dried under vaccum (2.364 g, 69.16 %).

Elemental analysis (%) for $C_{46}H_{82}Ga_2O_{10}\cdot NaCl$ (993.03): C, 55.64, H, 8.32; Found: C, 55.55, H, 9.09. IR (KBr): 2963, 2867, 2832 (ν C-H), 1593, 1570, 1554, 1539, 1507 (ν C=O), 1417 (ν C-H), 1059 (ν C-O) cm^{-1}.

[$Ga_4(pPy)_2(dpm)_6$] ·EtOH (Ga_4pPy ·EtOH)

[$Ga_2(OMe)_2(dpm)_4$] (200.2 mg, 0.2016 mmol) was added to a $GaCl_3$ solution in EtOH (4.85 mL of a 0.0295 M solution, 0.143 mmol). After, Et_2O (20 mL) was added waiting that the solution became clear. Sequentially, piperidine (58.0 µL, 0.586 mmol) and, after 10’, H_3pPy (0.1048 g, 0.5720 mmol) suspended in EtOH (3 mL) were added to the reaction mixture. The system was left under stirred overnight at room temperature. The precipitate was filtered by Gooch filtration (G4) and discharged. Slow vapour diffusion of EtOH (50 mL) into the colourless and clear solution gave colorless and X-ray quality crystals after seven days. The crystals was collected and washed with external diffusion solution and then with EtOH (5 mL). Afterwards, the crystals were dried under vacuum for 30’ (0.1912 g, 77.70%).

Elemental analysis (%) calcd for $C_{88}H_{146}Ga_4N_2O_{20}$ (1830.99): C, 57.73, H, 8.04, N, 1.53; found: C, 58.20; H, 8.17; N, 1.53.

IR (KBr). 3388 ($\nu_{O-H,EtOH}$), 2964, 2926, 2868 (ν_{C-H}), 1598, 1571, 1554, 1540, 1508 ($\nu_{C=O,C=N}$), 1416 (δ_{C-H}), 1103, 1075 (ν_{C-O}), 597 (δ_{pPy}) cm^{-1}.

^1H NMR (400 MHz, benzene-d_6, 298 K). δ 8.54 (dd, 4H·γ, *o*-H, ppp), 8.49 (dd, 4H·(1-γ), *o*-H, pps), 7.44 (dd, 4H·γ, *m*-H, ppp), 7.33 (dd, 4H·(1-γ), *o*-H, pps), 5.80 (s, 2H·(1-γ), CH, pps), 5.75 (s, 2H·(1-γ), CH, pps), 5.73 (s, 6H·γ+2H·(1-γ), CH, ppp+pps), 5.48 (dd, 2H·(1-γ), CH_2, pps), 5.44 (dd, 6H·γ, CH_2, ppp), 5.36 (dd, 2H·(1-γ), CH_2, pps), 4.92 (dd, 2H·(1-γ), CH_2, pps), 4.90 (dd, 6H·γ, CH_2, ppp), 4.86 (dd, 2H·(1-γ), CH_2, pps), 4.60 (dd, 2H·(1-γ), CH_2, pps), 4.47 (dd, 2H·(1-γ), CH_2, pps), 1.48 (s, 18H·(1-γ), ^{t}Bu, pps), 1.34 (s, 54H·γ +18H·(1-γ), ^{t}Bu, ppp+pps), 1.32 (s, 18H·(1-γ), ^{t}Bu, pps), 1.14 (×2) (s, 36H·(1-γ), ^{t}Bu, pps), 1.13 (s, 54H·γ, ^{t}Bu, ppp), 1.12 (s, 18H·(1-γ), ^{t}Bu, pps), 3.31 (q, 1.93H, CH_2 EtOH), 0.94 (t, 2.90, CH_3 EtOH), 3.26 (q, 0.52H, CH_2 Et_2O), 0.52 (s, br, OH) ppm. [γ = 0.67 e 1-γ = 0.33 are the molar fractions, respectively, of ppp and pps isomers in solutions.]

SpinWorks 4: Ga4pPy2dpm6*EtOH ib C6D6
T=298K

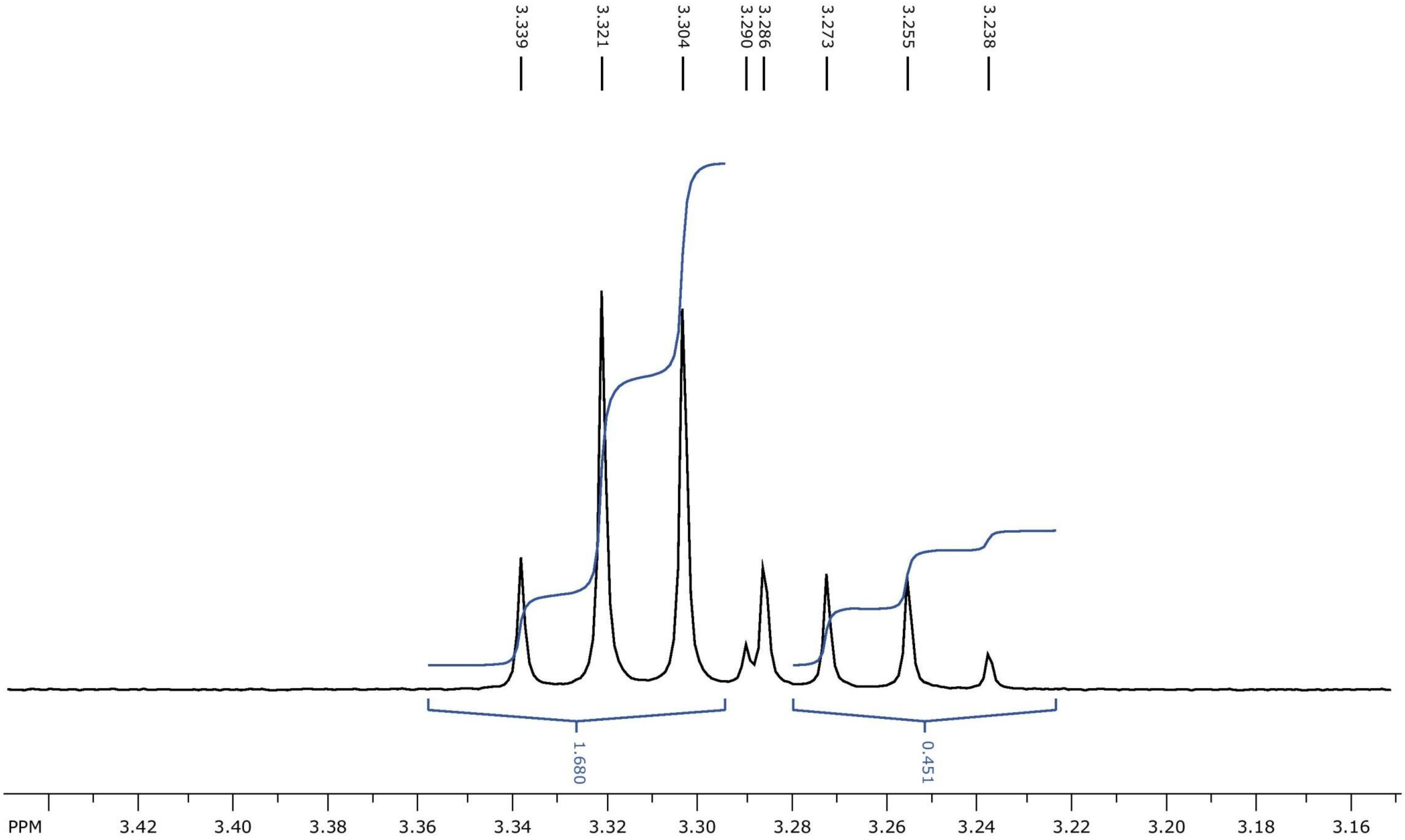

file: ...:\DATI CIGS\20141014\Ga4_400\1\fid expt: <zg30>
transmitter freq.: 400.134001 MHz
time domain size: 65536 points
width: 11990.41 Hz = 29.9660 ppm = 0.182959 Hz/pt

freq. of 0 ppm: 400.129996 MHz
processed size: 32768 complex points
LB: 0.000 GF: 0.0000
Hz/cm: 4.802 ppm/cm: 0.01200

SpinWorks 4: Ga4pPy2dpm6*EtOH ib C6D6
T=298K

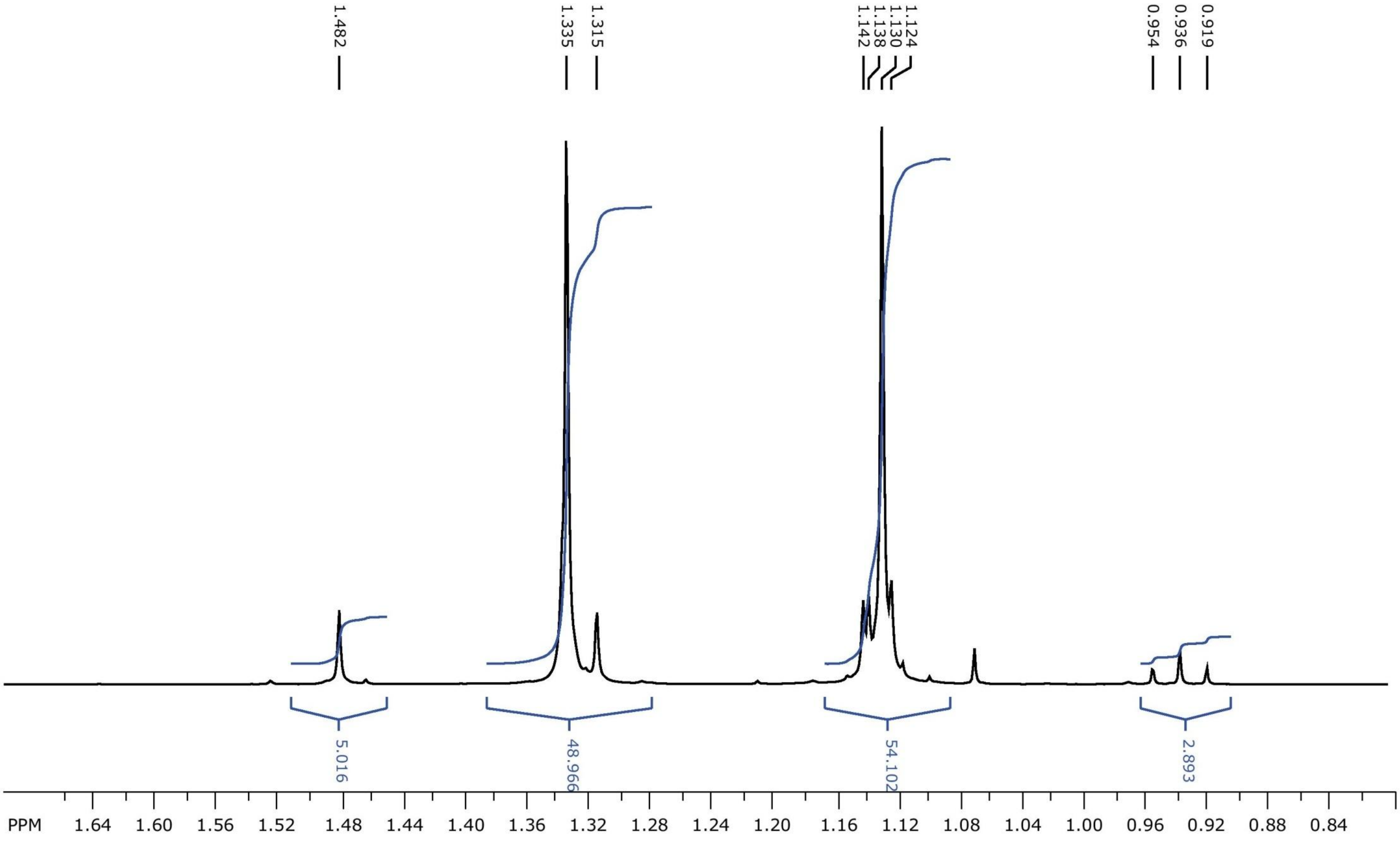

file: ...:\DATI CIGS\20141014\Ga4_400\1\fid   expt: <zg30>
transmitter freq.: 400.134001 MHz
time domain size: 65536 points
width: 11990.41 Hz = 29.9660 ppm = 0.182959 Hz/pt
number of scans: 32

freq. of 0 ppm: 400.129996 MHz
processed size: 32768 complex points
LB: 0.000   GF: 0.0000
Hz/cm: 14.405   ppm/cm: 0.03600

SpinWorks 4: Ga4pPy2dpm6*EtOH ib C6D6
T=298K

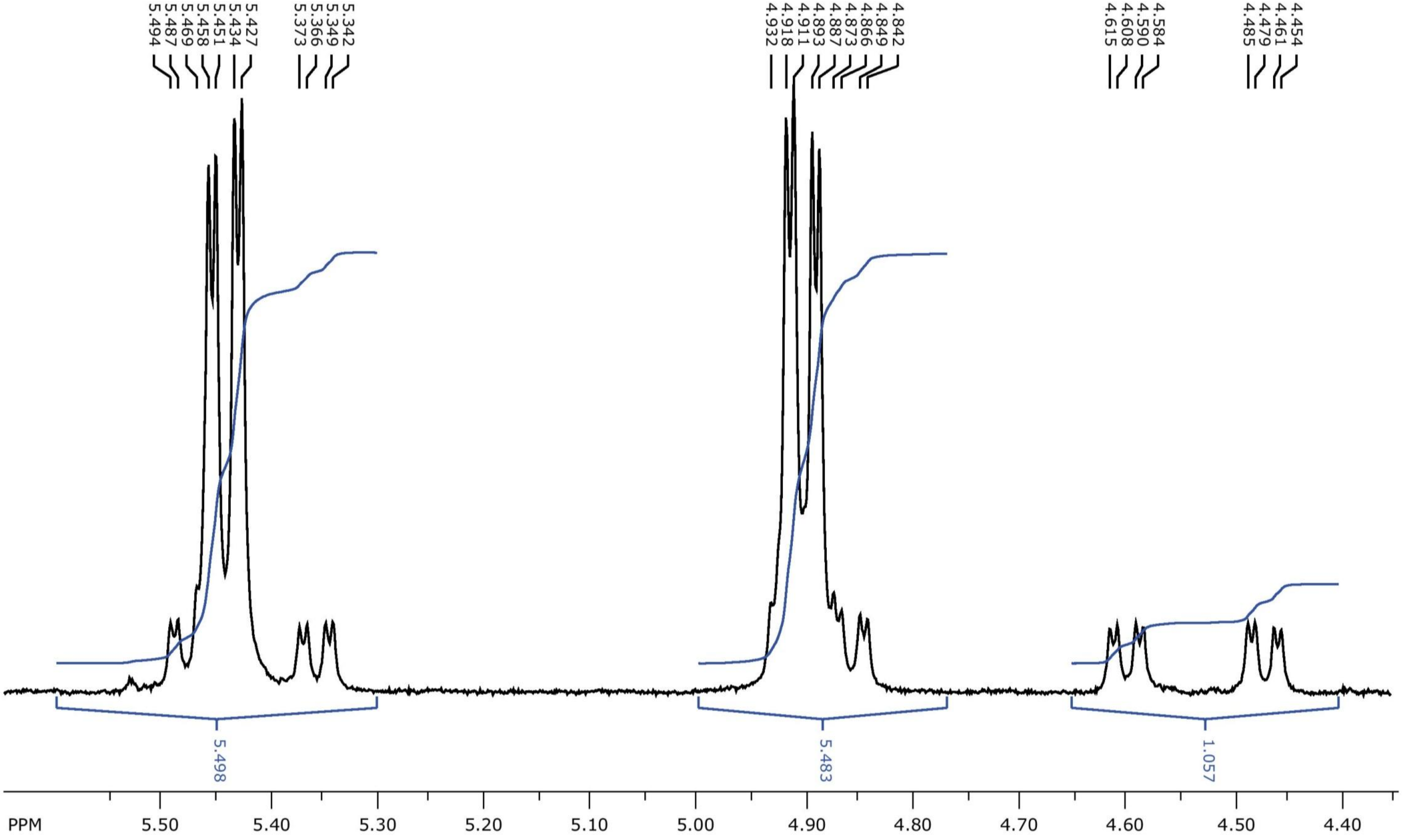

file: ...:\DATI CIGS\20141014\Ga4_400\1\fid   expt: <zg30>
transmitter freq.: 400.134001 MHz
time domain size: 65536 points
width: 11990.41 Hz = 29.9660 ppm = 0.182959 Hz/pt
number of scans: 32

freq. of 0 ppm: 400.129996 MHz
processed size: 32768 complex points
LB: 0.000   GF: 0.0000
Hz/cm: 20.807   ppm/cm: 0.05200

SpinWorks 4: Ga4pPy2dpm6*EtOH ib C6D6
T=298K

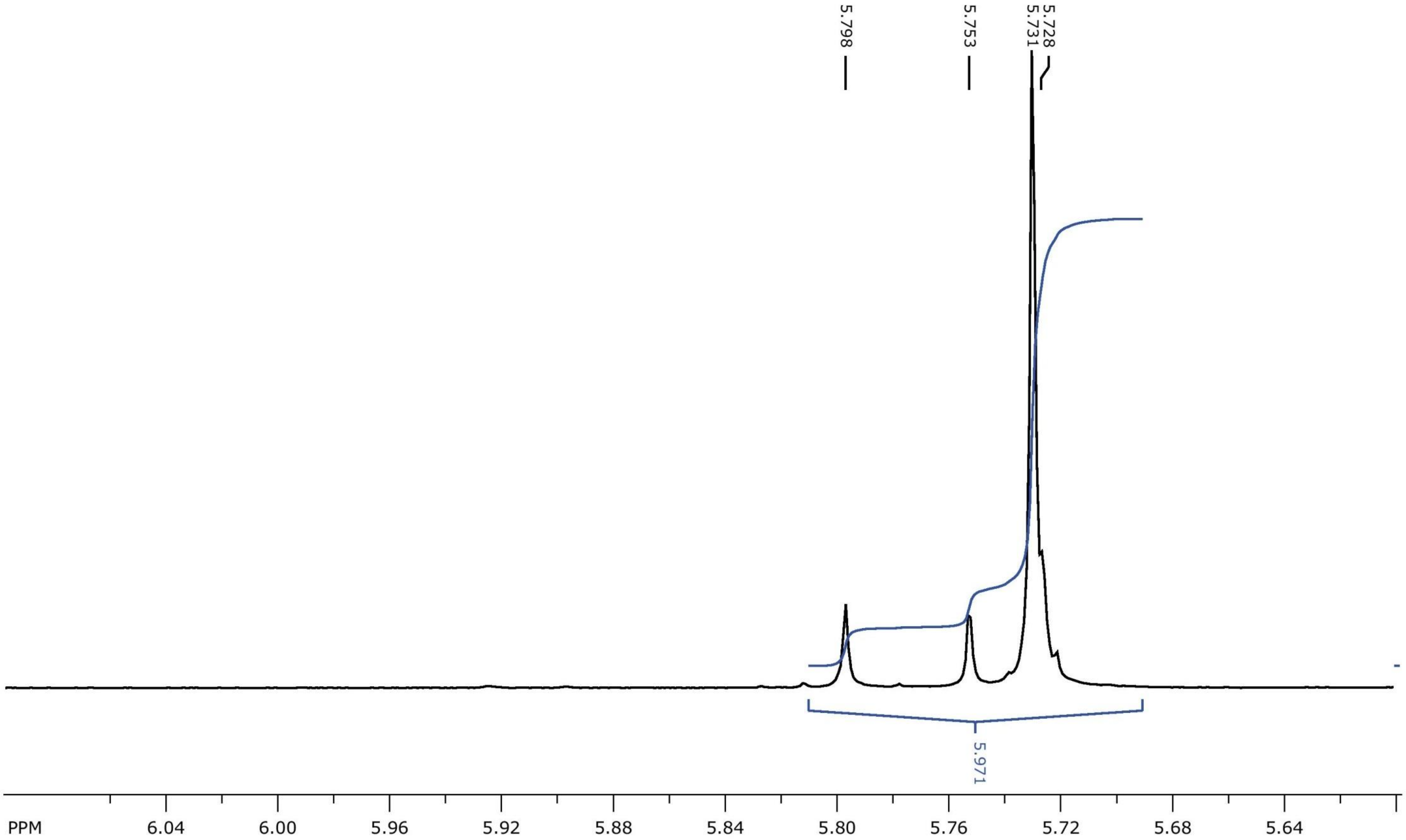

file: ...:\DATI CIGS\20141014\Ga4_400\1\fid   expt: <zg30>
transmitter freq.: 400.134001 MHz
time domain size: 65536 points
width: 11990.41 Hz = 29.9660 ppm = 0.182959 Hz/pt
number of scans: 32

freq. of 0 ppm: 400.129996 MHz
processed size: 32768 complex points
LB: 0.000   GF: 0.0000
Hz/cm: 8.003   ppm/cm: 0.02000

SpinWorks 4: Ga4pPy2dpm6*EtOH ib C6D6
T=298K

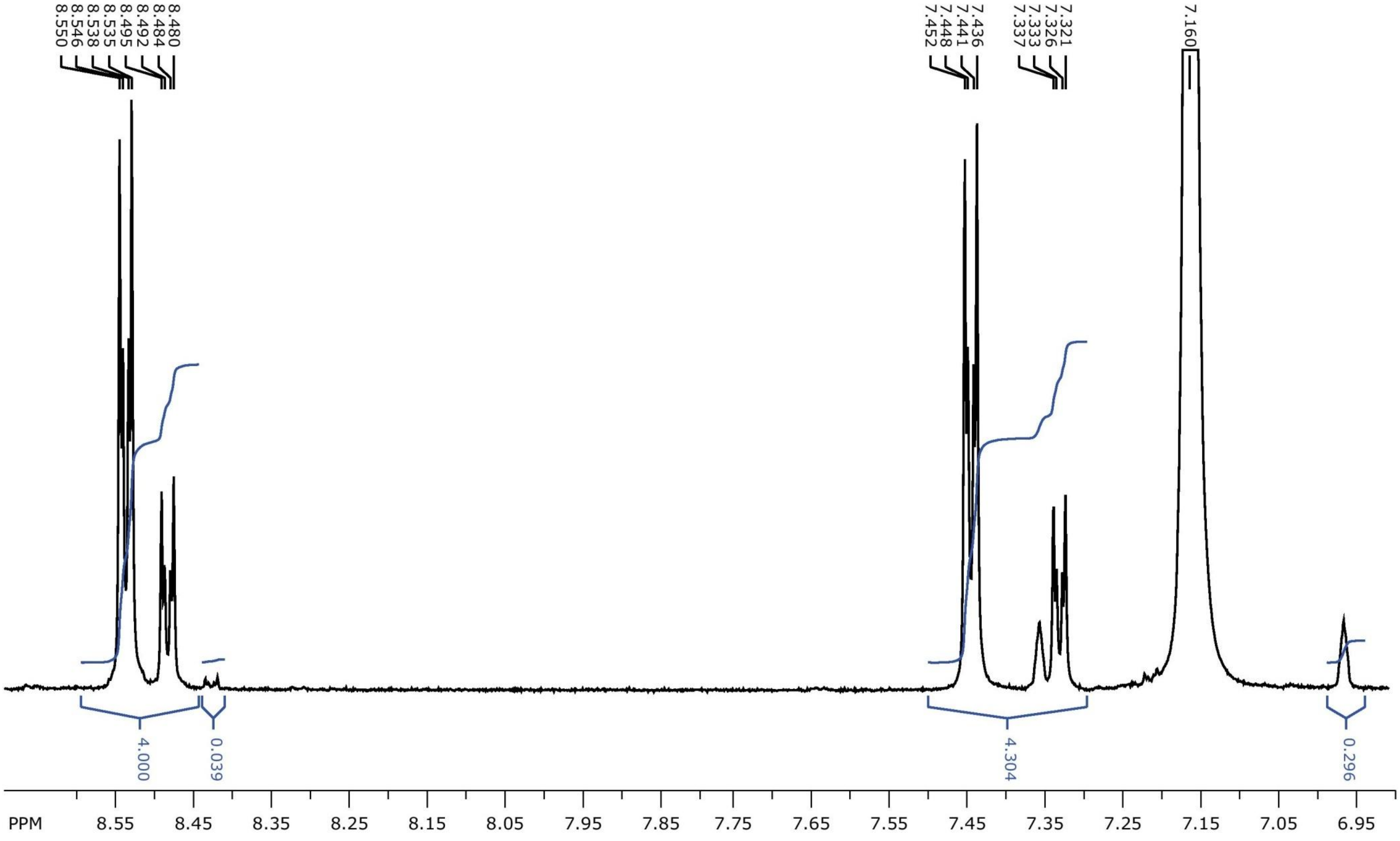

file: ...:\DATI CIGS\20141014\Ga4_400\1\fid   expt: <zg30>
transmitter freq.: 400.134001 MHz
time domain size: 65536 points
width: 11990.41 Hz = 29.9660 ppm = 0.182959 Hz/pt
number of scans: 32

freq. of 0 ppm: 400.129996 MHz
processed size: 32768 complex points
LB: 0.000   GF: 0.0000
Hz/cm: 28.809   ppm/cm: 0.07200

Structural characterization

Crystals of **Ga_4pPy**·EtOH grow as colourless parallelepipeds: the space group is monoclinic *C2/c* and the asymmetric unit contains half Ga_4 cluster. The four gallium(III) ions are exactly coplanar and Ga3 is symmetry equivalent to Ga3′. Disregarding the tripodal ligands, the molecule has idealized D_3 symmetry but the actual crystallographic symmetry is only C_2. While the coordination spheres of Ga1 and Ga2 are ordered within experimental resolution, the *β*-diketonates bound to Ga3 and Ga3′ are disordered and display two coordination modes: propeller (p) and sandwich (s), refined with complementary occupancy factors [0.833(2) and 0.167(2)]. Consequently, the crystal lattice in principle comprises three different isomers called ppp, pps (or psp) and pss. If *β*-diketonato ligands adopt independent coordination modes on Ga3 and Ga3′, the three isomers are expected to occur in the following proportions: 69.39 (ppp), 27.82 (pps or psp) and 2.79 (pss)%. All non-hydrogen atoms were refined anisotropically, unless otherwise previously noted. The hydrogen atoms were added in idealized positions and assigned isotropic displacement parameters constrained to those of the attached carbon atoms, while hydroxyl H atoms were treated using AFIX 143 instruction.

$[Ga_4(pPy)_2(dpm)_6][Ru_2(OAc)_4]$ (Ga_4Ru_2(II,II))

A light brown solution of $[Ru_2(OAc)_4(MeOH)_2]$ (18 mg, 0.0398 mmol) in anhydrous THF (12 mL) was layered over a red solution of **Ga_4pPy**·EtOH (72 mg, 0.0403 mmol) in anhydrous DCM (20 mL), and left to liquid diffusion for ten days. Tiny pale dark red crystals of the title compound were formed, that can be isolated, washed with *n*-hexane and dried. In order to preserve the crystallinity, the compound has to be kept in its mother liquor or into grease.

Elemental analysis (%) calcd for $C_{92}H_{146}Ga_4N_2O_{26}Ru_2$ (2177.17): C, 50.75; H, 6.76; N, 1.29. Found for dried sample: C, 51.65; H, 7.16; N, 1.32. Calcd with one THF molecule: $C_{96}H_{154}Ga_4N_2O_{27}Ru_2$ (2249.28): C, 51.26; H, 6.90; N, 1.25.

MALDI ToF/ToF (THF) *m/z* = 2177.7905 ($[Ga_4(pPy)_2(dpm)_6Ru_2(AcO)_4]^+$ 2177.5305, 2%), 1761.8319 ($[Ga_4(pPy)_2(dpm)_6 + Na]^+$ 1761.6555, 5%), 438.1942 ($[Ru_2(AcO)_4]^+$ 438.8633, 5%), 435.1917 ($[Ga(dpm)_2]^+$ 435.2020, 100%).

$[Ga_4(pPy)_2(dpm)_6][Ru_2(OAc)_4](BF_4)$ (Ga_4Ru_2(II,III)) *Method a*

Compound **Ga_4pPy**·EtOH (13.8 mg, 0.00773 mmol) was dissolved in THF (3 mL). After a solution of $[Ru_2(OAc)_4(THF)_2](BF_4)$ (0.89 mL of a 8.61 mM solution in THF, 0.0077 mmol) was added to a solution of **Ga_4pPy**·EtOH (13.8 mg, 0.00773 mmol) in THF (3 mL), and then stirred for 10’. The colour changed from red-brown to orange. After filtration on cotton, slow vapor diffusion of anhydrous toluene (5 mL) gave the title compound as tiny light red crystals, which were extensively washed with anhydrous dichloromethane till colorless washing (11.7 mg, 66.9 %).

Elemental analysis (%) calcd for $C_{92}H_{146}BF_4Ga_4N_2O_{26}Ru_2$ (2263.97): C, 48.81; H, 6.50; N, 1.24. Found for dried sample: C, 48.80; H, 6.37; N, 1.34. IR (KBr). 2964, 2926, 2869 ($\nu_{C–H}$), 1597, 1570, 1539, 1508 ($\nu_{C=O,C=N}$), 1444 (ν_{AcO}), 1416 ($\delta_{C–H}$), 1105, 1073 ($\nu_{C–O}$), 1084 (ν_{BF4}), 691 (δ_{AcO}), 598 (δ_{pPy}) cm^{-1}. MALDI ToF-ToF (THF) *m/z* = 2177.6287 ($[Ga_4(pPy)_2(dpm)_6Ru_2(AcO)_4]^+$ 2177.5305, 5%), 1761.7147 ($[Ga_4(pPy)_2(dpm)_6 + Na]^+$ 1761.6555, 5%), 438.8242 ($[Ru_2(AcO)_4]^+$ 438.8633, 5%), 435.1608 ($[Ga(dpm)_2]^+$ 435.2020, 100%).

$[Ga_4(pPy)_2(dpm)_6][Ru_2(OAc)_4](BF_4)$ (Ga_4Ru_2(II,III)) *Method b*

A solution of $[Ru_2(OAc)_4(THF)_2](BF_4)$ (1.17 mL of a 8.61 mM in THF, 0.01008 mmol, diluted with 3 mL of clean THF) was layered over a colourless solution of **Ga_4pPy**·EtOH (18.0 mg, 0.01008 mmol) in DCM (5 mL) and left to liquid diffusion for ten days. Tiny pale dark red crystals of the title compound were formed, that can be isolated, washed with *n*-hexane and dried. In order to preserve the crystallinity, the compound has to be kept in its mother liquor or into grease.

Elemental analysis (%) calcd for $C_{92}H_{146}BF_4Ga_4N_2O_{26}Ru_2$ (2263.97): C, 48.81; H, 6.50; N, 1.24. Found for dried sample: C, 48.40; H, 6.22; N, 1.01.

IR (KBr): 2964, 2926, 2869 ($\nu_{C–H}$), 1595, 1569, 1540, 1505 ($\nu_{C=O,C=N}$), 1442 (ν_{AcO}), 1413 ($\delta_{C–H}$), 1105, 1073 ($\nu_{C–O}$), 1084 (ν_{BF4}), 690 (δ_{AcO}), 596 (δ_{pPy}) cm^{-1}.

Magnetic measurements

Dc susceptibility data were recorded on 10.99 and 4.25 mg crystalline samples of **Ga_4Ru_2(II,II)** and **Ga_4Ru_2(II,III),** obtained with *Method a*, respectively. The first sample undergoes fast oxidation in air, then the sample was subject to special treatment: it was prepared into a dry-box and the crystals coated with vacuum grease inside a polycarbonate capsule, which was finally sealed and wrapped with Teflon. Magnetic susceptibility of **Ga_4Ru_2(II,III)** was measured from 2.0 to 300 K with applied fields of 1 kOe below 25 K, and 10 kOe for $T \geq 25$ K in the remaining temperature range. In other side, magnetic susceptibility of **Ga_4Ru_2(II,II)** was measured from 1.8 to 300 K with applied fields of 30 kOe. Data reductions were carried out subtracting the sample holder and addenda contributions, using 2177.17 and 2263.95 as molecular weights and -1144.80×10^{-6} and -1176.80×10^{-6} emu mol^{-1} as diamagnetic corrections, estimated from Pascal's constants.[154]

Synthesis of $[Fe_4(L^{pPy})_2(dpm)_6][Ru(tBuTPP)(CO)]_2$ (1·Fe_4pPy·1)

Method I: **Fe_4pPy**·2EtOH (17.0 mg, 0.00958 mmol) and **1** (19.8 mg, 0.0205 mmol) were dissolved together in toluene (4 mL) obtaining a violet solution. A bright red-brown microcrystalline solid, suitable for X-ray diffraction, was obtained after two months of slow evaporation of the solution (few mg's, yield n.d.).

Elemental analysis (%) calcd for $C_{145}H_{194}Fe_4N_6O_{19}Ru \cdot 3C_7H_8$ (2926.04): C, 68.14; H, 7.51; N, 2.87%. Found: C, 68.11; H, 7.33; N, 3.41.

IR (KBr): ν_{max}/cm^{-1} 2963, 2925, 2904, 2886 (νC–H), 1955 (νC≡O), 1593, 1576, 1564, 1549, 1537, 1506 (νC=O,C=N), 1401, 1385, 1357 (δC–H), 1108 (νC–O), 1008 (νC–N).

MALDI ToF (DCM): *m/z* 2622.294 ($[M - CO + H]^+$, 5%, calc. for $C_{144}H_{195}Fe_4N_6O_{18}Ru$: 2622.102), 1876.911 ($[Ru(p^tBuTPP)]_2^+$, 20, calc. for $C_{120}H_{120}N_8Ru_2$: 1876.774), 1499.651 ($[Fe_4(pPy)_2(dpm)_5]^+$, 5, calc. for $C_{73}H_{115}Fe_4N_2O_{16}$: 1499.564), 938.465 ($[Ru(p^tBuTPP)]^+$, 100, calc. for $C_{60}H_{60}N_4Ru$: 938.387).

^{1}H NMR (200 MHz, toluene-d_8, 293 K) δ = 1.4 (s, 36H, ^{t}Bu-*H* of **2**), 7.25 (br s, 8H, *o*-H of **2**), 8.25 (br s, 8H, *m*-H of **2**), 8.7 (br s, 8H, *βH* of **2**), 11 (br s, 112H, $Fe_4{}^t$Bu-*H* + Fe_4-*o*-Py-*H*) ppm.

Method IIa: **Fe$_4$pPy**·2EtOH (8.0 mg, 0.0045 mmol) was dissolved in a THF:EtOH 3:1 mixture (4 mL) and then solid **1** (9.1 mg, 0.094 mmol) was added and the violet mixture was stirred at room temperature, observing the total dissolution in 15 minutes. After 12 h there was the precipitation of a bright red-brown solid, which was collected by filtration on Gooch G4, washed with EtOH (3 mL) and dried (5.5 mg, 3615.87 g/mol, 34%).
IR (KBr): ν_{max}/cm^{-1} 2961, 2922, 2902, 2884 (νC–H), 1957 (νC≡O), 1591, 1576, 1562, 1547, 1535, 1505 (νC=O,C=N), 1401, 1383, 1355 (δC–H), 1108 (νC–O), 1008 (νC–N).

Method IIb: **Fe$_4$pPy**·2EtOH (17.0 mg, 0.00958 mmol) was dissolved in THF (2 mL) obtaining an orange solution. **1** (19.8 mg, 0.0205 mmol) was then added, together with further THF (1.5 mL) to improve dissolution, obtaining a violet solution after 3 h of stirring at room temperature. This was transferred in a test tube and stratified with EtOH (18 mL), which led to the formation of a bright red-brown microcrystalline powder after one month at finished diffusion, which was filtered on Gooch G4, washed with EtOH (2 × 3 mL) and dried (16.8 mg, 3615.87 g/mol, 48.4%).
Elemental analysis (%) calcd for $C_{206}H_{254}Fe_4N_{10}O_{20}Ru_2$ (3615.87): C, 68.43; H, 7.08; N, 3.87%. Found: C, 67.68; H, 7.25; N, 3.48.

IR (KBr): ν_{max}/cm^{-1} 2964, 2904, 2867 (νC–H), 1954 (νC≡O), 1592, 1575, 1564, 1549, 1538, 1505 (νC=O,C=N), 1402, 1385, 1358 (δC–H), 1109 (νC–O), 1008 (νC–N).

Magnetic Measurements

DC magnetic data were recorded on 8.57 mg powder samples of **1·Fe$_4$pPy·1**, packed in a Teflon pellet with applied fields of 1 kOe from 1.9 to 30 K and of 10 kOe from 30 to 300 K. Isothermal magnetization data were also registered at 1.9 and 4.5 K in fields up to 50 kOe. Data reduction was carried out by using 3615.87 as molecular weights and -2192.36×10^{-6} emu mol^{-1} as diamagnetic contribution, estimated from the Pascal's constants.[154] AC susceptibility data were recorded on the same sample.

Photophysical measurements

UV-vis absorption spectra were recorded with a Jasco V-570 UV/Vis/NIR spectrophotometer. Emission spectra were taken on a Spex Fluoromax-2 spectrofluorimeter, equipped with Hamamatsu R3896 tubes.

Nanosecond transient absorption measurements were performed with an Applied Photophysics laser flash photolysis apparatus, usingλ = 532 nm with Surelite Continuum II Nd/YAG laser (half-width 6-8 ns) as excitation source. Transient detection using photomultiplieroscilloscope combination (Hamamatsu R928, LeCroy 9360) or gated intensified CCD-Camera (Princeton Instruments PI-MAX II, with Acton SpectraPro 2300i triple grating flat field monochromator, RB GenII intensi- fier, ST133 controller, and a PTG pulser).

{[$Fe_4(pPy)_2(dpm)_6]_2Ag$}(ClO_4) (Fe_4Ag)

Method Ia. $AgClO_4$ (0.92 mL of a 0.00786 mol L^{-1} solution in THF, 0.0721 mmol) was added to a solution of **Fe_4pPy**·2EtOH (25.6 mg, 0.0144 mmol) in THF (2.0 mL). The resulting orange solution was stirred for 30 minutes and then carefully layered over DCM (3.0 mL) into a test tube and left undisturbed until diffusion was complete (ca. 7 days). The red X-ray quality cubic crystals so formed were isolated by filtration, quickly washed with a DCM:THF 1:1 mixture (1 mL) and dried under vacuum for 30 minutes without affecting crystallinity (13.3 mg, 51.6%).

Elemental analysis (%) calcd for $C_{168}H_{268}AgClFe_8N_4O_{40}$ (3574.08): C, 56.46; H, 7.56; N, 1.57%. Found: C, 56.36; H, 7.81; N, 1.72.

Method Ib. $AgClO_4$ (0.16 mL of a 0.0199 mol L^{-1} solution in THF, 0.0033 mmol) was added to a solution of **Fe_4pPy**·2EtOH (14.2 mg, 0.00799 mmol) in THF (2 mL). After stirring for 20 minutes, the orange solution was quickly filtered and then put in vapour diffusion with toluene (4.8 mL). After one month the red X-ray quality cubic crystals formed at the bottom of the test tube were isolated, washed with toluene (1 mL), *n*-hexane (2 × 5 mL) and dried in vacuum, without affecting the crystallinity (few mg's, yield n.d.).

Elemental analysis (%) calcd for $C_{168}H_{268}AgClFe_8N_4O_{40}$ (3574.08): C, 56.46; H, 7.56; N, 1.57. Found: C, 56.68; H, 7.88; N, 1.56.

Method II. A solution of $AgClO_4$ in THF (0.0199 mol L^{-1}, 0.22 mL, 0.0043 mmol) was diluted with THF to 2 mL, and then layered over a solution of **Fe_4pPy**·2EtOH (15.2 mg, 0.00856 mmol) in DCM (2 mL). After one week, red X-ray quality cubic crystals formed on the walls of the test tube; they were isolated by filtration, quickly washed with a DCM:THF 1:1 mixture (1 mL) and dried in vacuum without affecting the crystallinity (few mg's, yield n.d.).

Elemental analysis (%) calcd for $C_{168}H_{268}AgClFe_8N_4O_{40}$ (3574.08): C, 56.46; H, 7.56; N, 1.57. Found: C, 56.35; H, 7.63; N, 1.67.

IR (KBr): ν_{max}/cm^{-1} 2964s and 2904w (CH_2, CH_3), 2865w (CH_{dpm}), 1592s, 1576s, 1564s, 1536s, 1506s (C=C, C=O, C=N), 1402s, 1385s, 1357s (CH), 1108br (ClO_4, C–O), 1075w (C–O), 561 (Fe–O).

MALDI ToF/ToF (with matrix): *m/z* 1791.72 ($[Fe_4(pPy)_2(dpm)_6Ag]^+$, 50%, calcd for $C_{84}H_{134}AgFe_4N_2O_{18}$: 1791.61), 1184.27 ($[Fe_4(pPy)_2(dpm)_6Ag - Fe(dpm)_3]^+$, 100, calcd for $C_{51}H_{77}AgFe_3N_2O_{12}$: 1184.26), 422.16 ($[Fe(dpm)_2]^+$, 45, calcd for $C_{22}H_{38}FeO_4$: 422.21).

MALDI ToF/ToF (no matrix): *m/z* 1791.78 ($[Fe_4(pPy)_2(dpm)_6Ag]^+$, 75%), 1721.83 ($[Fe_4(pPy)_2(dpm)_6 + K]^+$, 1, calcd for $C_{84}H_{134}Fe_4KN_2O_{18}$: 1721.67), 1705.85 ($[Fe_4(pPy)_2(dpm)_6 + Na]^+$, 15, calcd for $C_{84}H_{134}Fe_4N_2NaO_{18}$: 1705.69), 1499.68 ($[Fe_4(pPy)_2(dpm)_6 - dpm]^+$, 20, calcd for $C_{73}H_{115}Fe_4N_2O_{16}$: 1499.56), 1184.34 ($[Fe_4(pPy)_2(dpm)_6Ag - Fe(dpm)_3]^+$, 40), 422.20 ($[Fe(dpm)_2]^+$, 100).

X-ray crystal structure determination

Crystal XRD on **Fe_4Ag** was carried out at 110(2) K, giving 79899 data collected up to θ = 65.75° were merged in cubic Laue group *m*–3*m* with *R*(merge) = 0.063; general systematic absences pointed to a face-centred lattice. Zonal systematic absences were as follows (T = true, F = false): 0*kl*, *k*+*l*=4*n*, <*I*/σ> T/F = 14.01/0.46; *h0l*, *h*+*l*=4*n*, <*I*/σ> T/F = 19.63/0.68; *hk*0, *h*+*k*=4*n*, <*I*/σ> T/F = 15.61/0.52; *hhl*, *l*=2*n*, <*I*/σ> T/F = 11.10/0.73. These are suggestive of extinction symbol *F d – c*, which has *Fd*–3*c* (n. 228) as the only space group. The structure was indeed successfully solved in this space group and refined on F_o^2 by standard methods including reflections with θ up to 63.5°, using SIR92[142] and SHELXL2014[155] programs implemented in the WINGX v2013.3 suite.[144] All non-hydrogen atoms were refined anisotropically, unless otherwise noted, while hydrogen atoms were added in idealized positions, allowed to ride on the parent carbon atoms and treated isotropically with *U*(H) = 1.2U_{eq}(C) for methylene, methine and aromatic hydrogens and *U*(H) = 1.5U_{eq}(C) for methyl hydrogens. In spite of the low temperature data collection, all atoms displayed large displacement parameters, consistent with the value *U*(mean) = 0.126 Å^2 obtained from Wilson plot. The structure exhibits at least three different types of disorder, which persist in space groups of lower (down to monoclinic) symmetry. The first type of disorder is related to the fact that the 4-pyridyl ring develops along a threefold crystallographic axis. The second type of disorder originates from the occurrence of a minority fraction of Fe_4 complexes rotated by 60° around the Ag···Fe_4···Ag direction, with coinciding central ions (Fe1) but distinct peripheral metals (Fe2 and Fe2a). The Fe and O atoms, as well as the CH_2 carbons of this minority component were clearly located in ΔF maps. The third type of disorder lies in the adoption of two different coordination modes by dpm^- ligands bound to Fe2 (propeller-like, *p*, and sandwich-like, *s*), as found in few other isostructural complexes. Because the different components have extensively overlapping *t*Bu's, dpm^- ligands were initially refined as rigid groups. In the final stages of refinement, hard DFIX restraints were introduced on 1,2 and 1,3 distances, thus allowing for torsion angle optimization. The model converged to a 0.867(2) fraction of majority component (with ca. 60:40 proportion of dpm^- ligands coordinated in a propeller- and sandwich-like fashion, respectively) and a 0.133(2) fraction of 60°-rotated complex, for which only propeller-like dpm^- ligands were refined. Rigid-group restraints (RIGU) were applied to the anisotropic displacement parameters (ADPs) of dpm^- ligands bound to Fe2, with approximately isotropic behaviour for *t*Bu groups (ISOR 0.03). A flat geometry was imposed to the 4-pyridyl ring, with further geometrical restraints to preserve the expected *mm*2 symmetry and rigid-group restraints (RIGU) to its ADPs. The C and O atoms of dpm^- ligands and CH_2–O groups bound to Fe2a were refined isotropically; only two *U* values (forced to be similar within 0.02 Å^2) were used for dpm^- ligands, one for methyl groups and one for the remaining C and O atoms. A perchlorate ion was located around a threefold axis and refined with a common isotropic displacement parameter for the O atoms and an idealized tetrahedral geometry with Cl–O = 1.414(10) Å. To ensure physically realistic displacement parameters, the occupancy had to be lowered to 0.5, indicating that half of the perchlorate ions are likely to be extensively disordered in the large voids of the structure. The perchlorate lies close to 4-pyridyl rings, with short C···O contacts (i.e.: C10(H)···O5 = 3.563 Å, C10–H10···O5 = 161.5°). The data set was treated with the command SQUEEZE of the PLATON program.[156] When the perchlorate ion is removed and the model re-refined until convergence, the unit cell contains 12415 Å^3 (14.3%) of solvent-accessible voids and an electron count per unit cell of 780. Considering that one perchlorate ion possesses 50 electrons, the calculated total electron count per unit cell (Z = 16, F_d–3*c*) is of 800 electrons, in excellent agreement with the SQUEEZE calculated value. The above statement verifies that single-crystals were indeed perfectly dried and cavities contain only perchlorate ions. Based on the NMR solvent content (2.6 DCM, 2.1 THF per unit formula), and attributing molecular volumes of 110 Å^3 for DCM, 135 Å^3 for THF and about 100 Å^3 for perchlorate ion one calculates a total volume of 10712 Å^3, easily hosted by the previous calculated solvent-accessible.

Magnetic measurements

Dc magnetic data were recorded on 9.46 mg crystalline sample of **Fe_4Ag**. Magnetic susceptibilities were measured from 1.9 to 300 K with applied fields of 1 kOe below 30 K and 10 kOe in the remaining temperature range. Isothermal magnetization curves were registered up to 50 kOe at 1.9, 2.5 and 4.5 K. Data reductions were carried out subtracting the sample holder and addenda contributions, using 1787.04 (3574.08/2, in order to reduce to a single Fe_4 cluster) as molecular weight and -986.84×10^{-6} emu mol^{-1} as diamagnetic correction, estimated from Pascal’s constants.[154] Ac susceptibility data were recorded on the same sample used for dc measurements, at temperatures down to 1.8 K and frequencies of the oscillating field ν = 10–10000 Hz.

MicroSQUID measurements

In addition to general details reported above, for **Fe_4Ag**, due to the delay coming from the superconducting field coils, magnetic field values recorded with increasing field are slightly overestimated by an amount proportional to the field sweep rate. The correction is –1.4 mT at 0.280 T s^{-1} and –0.01 mT at 0.002 T s^{-1}.

Bibliography

[1] D. Gatteschi, R. Sessoli, J. Villain, *Molecular Nanomagnets*, Oxford University Press: Oxford**, 2006**.

[2] H. Miyasaka, M. Yamashita, *Dalton Trans.* **2007**, 399–406.

[3] G. Cosquer, M. Morimoto, M. Irie, A. Fetoh, B. K. Breedlove, M. Yamashita, *Dalton Trans.* **2015**, *44*, 5996–6002.

[4] D. Pinkowicz, H. I. Southerland, C. Avendaño, A. Prosvirin, C. Sanders, W. Wernsdorfer, K. S. Pedersen, J. Dreiser, R. Clérac, J. Nehrkorn, et al., *J. Am. Chem. Soc.* **2015**, *137*, 14406–14422.

[5] R. Ababei, C. Pichon, O. Roubeau, Y. G. Li, N. Bréfuel, L. Buisson, P. Guionneau, C. Mathonière, R. Clérac, *J. Am. Chem. Soc.* **2013**, *135*, 14840–14853.

[6] A. Caneschi, D. Gatteschi, R. Sessoli, A. L. Barra, L. C. Brunel, M. Guillot, *J. Am. Chem. Soc.* **1991**, *113*, 5873–5874.

[7] L. Thomas, F. Lionti, R. Ballou, D. Gatteschi, R. Sessoli, B. Barbara, *Nature* **1996**, *383*, 145–147.

[8] R. A. Layfield, *Organometallics* **2014**, *33*, 1084–1099.

[9] S. Gómez-Coca, D. Aravena, R. Morales, E. Ruiz, *Coord. Chem. Rev.* **2015**, *289-290*, 379–392.

[10] Y.-S. Ding, N. F. Chilton, R. E. P. Winpenny, Y.-Z. Zheng, *Angew. Chem. Int. Ed.* **2016**, *55*, 16071–16074.

[11] L. Bogani, W. Wernsdorfer, *Nat. Mater.* **2008**, *7*, 179–186.

[12] W. Wernsdorfer, N. E. Chakov, G. Christou, **2004**, *70*, 132413.

[13] S. Sanvito, *J. Mater. Chem.* **2007**, *17*, 4455–4459.

[14] J. D. Rinehart, M. Fang, W. J. Evans, J. R. Long, *Nat. Chem.* **2011**, *3*, 538–42.

[15] F. Troiani, M. Affronte, *Chem. Soc. Rev.* **2011**, *40*, 3119–3129.

[16] C. S. Wu, G. R. Rossman, H. B. Gray, G. S. Hammond, H. J. Schugar, *Inorg. Chem.* **1972**, *11*, 990–994.

[17] S. Accorsi, A. L. Barra, A. Caneschi, G. Chastanet, A. Cornia, A. C. Fabretti, D. Gatteschi, C. Mortalò, E. Olivieri, F. Parenti, et al., *J. Am. Chem. Soc.* **2006**, *128*, 4742–4755.

[18] L. Gregoli, C. Danieli, A. L. Barra, P. Neugebauer, G. Pellegrino, G. Poneti, R. Sessoli, A. Cornia, *Chem. Eur. J.* **2009**, *15*, 6456–6467.

[19] A. Nava, L. Rigamonti, E. Zangrando, R. Sessoli, W. Wernsdorfer, A. Cornia, *Angew. Chem. Int. Ed.* **2015**, *54*, 8777–8782.

[20] S. Gómez-Coca, A. Urtizberea, E. Cremades, P. J. Alonso, A. Camón, E. Ruiz, F. Luis, *Nat. Commun.* **2014**, *5*, DOI 10.1038/ncomms5300.

[21] N. Ishikawa, M. Sugita, T. Ishikawa, S. Koshihara, Y. Kaizu, *J. Am. Chem. Soc.* **2003**, *125*, 8694–8695.

[22] D. N. Woodruff, R. E. P. Winpenny, R. A. Layfield, *Chem. Rev.* **2013**, *113*, 5110–5148.

[23] G. A. Craig, M. Murrie, *Chem. Soc. Rev.* **2015**, *44*, 2135–2147.

[24] R. D. L. Carlin, *Magnetochemistry*, Springer-Verlag: Berlin, **1986**.

[25] O. Kahn, *Molecular Magnetism*, VCH: Weinheim, **1993**.

[26] K. Kambe, *J. Phys. Soc. Jpn.* **1950**, *5*, 48.

[27] S. Gaemers, J. van Slageren, C. M. O'Connor, J. G. Vos, R. Hage, C. J. Elsevier, *Organometallics* **1999**, *18*, 5238–5244.

[28] A. L. Barra, A. Caneschi, A. Cornia, F. De Fabrizi Biani, D. Gatteschi, C. Sangregorio, R. Sessoli, L. Sorace, *J. Am. Chem. Soc.* **1999**, *121*, 5302–5310.

[29] A. Cornia, A. C. Fabretti, P. Garrisi, C. Mortalò, D. Bonacchi, D. Gatteschi, R. Sessoli, L. Sorace, W. Wernsdorfer, A.-L. Barra, *Angew. Chem. Int. Ed.* **2004**, *43*, 1136–1139.

[30] N. Regnault, T. Jolicœur, R. Sessoli, D. Gatteschi, M. Verdaguer, *Phys. Rev. B* **2002**, *66*, 054409.

[31] C. Raghu, I. Rudra, D. Sen, S. Ramasesha, *Phys. Rev. B - Condens. Matter Mater. Phys.* **2001**, *64*, 644191–644199.

[32] D. Gatteschi, A. L. Barra, A. Caneschi, A. Cornia, R. Sessoli, L. Sorace, *Coord. Chem. Rev.* **2006**, *250*, 1514–1529.

[33] R. Caciuffo, G. Amoretti, A. Murani, R. Sessoli, A. Caneschi, D. Gatteschi, *Phys. Rev. Lett.* **1998**, *81*, 4744–4747.

[34] A. Bencini, D. Gatteschi, *EPR of Exchange Coupled Systems , Springer-Verlag, Berlin, 1990.*, **1990**.

[35] D. Gatteschi, R. Sessoli, *Angew. Chem. Int. Ed.* **2003**, *42*, 268–297.

[36] L. Thomas, F. Lionti, R. Ballou, D. Gatteschi, R. Sessoli, B. Barbara, *Nature* **1996**, *383*, 145–147.

[37] O. Waldmann, *Inorg. Chem.* **2007**, *46*, 10035–10037.

[38] R. Tiron, W. Wernsdorfer, D. Foguet-Albiol, N. Aliaga-Alcalde, G. Christou, *Phys. Rev. Lett.* **2003**, *91*, 227203.

[39] D. P. Goldberg, J. Telser, J. Krzystek, A. Garrido Montalban, L. C. Brunel, A. G. M. Barrett, B. M. Hoffman, *J. Am. Chem. Soc.* **1997**, *119*, 8722–8723.

[40] W. Wernsdorfer, *Science (80-.).* **1999**, *284*, 133–135.

[41] S. Hill, R. S. Edwards, N. Aliaga-Alcalde, G. Christou, *Science (80-.).* **2003**, *302*, 1015–1018.

[42] T. N. Nguyen, W. Wernsdorfer, K. A. Abboud, G. Christou, *J. Am. Chem. Soc.* **2011**, *133*, 20688–20691.

[43] J. Yoo, W. Wernsdorfer, E. C. Yang, M. Nakano, A. L. Rheingold, D. N. Hendrickson, *Inorg. Chem.* **2005**, *44*, 3377–3379.

[44] L. Lecren, O. Roubeau, C. Coulon, Y. Li, X. F. Le Goff, W. Wernsdorfer, H. Miyasaka, R. Clérac, *J. Am. Chem. Soc.* **2005**, *127*, 17353–17363.

[45] L. Lecren, O. Roubeau, Y.-G. Li, X. F. Le Goff, H. Miyasaka, F. Richard, W. Wernsdorfer, C. Coulon, R. Clérac, *Dalton Trans.* **2008**, 755–766.

[46] H. Miyasaka, K. Nakata, K. I. Sugiura, M. Yamashita, R. Clérac, *Angew. Chem. Int. Ed.* **2004**, *43*, 707–711.

[47] L. Lecren, W. Wernsdorfer, Y. Li, A. Vindigni, H. Miyasaka, R. Clérac, **2007**, *129*, 5045–5051.

[48] S. K. Das, B. Song, A. Mahler, V. N. Nesterov, A. K. Wilson, O. Ito, F. D. Souza, *J. Phys. Chem. C* **2014**, *118*, 1–22.

[49] S. I. Ohkoshi, S. Ikeda, T. Hozumi, T. Kashiwagi, K. Hashimoto, S. I. Ohkoshi, *J. Am. Chem. Soc.* **2006**, *128*, 5320–5321.

[50] W. Wernsdorfer, N. Aliaga-Alcalde, D. N. Hendrickson, G. Christou, *Nature* **2002**, *416*, 406–409.

[51] R. Bagai, W. Wernsdorfer, K. A. Abboud, G. Christou, *J. Am. Chem. Soc.* **2007**, *129*, 12918–12919.

[52] R. Tiron, W. Wernsdorfer, N. Aliaga-Alcalde, G. Christou, *Phys. Rev. B* **2003**, *68*, 140407.

[53] R. Inglis, L. F. Jones, K. Mason, A. Collins, S. A. Moggach, S. Parsons, S. P. Perlepes, W. Wernsdorfer, E. K. Brechin, *Chem. Eur. J.* **2008**, *14*, 9117–9121.

[54] R. Inglis, S. M. Taylor, L. F. Jones, G. S. Papaefstathiou, S. P. Perlepes, S. Datta, S. Hill, W. Wernsdorfer, E. K. Brechin, *Dalton Trans.* **2009**, 9157.

[55] E. C. Yang, W. Wernsdorfer, L. N. Zakharov, Y. Karaki, A. Yamaguchi, R. M. Isidro, G. Di Lu, S. A. Wilson, A. L. Rheingold, H. Ishimoto, et al., *Inorg. Chem.* **2006**, *45*, 529–546.

[56] E.-C. Yang, W. Wernsdorfer, S. Hill, R. S. Edwards, M. Nakano, S. Maccagnano, L. N. Zakharov, A. L. Rheingold, G. Christou, D. N. Hendrickson, *Polyhedron* **2003**, *22*, 1727–1733.

[57] A. Das, K. Gieb, Y. Krupskaya, S. Demeshko, S. Dechert, R. Klingeler, V. Kataev, B. Büchner, P. Müller, F. Meyer, *J. Am. Chem. Soc.* **2011**, *133*, 3433–3443.

[58] R. W. Saalfrank, A. Scheurer, I. Bernt, F. W. Heinemann, A. V. Postnikov, V. Schünemann, A. X. Trautwein, M. S. Alam, H. Rupp, P. Müller, *Dalton Trans.* **2006**, 2865–2874.

[59] L. Margheriti, M. Mannini, L. Sorace, L. Gorini, D. Gatteschi, A. Caneschi, D. Chiappe, R. Moroni, F. B. de Mongeot, A. Cornia, et al., *Small* **2009**, *5*, 1460–1466.

[60] L. Rigamonti, M. Piccioli, L. Malavolti, L. Poggini, M. Mannini, F. Totti, B. Cortigiani, A. Magnani, R. Sessoli, A. Cornia, *Inorg. Chem.* **2013**, *52*, 5897–5905.

[61] L. Rigamonti, A. Nava, M.-E. Boulon, J. Luzon, R. Sessoli, A. Cornia, *Chem. Eur. J.* **2015**, *21*, 12171–12180.

[62] T. K. Prasad, G. Poneti, L. Sorace, M. J. Rodriguez-Douton, A.-L. Barra, P. Neugebauer, L. Costantino, R. Sessoli, A. Cornia, *Dalton Trans.* **2012**, *41*, 8368.

[63] R. H. Cole, J. Cole, *J. Chem. Phys.* **1941**, 341–352.

[64] C. Dekker, A. F. M. Arts, H. W. Wijn, A. J. Van Duyneveldt, J. A. Mydosh, *Phys. Rev. B* **1989**, *40*, 11243–11251.

[65] R. Sessoli, D. Gatteschi, A. Caneschi, M. A. Novak, *Nature* **1993**, *365*, 141–143.

[66] M. J. Rodriguez-Douton, M. Mannini, L. Armelao, A.-L. Barra, E. Tancini, R. Sessoli, A. Cornia, *Chem. Commun.* **2011**, *47*, 1467–1469.

[67] L. Rigamonti, M. Piccioli, L. Malavolti, L. Poggini, M. Mannini, F. Totti, B. Cortigiani, A. Magnani, R. Sessoli, A. Cornia, *Inorg. Chem.* **2013**, *52*, 5897–5905.

[68] E. Tancini, M. Jesus Rodriguez-Douton, L. Sorace, A. L. Barra, R. Sessoli, A. Cornia, *Chem. Eur. J.* **2010**, *16*, 10482–10493.

[69] K. C. M. Westrup, M.-E. Boulon, P. Totaro, G. G. Nunes, D. F. Back, A. Barison, M. Jackson, C. Paulsen, D. Gatteschi, L. Sorace, et al., *Chem. Eur. J.* **2014**, *20*, 13681–13691.

[70] L. Rigamonti, A. Cornia, A. Nava, M. Perfetti, M.-E. Boulon, A.-L. Barra, X. Zhong, K. Park, R. Sessoli, *Phys. Chem. Chem. Phys.* **2014**, *16*, 17220–17230.

[71] M. Perfetti, F. Pineider, L. Poggini, E. Otero, M. Mannini, L. Sorace, C. Sangregorio, A. Cornia, R. Sessoli, *Small* **2014**, *10*, 323–329.

[72] G. Wilkenson, M. Rosemblum, C. Whiting, R. B. Woodward, *J. Am. Chem. Soc.* **1952**, *74*, 2123.

[73] V. E. O. Fischer, W. Pfab, *Zeitschrift fur Naturforsch.* **1952**, *7b*, 377.

[74] J. D. Dunitz, L. E. Orgel, R. A. Rich, *Acta Crystallogr.* **1956**, *9*, 373–375.

[75] R. K. Bohn, A. Haaland, *J. Organomet. Chem.* **1966**, *5*, 470.

[76] A.-C. Ribou, J.-P. Launay, M. L. Sachtleben, H. Li, C. W. Spangler, *Inorg. Chem.* **1996**, *35*, 3735–3740.

[77] J. H. K. Yip, J. Wu, K. Y. Wong, K. W. Yeung, J. J. Vittal, *Organometallics* **2002**, *21*, 1612–1621.

[78] J. H. K. Yip, J. Wu, K. Y. Wong, K. P. Ho, C. S. N. Pun, J. J. Vittal, *Organometallics* **2002**, *21*, 5292–5300.

[79] A. Albinati, F. Fabrizi De Biani, P. Leoni, L. Marchetti, M. Pasquali, S. Rizzato, P. Zanello, *Angew. Chem. Int. Ed.* **2005**, *44*, 5701–5705.

[80] V. V. Pavlishchuk, A. W. Addison, *Inorg. Chim. Acta* **2000**, *298*, 97–102.

[81] W. E. Britton, R. Kashyap, M. El-Hashash, M. El-Kady, M. Herberhold, *Organometallics* **1986**, *5*, 1029–1031.

[82] H. Grimes, S. R. Logan, *Inorg. Chim. Acta* **1980**, *45*, 223–224.

[83] J. C. D. Brand, W. Snedden, *Trans. Faraday Soc.* **1957**, *53*, 894.

[84] G. Z. Suleimanov, P. V. Petrovskii, Y. S. Bogachev, I. L. Zhuravleva, E. I. Fedin, I. P. Beletskaya, *J. Organomet. Chem.* **1984**, *262*, c35–c37.

[85] W. Bracke, H. J. Cheng, J. M. Pearson, M. Szwarc, *J. Am. Chem. Soc.* **1969**, *91*, 203–204.

[86] A. Bell, A. Ledwith, D. C. Sherrington, *J. Chem. Soc.* **1969**, 2719–2720.

[87] G. Masson, P. Beyer, P. W. Cyr, A. J. Lougv, L. Manners, *Macromolecules* **2006**, *39*, 3720–3730.

[88] B. S. Furniss, A. J. Hannaford, P. W. G. Smith, A. R. Tatchell, *Vogel's Textbook of Practical Organic Chemistry*, **1989**.

[89] P. Zanello, A. Cinquantini, S. Mangani, G. Opromolla, L. Pardi, C. Janiak, M. D. Rausch, *J. Organomet. Chem.* **1994**, *471*, 171–177.

[90] A. Cinquantini, G. Opromolla, P. Zanello, G. Giorgi, *J. Organomet. Chem.* **1993**, *444*, 179–183.

[91] Š. Toma, A. Gáplovský, M. Hudeček, Z. Langfelderová, *Monatshefte für Chemie* **1985**, *116*, 357–364.

[92] N. G. Connelly, W. E. Geiger, *Chem. Rev.* **1996**, *96*, 877–910.

[93] C. J. Donahue, E. R. Donahue, *J. Chem. Educ.* **2013**, *90*, 1688–1691.

[94] C. Danieli, A. Cornia, C. Cecchelli, R. Sessoli, A. L. Barra, G. Ponterini, B. Zanfrognini, *Polyhedron* **2009**, *28*, 2029–2035.

[95] D. Menozzi, E. Biavardi, C. Massera, F.-P. Schmidtchen, A. Cornia, E. Dalcanale, *Supramol. Chem.* **2010**, *22*, 768–775.

[96] L. Vergnani, A.-L. Barra, P. Neugebauer, M. J. Rodriguez-Douton, R. Sessoli, L. Sorace, W. Wernsdorfer, A. Cornia, *Chemistry* **2012**, *18*, 3390–3398.

[97] M. a. S. Aquino, *Coord. Chem. Rev.* **1998**, *170*, 141–202.

[98] M. A. S. Aquino, *Coord. Chem. Rev.* **2004**, *248*, 1025–1045.

[99] T. A. Stephenson, G. Wilkinson, *J. Inorg. Nucl. Chem.* **1966**, *28*, 2285–2291.

[100] F. A. Urbanos, M. C. Barral, R. Jimenez-Aparicio, *Polyhedron* **1988**, *7*, 2597–2600.

[101] M. C. Barral, R. Jiménez-Aparicio, J. L. Priego, E. C. Royer, E. Gutiérrez-Puebla, C. R. Valero, *Polyhedron* **1992**, *11*, 2209–2215.

[102] M. C. Barral, R. Gonzalez-Prieto, R. Jimenez-Aparicio, J. L. Priego, M. R. Torres, F. A. Urbanos, *Inorg. Chim. Acta* **2005**, *358*, 217–221.

[103] M. Mikuriya, D. Yoshioka, M. Handa, *Coord. Chem. Rev.* **2006**, *250*, 2194–2211.

[104] M. Handa, D. Yoshioka, M. Mikuriya, I. Hiromitsu, K. Kasuga, *Mol. Cryst. Liq. Cryst* **2002**, *376*, 257–262.

[105] F. D. Cukiernik, A.-M. Giroud-Godquin, P. Maldivi, J.-C. Marchon, *Inorg. Chim. Acta* **1994**, *215*, 203–207.

[106] E. J. Beck, K. D. Drysdale, L. K. Thompson, L. Li, C. a Murphy, M. a S. Aquino, *Inorg. Chim. Acta* **1998**, *279*, 121–125.

[107] W. Wernsdorfer, S. Bhaduri, A. Vinslava, G. Christou, *Phys. Rev. B* **2005**, *72*, 214429.

[108] F. D. Cukiernik, A. M. Giroud-Godquin, P. Maldivi, J. C. Marchon, *Inorg. Chim. Acta* **1994**, *215*, 203–207.

[109] L. Norel, M. Feng, K. Bernot, T. Roisnel, T. Guizouarn, K. Costuas, S. Rigaut, *Inorg. Chem.* **2014**, *53*, 2361–2363.

[110] A. J. Lindsay, G. Wilkinson, *J. Chem. Soc., Dalton Trans.* **1985**, 2321–2326.

[111] V. Miskowski, T. Loehr, H. Gray, *Inorg. Chem.* **1987**, *26*, 1098–1108.

[112] R. J. H. Clark, L. T. H. Ferris, *Inorg. Chem.* **1981**, *20*, 2759–2766.

[113] R. J. H. Clark, M. M. L. Franks, *J. Chem. Soc., Dalton Trans.* **1976**, 1825–1828.

[114] G. N. Newton, S. Yamashita, K. Hasumi, J. Matsuno, N. Yoshida, M. Nihei, T. Shiga, M. Nakano, H. Nojiri, W. Wernsdorfer, et al., *Angew. Chem. Int. Ed.* **2011**, *50*, 5716–5720.

[115] S. Fortier, J. J. Le Roy, C. H. Chen, V. Vieru, M. Murugesu, L. F. Chibotaru, D. J. Mindiola, K. G. Caulton, *J. Am. Chem. Soc.* **2013**, *135*, 14670–14678.

[116] M. Mikuriya, D. Yoshioka, A. Borta, D. Luneau, D. Matoga, J. Szklarzewicz, M. Handa, *New J. Chem.* **2011**, *35*, 1226–1233.

[117] B. Ballarin, G. A. Battiston, F. Benetollo, R. Gerbasi, M. Porchia, D. Favretto, P. Traldi, *Inorg. Chim. Acta* **1994**, *217*, 71–78.

[118] E. Iengo, G. D. Pantoş, J. K. M. Sanders, *Chem. Sci.* **2011**, *2*, 676–685.

[119] A. Yella, H.-W. Lee, H. N. Tsao, C. Yi, a. K. Chandiran, M. K. Nazeeruddin, E. W.-G. Diau, C.-Y. Yeh, S. M. Zakeeruddin, M. Gratzel, *Science (80-.).* **2011**, *334*, 629–634.

[120] M. G. Walter, A. B. Rudine, C. C. Wamser, *J. Porphyr. Phthalocyanines* **2010**, *14*, 759–792.

[121] L.-L. Li, E. W.-G. Diau, *Chem. Soc. Rev.* **2013**, *42*, 291–304.

[122] M. E. El-Khouly, O. Ito, P. M. Smith, F. D'Souza, *J. Photochem. Photobiol. C Photochem. Rev.* **2004**, *5*, 79–104.

[123] S. Fukuzumi, T. Honda, T. Kojima, *Coord. Chem. Rev.* **2012**, *256*, 2488–2502.

[124] M. O. Sinnokrot, C. D. Sherrill, *J. Phys. Chem. A* **2004**, *108*, 10200–10207.

[125] L. Rigamonti, C. Cotton, A. Nava, H. Lang, T. Rüffer, M. Perfetti, L. Sorace, A.-L. Barra, Y. Lan, W. Wernsdorfer, et al., *Chem. Eur. J.* **2016**, *22*, 13705–13714.

[126] S. R. Batten, N. R. Champness, X.-M. Chen, J. Garcia-Martinez, S. Kitagawa, L. Öhrström, M. O'Keeffe, M. P. Suh, J. Reedijk, *CrystEngComm* **2012**, *14*, 3001–3004.

[127] S. R. Batten, N. R. Champness, X.-M. Chen, J. Garcia-Martinez, S. Kitagawa, L. Öhrström, M. O'Keeffe, M. Paik Suh, J. Reedijk, *Pure Appl. Chem.* **2013**, *85*, 1715–1724.

[128] L. Öhrström, *Crystals* **2015**, *5*, 154–162.

[129] Y. Shen, H.-B. Zhu, J. Hu, Y. Zhao, *CrystEngComm* **2015**, *17*, 2080–2082.

[130] D. Naumann, W. Tyrra, A. von Foullon, I. Pantenburg, *Z. Anorg. Allg. Chem.* **2009**, *635*, 862–868.

[131] M. Marinšek, A. Meden, T. Skalar, M. Kasunič, *Acta Chim. Slov.* **2014**, *61*, 439–46.

[132] Q. Gao, J. Xu, D. Cao, Z. Chang, X.-H. Bu, *Priv. Commun.* **2015**, CCDC 1029711.

[133] P. Erler, P. Schmitt, N. Barth, A. Irmler, S. Bouvron, T. Huhn, U. Groth, F. Pauly, L. Gragnaniello, M. Fonin, *Nano Lett.* **2015**, *15*, 4546–4552.

[134] C. J. H. Jacobsen, E. Pedersen, J. Villadsen, H. Weihe, *Inorg. Chem.* **1993**, *32*, 1216–1221.

[135] L. Sorace, M.-E. Boulon, P. Totaro, A. Cornia, J. Fernandes-Soares, R. Sessoli, *Phys. Rev. B* **2013**, *88*, 104407.

[136] M. Perfetti, G. Cucinotta, M.-E. Boulon, F. El Hallak, S. Gao, R. Sessoli, *Chem. Eur. J.* **2014**, *20*, 14051–14056.

[137] M. Perfetti, E. Lucaccini, L. Sorace, J. P. Costes, R. Sessoli, *Inorg. Chem.* **2015**, *54*, 3090–3092.

[138] J. Liu, B. Wu, L. Fu, R. B. Diener, Q. Niu, *Phys. Rev. B* **2002**, *65*, 224401.

[139] W. L. F. Armarego, C. L. L. Chai, *Purification of Laboratory Chemicals*, **2003**.

[140] E. Alessio, M. Macchi, S. Heat, L. G. Marzilli, *Chem. Commun.* **1996**, 1411–1412.

[141] F. Menges, *Spekwin32, version 1.72.2*, Berchtesgaden, **2000-2016**.

[142] A. Altomare, G. Cascarano, C. Giacovazzo, A. Guagliardi, *J. Appl. Crystallogr.* **1993**, *26*, 343–350.

[143] G. M. Sheldrick, *SHELX-97, Programs Cryst. Struct. Anal. (Release 97-2)* **1997**, University of Gottingen, Germany.

[144] L. J. Farrugia, *J. Appl. Crystallogr.* **1999**, *32*, 837–838.

[145] C. F. Macrae, I. J. Bruno, J. A. Chisholm, P. R. Edgington, P. McCabe, E. Pidcock, L. . Rodriguez-Monge, R. Taylor, J. van de Streek, P. A. Wood, *J. Appl. Crystallogr.* **2008**, *41*, 466–470.

[146] W. Kabsch, *XDS. Acta Cryst.* **2010**, *D66*, 125–132.

[147] A. G. W. Leslie, H. R. Powell, in *Evol. Methods Macromol. Crystallogr. Struct. Path to Underst. Mech. Action CBRN Agents* (Eds.: R.J. Read, J.L. Sussman), Springer Netherlands, Dordrecht, **2007**, pp. 41–51.

[148] U. ZHEEV LAPACK Driver Routine (version 2.0), Univ. of Tennessee, Univ. of California Berkeley, NAG Ltd., Courant Institute, Argonne National Lab, and Rice University, **1994**.

[149] C. P. L. L. W. D. MINUIT., *MINUIT Funct. Minimization Error Anal. (version 94.1), Cern. Geneva,*

Switzerland, **1994-1998**.

[150] O. E04FCF NAG Ltd., *NAG Fortran Libr. Routine (Mark 17)* NAG Ltd, **1996**.

[151] W. Wernsdorfer, *Adv. Chem. Phys.* **2011**, *118*, 99–190.

[152] J. Hu, D. L. Mattern, *J. Org. Chem.* **2000**, *65*, 2277–2281.

[153] A. I. Vogel, *Textbook of Quantitative Chemical Analysis*, **1989**.

[154] G. A. Bain, J. F. Berry, *J. Chem. Educ.* **2008**, *85*, 532–536.

[155] G. M. Sheldrick, *Acta Crystallogr.* **2015**, *C71*, 3–8.

[156] A. L. Spek, *J. Appl. Cryst.* **2003**, *36*, 7–13.